Probing Galaxy Evolution with AKARI

Thesis

The Open University

Probing Galaxy Evolution With AKARI

A thesis submitted for the degree of Doctor of Philosophy

Astronomy Discipline, Department of Physical Sciences

Helen Rosemary Davidge, BSc

The Open University

30th June 2016

Abstract

This thesis presents the first detailed analysis of three extragalactic fields observed by the infrared satellite, AKARI. AKARI is the only telescope able to observe deeply in the Spitzer/IRAC - Spitzer/MIPS band gap of $8-24\,\mu$m. The first analysis of these extragalactic fields, was to perform galaxy number counts, the most basic statistical property of galaxy populations. Presented are the counts at 3, 4, 7, 11, 15 and 18 μm. These number counts were compared with published results and galaxy evolution models. These models are dependent on both the Spectral Energy Distribution (SED) templates and evolution of the galaxy types. The phenomenological backwards evolution model of Pearson (2005) appeared to be consistent with the number counts. To probe this, number counts were extracted from below the survey limit by performing Probability of Deflection (P(D)) fluctuation analysis. The Pearson model was found to be consistent with the 11 μm P(D) analysis but not with the 15 μm. The results from the 15 μm P(D) analysis indicates that the Pearson model under predicts the evolution of star forming galaxies. Multi-wavelength band-merged catalogues for the two deep extragalactic fields were created using AKARI data from the work of this thesis and ancillary data. The separation of galaxy type using AKARI/IRC filter colours was explored. For $z < 2$ a separation criteria was found for Active Galactic Nuclei (AGN), but to accurately classify galaxy type, SED fitting is required. Submm-selected galaxies detected by AKARI were found to resemble scaled-up normal local spiral galaxies, rather than starbursts, consistent with them lying on the high-redshift 'main sequence' unlike local ultraluminous infrared galaxies. The thesis concludes by measuring the the percentage of the far-infrared Cosmic Infrared Background (CIB) resolved by AKARI mid-infrared galaxies. By performing stacking analysis on a Herschel/SPIRE 250 μm image of AKARI galaxy positions, it was found that AKARI mid-infrared galaxies resolve $\sim 10\%$ of the 250 μm CIB.

Acknowledgements

Firstly thank you to my supervisors Stephen Serjeant, for taking me on as a PhD student, and to Chris Pearson for adopting me as a student.
Domo arigato gozaimasu (thank you very much) to the Infrared Astronomy group at JAXA in Japan, especially Kazumi Murata for all those Skype meetings, Hideo Matsuhara for hosting me as a JSPS Summer Fellowship student and Takehiko Wada for his help with the AKARI instrumentation.
Closer to home, at the Open University, a special thanks goes to Laia Barrufet, Ben Dryer, Chris Sedgwick and Jo Jarvis and my colleagues in the PhD student office.
Lucia Marchetti and Mattia Vaccari have been most useful with providing the Spitzer Data Fusion catalogue and help with use of LePhare.
A thank you to Jessica Krick for the use of the IRAC Dark Field multi-wavelength catalogue.
Also thank you to Francis Ring of the William Herschel Society, for information about Herschel's discovery of infrared radiation.
None of the work of this thesis could have been done without the help of my other half, Graham Woodhouse.
I would especially like to thank Aleksi Suutarinen, Andrew Clements, Vicky Bending, Jean-David Bodénan, Anna Parrika, Tobias Hastings, Alex Barrett, Zoë Ellery, Rebecca Brodeur, Ashley James, Do Young Kim and Roger Axtell for all their support and for putting up with me!
Thanks to Martin Davidge for all those science and maths chats dating back further than I can remember, to Sally-Jane Davidge for always being on the other end of a telephone, and to Sarah and Simon Davidge for all those Facebook chats.
Also thanks for the support from the STFC Dyslexia Working Group, especially Judi Stewart.
And finally thanks to Eigenvalue, Mistborn, UFRP and Dancebox for keeping me sane!

Was it all worth it, yes, it was a worthwhile experience!

- Freddie Mercury

Contents

List of Figures

Chapter 1

Introduction to Space Infrared Astronomy

My story... begins as all good stories should... once upon a time

These Old Shades - Georgette Heyer

1.1 Introduction

This chapter provides a background on infrared extragalactic astronomy. Section 1.2 gives a very brief summary of the discovery of infrared radiation and then summarises some of the main galaxy types observed at infrared wavelengths. Section 1.3 discusses previous infrared satellites and Section 1.4 leads on to discuss the main contributions to our understanding of galaxy evolution by these missions. Section 1.5 gives a brief overview of the thesis.

1.2 Infrared Radiation

Infrared radiation was first detected by William Herschel in 1800. By splitting sunlight up using a prism and placing a thermometer next to the red end of the projected visible spectrum, Herschel showed that there was thermal radiation next to the red coloured

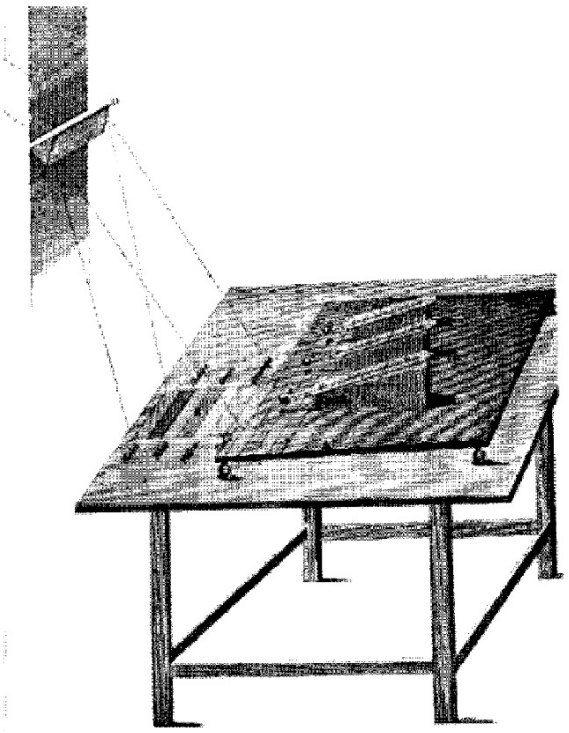

Figure 1.1: Figure showing the drawing in Herschel (1800a) of the experiment which discovered infrared radiation. Sunlight is split by the prism (top left) and the spectrum is shone onto the table. Shown on the table are three thermometers (the triangular shapes), one thermometer is measuring the temperature of the infrared radiation and the other two act as a control.

light. Figure 1.1 shows a drawing of the experiment. William Herschel had discovered the first non-visible light and called this calorific (heat) rays (Herschel, 1800b). The part of the electromagnetic spectrum that Herschel had discovered is now known as infrared radiation. 'Infrared' is broadly used to refer to the part of the electromagnetic spectrum between optical light and submillimetre (submm) light. For the work in this thesis, near-infrared may be considered to have a wavelength range of $\sim 1-5\,\mu$m, mid-infrared may be considered to be $\sim 5-40\,\mu$m and far-infrared may be considered to be $\sim 40-350\,\mu$m.

Studying galaxies using data obtained by infrared satellites is the main topic of this thesis. Multi-wavelength data from much of the electromagnetic spectrum is required to fully understand the physical processes in galaxies. For galaxy evolution the infrared is a key wavelength range to study. The near-infrared galaxy emission is normally dominated by the Rayleigh-Jeans tail of evolved stellar populations. The

mid-infrared contains thermal emission from Active Galactic Nuclei (AGN) torus. In star forming galaxies the mid-infrared also contains thermal emission of dust from re-radiated starlight. Star forming galaxy spectra also contain strong polycyclic aromatic hydrocarbon (PAH) features, thermal emission from dust surrounding hot young stars emitting in the UV, and a silicate absorption feature. The far-infrared contains the peak of the thermal emission from dust in the interstellar medium (ISM), known as Giant Molecular Clouds (GMC). By studying infrared emission, one is able to probe processes in galaxies not visible in optical light. Galaxies which contain large amounts of dust absorb optical starlight and re-radiate it at longer wavelengths in the infrared.

As a result of advancements in infrared astronomy many exotic and unexpected types of galaxies have been discovered. In the near-infrared, galaxies at $z > 2$ have been discovered with large J-band (1.25 μm) magnitudes compared with the K-band (2.2 μm), known as Distant Red Galaxies (DRGs). These are thought to be dusty star forming galaxies or galaxies containing old stellar populations (Franx et al., 2003). Luminous in the mid-infrared are Dust Obscured Galaxies (DOGs) which exhibit strong 24 μm emission in the R-band/24 μm colour. DOGs are thought to be starburst or active galaxies, possibly at a later stage in their evolution than submillimetre Galaxies (see below), i.e. after a massive merger (Pope et al., 2008). At far-infrared/submm wavelengths submillimetre Galaxies (SMGs) have been observed. They are thought to be massive starburst galaxies, possibly undergoing a galaxy merger, and believed to be the progenitors of giant elliptical galaxies in the local Universe (Takagi et al., 2004). Observed in the mid and far-infrared are Luminous Infrared Galaxies (LIRGs), Ultraluminous Infrared Galaxies (ULIRGs) and Hyperluminous Infrared Galaxies (HLIRGs), with infrared luminosities of $10^{11} - 10^{12}\,L_{\odot}$, $10^{12} - 10^{13}\,L_{\odot}$ and $> 10^{13}\,L_{\odot}$ respectively. These galaxies are thought to be a combination of starburst and AGN. It is currently uncertain what caused this large amount of star formation (Farrah et al., 2004).

It is difficult to observe the infrared from ground based observatories, because the Earth's atmosphere is opaque or greatly reduces the signal over much of the infrared. At wavelengths $1 - 2.5\,\mu$m, the Earth's atmosphere has strong hydroxyl (OH) absorp-

tion lines and molecular hydrogen lines. At wavelengths $\gtrsim 2.5\,\mu$m the atmosphere acts like a black body, with a peak temperature of $\sim 250\,$K, caused by water vapour (Kashlinsky, 2005). Thus only specific wavelength bands can be observed from ground based facilities, in between the absorption features. Ground based facilities have a further problem attempting to observe even these specific wavelengths, due to thermal background emission from the Earth's atmosphere, the Earth and the telescope itself. To be able to observe the whole of the infrared with as small an amount of thermal background radiation as possible, a satellite is required.

1.3 Infrared Satellites

1.3.1 The Infrared Astronomical Satellite

The first infrared satellite was the Infrared Astronomical Satellite (IRAS). IRAS was a joint UK, USA and Dutch mission, which launched in 1983. It had three instruments on board; the Survey Array, able to image at 12, 25, 60 and $100\,\mu$m, the Low Resolution Spectrometer (LRS) which contained a stills spectrometer with wavelength range $7.5-23\,\mu$m, and a Chopped Photometric Channel (CPC), which could image at 50 and $100\,\mu$m simultaneously (Neugebauer et al., 1984). Prior to IRAS, astronomically speaking, the infrared was a fairly unknown wavelength range, due to the lack of coverage from ground based facilities. IRAS proved that there is an infrared sky and performed the first infrared all sky survey, surveying 96% of the sky. From these images several source catalogues were created (Soifer et al., 1987). Using the faint source catalogue of IRAS the first high-redshift HLIRG, was discovered. The source was calculated to lie at the then very high redshift of $z = 2.286$ and to be even more luminous in the infrared than the previously discovered LIRG type of galaxy (Rowan-Robinson et al., 1991). IRAS data was used to make the first measurements of the local far-infrared luminosity function (Lawrence et al. (1986) and Saunders et al. (1990)). The infrared luminosity function was found to drop-off less steeply than predicted by

the then current models. The bright end of the local luminosity function was found to be dominated by starburst galaxies and AGN.

1.3.2 Cosmic Background Explorer

The next infrared and microwave satellite, launched in 1989, was NASA's Cosmic Background Explorer (COBE). The main aim of the mission was to measure the Cosmic Microwave Background (CMB) and the Cosmic Infrared Background (CIB) from 1 μm to 10 mm. COBE contained three instruments, the Far-Infrared Absolute Spectrometer (FIRAS) observing at $100-500\,\mu$m and $500\,\mu$m-10 mm, the Differential Microwave Radiometers (DMR) observing at millimetre (mm) wavelengths, and the Diffuse Infrared Background Experiment (DIRBE) imaging at 1.25, 2.2, 3.5, 4.9, 12, 25, 60, 100, 140 and 240 μm (Boggess et al., 1992). COBE/FIRAS made the first all sky map of the CMB. Measurements showed that the CMB was best fit by a blackbody spectrum with a temperature of 2.735 ± 0.06 K. Providing that the CMB was indeed thermal gave direct observational evidence to confirm a prediction of the big bang model (Mather et al., 1990). Continuing the work of COBE, Wilkinson Microwave Anisotropy Probe (WMAP) and Planck measured the CMB with a greater precision (see below). COBE/DMR was designed to study the anisotropies in the CMB. Results using the DMR showed how gravitational instabilities in the early Universe led to structure formation (Smoot et al., 1991). Work had been performed using data obtained by IRAS to measure the absolute value for the CIB; but this work had only been able to place upper limits (Hauser & Dwek, 2001). Using COBE/FIRAS data gave the first tentative detection of the CIB in the wavelength range $400-1000\,\mu$m (Puget et al., 1996). Data from COBE/DIRBE gave absolute measurements of the CIB in the far-infrared at 140 and 240 μm and the first tentative detections of the CIB in the near-infrared at 2.2 and 3.5 μm. Due to being unable to fully remove all the foregrounds, DIRBE data were only able to place upper limits on the CIB on the other six filters (Hauser et al. (1998), Dwek & Arendt (1998), Wright & Reese (2000) and Gorjian et

al. (2000)). The discovery and measurements of the CIB are discussed in more detail in Section 6.2.

1.3.3 Infrared Space Observatory

The Infrared Space Observatory (ISO), launched in 1995, was a European Space Agency (ESA) mission. ISO had four instruments on board (Kessler et al., 1996): the ISO-CAM, a two channel camera observing $2.5-5.5\,\mu$m and $4-18\,\mu$m (Cesarsky et al., 1996); the ISOPHOT, a multi-band photopolarimeter, made up of a photo-polarimeter ($3-120\,\mu$m), an imaging array ($40-240\,\mu$m), a polarimeter (24 and $170\,\mu$m) and a spectrophotometer ($2.5-12\,\mu$m) (Lemke et al., 1996); the other two instruments on board ISO were the Long Wave Spectrometer (LWS) observing $43-196.9\,\mu$m and the Short Wave Spectrometer (SWS) observing $2.38-45.2\,\mu$m (Clegg et al. (1996) and de Graauw et al. (1996)). Infrared luminosity functions created using ISO data have shown that dust evolution in galaxies is greater than thought by the then contemporary models, at least up to $z=1$ (Rowan-Robinson et al., 1997). The $90\,\mu$m ISO luminosity function was found to be in general agreement with that predicted by IRAS (Serjeant et al., 2004). Data from the ISO mission confirmed that dust and large molecules absorb a single UV/optical photon and then re-radiate it as thermal emission in the near and mid-infrared. ISO data could separate mid-infrared emission from nearby elliptical and lenticular galaxies into interstellar medium, stellar emission and AGN emission. Work which was carried out showed how useful the mid-infrared part of a galaxy's spectral energy distribution (SED) is in separating different types of active galaxies, specifically by studying the PAH features (Genzel & Cesarsky, 2000). It was in this mission that the eleven extragalactic fields known as the European Large Area ISO Survey (ELAIS) were observed (Oliver et al., 2000). ELAIS North One (ELAIS-N1) will be discussed in more detail in Section 3.4 as one of the three extragalactic fields studied in this thesis.

1.3.4 The Infrared Telescope in Space

The Infrared Telescope in Space (IRTS) was Japan's first orbiting infrared telescope. In 1995, the IRTS was flown on board the Space Flyer Unit (SFU) for 30 days. The IRTS contained four instruments, the Near-Infrared Spectrometer (NIRS) ($1.38-3.98\,\mu$m), the Mid-Infrared Spectrometer (MIRS) ($4.5-11.7\,\mu$m), the Far-Infrared Line Mapper (FILM) (155.3 and 160.3μm) and the Far-Infrared Photometer (FIRP) (150, 250, 400 and $700\,\mu$m) (Murakami et al., 1996). This survey telescope was mainly used to observe Galactic emission, but the IRTS also made 24 measurements of the CIB between $1.4-4.0\,\mu$m using the NIRS (Matsumoto et al., 2005).

1.3.5 Spitzer

Following on from COBE, NASA's next infrared space mission was Spitzer. Spitzer, one of NASA's four Great Observatories, was launched in 2003, and had three instruments on board: the Infrared Array Camera (IRAC) imaging at 3.6, 4.5, 5.8 and $8.0\,\mu$m; the Infrared Spectrograph (IRS) with four spectrographs ($5.2-7.7$, $7.4-14.5$, $14.0-21.3$ and $19.5-38.0\,\mu$m) and two low resolution imaging filters ($13.3-18.7$ and $18.5-26.0\,\mu$m); the Multi-band Imaging Photometer for Spitzer (MIPS) observing at 24, 70 and $160\,\mu$m (Werner et al., 2004). Spitzer performed many surveys of extragalactic fields. Due to the sensitivity of the telescope, particularly at $24\,\mu$m, Spitzer was able to observe galaxies in the infrared out to higher redshifts; thus probing galaxy evolution over a larger redshift range and was able to measure star formation and stellar masses in galaxies at a higher redshift than previously. Early MIPS $24\,\mu$m galaxy number counts are in agreement with those predicted by ISO data. The number counts show there is strong galaxy evolution, and that the infrared luminosity function is dominated by LIRGs (Le Floc'h et al., 2005). Deep $24\,\mu$m number counts have also shown that there galaxies have strong evolution. The deep counts show a peak, which the ISO counts did not, this is thought to be caused by a new population of fainter sources, not detected by ISO (Papovich et al., 2004). The 5.8 and $8.0\,\mu$m IRAC galaxy

number counts show evidence of shorter wavelength PAH features (Fazio et al., 2004). IRAC sources have resolved $\sim$50 % of the CIB detected by COBE/DIRBE (Ashby et al., 2015).

Data from several Spitzer surveys have been used in this thesis, including Spitzer Wide-Area Infrared Extra-galactic Survey (SWIRE) (Lonsdale et al., 2003) and the Spitzer Extragalactic Representative Volume Survey (SERVS) (Mauduit et al., 2012). Both of these two surveys observed ELAIS-N1, SWIRE during the cryogenically cooled phase, and SERVS during the warm phase of the mission. Much work has been performed on cross-matching the source catalogues from these two surveys with ancillary data, known as the Spitzer Data Fusion, see Section 5.2.1 for further details about the catalogues (Vaccari, 2016). One of the Spitzer Data Fusion band-merged catalogues, European Large Area ISO Survey (ELAIS) North one (N1) was cross-matched with the ELAIS-N1 AKARI galaxy catalogue created as part of the work of this thesis, this is discussed in Section 5.3.2. Also in the thesis the band-merged catalogue created by Krick et al. (2009) of the IRAC Dark Field, an IRAC calibration field, has been cross-matched with the AKARI galaxy catalogue, which is discussed in Section 5.3.3. In Chapter 4 of this thesis, the IRAC 3.6, 4.5 and 8.0 μm galaxy number counts of Fazio et al. (2004) and the IRS 16 μm number counts of Teplitz et al. (2011) are compared with the AKARI number counts of ELAIS-N1, the IRAC Dark Field and the AKARI Deep Field South.

1.3.6 AKARI

Much of the work of this thesis has used data from the AKARI telescope. AKARI is described in more depth in Section 2.2. This subsection will provide just a brief summary of the mission. Continuing from the work of IRTS, AKARI was Japan's first dedicated infrared satellite, launched in 2006, with collaboration from Europe and South Korea. AKARI had two instruments on board, the Far-Infrared Surveyor (FIS) and the InfraRed Camera (IRC), both of which were capable of imaging and

spectroscopy (Murakami et al., 2007). The FIS had four photometric bands at 65, 90, 140 and 160 μm, and two imaging Fourier-transform spectrometers ($60-110$ and $110-180\,\mu$m) (Kawada et al., 2007). The IRC had nine imaging filters at: 2.4, 3.2, 4.1, 7, 9, 11, 15, 18 and 24 μm. The IRC also had one prism ($1.8-5.2\,\mu$m) and four grisms ($2.5-5.0$, $5.4-8.4$, $7.5-12.9$ and $17.5-25.7\,\mu$m) (Onaka et al., 2007). One of the main aims of the AKARI mission was to perform an all sky survey in the infrared, which had only previously been done by one other satellite, IRAS. AKARI performed an all sky survey at 9, 18, 65, 90, 140 and 160 μm (Ishihara et al., 2010). Two extragalactic fields, well studied by AKARI are the North Ecliptic Pole (NEP) and the AKARI Deep Field South (ADF-S) (Matsuhara et al., 2006). IRC data has been used to create the largest asteroid catalogue in the mid-infrared (Usui et al., 2011). One of the motivations behind the choice of wavelength for the IRC filters was to study the mid-infrared PAH features in galaxies. Higher redshift ULIRGs appear to have more luminous PAH features than local Universe ULIRGs (Takagi et al., 2010). Infrared luminosity functions have been derived using AKARI sources. Similar to Spitzer luminosity functions, they show strong galaxy evolution and are dominated by flux from ULIRGs and LIRGs (Goto et al., 2010).

AKARI/IRC observations of the ADF-S have been used for the work of this thesis, see Chapter 3.

1.3.7 Herschel Space Telescope

The Herschel Space Telescope, part of the ESA's 'Horizon 2000', was launched in 2009. With a 3.5 m primary mirror, Herschel was the largest space telescope. It had three instruments on board: the Photodetector Array Camera and Spectrometer (PACS), with three band imaging at $60-85$, $85-130$, $130-210\,\mu$m and a single spectrometer at $55-210\,\mu$m; the Spectral and Photometric Imaging Receiver (SPIRE), with three imaging bands at 250, 350 and 500 μm and two Fourier transform spectrometers observing at $194-324$ and $316-671\,\mu$m; and the Heterodyne Instrument for the

Far-Infrared (HIFI), which observed at $157-212\,\mu$m (Pilbratt et al., 2010). As Herschel/SPIRE was the first instrument able to probe deeply in the longer far-infrared and submm wavelengths, thus it was able to observe galaxies for the first time, which were not visible at shorter wavelengths. SPIRE data combined with PACS data has greatly added to our understanding of galaxy evolution. Herschel covers the peak of re-radiated starlight by dust in star forming galaxies. In many cases these dusty star forming galaxies are not visible at shorter wavelengths, due to absorption in the UV, optical and near-infrared. Thus Herschel idea to observe how star forming galaxies have evolved.

Herschel had several cosmology key programmes to observe deeply, specific extragalactic deep field, including: PACS Evolutionary Probe (PEP) (Lutz et al., 2011), Herschel Astrophysical Terahertz Large Area Survey (H-ATLAS) (Eales et al., 2010a), Great Observatories Origins Deep Survey (GOODS Herschel) (Elbaz et al., 2011) and Herschel Multi-tiered Extragalactic Survey (HerMES) (Oliver et al., 2012). One of the main science motivations behind Herschel was to understand galaxy formation and evolution. Mainly by using the key surveys listed above, Herschel has greatly added to our knowledge of galaxy evolution. A brief summary of some of these main contributions are described below.

One key result from Herschel is that a much higher percentage of stars formed steadily in star forming galaxies, as apposed to part of an intense starburst episode, than previously thought. Elbaz et al. (2011), used both PACS and SPIRE data from the GOODS Herschel key programme to study galaxies at $z < 2.5$. They combined these data with ancillary IRAS, ISO, Spitzer and AKARI data, and fitted SEDs to $\sim$2000 sources. Elbaz et al. (2011) separated star forming galaxies from starburst galaxies by using the ratio of total infrared flux and the rest frame $8\,\mu$m flux. This separation used the $7.7\,\mu$m PAH feature. Star formation in star forming galaxies is thought to be distributed throughout the galaxy, thus the galaxy has strong PAH features. Whereas, in starbursts, galaxies which are undergoing a violent and rapid burst of star formation, the star forming region is normally concentrated in specific regions of the galaxy. Due

to the intense UV radiation from this region, a percentage of the PAHs are destroyed, thus PAH emission is suppressed. Using their separation criteria, Elbaz et al. (2011) found that $\sim 20\,\%$ of their sources are starburst, whereas the rest are star forming. Thus passive star formation is the dominate type of star formation for $z < 2.5$; which includes the peak of star formation, $z \sim 2$ (see Figure 1.2 for the peak of star formation history).

The results of Elbaz et al. (2011) are in agreement with those of Rodighiero et al. (2011), who also found that there is a much higher percentage of passive star formation as apposed to star formation in an intense starburst. Rodighiero et al. (2011) use PACS data combined with optical and near-infrared ancillary data to investigate the star formation rate density at $1.5 < z < 2.5$, which covers the peak of cosmic star formation history. Rodighiero et al. (2011) found that in this redshift range starbursts contribute to $\sim 10\,\%$ of the cosmic star formation density. They state that though not a major contribution to star formation, the study of starbursts is important to understand galaxy evolution, as they are thought to be star forming galaxies evolving into elliptical galaxies.

An early galaxy evolution result from combining PACS and SPIRE data showed that over a large redshift range, star formation is fairly similar in both galaxies which contain an AGN, and those which do not (Elbaz et al., 2010). SPIRE data has shown that there is a much higher than expected star formation rate in early galaxies; with the discovery of a massive starburst galaxy at $z = 6.34$ (Riechers et al., 2013). SPIRE data have also been used to investigate the suppression of star formation by powerful AGN in high-z galaxies, as it is believed that AGN quenches star formation. Page et al. (2012) discoverd that star formation in galaxies containing a very powerful AGN is indeed suppressed. More recently PACS data has been used to investigate AGN quenching of star formation. Tombesi et al. (2015) found the first detection of a powerful molecular outflow from a ULIRG. This is believed to be an outflow from an AGN accretion disk. This explains how the presence of an AGN can cause quenching of star formation in its host galaxy. Another more recent paper shows that by cross-matching

the positions of overdense regions in Planck data with sources in detected by SPIRE, galaxies, galaxy clusters and lensed galaxies in the redshift range $2 < z < 4$ can be found (Planck Collaboration et al., 2015). This is thought to be a good way to study structure formation.

Using H-ATLAS data, Negrello et al. (2010) demonstrated a new way to detect strongly-lensed bright submm galaxies (SMG). Their method used the assumption that 500 μm submm sources with redshift $z > 1$ with a flux $\gtrsim 100$ mJy are very rare. They investigated a subsample of the sources in the 500 μm SPIRE, H-ATLAS catalogue with a flux > 500 mJy. By cross-matching these sources with shorter wavelength ancillary data, Negrello et al. (2010) were able to remove all nearby and Galactic sources. They then removed the foreground galaxies in the 5 lensed candidates by performing spectroscopic follow-up work. They believe that all 5 sources are ULIRGs. This novel approach to detecting strongly-lensed SMGs was made possible with Herschel, as Herschel was the first telescope able to perform large area submm surveys, of which H-ATLAS was one of the largest. González-Nuevo et al. (2012) improved upon the selection method of Negrello et al. (2010) to detect fainter lensed systems. González-Nuevo et al. (2012) also used H-ATLAS data to demonstrate their selection method, which is known as Herschel ATLAS Lensed Objects Selection (HALOS). The HALOS method also uses the assumption that the brighter flux galaxies are dominated by lensed objects. The method differs to that of Negrello et al. (2010) in that all three SPIRE bands are used. Candidate lensed sources are selected with 350 μm flux > 85mJy and 250 μm flux > 35 mJy. HALOS then uses deep near-infrared data to separate lensed objects from bright non-lensed sources. They have extended the selection to fainter flux systems and thus have a more representative sample of star forming galaxies, than those found by Negrello et al. (2010). From a subsample of the H-ATLAS data they found 31 candidate strongly-lensed galaxies, González-Nuevo et al. (2012) state that in the entire H-ATLAS survey their method should detect ~ 1000 strongly-lensed sources, whereas the method of Negrello et al. (2010) would find ~ 100 candidates. Negrello et al. (2010) state that their method is ~ 100 % efficient, whereas the method

of González-Nuevo et al. (2012) is ~ 70 % efficient.

Herschel extragalactic deep field data has been used to create far-infrared and submm galaxy number counts and to resolve sources contributing to the CIB. Briefly discussed below are a selection of number count work and resolving of the CIB using Herschel sources. Berta et al. (2010) presented PACS galaxy number counts using early PEP data. Comparison with the then contemporary galaxy evolution models, showed that the models over predicted the peak of number count and the number of fainter galaxies. Berta et al. (2010) also used the PEP sources to resolve 45 and 52 % of the CIB at 100 and 160 μm respectively. They found that the galaxies contributing to the CIB are mainly LIRGs and ULIRGs. Oliver et al. (2010) used HerMES data to create galaxy number counts for the three SPIRE bands. Comparing the counts with existing galaxy evolution models, they found that though the models follow the general trend of the counts, most models over predict the bright end counts, i.e. $S > 100$ mJy. They observed a much steeper than predicted rise in number counts for $20\,\text{mJy} < S < 100\,\text{mJy}$. Oliver et al. (2010) stated that they resolve 15, 10 and 6 % of the CIB at 250, 350 and 500 μm respectively. They state that the faint end number counts are dominated by confusion. The work of Glenn et al. (2010) attempted to extract information from the image below the confusion limit using Probability of Deflection (P(D)) analysis. P(D) analysis is discussed in more detail in Chapter 4 and the work of Glenn et al. (2010) is discussed in more detail in Section 4.2. Glenn et al. (2010) used early HerMES data to create parameterised galaxy number counts models for all three of the SPIRE bands. They found that a non-physical parametric model fits the number counts of Oliver et al. (2010) well, but is inconsistent with existing galaxy evolution models. As discussed above, previous models have over predicted the bright end number counts slope, Glenn et al. (2010) stated that the models are probably over predicting the number of ULIRGs and possibly LIRGs. Glenn et al. (2010) calculated the amount of the CIB which their parameterised galaxy number counts model resolves; which is 64, 60 and 43 % at 250, 350 and 500 μm.

Several luminosity functions have been derived using Herschel data. Eales et al.

(2010b) presented the first HerMES submm luminosity function at 250 μm. They split the galaxies into six redshift intervals between $0 < z < 2$, and found that the 250 μm luminosity function has strong evolution at $z < 1$, but weak evolution at $1 < z < 2$. Using optical Hubble data, Eales et al. (2010b) found that many of their sources are spiral galaxies, thus Herschel is probing a different type of galaxy to Submillimetre Common Users Bolometer Array (SCUBA), which are dominated by major-merger galaxies. Gruppioni et al. (2013) presented very detailed work on the infrared luminosity functions, using PEP PACS data and HerMES SPIRE data, for galaxies up to a redshift of $z \sim 4$. This paper describes the first time that the evolution of the different galaxy populations contributing to the infrared has been studied using such a comprehensive sample. The paper also presented the SED fitting of the PEP sources with ancillary data, which enabled the galaxies to be separated into five different galaxy types. Gruppioni et al. (2013) found that as a whole the galaxies contributing to the infrared luminosity functions have positive evolution in luminosity and a negative evolution in density. Investigating the individual galaxy populations, Gruppioni et al. (2013) found that spiral galaxies dominate the luminosity functions at low redshifts ($z \lesssim 0.6$), whereas star forming and AGN composite objects are dominate up to $z < 2.5$ and AGN start to dominate at higher redshifts ($z > 2.5$). Gruppioni et al. (2013) showed that different types of galaxies evolve differently. They found that there are two distinct types of galaxy evolution; this explains why we predominantly see spiral and elliptical galaxies in the local Universe. The first type of galaxy evolution starts with a high redshift starburst galaxy, which evolves into a star forming and AGN composite object, which in turn evolves into a present day spiral. The second type starts with a star forming and AGN composite starburst, which evolves into a type 1 or 2 AGN, which in turn evolves into a present day elliptical galaxy. Galaxies from the first scenario all lie on the galaxy main sequence. The galaxy main sequence is discussed below in Section 1.4. Whereas galaxies from the second scenario all lie above the main sequence, indicating two distinct populations. Marchetti et al. (2016) presented a very comprehensive analysis of local and low redshift luminosity functions for the

three SPIRE wavelengths. They used HerMES data to investigate the $0.02 < z < 0.5$ luminosity function. Marchetti et al. (2016) found that the bright end of their luminosity functions are dominated by early-type spiral galaxies, while the lower luminosities are dominated by late-type spiral and irregular galaxies. The luminosity functions of Eales et al. (2010b) are in general agreement with those of Marchetti et al. (2016), in that there is a strong evolution in low redshift galaxies; but there is a discrepancy at lower luminosities. Marchetti et al. (2016) think this is due to the fact that Eales et al. (2010b) uses shallower Herschel data and less ancillary data. Marchetti et al. (2016) found that low redshift galaxies have a stronger positive evolution in luminosity, and a stronger negative evolution in density, than found by Gruppioni et al. (2013). Marchetti et al. (2016) believed the discrepancy could be due to the fact that the sample used in Gruppioni et al. (2013) to create the luminosity functions is narrower and deeper, and thus did not have as many low redshift samples.

Processed Herschel SPIRE data has been used in the work of this thesis. The SPIRE three band catalogue of the ELAIS-N1 deep field, observed as part of HerMES has been cross-matched with the AKARI ELAIS-N1 catalogue of this thesis, see Section 5.3.2. The IRAC Dark Field was used as a calibration field for SPIRE and as such is very deep Herschel data (Pearson et al., in prep). This thesis presents the first use of this SPIRE data. The three band galaxy catalogue of the IRAC Dark Field have been cross-matched with the AKARI catalogue, see Section 5.3.3. The SPIRE 250 μm IRAC Dark Field image was used in the work of Chapter 6 of this thesis, where the positions of the AKARI mid-infrared galaxies on the SPIRE image were stacked, to calculate how much of the 250 μm CIB the mid-infrared AKARI galaxies resolved.

1.3.8 Planck

The Planck satellite, an ESA mission, was launched with the Herschel Space Telescope in 2009. Planck had two instruments on board: the High Frequency Instrument (HFI), observing at 350, 550, 850, 1380 and 2100 μm; and the Low Frequency Instru-

ment (LFI), observing at 4.38, 7.50 and 10.00 mm (Tauber et al. (2010) and Planck Collaboration et al. (2014a)). The main aim of the mission was to measure the temperature, anisotropies and polarisation of the CMB. Results from Planck confirmed the COBE and WMAP results that the CMB is best fit by a thermal blackbody, in agreement with the lambda cold dark matter (ΛCDM) model for the Universe and the big bang nucleosynthesis model. Compared to WMAP, Planck data showed that the Hubble parameter ($H_\circ$) is smaller, that the dark energy density (Ω_Λ) is smaller and that the baryonic energy density (Ω_b) and dark matter energy density (Ω_m) is greater. Planck data were also used to calculate the CIB power spectra and to model at what redshift ranges the sources contributing to the CIB are likely to lie (Planck Collaboration et al., 2011).

1.3.9 Wide-field Infrared Survey Explorer

Following from the infrared all sky surveys of IRAS and AKARI, NASA launched the Wide-field Infrared Survey Explorer (WISE) in 2009. The main aim of the WISE mission was to perform an all sky survey at 3.4, 4.6, 12 and 22 μm (Wright et al., 2010). As well as creating comprehensive source catalogues, the WISE mission has compiled a mid-infrared asteroid catalogue, including the first Earth trojan asteroid (Wiegert et al. (1997) and Nugent et al. (2016)).

The WISE all sky survey source catalogue has been used in this thesis to create several steps in the optimised pipeline, the subject of Chapter 2. The locations of the WISE sources have been used to correct for AKARI/IRC image distortion and in the astrometry correction step, see Sections 2.4.3.8 and 2.4.3.12 respectively. The WISE source catalogue was also used to calculate the positional offset of the AKARI galaxies of Chapters 3 and 4.

1.4 Galaxy Evolution

The missions described in the previous section led to important developments in our understanding of galaxy evolution. Before the use of infrared satellites, in the late 1980s, there were two main opposing views on galaxy formation; monolithic collapse and hierarchical merging. The monolithic collapse model assumes that galaxies formed at high redshifts from clouds of primordial gas, based on observations of stars in the Milky Way Galaxy (Eggen et al., 1962). The hierarchical merging model assumes that protogalaxies formed in small 'clumps' of primordial matter and then merged together to form larger galaxies. In this theory the smallest galaxies formed first (White & Rees, 1978).

After the discoveries using IRAS of HLIRGs (see the discovery of Rowan-Robinson et al. (1991) in Section 1.3.1), a much higher rate of star formation had been observed for some galaxies in the infrared than predicted by models based on optical data. It was uncertain whether these ULIRGs and HLIRGs were powered by AGN or by starbursts. Due to the then high redshift of these galaxies, observations seemed to be implying that the most massive galaxies formed earlier than smaller galaxies, known as downsizing. Downsizing had first been observed in optical galaxies by the Low Resolution Imaging Spectrometer (LRIS) (Oke et al., 1995) on the Keck telescope (Cowie et al., 1996). Madau et al. (1996) attempted to calculate the star forming rates of UV, optical and near-infrared data by tracing the cosmic evolution in redshift, by plotting star formation rate against redshift, to give the cosmic star formation history. This type of diagram is known as a Madau (or Madau-Lilly) diagram. Madau et al. (1998) plotted this diagram using optical Hubble Space Telescope data of the Hubble Deep Field (HDF). The following infrared surveys placed further constraints on the Madau diagram. See Figure 1.2 for an example of a more recent Madau diagram.

ISO, following on from the work of IRAS, continued the work on understanding ULIRGs. ISO data showed that ULIRGs are merging galaxies and are comprised of composite starburst and AGN sources (Genzel & Cesarsky, 2000). The results from

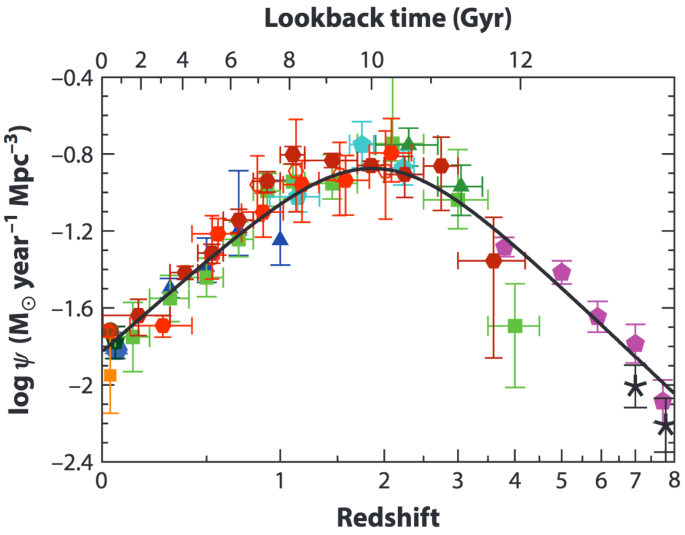

Figure 1.2: Figure showing the cosmic star formation history, plotting star formation rate against redshift and look back time (Madau & Dickinson (2014) and references therein).

observations of the HDF by ISO showed that ULIRGs have much higher comoving star formation rates than those in the local Universe (Rowan-Robinson et al., 1997), though the estimates were subsequently revised downwards (Aussel et al., 1998). Ground based facilities, observing in the submm, also observed very high star formation rates. Hughes et al. (1998) used SCUBA to observe the HDF and obtained the deepest submm image of the sky. They found large amounts of star formation at $z > 2$, which was over 5 times greater than expected from optical/UV surveys. In the submm to mm wavelengths high redshift $z \sim 2-5$ star forming galaxies have similar observed fluxes to the same population of galaxies at an intermediate redshift $z \sim 0.5-1$, due to negative k-corrections. In the submm and mm wavelengths, as a star forming galaxy is redshifted to higher and higher redshifts, due to the steepness in the Rayleigh-Jeans tail longward of the peak of the thermal dust emission, the increase in flux 'up' the Rayleigh-Jeans tail becomes greater than the reduction in flux due to increasing distance. Thus the more distant starburst galaxies appear brighter in flux. This new type of galaxy discovered by SCUBA is known collectively as submillimetre Galaxies (SMGs), because of their large amount of submm flux, see Section 1.2. These submm surveys gave more evidence for downsizing, as explained in the above paragraph.

After the ISO, the next infrared satellite was Spitzer, see Section 1.3.5 for a description of the Spitzer mission. Spitzer was able to go much deeper than previous infrared satellites, thus providing much more data and to greater accuracy. The new data provided by Spitzer were able to resolve some of the tension between the optical results and the infrared results for galaxy evolution. One such way in which this was shown, was by studying the Extragalactic Background Light (EBL). Dole et al. (2006) used Spitzer/MIPS data to constrain the CIB at 24, 70 and 160 μm. By combining their results with past detections of the CIB and Cosmic Optical Background (COB), they were able to present the best estimate of the EBL. The SED for the EBL showed that the total emission of the CIB roughly equal to the total emission of the COB. Dole et al. (2006) state that the emission due to galaxy formation and evolution in the optical and in the infrared (due to thermal re-radiation by dust) are roughly the same. This implies that, on average throughout the history of the Universe, about half of the optical photons in star forming galaxies are absorbed by dust and re-radiated in the infrared (Dole et al., 2006).

The next major infrared satellite after Spitzer was the Herschel Space Telescope, see Section 1.3.7 for a description of the Herschel mission. Herschel found an even larger sample of ULIRGs, HLIRGs and strong gravitationally lensed galaxies. By combining previous infrared satellite results, namely IRAS, ISO, Spitzer and AKARI, with Herschel data, a star formation density main sequence has been found. It has been shown that star forming galaxies have a 'main sequence'. This main sequence for a specific redshift range is given by Equation 1.1, where SFR is the star formation rate and M_* is either the stellar mass or gas mass of the galaxy.

$$log(\mathrm{SFR}) \propto log(M_*) \tag{1.1}$$

In the work of Noeske et al. (2007), who studied galaxies up to a redshift of $z = 1.1$, plotted stellar mass against star formation rate (SFR). They found that the galaxies which lie on the main sequence exhibit star formation, are more blue in colour, have

dust lanes or are dusty star forming galaxies, and are mainly elliptical, spiral and lenticular in morphology. Noeske et al. (2007) also investigated a sample of galaxies which lie off the main sequence, with a lower SFR. These galaxies were found to be mainly elliptical galaxies with no evidence of current star formation.

Elbaz et al. (2011) investigated this galaxy main sequence using Herschel PACS and SPIRE data of the two Great Observatories Origins Deep Field Survey (GOODS) North and South, by also plotting SFR against stellar mass. They find that the ratio of the galaxy's total infrared flux and the rest frame 8 μm flux defines the galaxy's position on the main sequence, for galaxies with $z < 3$. This is independent of the galaxy's luminosity and redshift. The galaxy main sequence is used to separate normal star forming galaxies, which lie on the main sequence, and galaxies with large amounts of star formation, which lie off it. This distinction using the total infrared and 8 μm ratio is due to the fact that normal star forming galaxies have strong PAH emission, but this emission is suppressed in galaxies with a compact strong star forming region. Elbaz et al. (2011) discovered that high redshift LIRGs and ULIRGs lie on the main sequence, whereas the local Universe LIRGs and ULIRGs lie off it. This indicates that the star formation in high-z LIRGs and ULIRGs is much less compact, than those in the local Universe. Figure 1.3 shows local Universe galaxies plotted on the galaxy main sequence. The red dots are local compact objects, which are mostly ULIRGs, these sources lie off the main sequence. Using this galaxy sequence, Elbaz et al. (2011) discovered that many AGN also contain a compact region of intense star formation.

Genzel et al. (2010) present the first results of the use of CO line emission from galaxies to investigate the relationship between star formation rate and galaxy gas mass. This is known as the Kennicutt-Schmidt relation (Kennicutt, 1998). Genzel et al. (2010) used multi-wavelength data, including Herschel data, over the redshift $1 < z < 3$. They find that star forming galaxies of both high and low redshift follow the same trend on the galaxy gas mass against star formation efficiency (SFE) plot, the star forming galaxy main sequence. Genzel et al. (2010) find that for both high and low redshift luminous and ultra-luminous galaxies, which are undergoing merger events, lie off this

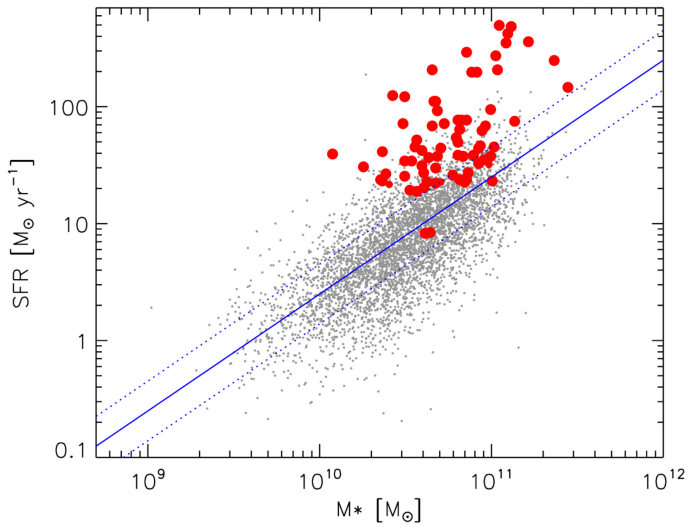

Figure 1.3: A galaxy main sequence plot of local galaxies. The red dots are local compact objects and lie off the main sequence (Elbaz et al., 2011).

main sequence, due to having a greater SFR. Sargent et al. (2014) also investigated the SFR/galaxy gas mass ratio, by using multi-wavelength data of CO detected galaxies and by creating a set of simulated data from a sample of galaxies over the redshift range $0 < z < 2$. Their findings show that their galaxies lie along two lines on the SFR/galaxy gas mass main sequence plots, with one track occupied by star forming galaxies and the other by starburst galaxies, both fitted by power laws. They state that these two different galaxy populations are separated more strongly when using the Kennicutt-Schmidt relation, than using SFR/galaxy stellar mass. Sargent et al. (2014) state that local ULIRGs do not lie on either track, indicating that local ULIRGs are a different type of galaxy to high redshift ULIRGs. This is agreement with the findings of Elbaz et al. (2011).

A wavelength range in the infrared, which is currently under-constrained, is the Spitzer/IRAC Spitzer/MIPS band gap between 8 and 24 μm. As noted earlier, the only satellite able to observe deeply in this wavelength range is the AKARI telescope. The AKARI telescope has four filters covering this part of the mid-infrared.

1.5 Overview of the Thesis

The main aim of this thesis is to perform the first analysis of several extragalactic fields observed by AKARI, then by using extracted galaxy sources in these fields to test different galaxy evolution models, classify galaxy type using the AKARI/IRC colour-colour space and using the extracted sources to resolve a percentage of the cosmic far-infrared background (CIB).

The AKARI telescope, mission and the standard pipeline written to process AKARI/IRC raw frames are summarised in Chapter 2. The standard AKARI pipeline was unable to process many of the extragalactic fields observed by AKARI, mainly due to image distortion, astrometry offset and instrumental artefacts. The first part of this thesis is described in Chapter 2, which was to create a new pipeline, optimised for processing extragalactic deep fields. This pipeline was optimised for point source extraction and also to produce high signal to noise final mosaicked images.

For this thesis, the optimised pipeline was tested on three extragalactic fields: two narrow but deep fields, ELAIS-N1 and the IRAC Dark Field discussed in Section 3.4 and 3.3 respectively, and one shallow but wide field, the AKARI Deep Field South (ADF-S), discussed in Section 3.5. These three fields are well known regions of the sky, and have been observed at many wavelengths, but have no other observations in the AKARI mid-infrared wavelength range. This thesis presents the first analysis of the AKARI/IRC data of the two extragalactic deep fields and the first number count work of the shallow field.

Once processed by the optimised pipeline, galaxy catalogues for each of the three extragalactic fields were extracted. Galaxy number counts were then calculated for the filters of the extragalactic fields. In Chapter 3 the number counts of the ELAIS-N1 and ADF-S are compared with a non-evolving galaxy model. In Chapter 4 all the number counts are compared with previously published number counts and galaxy evolution models. The number counts of this thesis are in general agreement with published number counts. In some places the galaxy evolution models do not fit the number

counts. This is discussed in Section 3.9.3.

Chapter 4 also presents the results of Probability of Deflection (P(D)) fluctuation analysis for two of the AKARI filters of the IRAC Dark Field number counts. The results of the P(D) analysis are compared with the predicted galaxy number counts of the model of Pearson (2005).

The AKARI galaxy catalogues of the two deep fields are cross-matched with ancillary data in Chapter 5, to create multi-wavelength band-merged catalogues. Using the band-merged catalogues, the AKARI and Spitzer/MIPS 24 μm colour-colour space is explored. Just using the AKARI/IRC colours to track the redshifted PAH features moving through the AKARI filters proved not to be so successful at separating galaxy types. Chapter 5 highlights the fact that SED fitting is required to be performed to confidently characterise galaxy type. The results of plotting the AKARI selected galaxies in AKARI/MIPS/SPIRE colour-colour plots shows that there is a population of high redshift 'normal' spiral galaxies, which are likely to be ULIRGs.

The final science chapter, Chapter 6, presents the stacking analysis work of the AKARI mid-infrared galaxy positions on the Herschel/SPIRE 250 μm IRAC Dark Field image to measure the percentage of the CIB resolved by the AKARI sources. This is the first science work performed using the SPIRE IRAC Dark Field images.

Chapter 7 presents the conclusions of this thesis. The chapter also discusses further work which could be performed using the optimised pipeline, the existing multi-wavelength band-merged catalogues and further analysis of the Herschel/SPIRE IRAC Dark Field images.

Chapter 2

Description of a Data Pipeline for Processing AKARI Extragalactic Deep Field Images

One who aspires to greatness should read and study

-Yoshida Shoin

2.1 Introduction

This chapter presents the new pipeline written for processing the extragalactic deep field images, which are the topic of Chapters 3, 4, 5 and 6. Section 2.2 gives a detailed description of the Japanese infrared satellite, AKARI; in particular the InfraRed Camera (IRC) instrument on board. The standard pipeline written for processing AKARI/IRC frames is discussed in Section 2.3. Section 2.4 describes the new pipeline written for the work in this thesis. The pipeline was created for processing extragalactic deep fields. It was optimised for point source extraction and to create images which have high signal to noise. This Section provides a summary of all the steps in the optimised pipeline, with comparisons between the output of the standard pipeline and the optimised pipeline.

2.2 AKARI: Overview

2.2.1 Launch and Orbit

AKARI was Japan's first dedicated infrared satellite. It was launched from the Uchinoura Space Centre, Southern Japan, on board JAXA's M-V8 launch vehicle on 21 February 2006, 21:28 UTC and operational until 24 November 2011. AKARI was initially named IRIS, and prelaunch it was known as ASTRO-F. After launch it was renamed AKARI; it is traditional for Japanese space missions to be renamed at this point. The word AKARI is roughly translated as 'a distant faint light' (Murakami et al., 2007).

AKARI orbited the Earth in a Sun-synchronous polar orbit along the 'twilight zone', i.e. the day-night boundary. A Sun-synchronous orbit means that the orbit of AKARI had been designed so that the telescope was pointing at an angle roughly perpendicular to the line between the Earth and the Sun. On such a dawn/dusk orbit the solar time of the region of the equator over which AKARI passed was always about sunrise or sunset. AKARI was at a height of 745^{+145}_{-0} km, had an orbital period of ~ 100 minutes and pointed at an angle of 90 ± 1 degrees from the Sun. AKARI had two different observing modes, the survey mode and pointing mode. When AKARI was observing in survey mode, the telescope pointed perpendicular to both the Sun and the Earth. During a pointing mode observation, when AKARI was imaging a specific area of the sky, a single pointing observing time was limited to 10 minutes because the telescope needed to remain roughly perpendicular to the Sun and the Earth. The orientations for these two different modes can be seen in Figure 2.1.

2.2.2 Instruments On board AKARI

The AKARI satellite comprised two elements, the bus module and the cryostat. The bus module contained the power supply, the spacecraft attitude control, data acquisition, the telecommunication link to the ground station, data recorder, and other pieces

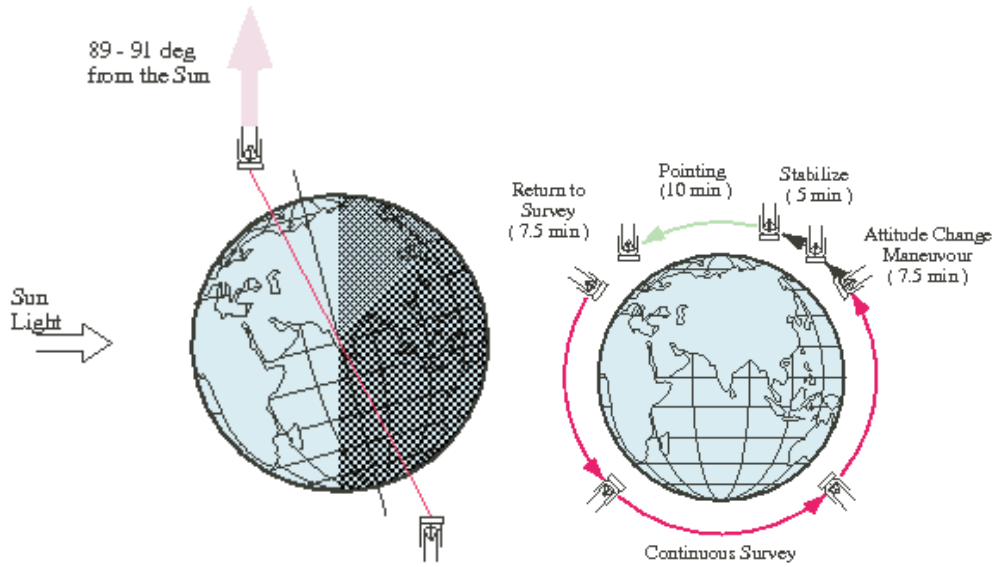

Figure 2.1: The two different orbital modes of AKARI. The image on the left shows the orbit of AKARI while in survey mode, and the image on the right shows the orbit of AKARI while in pointing mode (ASTRO-F User Support Team, 2005).

of 'house-keeping'. The attitude of the satellite means the inclination of the three principal axes of AKARI, which are the two dimensions perpendicular to the Sun-satellite direction and the alignment of the bus module and the cryostat, i.e. the direction in which the spacecraft is pointing. The spacecraft attitude control unit contained the IRU (a gyro). This measured motion in the satellite. The attitude control unit also contained the Two-dimensional Fine Sun Sensors (TFSS) that measured the angle between the sun and the satellite and the two Star Sensors (STT) which measured the change in the angle between the bus module and the cryostat, and the AOCU (a computer) that provided further information about the satellite's attitude. The second part of the AKARI satellite was the cryostat. This contained the Scientific Instrument Assembly (SIA), which in turn contained the telescope and Focal-Plane Instruments (FPI), all of which were cryogenically cooled. The SIA was cooled to a temperature of ~ 6 K. The SIA was shielded from heat by two layers of Vapour Cooled Shield (VCS), which was cooled by helium gas, evaporated from the tank. The inner VCS also had mechanical coolers. The FPI was further cooled down to a temperature of $\sim 2.0 - 2.2$ K. At launch AKARI had 170 litres of liquid helium, which was expected to last for 550 days. On board AKARI was a Ritchey-Chrétien telescope, with a physical diameter

of 71 cm and an effective aperture diameter of 68.5 cm. The difference in physical and effective diameter is due to the fact that the mirror was not completely circular. The telescope had a focal ratio of 6.1 (the focal length divided by the effective aperture) and was cooled to a temperature of ~ 5.8 K by helium vapour. The FPI contained the two main instruments on board AKARI, the Far-Infrared Surveyor (FIS) observing at $50-180\,\mu$m (Kawada et al., 2007) and the InfraRed Camera (IRC) observing at $1.5-26.5\,\mu$m (Onaka et al., 2007). The FPI also contained two focal-plane star sensors (FSTS) observing in the J-band ($1.25\,\mu$m) for observing guide stars (ASTRO-F User Support Team, 2005).

2.2.3 The IRC

The IRC contained three detectors, which were hybrid sensors of infrared photo-diodes and complementary metal-oxide semi conductors (CMOS). The three detectors were: the near-infrared (NIR), the mid-infrared short (MIR-S) and the mid-infrared long (MIR-L), each of which had three filters and one prism/grism. The layout of the three detectors in the SIA is shown in Figure 2.2, and a cross-sectional view of each of the three detectors is shown in Figure 2.3. The NIR detector was a 512 x 412 pixel InSb array, with Field of View (FoV) of 9.3 x 10.0 arcminutes. The MIR-S detector was a 256 x 256 pixel Si:As array, with FoV of 9.1 x 10.0 arcminutes. The MIR-L detector was a 256 x 256 pixel stressed Si:As array, with FoV of 10.3 x 10.2 arcminutes. The nine broadband filters were centred on: 2.4, 3.2, 4.1, 7.0, 9.0, 11.0, 15.0, 18.0 and $24.0\,\mu$m. Table 2.1 shows the imaging specifications of the nine AKARI/IRC filters, these specifications did not alter during the mission. The imaging area is smaller than the array, because the area of the array around the slit was masked. Figure 2.4 shows the FoV for the three detectors, and the positions of the slit area for each detector. As can be seen in Figure 2.4 the NIR and MIR-S detectors shared the same FoV; the FoV of the MIR-L detector was offset by ~ 20 arcminutes (Onaka et al., 2007).

The IRC had seven fixed Astronomically Observed Template (AOT) combinations of

exposure time, filter exchange and dithering operation. Five of the AOTs were for pointing mode and two were for survey mode. The seven AOTs were: IRC00, IRC02, IRC03, IRC04, IRC05, IRC11 and IRC51. IRC00 was designed for deep imaging. This AOT had a dither. IRC00 was a one filter mode, hence only one filter was observed for each detector. It had preset filters, i.e.: N2, S9W and L18W; N3, S7 and L15; N4, S11 and L24. This AOT was only used during the calibration stage of the mission. IRC05 was used instead, because it had a better signal to noise. IRC02 used a two filter mode and was for general purpose imaging. It used filters N3, N4, S7, S11, L15 and L24, and was dithered. The NIR filters each had 4 long exposures and the MIR-S and L filters each had 12 long exposures. The IRC03 was also for general purpose imaging. It used a three filter mode, hence all filters were used. The NIR filters each had 3 long exposures and the MIR-S and L filters each had 9 long exposures. IRC03 had a slightly different dithering pattern from IRC02. Both the IRC02 and IRC03 had a set of dark frames at the beginning and end of the observation. Part of the pointing time was spent rotating the filter wheel and telescope dither. IRC04 was for spectroscopic observations, and was not dithered. IRC05 was for deep pointings and, like IRC00, had a one filter mode. Unlike IRC00 it was not dithered. The NIR had 5 long exposures and the MIR-S and L each had 30 long exposures. Each IRC05 pointing had two sets of dark frames at the beginning and end. The preset filters for IRC05 were the same as those for IRC00. During the mission IRC05 was used for all deep pointings instead of IRC00. IRC11 and IRC51 were for the slow scan mode. While on pointing mode, an individual pointing comprised of n number of exposure cycles (also known as a frame unit in other literature). An exposure cycle was made up of 1 short NIR frame, 1 long NIR frame, 1 (or 2 for IRC05) short MIR-S/L frames and 3 (or 6 for IRC05) long MIR-S/L frames. This is shown in Figure 2.5. Note that the NIR and MIR-S/L frames were taken simultaneously. (Onaka et al., 2007).

Table 2.1: Specifications of the 9 filters in the IRC.

Channel	Name	Filter	Wavelength μm	Centre μm	Width μm	Detector	Array	Imaging FoV arcmin	Pixel scale arcsec
NIR	N2	filter	1.7-2.7	2.43	0.68	InSb	512 x 412	9.3 x 10.0	1.46 x 1.46
NIR	N3	filter	2.7-3.7	3.16	1.12	InSb	512 x 412	9.3 x 10.0	1.46 x 1.46
NIR	N4	filter	3.7-5.5	4.14	1.22	InSb	512 x 412	9.3 x 10.0	1.46 x 1.46
MIR-S	S7	filter	5.8-8.4	7.3	2.6	Si:As	256 x 256	9.1 x 10.0	2.34 x 2.34
MIR-S	S9W	filter	6.5-11.6	9.1	4.3	Si:As	256 x 256	9.1 x 10.0	2.34 x 2.34
MIR-S	S11	filter	8.6-14.1	10.7	4.7	Si:As	256 x 256	9.1 x 10.0	2.34 x 2.34
MIR-L	L15	filter	12.4-19.4	15.7	6.2	Si:As	256 x 256	10.3 x 10.2	2.51 x 2.39
MIR-L	L18W	filter	13.9-25.3	18.3	10.0	Si:As	256 x 256	10.3 x 10.2	2.51 x 2.39
MIR-L	L24	filter	20.4-26.5	23.0	5.4	Si:As	256 x 256	10.3 x 10.2	2.51 x 2.39

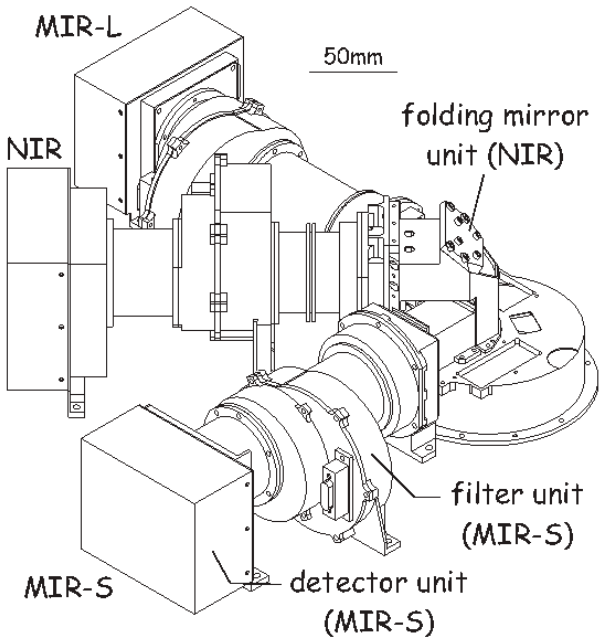

Figure 2.2: The layout of the three IRC detectors (Onaka et al., 2007).

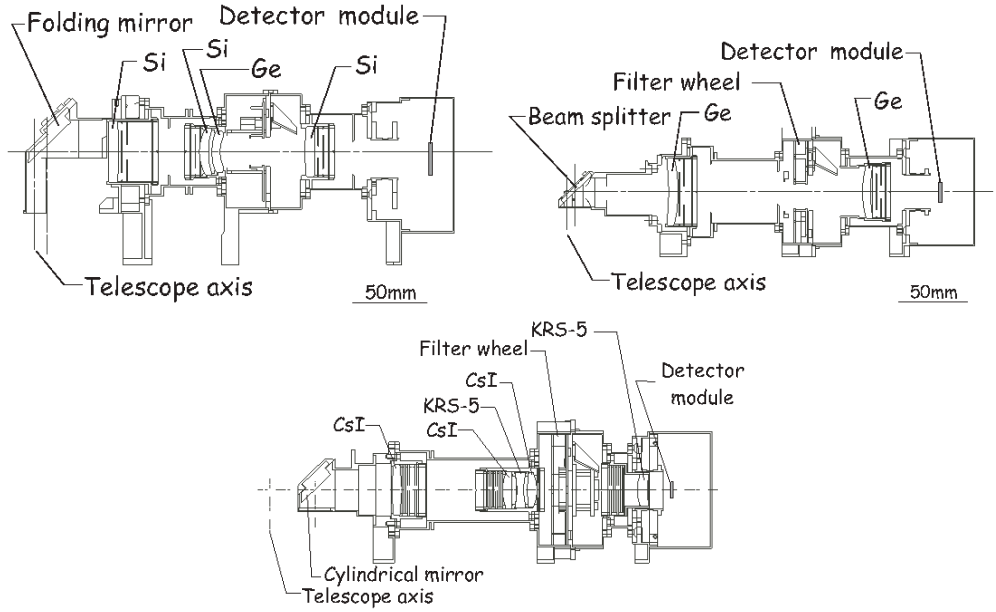

Figure 2.3: A cross-sectional view of the three IRC channels. The image on the top left shows NIR channel. The figure on the top right shows the MIR-S channel. The bottom image shows the MIR-L channel. Note the beam splitter on the MIR-S channel which splits the light to the NIR and MIR-S detectors, hence the NIR and MIR-S frames have the same field of view. (Onaka et al., 2007).

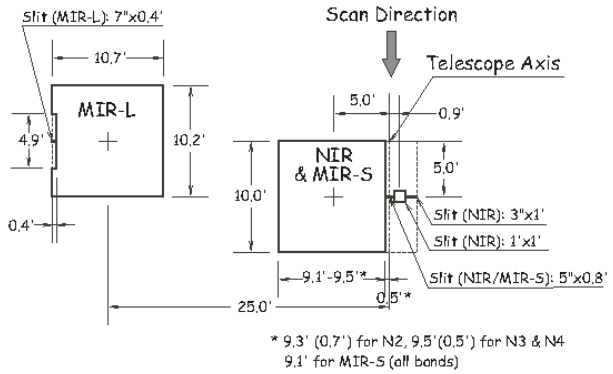

Figure 2.4: The field of view for the three IRC detectors. Note that the NIR and MIR-S detectors have the same field of view, due to the use of a beam splitter (Onaka et al., 2007).

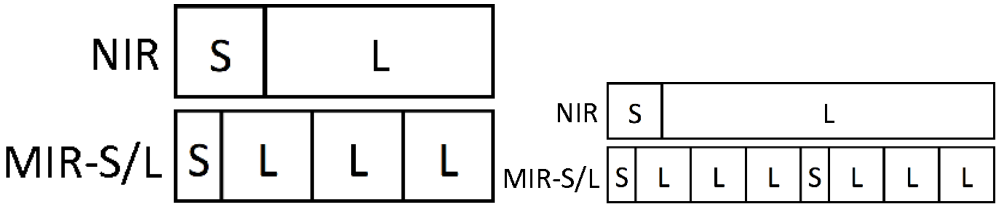

Figure 2.5: The two different exposure cycles for the IRC while in pointing mode. The left image shows the exposure cycle for IRC02, IRC03 and IRC04. The right image shows the exposure cycle for IRC05 (Onaka et al., 2007).

2.2.4 Observations and Mission Phases

There are four different types of AKARI/IRC observations: detector and calibration time (DT), Large Area Survey (LS), Mission Programme (MP) and Open Time Programme (OT). DT was used for calibration of the instruments. LS observations included the All Sky Survey, repeated pointings of the North Ecliptic Pole (NEP) and the Large Magellanic Cloud (LMC) (Wada et al. (2008), Ishihara et al. (2010)). MP is a set of 15 programmes of pointed observations. These were guaranteed time programmes for AKARI team members. All of these observations are now available to the public. This took up 70% of the pointed observation time (not including the NEP and LMC pointings). The OT observations made up the remaining 30% of the time for Phase 2 pointed observations (Murakami et al., 2007).

The AKARI mission was divided into four phases. Phase 0, from 13th April 2006 to 8th of May 2006, when all the performance verification was carried out. This included a thorough check of the spacecraft systems and the FPI, inflight calibration of the instruments and test observations (ASTRO-F User Support Team, 2009). Phase 1, from 8th May 2006 to 10th November 2006, was when AKARI performed most of the all sky survey (Ishihara et al., 2010). Phase 2, which was predominantly guaranteed time observations (Mission Programmes) and Open Time observations, was from November 2006 to 26th August 2007. During Phases 1 and 2, the telescope and instruments, including the IRC unit, were cryogenically cooled to 6 K. The supply of liquid helium coolant was exhausted on 26th August 2007, thus the SIA was only cooled to 40 K. This meant that the MIR-S and MIR-L detectors did not function. Some performance verification was carried out at the start of Phase 3. During Phase 3 only the NIR detector was operating (at 40 K), this was mainly Open Time observations (Murakami et al. (2007) and Egusa et al. (2015)). Phase 3 mission programmes commenced on 1st June 2008, and Open Time programmes commenced on 15th October 2008. AKARI was decommissioned on 24th November 2011 (ASTRO-F User Support Team, 2009).

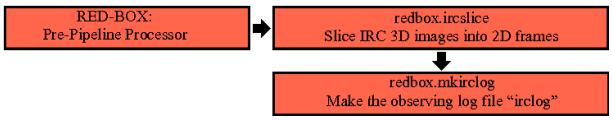

Figure 2.6: The redbox from the standard IRC pipeline.

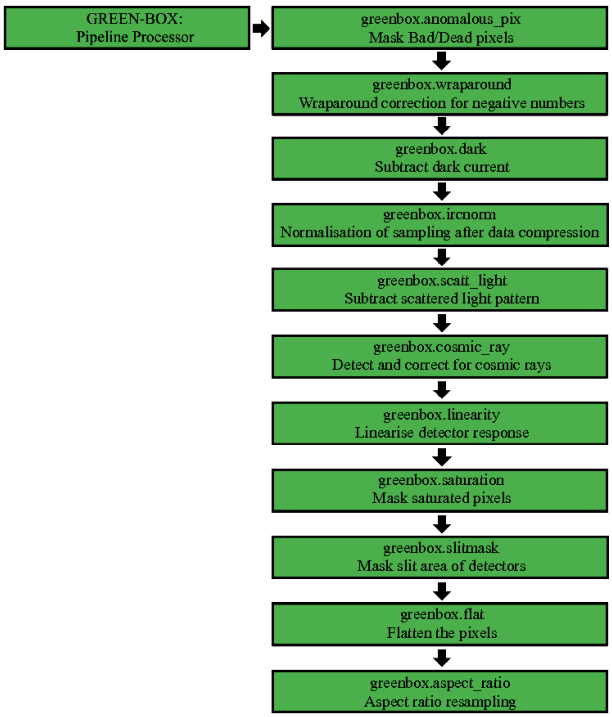

Figure 2.7: The greenbox from the standard IRC pipeline.

2.3 The Standard IRC Pipeline

The original standard IRC imaging pipeline (version 20110304) used to populate the AKARI data archive runs in the IRAF [1] environment. The standard pipeline is subdivided into three parts: the pre-pipeline (see Section 2.3.1), the pipeline (see Section 2.3.2) and the post-pipeline (see Section 2.3.3). The pre-pipeline slices the 3D data cubes into 2D image frames and creates the log text file for use in subsequent steps. The main pipeline is comprised of eleven steps. The steps correct for some instrumental artefacts, perform dark subtraction and flat fielding. The post-pipeline has four steps to coadd the individual frames from each pointing and a World Coordinate System (WCS) correction step (Lorente, 2007).

[1] IRAF is distributed by the National Optical Astronomy Observatory, which is operated by the Association of Universities for Research in Astronomy, Inc., under cooperative agreement with the National Science Foundation.

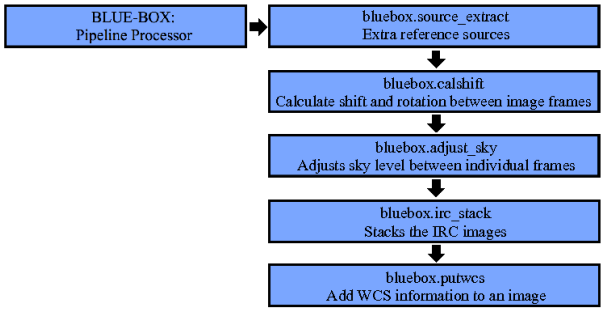

Figure 2.8: The bluebox from the standard IRC pipeline.

2.3.1 Redbox: the Pre-Pipeline

The pre-pipeline steps, which are part of the standard toolkit pipeline, are referred to as the 'redbox' in the IRC User Manual. See Figure 2.6 for the steps in the pre-pipeline. The pre-pipeline is run on one pointing at a time. It only has one variable which can be edited: this is the 'verbose' flag for whether the information about the processing is printed to screen.

2.3.1.1 Ircslice Step

The first of the two steps in the standard pre-pipeline is the ircslice step. The raw data in the AKARI archive are stored as 3D data cubes; a single pointing contains multiple raw data cubes. Each data cube contains the information for a set of frames for one individual filter. All the raw data cubes contain one short exposure frame and either one (for NIR) or three (for MIR-S and L) long exposure frames. This is the same for the raw dark frame data cubes and the raw imaging frame data cubes. The ircslice step slices these raw 3D data cubes into individual fits frames. These fits frames are then ready to be processed by the standard pipeline, or can be opened by any fits editor.

2.3.1.2 Mkirclog Step

The second step in the standard pre-pipeline is the mkirclog step. The mkirclog step creates an observing log file, named *irclog* step. This is saved to the same file as the frames sliced by ircslice. This log contains:

FRAME - The file name of each frame in the pointing.

OBJECT - The name of the pointing target.

NAXIS - The number of pixels in a cross-scan of the frame, i.e. the number in the x direction. This is 412 for the NIR detector frames and 256 for MIR-S and L detector frames.

FLITER - The filter name, i.e. one of the nine filters, 'DARK' for a dark frame or 'UNDEF' for a frame with an error.

RA-SET - The coordinate for the right ascension of the centre of the frame.

DEC-SET - The coordinate for the declination of the centre of the frame.

AOT - The AOT of the pointing.

EXPID - The frame number for a set of exposures, i.e. 1 for the short exposure, 2 for the long NIR exposure and 2, 3, or 4 for the long MIR-S and L exposures.

IDNUM - The pointing ID.

SUBID - The number given to the pointing for a multiple set of observations.

2.3.2 Greenbox: the Pipeline

Once a pointing has been through the redbox pre-pipeline, the raw frames are ready to be processed by the greenbox pipeline. See Figure 2.7 for the steps in the standard pipeline. At the start of each step in the greenbox pipeline, the frames in the pointing are read from disk, and at the end of each step the frames are saved back to disk, with the prefix for the step added to the file name. Table 2.2 shows the associated letters added to the file for each step.

2.3.2.1 Anomalous Pixel Step

The first step in the standard pipeline masks dead and hot pixels. The mask was created using pre-flight data.

Table 2.2: The prefix to the frames associated with each standard pipeline step.

Pipeline Step	Prefix
Anomalous Pixels	a
Wraparound	w
Dark Subtraction	D
Normalisation	n
Scattered Light Rejection Pattern	c
Cosmic Ray Rejection	C
Linearity Correction	l
Saturation	s
Slit Mask	m
Flat Fielding	f
Aspect Ratio Sampling	e
Extract Bright Reference Sources	S
Calculate Shift & Rotation to Match Frames	R
Adjust Sky Level	A

2.3.2.2 Wraparound Correction Step

Due to constraints on the size of data sent from the telescope back to Earth, for very small negative values, the 'sign bit' (i.e. positive or negative sign) is not included. Hence pixels with a very small negative value are seen in the raw frames as very large positive values. These large values are less than the telescope saturation limit. This step applies the correction from Equation 2.1, for pixels with value less than -11953 ADU (Analogue to Digital Units).

$$A_{\text{corrected}} = A_{\text{uncorrected}} + 2^{16} \tag{2.1}$$

2.3.2.3 Dark Subtraction Step

The standard pipeline has two different options to correct for the dark current. The pipeline has a 'super-dark', which was made using pre-flight testing data. For long exposure MIR-S and L frames, the user has the option to use a 'self-dark'. The self-dark is created for the pointing during the running of the pipeline. The self-dark is an average of the darks taken by the MIR-S or L detector at the start and end of the

pointing. No self-dark is created for short exposure frames or NIR detector frames.

2.3.2.4 Normalisation Step

Fowler sampling is used to reduce the detector readout noise. This method takes n readings and sums the image arrays, where n is given by the Fowler number (Lorente, 2007). This step also corrects for the 'least significant bit' for each pixel, being omitted when the data are transmitted back to Earth. The correction applied to each pixel is given by Equation 2.2, where the Fowler number is 4 for long exposure images and 0.25 for short exposure images.

$$A_{\text{corrected}} = \frac{A_{\text{uncorrected}} * 2^{\text{bitshift}}}{\text{Fowler number}} \tag{2.2}$$

2.3.2.5 Scattered Light Rejection Pattern Step

The IRC frames suffer from a scattered light pattern, caused by photons reflected off the edges of the detectors and onto the image array. This step in the standard pipeline uses a template image and subtracts the scattered light pattern from the MIR-S frames.

2.3.2.6 Cosmic Ray Rejection Step

This step in the standard pipeline uses the IRAF procedure 'cosmicrays' to detect cosmic rays and set the flagged pixels to -9999.90 ADU.

2.3.2.7 Linearity Correction Step

This step in the standard pipeline corrects for detector non-linearity at specific flux values. Each detector's linearity was tested pre-flight and inflight, by shining a calibrator lamp on the detectors. Pre-flight it was assumed that pixels with a flux value greater than about 5000 ADU did not behave linearly. In-flight testing showed that pixels only behaved linearly with a flux less than 1000 ADU. This step scales the flux of pixels greater than 1000 ADU. Pixels with flux less than this remain unscaled.

2.3.2.8 Saturation Step

This step uses the short exposure frames to flag saturated pixels, then the locations in the associated long exposure frames are masked. The saturated values for the short exposure frames are $\sim$ 12500 ADU for the NIR detectors and $\sim$ 33000 ADU for the MIR-S and L detectors

2.3.2.9 Slit Mask Step

This step in the standard pipeline masks the slit area in each frame. The slit area is the spectroscopic slit and the area around it, which does not receive any signal from the sky.

2.3.2.10 Flat Fielding Step

This step corrects for flat fielding. Each of the nine filters has a 'super-flat' created for it. Due to the time dependent artefact in the MIR-S frames (see Section 2.4.3.4 for a further explanation), the standard pipeline provides a flat containing this artefact. Due to the time dependent nature of this, in a subsequent edit to the standard pipeline, three time dependent flats are given for the time scale of this artefact (Egusa et al., 2015).

2.3.2.11 Aspect Ratio Sampling Step

This step in the standard pipeline performs a linear aspect ratio correction, and a distortion correction for NIR and MIR-S frames. The NIR distortion correction was created by mapping the AKARI sources to the Two Micron All-Sky Survey (2MASS) sources. The MIR-S distortion correction was made using Asymptotic Giant Branch (AGB) globular cluster stars. The distortion correction is applied to each frame individually, and is a first order correction (Wada, priv. Comm.). Apart from correcting for the aspect ratio, there is no distortion correction for MIR-L frames.

2.3.3 Bluebox: the Post-Pipeline

The frames processed by the greenbox standard pipeline are not 'science ready'. The bluebox standard post-pipeline performs the extra processing required and coadds the frames. See Figure 2.8 for the steps in the standard post-pipeline. When using the standard post-pipeline, all the frames are required to be from the same pointing and observed through the same filter. The standard post-pipeline does not perform mosaicking or photometry.

There is a separate coadd step for MIR-L frames which do not have many bright sources to align the frames. This separate step uses header information from MIR-S frames, imaged simultaneously with the MIR-L frames in question.

2.3.3.1 Extract Bright Reference Sources Step

This step 're-bins' each frame into a 1024 by 1024 image for NIR and 512 by 512 for MIR-S and L. The step then extracts the bright sources (normally stars) contained in a single frame and creates a source list. In the case of MIR-S and L, for each frame a median boxcar filtered image is created and then this image is subtracted from the frame. This is performed before source extraction. This extra part of the step is performed so the effects of Earthshine light and scattered light is reduced in source extraction.

2.3.3.2 Calculate Shift and Rotation to Match Frames Step

This step uses the first frame in the set of frames being processed by the post-pipeline as a reference frame. The step then aligns the subsequent frames to this frame. The step uses the source list created in the 'Extract Bright Reference Sources' step. There is a minimum number of extracted bright sources required to perform the alignment.

2.3.3.3 Adjust Sky Level Step

This step first subtracts the median sky value off each frame. An average of the median sky values from all the frames being processed by the post-pipeline step is calculated, and this value is added to each frame. There is an option to subtract a median boxcar filtered image from each frame. This step is to correct for Earthshine light and scattered light.

2.3.3.4 Image Stacking Step

This step stacks all the frames being processed by the post-pipeline. The coadded fits file is then saved to disk. A noise image is also created. The values of the pixels in the noise image are assigned the σ value of the pixel value in the coadded image. This does not correct for gain, dark current etc.

2.3.3.5 Convert to WCS Coordinates Step

This step matches the 2MASS catalogue coordinates to the coadded image, and then adds WCS information to the coadded image.

2.3.4 Outstanding Issues with the Standard Pipeline

There are several outstanding issues with the original standard IRC pipeline. The raw frames suffer from an astrometry error. To be aligned with WCS, each frame needs to be jitter corrected. The existing pipeline makes a partial correction for this error. The raw IRC frames are also warped. This warping is due to optical distortion, and because the detectors are not completely flat. Frames from several of the IRC filters are badly affected by reflected Earthshine light. This creates a change in flux gradient across the frame. The standard pipeline does not correct for image warping or the Earthshine gradient. Finally, for every step in the standard pipeline, each frame is read from file and edited, the original frame is deleted and then the edited frame is written to file. This makes the existing pipeline slow to run when processing a large number

of frames. Note that Egusa et al. (2015) have recently provided an improved pipeline toolkit that provides some improvement. However, many of the above issues remain to varying degrees.

Moreover, the standard pipeline is written to process generic IRC observations and hence is not at all optimised for the specific processing of extragalactic images and with the view of point source extraction.

2.4 A New Pipeline Optimised for Deep Fields

2.4.1 Overview

The work in this thesis presents a new pipeline optimised for the processing of extragalactic images, hereafter referred to as the optimised pipeline. The optimised pipeline was written in the Interactive Data Language (IDL) [2], in order to take advantage of IDL's array based processing, which is well suited to the IRC data sets. IDL is an array based language, while IRAF is not.

2.4.2 Pre-Pipeline

The raw 3D data cubes are sliced into 2D frames using the standard pre-pipeline (see Section 2.3.1). The optimised pipeline requires frames to be of the same filter, and from a similar time period. After running a pointing through the standard pre-pipeline, the frames are run through an optimised pre-pipeline step. This step separates frames from a single pointing into the nine filters and darks.

2.4.3 Pipeline

In order to make the optimised pipeline efficient and avoid excessive reading and writing to disk, all frames are passed as IDL arrays between processing steps. The first stage in creating the new pipeline, was to replicate as many of the standard pipeline

[2]Interactive Data Language: http://www.exelisvis.com/Products Services/IDL.aspx

steps in the new optimised pipeline as possible, i.e. convert all the IRAF procedures to IDL procedures. Once the new pipeline, written in IDL, was replicating the standard pipeline steps, the existing steps in IDL were edited, where necessary, and more steps were written. Comparing the first version of the new IDL pipeline with the standard pipeline, the wraparound and normalisation steps, all replicated the analogous step in the standard pipeline exactly. The frames processed by the scattered light step, the linearity step and the flat field step in the new pipeline varied slightly from the same frames processed by the same steps in the standard pipeline. The difference was only very small, and thought to be due to rounding errors. The cosmic ray step in the standard pipeline did not flag any pixels as cosmic rays, hence there were no frames to compare with those frames processed by the cosmic ray step in the new pipeline. Due to the fact that the standard pipeline combines the wraparound step, the saturated step and the anomalous pixels step into the mask step, it was not possible to compare these steps individually. The frames processed by the dark step in the new pipeline were different from the same frames being processed by the standard pipeline's dark step. This is thought to be due to the different way the two pipelines calculate the value of the mode. Once all the steps in the new pipeline were replicating the steps of the standard pipeline, the new pipeline was then edited to create the optimised pipeline.

The first part of the optimised pipeline is a routine which calls the different steps of the pipeline. The first step reads in all the frames in the directory passed to the pipeline. The frames need to be of the same filter and have a similar observation date. The first step creates a structure to hold the frame, the associated header, the noise array, the noise header, the mask array and the mask header. The standard pipeline does not create a mask or noise image for each frame. An array is created to hold each frame's structure. The subsequent steps of the optimised pipeline are shown in Figure 2.9.

The steps which are the same as in the standard pipeline have dashed lines around them in Figure 2.9; these are the normalisation and linearity steps, and are discussed in Section 2.3.2.4 and Section 2.3.2.7.

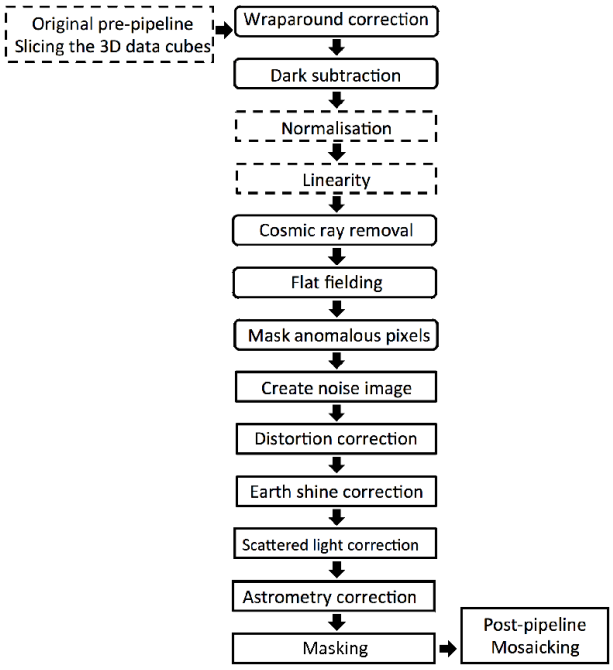

Figure 2.9: Outline of the steps in the optimised pipeline. The dashed boxes are steps copied directly from the standard pipeline, the rounded boxes are based on steps from the standard pipeline, and the cornered boxes are steps created for the optimised pipeline.

2.4.3.1 Wraparound Correction

Due to telemetry constraints on data size, all the data were compressed on board; all pixels with a flux greater than 2^{16} ADUs were 'wrapped around' to a pixel value less than -11953.8 ADU (Lorente, 2007).

Figure 2.10 shows examples of artefacts created by a bright (many times more than detector full well) object (star, hot pixel, cosmic ray) being viewed by the detector. There are two clear effects: every fourth pixel after the pixel which the bright object is incident on, shows a brighter value; and the column in which the bright object pixel is situated also shows an increase in signal. The first effect, termed muxbleed, is understood to be due to the extreme amount of signal charge not being completely reset from the output chain, resulting in an offset to subsequent reads from that output (of which there are four nodes, thus this affect is repeated every four pixels) for some time until that signal has decayed in the electronics. The second effect, often referred to as column pull-down, is likely to be a blooming effect during the integration time.

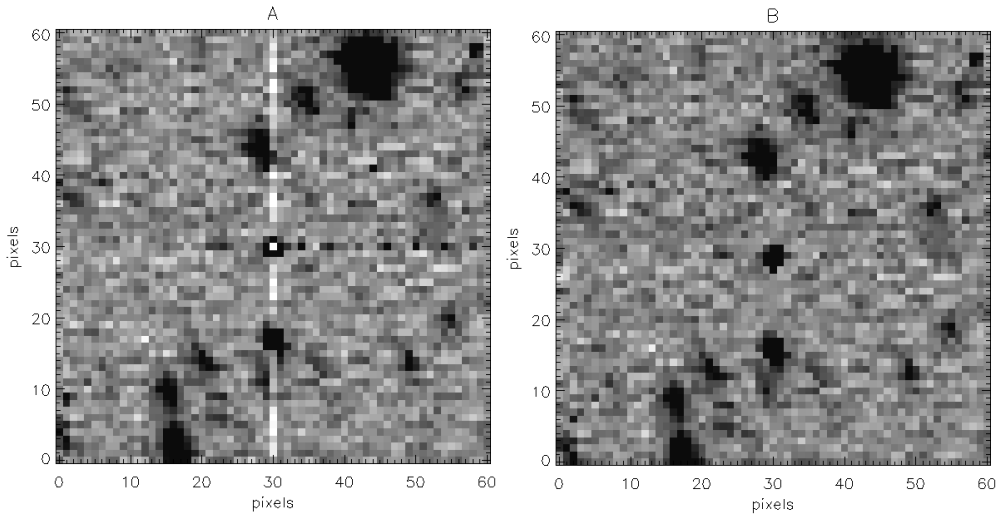

Figure 2.10: A close up of a single N3 frame; (A) the raw frame, (B) the processed frame with muxbleed removed. The saturated pixel causing the artefact is at pixel number (30, 30).

Blooming is when a large number of photons (or a single very high energy photon) fill the electron capacity of the pixel it had landed on. The electron charge then fills the next pixel and so on, until all the photons have been absorbed.

The first step in the optimised pipeline is to check each NIR frame for pixels with a value less than -11953.8 ADU. The location of the pixel is flagged in the mask image, as are all the pixels in the same column (damaged by the column pull-down effect) and every fourth pixel for the following two rows (due to the muxbleed effect). Section 2.4.3.6 shows how an interpolated value is given to each flagged pixel.

In the creation of the optimised pipeline, a new artefact in many of the NIR images has been discovered. The artefact is a pattern, with sets of four pixels with increased flux and decreased flux, as shown in Figure 2.11. As the pattern is in sets of four, it is presumed to be linked to the four read out nodes. Further work is required to research how to remove this artefact.

The wraparound step in the optimised pipeline also performs the role of the saturated pixel step in the standard pipeline. This negates the need to use the associated short exposure frame.

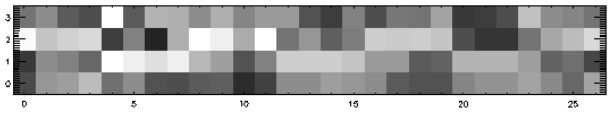

Figure 2.11: Close up of a NIR frame, showing the sets of four pixels and the increasing and decreasing flux.

2.4.3.2 Dark Subtraction

The optimised pipeline uses bespoke time dependent dark frames, selected from suitable pointings over Phase 2, as opposed to the generic dark frame used by the standard pipeline. For Phase 2 data, the dark step corrects for dark current counts. To compare the generic dark frame with the time dependent dark frame, an individual frame was processed by the optimised pipeline dark step, twice; once using the generic dark and once using the time dependent dark frame. A part of the frame just with sky background (i.e. no sources) was selected, and the standard deviation of the pixel values in that area for the frame was calculated for the two differently processed frames. This was repeated for several areas in the frame, and for several frames. The standard deviation of the time dependent dark frame was smaller, about two-thirds of the time.

2.4.3.3 Cosmic Ray Removal

Cosmic rays are high energy particles and are normally seen on individual frames as spot-like or streak-like bright artefacts. This is caused by the rays interacting within the detector. Apart from shielding, which can stop a percentage of cosmic rays, not much else can be done to stop this artefact; therefore they must be detected and removed from individual frames during the processing phase. Frames from all of the nine filters contain cosmic rays.

The standard pipeline assigns detected cosmic rays with a generic default value. The optimised pipeline detects cosmic rays in two places, in the cosmic ray step and during the coadding stage. The cosmic ray detection step in the optimised pipeline detects cosmic rays in individual frames.

Quite often the first NIR frame in a pointing contains a lot more cosmic rays than

subsequent frames. This is due to a build up of cosmic rays on the detector between pointings. The IDL procedure LA_COSMIC is used to remove the cosmic rays in the individual NIR frames. This removed the large number of cosmic rays from the first frame in a pointing, and from subsequent frames.

In the MIR-S and L bands the cosmic rays appear very similar to faint point sources, and the IDL procedure LA_COSMIC was found to remove some of the point sources as well. Even using a specifically written cosmic ray removal algorithm, some of the point sources were flagged as cosmic rays. So that flux from the point sources is not lost, point sources are masked before the cosmic ray removal, and then cosmic rays are detected using the sigma clipping algorithm, written for the optimised pipeline. The locations of all detected cosmic rays are flagged in the mask array. It can be seen in Figure 2.12 that many of the cosmic rays have been detected and removed. A second cosmic ray detection is performed during the frame coadding stage. This is mainly performed to detect any remaining cosmic rays that were incorrectly masked as point sources. The same sigma clipping algorithm is performed on each stack of pixels (one per frame), which will create one pixel in the final coadded image. To check the detected cosmic ray is not a faint point source, for the case of shallow fields a cosmic ray will be flagged if only one is detected in a stack of pixels. For deep fields a cosmic ray will be flagged if less than five cosmic rays are detected in a stack of pixels. This is performed so that point sources are not incorrectly detected and removed as cosmic rays.

2.4.3.4 Flat Fielding

The optimised pipeline has a generic flat field image for each of the nine filters. The optimised pipeline also provides an option to create a bespoke flat, created using frames of a similar date to the observation, from a file of fits images supplied by the user. If a user does not supply a file, the pipeline will use the bespoke time dependent flat, for the observing phase of the date range of observation and filter. Figures 2.13.b and 2.13.c compare using the IRAF pipeline flat with the optimised bespoke time dependent flat.

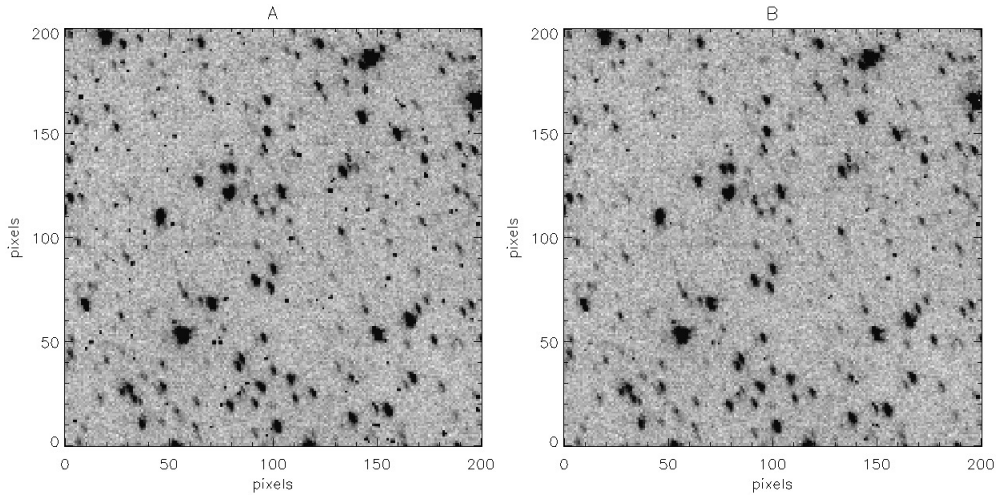

Figure 2.12: Close up of a N4 frame, (A) processed by the optimised pipeline but with cosmic rays not removed, (B) the same area of frame, but with cosmic rays removed

As can been seen in Figure 2.13.c, the standard pipeline flat does not remove all of the instrumental artefacts, e.g. the horizontal stripe, the vertical stripes, the rectangle at the centre of the left edge and the black region around the amplifier.

The optimised bespoke time dependent flat field image for a specific filter is created by stacking frames of that filter observed around the time of the pointing being processed. The values of the pixels in each column are sigma clipped and the mean value is then assigned to the corresponding pixel in the flat field image.

To remove as many instrumental artefacts as possible, it is advisable to create time dependent flats for each date range of a set of pointings. One prominent artefact removed by a bespoke flat field is the sora-mame (Japanese for the sky bean, hereafter called the bean). The bean appears in MIR-S detector images from the beginning of the mission to part way through Phase 2, where it disappeared 07/01/2007. The bean is a pattern of three almost circular shapes (see Figure 2.13.a). The shape of the bean is time dependent, and there is currently no generic model to remove it. Using a bespoke time dependent flat, the optimised pipeline is able to remove the bean. Comparison between the use of the generic flat field and a bespoke time dependent flat field can be seen in Figure 2.13

To test that the time dependent flat field image created by the optimised pipeline per-

formed a better flat fielding than the one provided by the standard pipeline, a similar test to the one used to test the dark subtraction was used. The same frame was processed by the optimised pipeline flat fielding step and the standard pipeline flat fielding step. Part of the frame with just sky background (i.e. no sources) was selected, the standard deviation of the pixel values in the selected area for the frame processed by the two different pipelines was calculated. This was repeated for several areas in the frame, and repeated for several frames. All of the three different detectors were tested. For all Phase 2 frames the time dependent flat had a smaller standard deviation in the background pixel values, and thus performed a better flat fielding.

2.4.3.5 Mask Anomalous Pixels

Anomalous pixels are damaged pixels on the detectors. The damage is normally caused by high energy particles, of which there are many in space, damaging the detector. Analysis of IRC frames shows there is an increase of damaged pixels over the duration of the mission. These damaged pixels (also known as 'hot' pixels) are visible in the frames as having a high dark current. This is known as displacement damage and is likely to have been caused by protons. The most damage was seen on the MIR-L, probably due to the lower number of optical elements on the light path. The MIR-S showed less damage; this is probably due to it being shielded by more optical elements along the light path. No damage was seen to the NIR. One reason for this might be that although the NIR has a similar number of elements in the optical path as the MIR-S, it does have a more complicated optical path, and this may have provided additional shielding. This damage is evident in later Phase 2 MIR-S and MIR-L images. There are two main artefacts, in addition to others discussed elsewhere in this thesis. A bespoke time dependent flat is unable to correct for these artefacts. In the MIR-S detector images there is a spread of hotter pixels in the lower right hand side of the frame. This is the part of the image nearest to the amplifier. The artefact is caused by the warming up of the amplifier and the rest of the telescope. This area needs to be masked in later Phase 2 MIR-S images. The other main artefact in later Phase 2 MIR-S and MIR-L

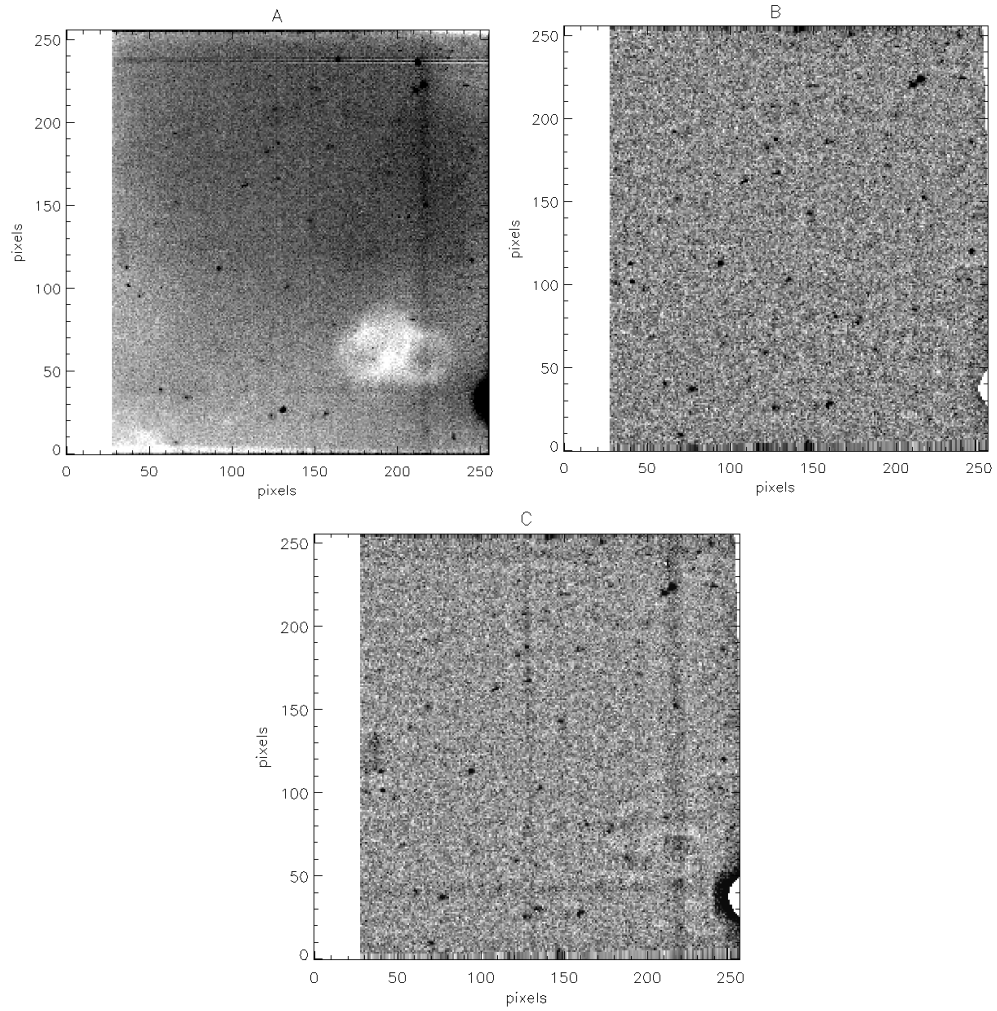

Figure 2.13: A single S11 frame showing the bean. (A) the raw frame, note the sky bean, the white patch in the bottom right. (B) is processed using a time dependent flat field, the sky bean has been fully removed. (C) is processed using the standard pipeline flat field, note that the sky bean has not been fully removed, and the horizontal and vertical artefacts have not been removed either.

images is that there are many more hot pixels.

During Phase 0 (13/04/2006 - 08/05/2006 Murakami et al. (2007)) a template was supplied by the instrument team for each of the three detectors flagging the locations of anomalous pixels. MIR-S and MIR-L masks are shown in Figure 2.14.a and Figure 2.14.b. For images taken after 01/05/2007, the optimised pipeline uses a bespoke template to flag the location of the anomalous pixels in the mask array associated with each image. The optimised hot pixel mask for MIR-S and MIR-L images is shown in Figure 2.14.c and Figure 2.14.d. The standard pipeline sets anomalous pixels to a default value (e.g. -9999.9 ADU) (Lorente, 2007). Section 2.4.3.6 shows how pixels flagged in the mask array in the optimised pipeline are assigned a value.

The hot pixels are not removed by a time dependent flat, due to the fact that the background flux of the image varies considerably during a single pointing (see Section 2.4.3.10). Figure 2.15 shows the hot pixel, with image coordinates $x = 95$, $y = 181$ from MIR-L detector frames, over an entire pointing. This demonstrates that for most of the pointing the hot pixel flux is greater than the background flux. In the case of the final few frames, the hot pixel flux is less than the background flux. Table 3.10 shows the pointings which were used to create the hot pixel mask. To create the hot pixel mask, a method similar to that which made the flat field image was used. First, all the frames were processed through the Earthshine light step. Then all the frames from one filter in the pointings listed in Table 3.10 were stacked, and the pixel values in a column were sigma clipped. The mean value of the column was then assigned to the pixel. Any pixel with a value greater than 1.025 ADU was flagged in the hot pixel mask. Note for AOT02 and AOT03, the final 3 frames were not used, and for AOT05, the final 9 frames were not used. The improvement made by the optimised hot pixel mask is shown in Figure 2.16, which shows before and after the removal of hot pixels, a coadded image is shown for clarity. The NIR detector does not appear to have the same later Phase 2 artefacts.

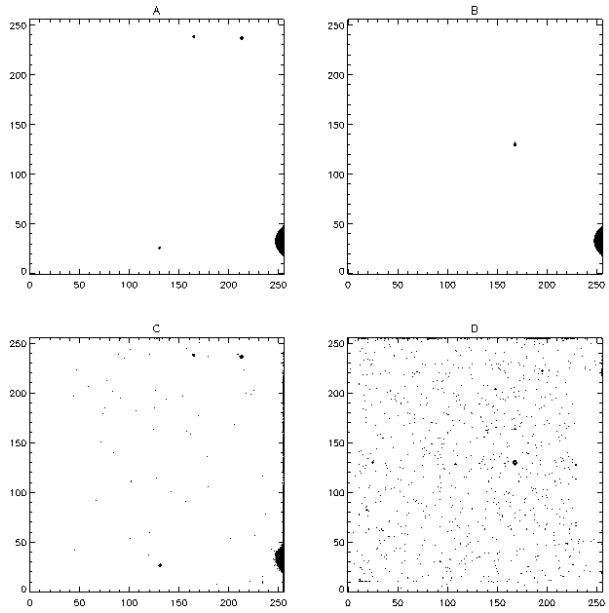

Figure 2.14: Hot pixel masks (A) shows the original MIR-S hot pixel mask, (B) shows the original MIR-L hot pixel mask. (C) shows the later Phase 2 hot pixel mask for MIR-S, (D) shows the later Phase 2 hot pixel mask for MIR-L, both created for the optimised pipeline.

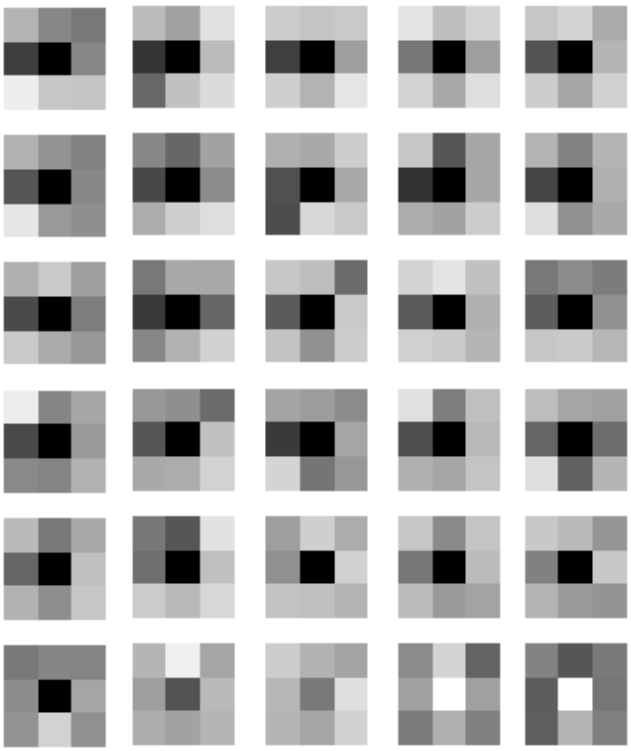

Figure 2.15: The centre pixel has x, y value of (95, 181). The figure shows how the flux of the hot pixel becomes less than that of the background flux, due to Earthshine light. These are negative images, hence the black pixels are the brightest.

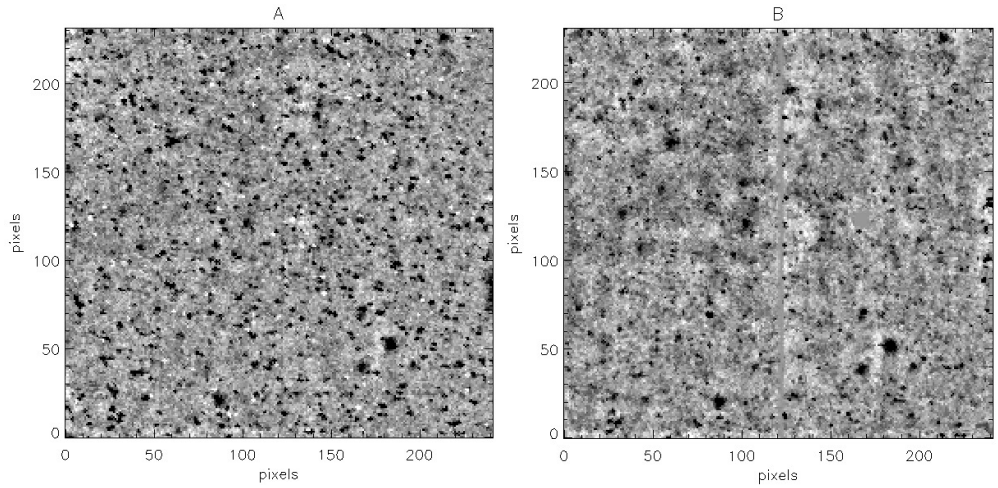

Figure 2.16: (A) shows a coadded image where the frames have been processed using an original hot pixel mask. (B) shows the same coadded image, but where the frames have been processed using the new hot pixel mask.

2.4.3.6 Mask Image

In the standard pipeline, pixels in the image, which have been identified as 'bad' pixels are set to a specific value, which has been set by the user; the preset value is -9999.90 ADU. As stated in the introduction to Section 2.4.1, the pipeline creates a mask array for each frame, the mask array has the same dimensions as the frame. The locations of bad pixels are flagged in the mask array; Figure 2.17 shows such a mask image. The steps in the optimised pipeline, which flag bad pixels are: wraparound correction, cosmic ray removal and mask anomalous pixels; see subsections 2.4.3.1, 2.4.3.3 and 2.4.3.5 respectively. Each step is assigned its own value in the bad pixel mask, e.g. the location of pixels flagged in cosmic ray removal are given the value 1 in the mask array. The mask array can be used when masking parts of the image in the coadding step or the bad pixel can be given an interpolated value. Flagged pixels in the data frame are replaced with interpolated values derived from the eight nearest pixels. If any of the eight nearest pixels are also flagged as bad pixels, then their value is not used. If all of the eight nearest pixels are flagged as bad pixels, then the bad pixel is assigned the mean average value of the image. This method does not work for a three (or greater) pixel wide column of bad pixels flagged in the wraparound correction. The locations of the eight nearest non-flagged pixels are shown in Figure 2.18. These are

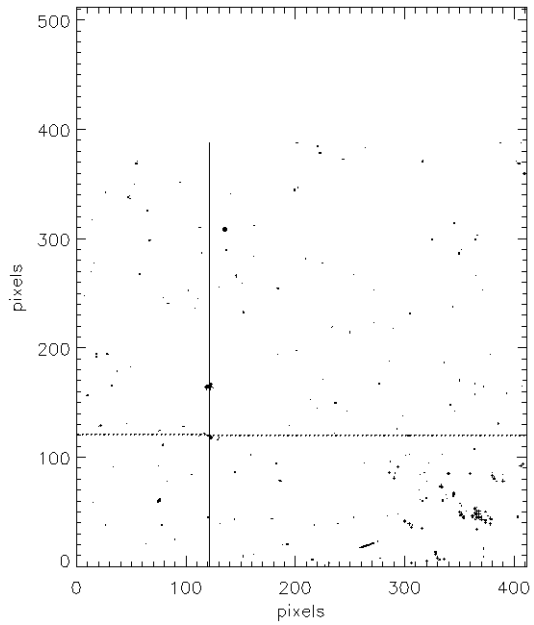

Figure 2.17: A N3 filter mask array, showing the locations of the pixels to mask.

used to give an interpolated value to a pixel flagged in the wraparound correction. The standard pipeline also masks the slit area, whereas the optimised pipeline does not, as it contains information about the dark current. The slit area is masked during the coadding stage.

2.4.3.7 Noise

The optimised pipeline creates a separate noise image for each frame. The standard pipeline does not create an individual noise image for each frame, but only creates a noise image of each coadded pointing. Individual noise images for each frame are required when performing noise weighted coadding. The noise value for each pixel is calculated using Equation 2.3 (Mortara and Fowler, 1981), where N_T is the total noise of the pixel. N_* is derived from the total number of photons. n_{pix} is the number of pixels, in this case 1. N_S is derived from the background number of photons, which is the background flux of the image. N_D is the total number of electrons caused by the dark current; this is found from the dark image. N_R^2 is the read out/shot noise of the pixel, which is calculated from the number of electrons.

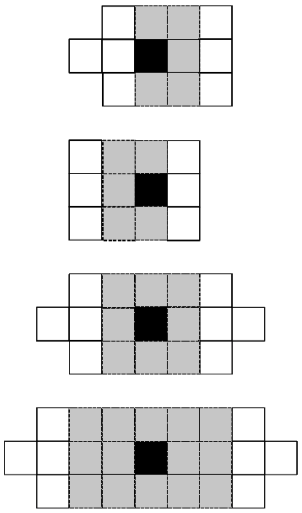

Figure 2.18: Figure showing different values given to pixels masked in the wraparound step, see Section 2.4.3.1. Black squares indicated the saturated pixel being given the interpolated value of the white squares. The grey squares are also saturated pixels.

$$N_T = \sqrt{N_* + n_{\mathrm{pix}}(N_S + N_D + N_R^2)} \tag{2.3}$$

Note that each noise image has the same distortion correction and astrometry correction as the associated image frame (see Sections 2.4.3.8 and 2.4.3.12). An analytic noise image is created for each image and used at the coadding stage.

2.4.3.8 Distortion Correction

Telescope optics and detectors can cause distortion in the IRC frames. The distortion varies from detector to detector, and there is also a small difference in distortion between each filter of the same detector. Moreover due to errors in AKARI astrometry (Section 2.4.3.12) this inaccuracy changes from frame to frame, which makes correcting for the distortion problematic. Although two frames from the same filter have the same distortion, they may have different inaccuracies in the astrometry.

This distortion is characterised using distortion polynomials. To create the distortion polynomials for the X and Y coordinates of the image from a specific filter, it is necessary to simultaneously fit the X and Y distortion polynomials and the astrometry offset. The first attempt at correcting the distortion was to attempt to correct for the jitter error

by aligning an AKARI point source with the 2MASS/WISE point source, in the same x, y position in all the frames which were being used to create the distortion polynomial. Even in a NIR frame, which has the greatest number of point sources, it was not possible to find point sources with exactly the same x, y position over multiple frames from different pointings. It was decided that to create the distortion correction polynomial, both the position of the point sources on the distorted/incorrect astrometry frame and the true galaxy position were required. Point source extraction on the IRC images gives the distorted/incorrect astrometry positions, while the true sky positions are obtained using the 2MASS catalogue (Skrutskie et al., 2006) for NIR detector frames and the WISE catalogue (Wright et al., 2010) for the MIR-S and MIR-L frames. The first attempt at distortion correction performed a partial correction. This partial correction was useful to mostly correct for the distortion, hence more AKARI and 2MASS/WISE point source matches could be made. Using these point source pairs, a χ^2 multi-parameter fitting program (Markwardt, 2009) was used to simultaneously fit the distortion and astrometry. Using an estimated distortion correction polynomial and astrometry correction the original AKARI point source position was corrected and compared to the 2MASS/WISE position. The distortion correction and the astrometry correction were then iterated until the difference between the AKARI positions and 2MASS/WISE positions were at a minimum χ^2. Using this method, a second order polynomial distortion correction was created for each filter.

The second order polynomial distortion correction for the x-axis and y-axis are given respectively by Equation 2.4 and Equation 2.5; where x is the original distorted x pixel position, y is the original distorted y pixel position, X' is the undistorted x pixel position, Y' is the undistorted y pixel position, P_{ij} is the x matrix transformation, Q_{ij} is the y matrix transformation, N is the order of polynomial, n is the square root of the number of elements of the matrix and k is the number of pairs.

$$X' = \sum_{i=0}^{N} \sum_{j=0}^{n} P_{ij} x^j y^i \tag{2.4}$$

$$Y' = \sum_{i=0}^{N} \sum_{j=0}^{n} Q_{ij} x^j y^i \tag{2.5}$$

For a second order polynomial, Equation 2.4 expands to give Equation 2.6; where the new non-distorted x pixel positions are given by the x'_{00}, x'_{1k} ... x'_{kk} diagonal in the solution.

$$\begin{pmatrix} y_0^0 & y_0^1 & y_0^2 \\ y_0^1 & y_1^1 & y_1^2 \\ \vdots & \vdots & \vdots \\ y_k^0 & y_k^1 & y_k^2 \end{pmatrix} \begin{pmatrix} P_{00} & P_{01} & P_{02} \\ P_{10} & P_{11} & P_{21} \\ P_{20} & P_{21} & P_{22} \end{pmatrix} \begin{pmatrix} x_0^0 & x_1^0 & \cdots & x_k^0 \\ x_0^1 & x_1^1 & \cdots & x_k^1 \\ x_0^2 & x_1^2 & \cdots & x_k^2 \end{pmatrix} = \begin{pmatrix} x'_{00} & x'_{01} & \cdots & x'_{0k} \\ x'_{10} & x'_{11} & \cdots & x'_{1k} \\ \vdots & \vdots & \ddots & \vdots \\ x'_{k0} & x'_{k1} & \cdots & x'_{kk} \end{pmatrix} \tag{2.6}$$

A similar polynomial is used to calculate the non-distorted y pixel positions, but using the matrix Q_{ij} instead of P_{ij}. The vector plot for the distortion correction for each of the nine filters is shown in Figure 2.19. Figure 2.20 shows the improvement to a single MIR-S frame as a result of using the distortion correction. Testing the distortion correction polynomials on the six IRC filters used during the work of thesis, they are accurate to within the Nyquist scale, i.e. less than half of the Full Width Half Maximum (FWHM). Table 2.3 shows the pixel error of the six filters.

The above method assumes that for each filter the distortion is not time dependent during Phase 2 of the AKARI mission. The distortion correction was tested on frames from November 2006 (early Phase 2), February 2007 (mid Phase 2) and July 2007 (late Phase 2), and no time dependency was found. Approximately 20 frames of different extragalactic deep fields were used to create the NIR distortion polynomials. Individual frames of extragalactic deep fields could not be used to create the MIR-S and MIR-L distortion correction polynomials. There are two main reasons for this: firstly, both raw and processed individual frames do not show many point sources (see Figure 2.13.b for an example of an individual MIR frame), secondly, in individual frames, point source extraction often incorrectly labels bad pixels as point sources, which would be removed in the coadding stage. For the χ^2 multi-parameter fitting to work correctly, each individual frame was required to have 20+ galaxies. Therefore frames of Galactic

Table 2.3: The positional error of the six IRC filters used in the work of this thesis.

Filter	positional error/pixels
N3	0.42
N4	0.63
S7	0.57
S11	0.69
L15	0.56
L18W	0.59

targets were used instead for the MIR-S and MIR-L images. The distortion correction also automatically corrects the aspect ratio.

2.4.3.9 Earthshine Artefact

IRC frames suffer from Earthshine light, caused by Sunlight reflected by the Earth onto the telescope. This artefact appears as an area of increased flux, which can move around from frame to frame on the image. The Earthshine artefact can be seen in images from all of the nine filters. The artefact is worse in the MIR detector images and during later Phase 2 observations. Figure 2.21 shows all 30 individual raw frames from a single S11 pointing observed during later Phase 2. The figure shows that the Earthshine artefact moves about the frame during a single pointing. A template or time dependent flat is not able to remove this artefact, because it moves over the frame. Individually for each frame, the Earthshine step in the optimised pipeline creates a boxcar median filtered image, with a box diameter of 20 pixels, and subtracts this from the original frame. A box with diameter of 20 pixels was chosen, as this was the minimum diameter before the flux of the point sources was altered. Figure 2.22 shows the improvement to a coadded pointing, after removal of the Earthshine artefact on each individual frame.

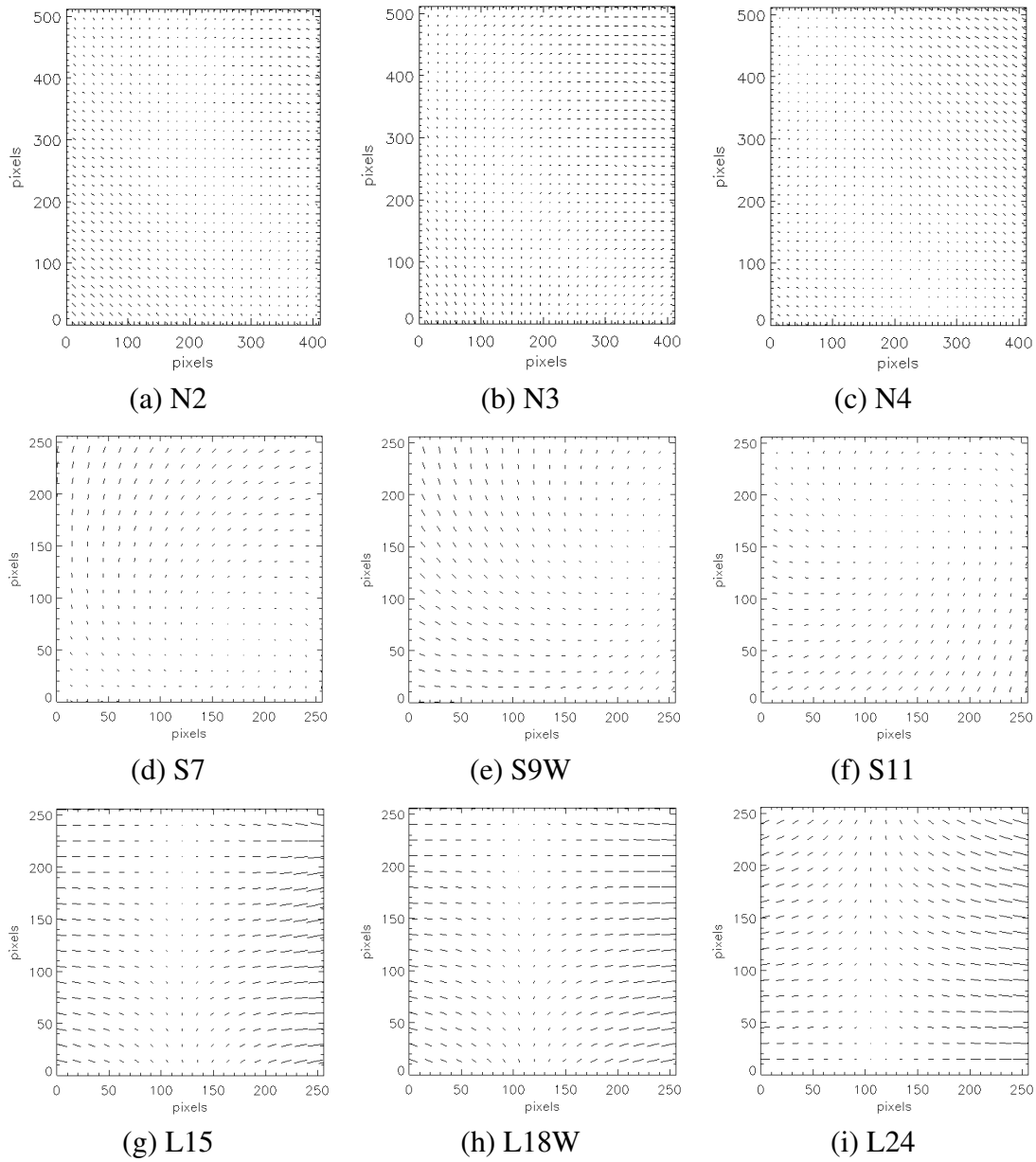

(a) N2 (b) N3 (c) N4

(d) S7 (e) S9W (f) S11

(g) L15 (h) L18W (i) L24

Figure 2.19: The figure shows the distortion correction polynomials for the nine filters.

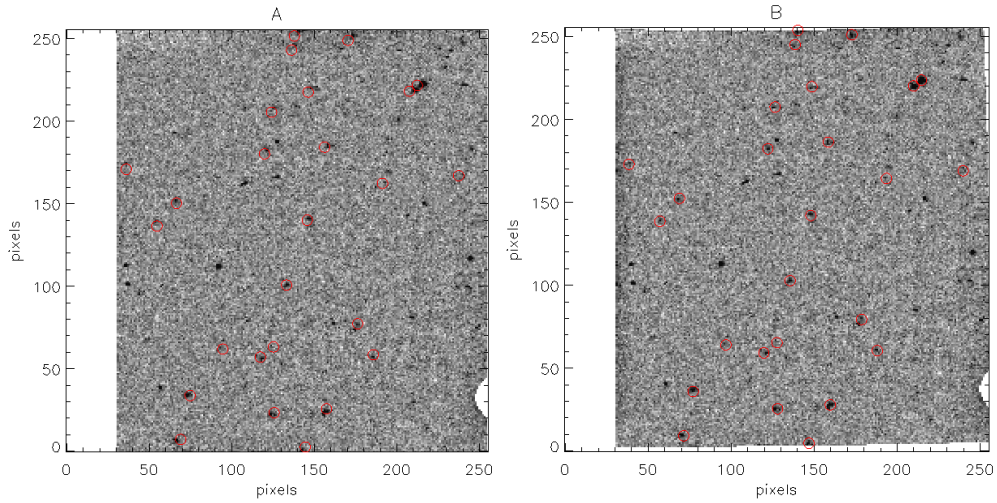

Figure 2.20: (A) shows a single S11 frame before the distortion correction is applied, and (B) shows the same frame after distortion correction has been applied. Over plotted is the WISE galaxy catalogue. Notice how in (B) the WISE galaxies are now aligned with the AKARI sources.

2.4.3.10 Earthshine Gradient

The background flux of each frame changes during a single pointing. This is present in all pointings, and the effect is greatest in MIR-S and MIR-L later Phase 2 images. This is caused by reflected Sunlight from the Earth. Figure 2.23 shows how much the average sky background flux alters over a single pointing. As can be seen in Figure 2.23, the flux variation follows the same pattern for different pointings. Figure 2.24 shows subsequent pointings of the same area of the sky that were taken approximately 100 minutes apart. This is the orbital period for the AKARI satellite, and hence the amount of reflected light during a pointing is repeated from pointing to pointing. The optimised pipeline corrects for this, by masking the point sources and calculating the average background flux for each frame. During the coadding stage (Sections 3.4, 3.5 and 3.3), the corresponding average value is subtracted from each frame. This means that all frames from a pointing can be used to create a coadded image.

2.4.3.11 Scattered Light

The MIR-L detector images suffer an additional artefact caused by scattered light (see Figure 2.25.a) caused by light reflecting off the array or filter and into the detector.

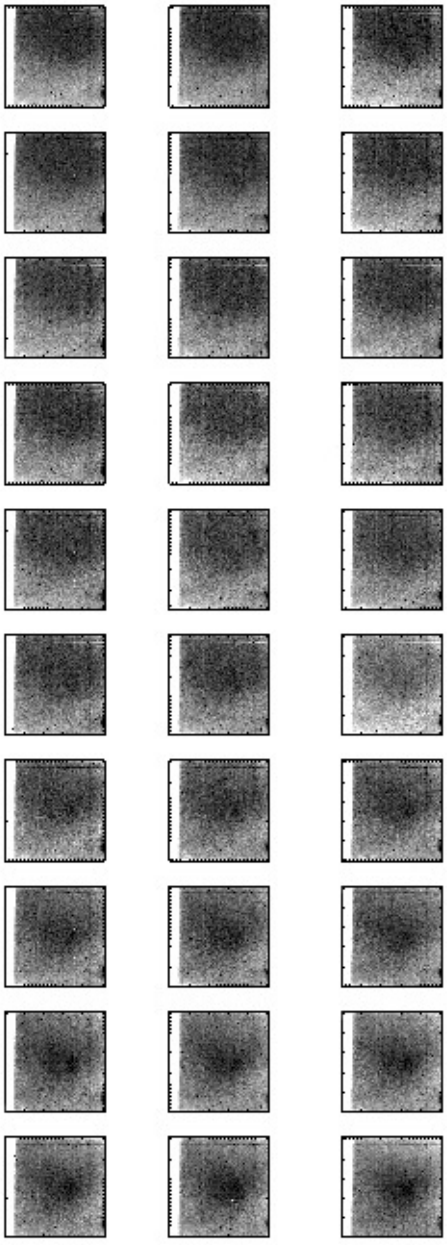

Figure 2.21: 30 raw frames from one S11 pointing from later Phase 2 data. Note how the Earthshine artefact ‘moves’ over the frame.

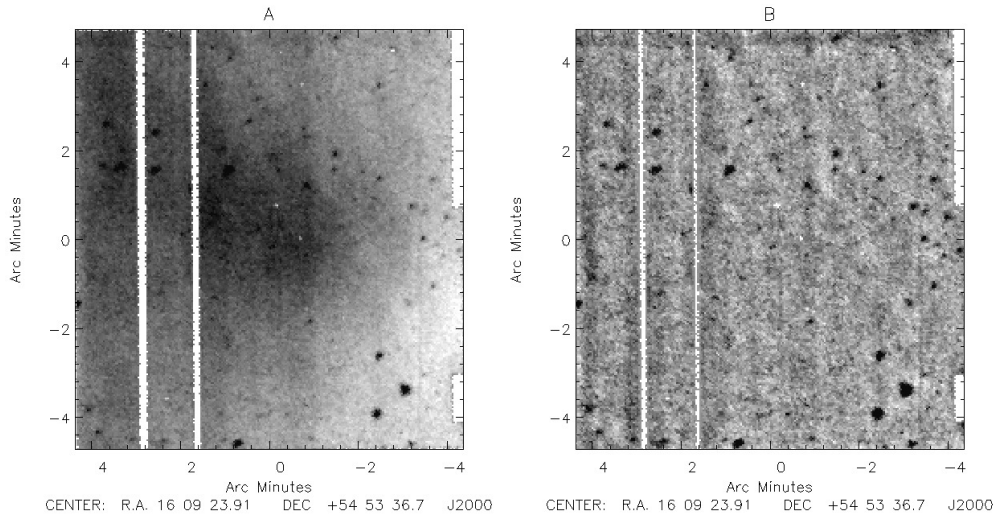

Figure 2.22: (A) shows a S11 coadded pointing of mid Phase 2 data. (B) shows the same coadded pointing processed by the pipeline. Note the removal of Earthshine light.

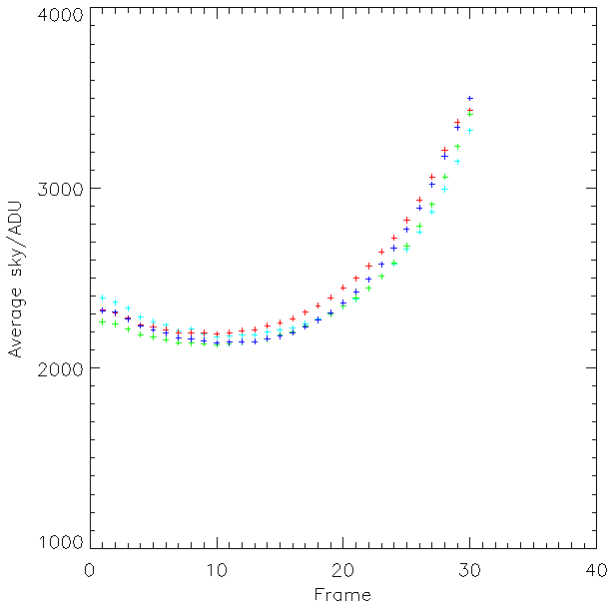

Figure 2.23: Image showing the change in average background flux of the frames over a pointing. Each different coloured set of crosses represents a different observation.

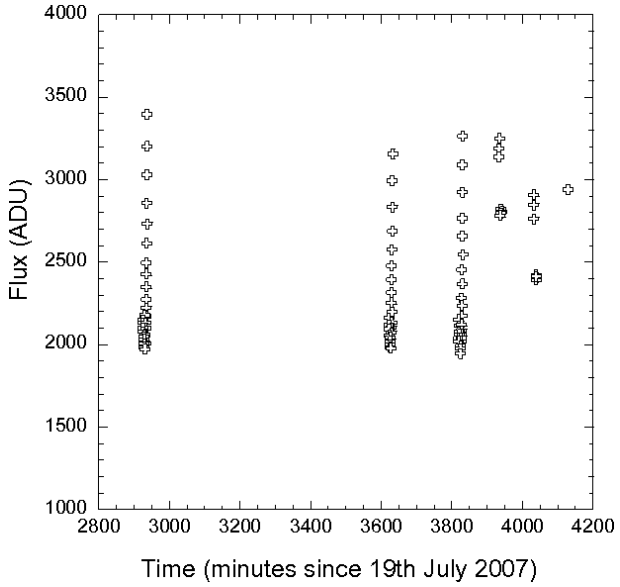

Figure 2.24: Image showing the time dependent change in background flux of the frames over a pointing.

This artefact is removed in the same pipeline step as the Earthshine light (see Section 2.4.3.9), by subtracting a boxcar median filtered image from the original frame. The removal of this artefact is demonstrated in Figure 2.25.

2.4.3.12 Astrometry Correction

IRC frames have a positional offset, due to telescope jitter, which varies from frame to frame. An example of such an offset is shown in Figure 2.26. It is believed that the jitter occurs because the star tracker is a Charge Coupled Device (CCD) and needs to be heated. Unfortunately the heating for the star tracker is only on or off. The 'on' temperature was too high, so it is switched on and when it reached the temperature required, it was then turned off. As it changed temperature the equipment expanded and contracted, hence the changes in jitter. In the past these astrometry offsets have prevented the successful processing of faint extragalactic deep fields. The standard pipeline coadds frames observed by the same filter in a single pointing and then corrects the astronomical offset on the final coadded image. In reality the astrometry needs to be corrected for each individual frame, because the offset can vary from frame to frame in the same pointing. The standard pipeline calculates the astrometry correction

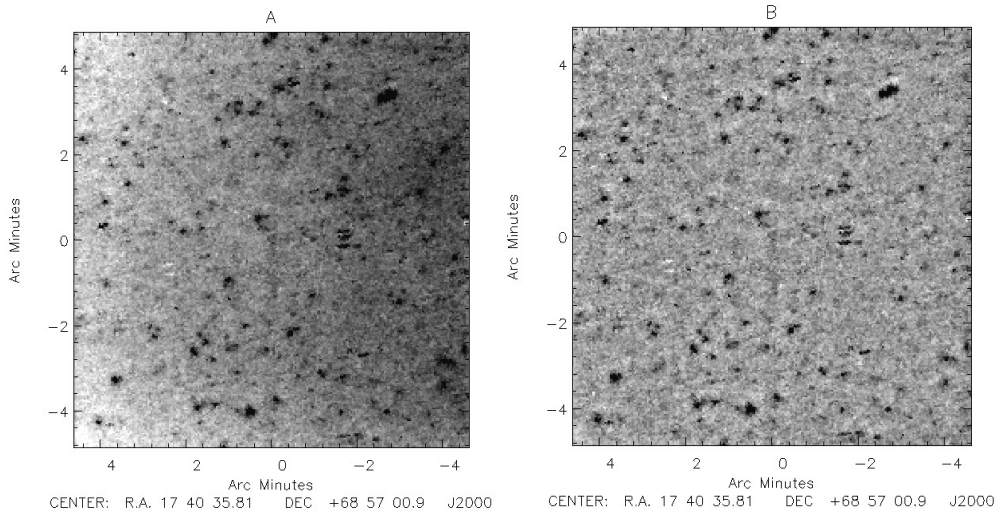

Figure 2.25: (A) shows the MIR-L detector scattered light artefact. (B) shows the removal of the scattered light artefact. A coadded image is shown for clarity.

for a single NIR frame and applies it to the MIR-S and MIR-L frames observed simultaneously with the NIR frame. However the astrometry correction for a single NIR frame can not always be applied to the six associated MIR-S and MIR-L frames, as the astrometry offset can be different between individual frames. The optimised pipeline corrects for the astrometry offset on each frame individually.

The astrometry correction step in the optimised pipeline corrects the astrometry of all the frames from a single pointing frame by frame, independently for each filter. The astrometry of the first frame in the pointing is corrected by aligning an extracted point source with the same source in the 2MASS (for NIR detector) or WISE (for MIR-S and MIR-L detectors) galaxy catalogues. Each subsequent frame of the same filter in the pointing is then aligned to the first frame by aligning the point sources. After the frames have been through the astrometry correction stage, they are ready to be coadded with frames from other pointings. In the astrometry correction, the headers for the noise image and mask array are edited to have the same astrometry as that associated with each frame.

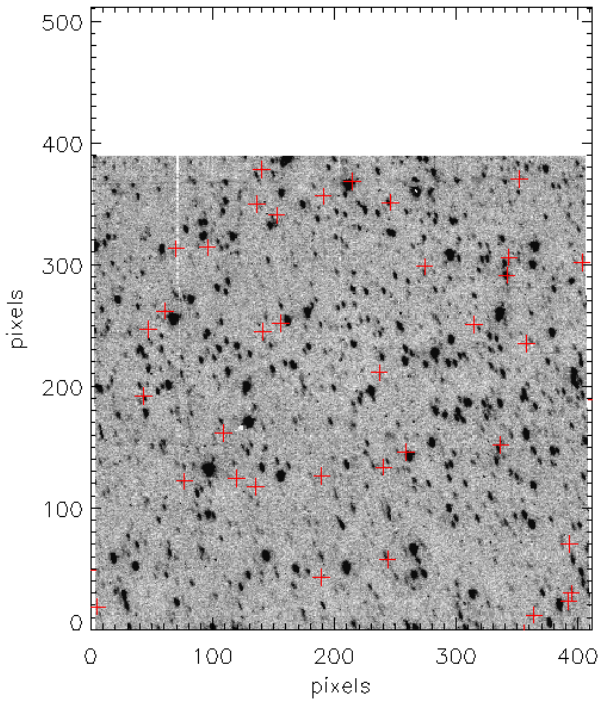

Figure 2.26: Figure showing the astrometry offset for a single N4 frame. The 2MASS galaxy catalogue is over plotted.

2.4.3.13 Masking Before Coadding

Due to the increased temperature of the telescope, as discussed in Section 2.4.3.5, and memory effects, images from the later stages of Phase 2 have artefacts, which neither a dedicated flat field or hot pixel mask are able to remove. Figure 2.27 shows the two different types of memory effects. In Figure 2.27.a the 'clover leaf' pattern memory effect has been caused by imaging a very bright source in a pointing observed up to a few hours prior to the frame in Figure 2.27.a. This artefact has a distinctive clover leaf pattern because the pointing observing the very bright source was dithered. The other type of memory effect is shown in Figure 2.27.b. This is caused by a bright source observed on the IRC array during an AKARI/FIS scanning observation, and hence the artefact appears as vertical lines. The pixels damaged by the warming up of the telescope and those affected by the memory effects do not have any useful information, and are therefore masked. The same area is masked for all frames in a pointing. Pointings of the same extragalactic field are masked separately. This masking is performed in the optimised pipeline after the astrometry distortion correction step and before the

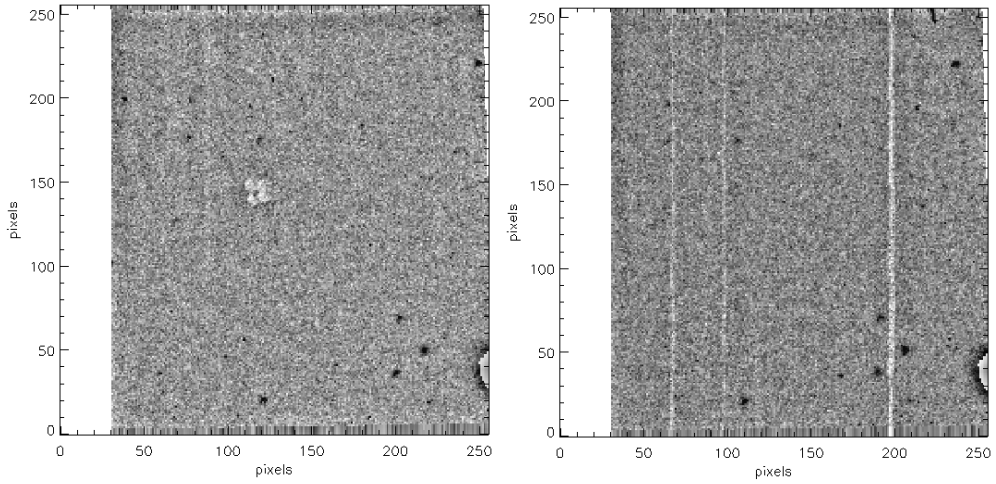

Figure 2.27: The image on the left shows the 'clover leaf' memory effect from a previous AKARI/IRC pointing, and the image on the right shows the vertical lines memory effect from a previous AKARI/FIS observation. Note both images show an artefact caused by the telescope warming up, close to the amplifier. This can be seen on the lower right hand side of each image.

coadding stage. Figure 2.28 demonstrates the improvement to an extragalactic deep field by performing masking on individual frames.

Several ghost artefacts have been discussed in previous papers. Murata et al. (2013) discuss a ghost artefact created by a bright source reflected about the image pixel position coordinates $x = 115$, $y = 350$. An example of this artefact is shown in Figure 3.5. This artefact was only present in the NIR images. The artefact was treated similarly to the memory effects discussed above, and masked where appropriate.

Arimatsu et al. (2011) discuss several ghost artefacts in the MIR bands, caused by bright sources. In the MIR-S band bright sources have a ghost artefact, repeating at about 24 pixels in the y-direction from the source. In both the MIR-S and L bands bright sources have a ghost artefact a little offset from the true source, and a set of two concentric artefacts, both bigger than the original source. As the extragalactic fields discussed in this paper do not have any overly bright sources in the MIR-S and MIR-L bands, it can be assumed that these artefacts are below the instrument noise level.

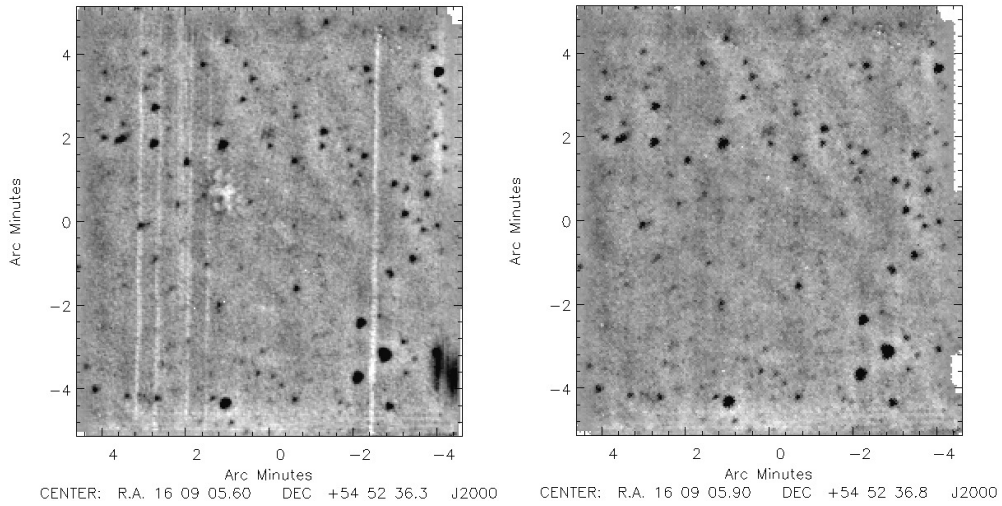

Figure 2.28: The image on the left shows the un-masked coadded pointing of the 5 S11 pointings of ELAIS-N1. The image on the right shows the same coadded pointings, but where the individual frames were masked before coadding.

2.4.4 Post-Pipeline

Once the individual frames have been processed through the optimised pipeline they are ready to be mosaicked into the final deep field images. Mosaicking was performed on the deep field images described in Chapter 3 and Chapter 4 by mosaicking all frames (from multiple pointings) of the same filter in the deep field together. Before mosaicking the frames, the sky background was subtracted off each frame; this was performed to remove the Earthshine gradient discussed in Section 2.4.3.10.

During mosaicking a second cosmic ray rejection is performed, as discussed in Section 2.4.3.3.

During the mosaicking stage the individual noise images associated with each frame are used, to create a noise weighted mosaicked image. The value for each pixel in the final mosaicked image is given by Equation 2.7, where n is the number of frames, F is the processed frame and N is the noise frame associated with the processed frame. The mosaicking stage also mosaics the individual noise images. The formula to create the mosaicked noise image is given by Equation 2.8.

$$F_{tot} = \frac{\sum_{i=1}^{n} \frac{F_i}{N_i^2}}{\sum_{i=1}^{n} \frac{1}{N_i^2}} \tag{2.7}$$

$$N_{tot} = \frac{1}{\sqrt{\sum_{i=1}^{n} \frac{1}{N_i^2}}} \tag{2.8}$$

The zero footprint drizzling method for the mosaicking was investigated for creating the AKARI mosaicked images. The drizzling method, which is the Variance-Pixel Linear Reconstruction algorithm of Fruchter & Hook (1997), was designed for Hubble Space Telescope (HST) images. The limiting case of drizzling with δ-function footprints is known as zero footprint (Serjeant et al., 2003). This is where a coarse pixel grid (e.g. the pixel size of the detector) of an individual frame is apportioned to a smaller area in a finer grid i.e. the flux from one coarse pixel is put into just one finer pixel, which is at the location of the centre of the coarse pixel. This is repeated for all coarse pixels in a frame and for all frames required to be mosaicked. With sufficient dithering, the data should populate all of the finer pixels. This zero footprint image can then be match-filtered for point sources. See Serjeant et al. (2003) and Pearson (2005) for examples of use of the zero footprint method. The zero footprint method was found not to be successful at creating mosaicked AKARI images in the work of this thesis. The method did not remove the cosmic rays as successfully. The main reason why the zero footprint method did not work as well was because of under sampling. This was caused by the fact that ELAIS-N1 and the IRAC Dark Field (see Section 3.15) which are both deep fields, did not have dithered pointings and secondly because there were too few pointings in each filter to overcome this problem.

2.5 Conclusions on the New Data Pipeline for Processing AKARI Data

This chapter provides a brief summary of the instrumentation onboard the AKARI satellite, information about the AKARI/IRC observations, the standard pipeline written to process AKARI/IRC data and a thorough description of a new optimised pipeline

for processing extragalactic deep fields.

The optimised pipeline replicates and in some cases improves upon the following steps from the standard pipeline: wraparound correction, dark subtraction, normalisation, linearity correction, cosmic ray removal, flat fielding and masking anomalous pixels. The optimised pipeline also performs steps, which the standard pipeline did not do on individual frames: creating a noise image, distortion correction, Earthshine light correction, scattered light correction, astrometry correction and masking.

Six of the above steps make significant improvements on the standard pipeline. The first is the flat fielding step. This removes instrumental artefacts which the standard pipeline was unable to do, e.g. the bean, see Figure 2.13. The second step is masking hot pixels in later Phase 2 data, which may otherwise be detected as point sources in the coadded image. As these hot pixels are not visible in the final frames of a pointing, due to Earthshine light heating the detector to a temperature greater than that of the hot pixels, they are not detected in the standard flat field image. The optimised pipeline uses a bespoke hot pixel mask. Figure 2.16 shows the improvement of using this mask, to a coadded image. AKARI data suffers from image distortion and astrometry offset, which in the past has made cross-matching with ancillary data sets hard to perform. The third significant improvement is the creation and use of a second order polynomial distortion correction for the x and y axes for each of the nine filters. The fourth improvement is correcting the astrometry offset on each individual frame before coadding. AKARI data, in particular later Phase 2 data, is badly effected by Earthshine light, both as a moving artefact on the image and as an increase of average flux of a frame over a pointing, caused by the warming up of the detector. The fifth major improvement of the optimised pipeline is the removal of both types of Earthshine light. Figure 2.22 shows an example of this. The final major improvement, is that individual frames are masked before the coadding stage, as apposed to after coadding. This means that less of the final image is masked, and thus has signal from a greater area. With the improvements described in this chapter, the AKARI frames processed by the optimised pipeline are science ready.

Chapter 3

Galaxy Number Counts and Catalogues from the IRAC Dark Field, ELAIS North 1 and AKARI Deep Field South

I had the means of an excellent education placed within my reach; a fondness for some of my studies, and a desire to excel in all

Jane Eyre - Charlotte Brontë

3.1 Introduction

To answer the current question of how galaxies evolve, the statistical properties of galaxy populations are required (Oliver et al., 2000). The most basic of these is galaxy number counts. Galaxy number counts show the number of galaxies per unit area within a specific flux range. Galaxy number counts were originally used as a way of determining the geometry of the Universe. Early discoveries using the results from radio galaxy number counts, showed that the Universe is inconsistent with a steady-state model (Rowan-Robinson, 1967). Subsequently galaxy number counts have been

used to study galaxy evolution, star formation history and the epoch of galaxy formation (Ellis, 1987). In order to study how different galaxy populations behave at different wavelengths, we need galaxy number counts at many wavelengths (Pearson & Rowan-Robinson, 1996). A population of galaxies which contribute strongly to the mid-infrared number counts, are dusty star forming galaxies (Elbaz et al., 1999). A way to study these galaxies, negating modelling the individual complicated dust features, is to perform galaxy number counts. Number counts study the population of galaxies as a whole, and can aid in constraining the evolution of dusty star forming galaxies (Murata et al., 2014a).

In this chapter the optimised pipeline is applied to three major legacy survey fields, the IRAC Dark Field, ELAIS North 1 and the AKARI Deep Field South, creating mosaicked images of the fields. Source catalogues and number counts are created using these mosaicked images. The number counts are compared with existing number counts work and galaxy number counts models.

This chapter is organised as follows: Section 3.2 explains how galaxy number counts are calculated, and how reliability and completeness corrections are performed. Section 3.3 gives a brief summary of the ancillary data in the IRAC Dark Field and data reduction of the AKARI data in this field. Section 3.4 summarises the ancillary data and image reduction of the AKARI ELAIS North 1 extragalactic deep field. The ancillary data and image reduction of the AKARI Deep Field South are summarised in Section 3.5. The creation of the galaxy catalogues is described in Section 3.6. The number counts work for all three extragalactic fields is presented in Section 3.7. These number counts are compared with non-evolution galaxy number count models in Section 3.8. Section 3.9 introduces appropriate number count models and some published number counts. These are compared with the number counts of this chapter.

3.2 Number Counts Theory

3.2.1 Calculation of Number Counts

When calculating the galaxy number counts, it is standard practice to plot galaxy number counts relative to the predictions for a spatially flat, non-evolving Universe; also known as Euclidean normalised number counts. Number counts are also known as source counts. A Euclidean space is the three dimensional coordinate system used to describe the Universe at non-relativistic speeds.

Galaxy number counts are counting the number of galaxies in a given survey with fluxes between S and $S+dS$, where dS is some small increment of S. The flux of one star/galaxy is given by Equation 3.1, where S is the flux of the source, L is the luminosity of the source and r is the distance from the source to the observer.

$$S = \frac{L}{4\pi r^2} \tag{3.1}$$

Taking the derivative with respect to r gives:

$$\frac{dS}{dr} = -\frac{L}{2\pi r^3} \tag{3.2}$$

$$\frac{dS}{dr} \propto \frac{L}{r^3} \tag{3.3}$$

Equation 3.3 can be re-written as:

$$\frac{dr}{dS} \propto \frac{r^3}{L} \tag{3.4}$$

Also from Equation 3.1

$$S \propto r^{-2} \tag{3.5}$$

$$r \propto S^{-1/2} \tag{3.6}$$

To find the number of galaxies (with identical flux) within a given radial shell from the observer, we need the volume of the shell. The area of the sphere of the shell is given by $4\pi r^2$, where r is the radius of the sphere. The thickness of the shell is given by dr. The volume can be approximated by the area multiplied by the thickness of the shell. Thus the volume of the shell is $4\pi r^2 dr$. Hence the number of galaxies in the shell is given by Equation 3.7. where ρ is the density of the galaxies.

$$dN = \rho \times 4\pi r^2 dr \tag{3.7}$$

$$dN \propto \rho r^2 dr \tag{3.8}$$

We need to know the number of galaxies between S and $S + dS$, hence we need the equation in terms of $\frac{dN}{dS}$. Multiplying both sides of Equation 3.8 by $\frac{dr}{dS}$ gives:

$$dN\frac{dr}{dS} = \rho r^2 dr\frac{dr}{dS} \tag{3.9}$$

From Equation 3.4 we know $\frac{dr}{dS} \propto \frac{r^3}{L}$

$$dN\frac{dr}{dS} = \rho r^2 dr\frac{r^3}{L} \tag{3.10}$$

Dividing both sides by dr

$$\frac{dN}{dr}\frac{dr}{dS} \propto \frac{\rho r^5}{L} \tag{3.11}$$

The two dr terms on the LHS panel cancel. Using Equation 3.6 where $r \propto S^{-1/2}$ gives:

$$\frac{dN}{dS} \propto S^{-5/2} \tag{3.12}$$

The above equation gives the number of galaxies in the flux range S to $S + dS$, for a flat Euclidean Universe; and is known as Euclidean differential source counts (Serjeant, 2010).

For galaxy number counts the flux S is plotted against $\frac{dN}{dS} S^{2.5}$ per flux per unit area.

If we live in a flat Euclidean Universe with non-evolving galaxies, then the differential galaxy number counts, as described above, when plotted on a log-log plot, should all lie along a horizontal line.

As the Universe is expanding, one would expect a small deviation from a horizontal line. What observational cosmologists are testing for is a much larger deviation from a horizontal line, which is caused by galaxies evolving. Galaxy evolution models are tested against the observed galaxy number counts. Galaxy evolution models are made up of percentages of different types of galaxies. By comparing observation with model, the evolution of the different types of galaxies can be probed (Patanchon et al., 2009).

3.2.2 Reliability

When performing source extraction on a mosaicked image, some non-galaxy sources will be mis-identified as real sources. Fine tuning the parameters in the source extraction will minimise fake source detection, but some are likely to remain. These mis-identified galaxies are normally due to noise in the image. Galaxy number counts need to be corrected for these false positive sources, which have been mis-identified as galaxies. These false positive sources will increase the number counts in the flux bins with the fake sources. There are several ways in which reliability can be tested. The most common way is to assume that there are as many negative fake sources as there are positive fake sources. By multiplying the mosaicked image by -1, the negative sources become positive and vice-versa. This negative image is then run through the source extraction software with the same settings as for the positive image. Though simple to perform, this method does rely on the assumption that there are as many negative fake sources as positive fake sources. If there are some particular artefacts

in the image, this assumption may not be true (Clements et al. (2011), Pearson et al. (2010), Pearson et al. (2014) and Murata et al. (2014a)). A second method is to use Monte Carlo simulations by creating a simulated noise realisation of the mosaicked image. Each simulated noise realisation is run through the source extraction software, again with the same settings. This is performed multiple times. This method assumes that all fake sources are caused by noise but will not find those fake sources caused by instrumental effects (Hatsukade et al., 2011). A third method is to visually inspect the mosaicked image at the positions of the point sources, which have a point source probability below a certain level. This method would be quite time consuming for large survey areas, and/or multi-wavelength filter sets for galaxy catalogues, as well as including a human error into the point source detection (Scott et al., 2010a). A fourth method is to create a difference image from two different observations of the same area. Then this difference image is run through the source extraction software. Fake sources should be detected as sources in the difference image (Oliver et al., 2010). This requires an absence of astrometry shifts between the observations. For the reliability correction of the IRAC Dark Field, ELAIS North 1 and AKARI Deep Field South number counts for the work in this thesis, the first method has been used. The second method was not used, due to the fact that it assumes that all fake sources are caused by noise, this is known not to be the case for AKARI e.g. AKARI is known to have Earthshine light residual. The third method was rejected due to it being time consuming and because it could include a human error. The fourth method was not employed because it relies on the fact that there is no astrometry error between observations. It is known that AKARI data have astrometry error. Section 3.7.3 gives the reliability correction for both extragalactic fields.

3.2.3 Completeness

A further correction which is required to be performed on the number counts is to correct for the galaxies that have not been detected during the source extraction. This is

called a completeness correction. This correction normally raises the faint end number count slope, because more faint galaxies will be un-detected in the source extraction, than brighter galaxies. It will particularly increase the numbers of galaxies close to the detection limit of the survey. By far the most common way to correct for completeness is to inject fake sources of a known flux and location into the mosaicked image and then run the image through the source extraction software, with the same settings as those for the original source extraction. By running Monte Carlo simulations of this i.e. repeating this multiple time for a specific flux range, the percentages of injected sources detected can be calculated. The simplest flux range is to use the range of each flux bin used to create the number counts. One problem with this method is the detected source may not be the injected source, but a true source, which was already present in the image. There are several slightly different variations of this method. The first method is to inject just one artificial fake source into the mosaicked image and run this through the source extraction. This is repeated many times for each flux range (Hatsukade et al., 2011). The second method is to inject many fake sources simultaneously into the mosaicked image and then run this image through the source extraction. Again, this is repeated for each flux range. To inject many fake sources simultaneously, one requires a large survey area (Clements et al. (2011), Pearson et al. (2010), Pearson et al. (2014) and Murata et al. (2014a)). A third method is similar to the second method, but injects the fake sources at a distance greater than a specific distance (normally some multiple of the FWHM, of the instrument) away from any real point sources. This is done to avoid creating a fake source/true source blend, but will not correct for a two-source blend, as the previous methods do (Scott et al. (2010a) and Hopwood et al. (2010)). A fourth method does not use a simulated fake source; instead, a real source is created empirically from the mosaicked image, and the flux is scaled to be that of the flux range. This method is useful when the Point Spread Function (PSF) of the detector is highly irregular (Fazio et al., 2004). After completeness correction has been performed, i.e. the number counts have been scaled accordingly, it must be decided at what completeness percentage the number counts will be cut.

For the number counts in this thesis, the first method has been used. The second method was rejected, because the IRAC Dark Field and ELAIS North 1 were not a large survey area. The third was not used due to the fact it does not correct for blended sources. The fourth method was not employed because it is known that the AKARI PSF shape is dependent on the position in the frame, so it was uncertain how representative the empirical PSF would have been. The results of Section 4.3 appear to indicate that an empirical PSF would be a better choice than a standard Gaussian PSF. Section 3.7.4 shows the completeness corrections for both extragalactic fields.

3.3 IRAC Dark Field

3.3.1 The IRAC Dark Field Survey Area and Ancillary Data

Observations of the IRAC Dark Field by Spitzer Infrared Array Camera (IRAC) were used in calibrating the instrumental background for IRAC frames. The deep field survey is a 20 by 20 arcminute area, centred on 17h40m00s and +69°00m00s (J2000), close to the North Ecliptic Pole (NEP). This survey area is a unique Spizter/IRAC deep field, as it was observed every two to three weeks over a 5+ year period with IRAC. The Spitzer/IRAC data in this area therefore is very deep. The location of the IRAC Dark Field was chosen due to it being an area of low zodiacal background, because it is free of bright stars and because of an absence of very extended sources. Also, specifically for the IRAC instrument it was chosen because the area is always observable by Spitzer (Krick et al., 2009). The IRAC Dark Field has follow-up observations in the X-ray by Chandra, in the optical by the Hale telescope at Palmer in the u', g', r' and i' filters, by the HST in F814W and also by the Multiple Mirror Telescope (MMT) Megacam in the Z-band (Krick et al., 2009). The area also has ancillary observations in the near-infrared from the National Optical Astronomy Observatory (NOAO) in the J-band, the MMT/SWIRC J and H band, and the Hale telescope at Palomar in the J, H and K-bands (Wilson et al. (2003) and Brown et al. (2008)). The IRAC Dark Field also has mid-

infrared Spitzer Multi-band Imaging Photometer (MIPS) data (Krick et al., 2009) and far-infrared data from Herschel/SPIRE (Pearson et al., in prep). The IRAC Dark Field has spectroscopic data in the optical from the HST (Krick et al., 2009). The area also has fairly shallow spectroscopic data in the near and mid-infrared from AKARI/IRC (PI Egami). A very comprehensive multi-wavelength catalogue, created by Krick et al. (2009) includes AKARI data processed by the standard AKARI/IRC pipeline. Processing the raw AKARI/IRC frames through the pipeline optimised for extragalactic deep field images as discussed in Chapter 2, should produce mosaicked images with a better removal of artefacts and a reduction in astrometry error for the point sources; hence a deeper catalogue to cross match with the one created by Krick et al. (2009).
The IRAC Dark Field was an AKARI Open Time survey (PI Egami), a 10 by 10 arcminute area centred on the Spitzer/IRAC Dark Field. Table 3.1 shows the AKARI/IRC pointings of the IRAC Dark Field. There were 34 successful pointings of the IRAC Dark Field. It was observed 19 times by the N4 and S11 filters, 10 times by the L15 filter and 5 times by the L18W filter. Note half of the observations were observed in October 2006 (late Phase 1) and the other half were observed in April/-May 2007 (mid Phase 2). The N4 and S11 frames were obtained during the same pointings. All pointings were observed using IRC05, the Astronomically Observed Template (AOT) for deep pointings, see Section 2.2.3 for a detailed explanation for the IRC AOTs. IRC05 does not have an option for dithered pointings, hence the IRAC Dark Field pointings were not dithered. Due to the fact that each of these pointings covered roughly the same area of sky, this is one of the deepest fields observed by AKARI/IRC.

3.3.2 Data Reduction pf the AKARI IRAC Dark Field

Section 2.4.1 describes the pipeline as part of this work, optimised for processing extragalactic deep fields. The IRAC Dark Field pointings were processed through the optimised pipeline.

Table 3.1: Observation log for the IRAC Dark Field pointings.

Pointing Number	Date	Filter	AOT
3030001-001	18/10/2006	N4 & S11	IRC05
3030001-003	18/10/2006	N4 & S11	IRC05
3030001-004	16/04/2007	N4 & S11	IRC05
3030001-005	19/10/2006	N4 & S11	IRC05
3030001-006	19/04/2007	N4 & S11	IRC05
3030001-007	27/10/2006	N4 & S11	IRC05
3030001-008	27/10/2006	N4 & S11	IRC05
3030001-009	27/10/2006	N4 & S11	IRC05
3030001-010	27/10/2006	N4 & S11	IRC05
3030001-011	28/10/2006	N4 & S11	IRC05
3030001-012	19/04/2007	N4 & S11	IRC05
3030001-013	20/04/2007	N4 & S11	IRC05
3030001-014	31/10/2006	N4 & S11	IRC05
3030001-015	21/04/2007	N4 & S11	IRC05
3030001-016	21/04/2007	N4 & S11	IRC05
3030001-017	21/04/2007	N4 & S11	IRC05
3030001-018	22/04/2007	N4 & S11	IRC05
3030001-019	22/04/2007	N4 & S11	IRC05
3030001-020	22/04/2007	N4 & S11	IRC05
3030002-001	10/10/2006	L15	IRC05
3030002-002	10/10/2006	L15	IRC05
3030002-003	12/10/2006	L15	IRC05
3030002-004	12/10/2006	L15	IRC05
3030002-005	23/04/2007	L15	IRC05
3030003-001	13/10/2006	L18W	IRC05
3030003-002	13/10/2006	L18W	IRC05
3030003-003	13/10/2006	L18W	IRC05
3030003-004	13/10/2006	L18W	IRC05
3030003-005	23/04/2007	L18W	IRC05
3031001-001	14/05/2007	L15	IRC05
3031001-002	14/05/2007	L15	IRC05
3031001-003	14/05/2007	L15	IRC05
3031001-004	15/05/2007	L15	IRC05
3031001-005	15/05/2007	L15	IRC05

The late Phase 1 S11 frames all suffer from a time dependent artefact, known as the bean (or sore-mame). This artefact can be seen in the lower right part of Figure 2.13.a. Section 2.4.3.4 states that the bean was present in all MIR-S frames from Phase 0 to 07/01/2007. The bean varies over a timescale of several days. The standard flat fields do not remove it. Section 2.4.3.4 explains how the optimised pipeline removes the bean artefact by using a very time dependent flat field. The flat field image was created using frames from less than three days difference from the pointing being processed by the pipeline. See Tables 3.3 to 3.4 for the pointings used to create the time dependent flat fields to remove the bean artefact. This method fully removed the bean. Tables 3.2, 3.5 and 3.6 give the pointings used to create the flat fields for the other IRAC Dark Field pointings.

When processing the IRAC Dark Field frames, the optimised hot pixel mask was used. Because the IRAC Dark Field frames were observed earlier on in the mission than ELAIS-N1 (which was observed late Phase 2) the detectors do not have as many damaged pixels. The standard hot pixel mask does not mask all the damaged pixels visible in the IRAC Dark Field frames. Section 2.4.3.5 shows how the optimised hot pixel mask was created.

The Earthshine light correction step was performed on the IRAC Dark Field frames. Late Phase 1 and mid Phase 2 data are not as badly affected by Earthshine light as late Phase 2, but it was still present in the MIR-S and MIR-L IRAC Dark Field frames.

The IRAC Dark Field frames required a smaller amount of masking of individual frames, than for ELAIS-N1 and ADF-S, the reason being that the observations were taken earlier in the mission, and hence the detectors had less damage.

Table 3.7 gives a list of frames not used to create the IRAC Dark Field mosaicked images. The ELAIS-N1 and ADF-S pointings also contained frames with an artificial stripe pattern. This is caused by a cosmic ray hitting the detector and is discussed in Section 3.4.2. The one frame badly affected by a cosmic ray hitting the detector has also been removed. The survey area of the IRAC Dark Field is 0.027 square degrees. Figure 3.1 shows the IRAC Dark Field deep field images from the optimised pipeline

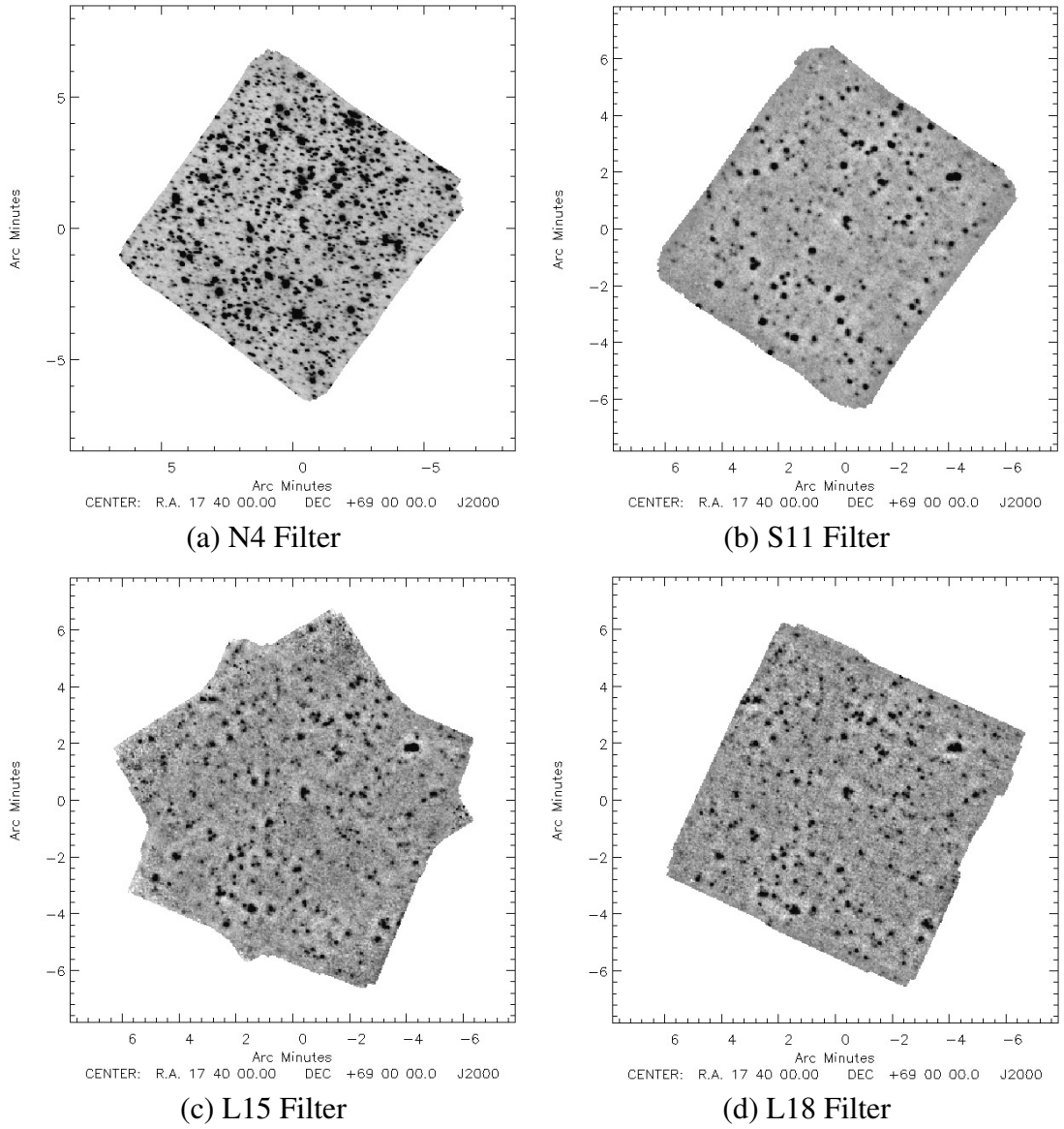

(a) N4 Filter (b) S11 Filter

(c) L15 Filter (d) L18 Filter

Figure 3.1: The IRAC Dark Field mosaicked images.

at 4, 11, 15 and 18 μm. The source extraction for the IRAC Dark Field is described in Section 3.6.1 and the galaxy number counts are described in Section 3.7.6.

3.4 ELAIS North 1

3.4.1 The ELAIS North 1 Survey Area and Ancillary Data

The ELAIS North 1 (hereafter ELAIS-N1) is one of 11 fields making up the European Large Area ISO Survey (ELAIS). The total survey area was 12 square degrees,

Table 3.2: Pointings used to create flat fields for IRAC Dark Field L15 and L18W images 01/10/2006 to 20/10/2006.

Pointing Number	Date	Programme	L15	L18W
1600009-001	01/10/2006	MP-AFSAS	12	-
2100520-001	07/10/2006	LS-LSNEP	9	9
2100548-001	01/10/2006	LS-LSNEP	9	9
2100549-001	13/10/2006	LS-LSNEP	9	9
2100589-001	07/10/2006	LS-LSNEP	-	9
2100590-001	16/10/2006	LS-LSNEP	-	9
2100641-001	04/10/2006	LS-LSNEP	-	9
2100642-001	11/10/2006	LS-LSNEP	-	9
2100643-001	17/10/2006	LS-LSNEP	-	9
2100705-001	02/10/2006	LS-LSNEP	-	9
2100706-001	07/10/2006	LS-LSNEP	-	9
2100707-001	13/10/2006	LS-LSNEP	-	9
2100708-001	19/10/2006	LS-LSNEP	-	9
2100782-001	05/10/2006	LS-LSNEP	-	9
2100784-001	15/10/2006	LS-LSNEP	-	9
2100785-001	10/10/2006	LS-LSNEP	-	9
2201080-001	02/10/2006	LS-LSLMC	12	-
2201081-001	03/10/2006	LS-LSLMC	9	-
3030002-001	10/10/2006	OT-ISAS-EGAMI	30	-
3190033-001	20/10/2006	OT-ISAS-COLVN	9	9
4250009-001	04/10/2006	OT-ESA-6AND7	12	-
4250017-001	03/10/2006	OT-ESA-6AND7	12	-
4250021-001	20/10/2006	OT-ESA-6AND7	12	-
5121016-001	01/10/2006	DT-DTIRC	9	9
5121017-001	17/10/2006	DT-DTIRC	9	9
5122016-001	01/10/2006	DT-DTIRC	9	-
5124032-001	13/10/2006	DT-DTIRC	9	-
5124033-001	14/10/2006	DT-DTIRC	6	-
5124034-001	17/10/2006	DT-DTIRC	9	-
Total number of frames			186	162

Table 3.3: Pointings used to create flat fields for IRAC Dark Field S11 images 20/10/2006 to 22/10/2006.

Pointing Number	Date	Programme	Number
1800005-001	20/10/2007	MP-VEGAD	12
1800228-001	21/10/2007	MP-VEGAD	12
1800229-001	22/10/2007	MP-VEGAD	12
3190024-001	21/04/2007	OT-ISAS-COLVN	6
3190033-001	20/04/2007	OT-ISAS-COLVN	6
5122017-001	15/10/2006	DT-DTIRC	6
Total number of frames			54

Table 3.4: Pointings used to create flat fields for IRAC Dark Field S11 images 26/10/2006 to 31/10/2006.

Pointing Number	Date	Programme	Number
1300049-001	28/10/2006	MP-CLEVL	12
1400062-001	29/10/2006	MP-ISMGN	12
1400515-001	29/10/2006	MP-ISMGN	12
2100787-001	29/10/2006	LS-LSNEP	6
2100875-001	26/10/2006	LS-LSNEP	6
2201139-001	26/10/2006	LS-LSLMC	6
2201153-001	29/10/2006	LS-LSLMC	6
3030001-007	27/10/2006	OT-ISAS-EGAMI	6
3030001-011	28/10/2006	OT-ISAS-EGAMI	6
Total number of frames			72

Table 3.5: Pointings used to create flat fields for IRAC Dark Field N4 images 20/10/2006 to 31/10/2006.

Pointing Number	Date	Programme	Number
1300049-001	28/10/2006	MP-CLEVL	4
1400062-001	29/10/2006	MP-ISMGN	4
1800005-001	20/10/2007	MP-VEGAD	4
1800211-001	25/10/2007	MP-VEGAD	4
1800228-001	21/10/2007	MP-VEGAD	4
1800229-001	22/10/2007	MP-VEGAD	4
1800244-001	28/10/2007	MP-VEGAD	5
2100550-001	25/10/2006	LS-LSNEP	2
2100591-001	25/10/2006	LS-LSNEP	2
2100644-001	23/10/2006	LS-LSNEP	2
2100709-001	24/10/2006	LS-LSNEP	2
2100786-001	24/10/2006	LS-LSNEP	2
2100874-001	23/10/2006	LS-LSNEP	2
2100787-001	29/10/2006	LS-LSNEP	2
2100875-001	27/10/2006	LS-LSNEP	2
3030001-007	27/10/2006	OT-ISAS-EGAMI	5
3030001-008	27/10/2006	OT-ISAS-EGAMI	5
3030001-009	27/10/2006	OT-ISAS-EGAMI	5
3030001-010	27/10/2006	OT-ISAS-EGAMI	5
3030001-011	28/10/2006	OT-ISAS-EGAMI	5
3190024-001	21/04/2007	OT-ISAS-COLVN	2
3190033-001	20/04/2007	OT-ISAS-COLVN	2
5122017-001	22/10/2006	DT-DTIRC	2
Total number of frames			76

Table 3.6: Pointings used to create flat fields for IRAC Dark Field N4, L15 and L18W images 13/04/2007 to 25/04/2007.

Pointing Number	Date	Programme	N4	S11	L15	L18W
1100121-001	21/04/2007	MP-AGNUL	-	-	-	3
1100133-001	15/04/2007	MP-AGNUL	-	-	-	3
1100134-001	22/04/2007	MP-AGNUL	-	-	-	3
1300106-001	22/04/2007	MP-CLEVN	-	-	30	-
1300106-002	22/04/2007	MP-CLEVN	-	-	30	-
1300106-003	22/04/2007	MP-CLEVN	-	-	30	-
1401001-001	19/04/2007	MP-ISMGN	-	12	9	-
1401003-001	20/04/2007	MP-ISMGN	-	12	9	-
1401057-001	20/04/2007	MP-ISMGN	-	9	9	-
1401070-001	20/04/2007	MP-ISMGN	-	12	9	-
1600949-001	14/04/2007	MP-AFSAS	-	12	12	-
1800255-001	16/04/2007	MP-VEGAD	-	-	6	-
1800311-001	18/04/2007	MP-VEGAD	-	-	9	-
1800312-001	20/04/2007	MP-VEGAD	4	-	12	-
1800336-001	20/04/2007	MP-VEGAD	-	-	12	-
1800337-001	20/04/2007	MP-VEGAD	-	-	9	-
1800343-001	20/04/2007	MP-VEGAD	-	-	12	-
1800344-001	11904/2007	MP-VEGAD	4	-	12	-
1800352-001	17/04/2007	MP-VEGAD	4	-	15	-
2110535-001	23/04/2007	LS-LSNEP	2	6	9	9
2110570-001	20/04/2007	LS-LSNEP	3	9	9	9
2110616-001	13/04/2007	LS-LSNEP	3	9	-	9
2110617-001	21/04/2007	LS-LSNEP	2	6	9	9
2110675-001	13/04/2007	LS-LSNEP	3	9	9	9
2110676-001	18/04/2007	LS-LSNEP	-	9	9	-
2110677-001	24/04/2007	LS-LSNEP	-	6	-	-
2110746-001	13/04/2007	LS-LSNEP	3	9	-	9
2110747-001	15/04/2007	LS-LSNEP	2	-	-	9
2110829-001	15/04/2007	LS-LSNEP	3	-	-	9
2110830-001	21/04/2007	LS-LSNEP	2	-	-	9
2110831-001	23/04/2007	LS-LSNEP	3	-	-	9
2110923-001	15/04/2007	LS-LSNEP	2	-	-	9
2110924-001	17/04/2007	LS-LSNEP	3	-	-	9
2110925-001	22/04/2007	LS-LSNEP	3	-	-	9
2110926-001	25/04/2007	LS-LSNEP	2	-	-	9
3030003-005	23/04/2007	OT-ISAS-EGAMI	-	-	-	30
3030004-013	24/04/2007	OT-ISAS-EGAMI	-	-	-	3
3180007-001	24/04/2007	OT-ISAS-COABS	-	-	-	3
3190017-001	17/04/2007	OT-ISAS-COLVN	2	6	-	9
3190018-001	18/04/2007	OT-ISAS-COLVN	2	6	-	9
3190020-001	18/04/2007	OT-ISAS-COLVN	2	6	-	9
3190025-001	16/04/2007	OT-ISAS-COLVN	2	6	-	9
3190026-001	16/04/2007	OT-ISAS-COLVN	3	9	-	9
3190027-001	17/04/2007	OT-ISAS-COLVN	-	6	-	-
3190032-001	18/04/2007	OT-ISAS-COLVN	-	6	-	-
3190034-001	16/04/2007	OT-ISAS-COLVN	-	6	-	-
3190035-001	17/04/2007	OT-ISAS-COLVN	-	9	-	-
3250005-001	21/04/2007	OT-IASA-SGPWD	-	-	-	3
3250005-002	21/04/2007	OT-IASA-SGPWD	-	-	-	3
4110013-001	14/04/2007	OT-ESA-DEAGB	-	-	-	3
4220016-001	20/04/2007	OT-ESA-SUBMM	4	12	-	-
4220022-001	13/04/2007	OT-ESA-SUBMM	5	12	-	-
4220023-001	13/04/2007	OT-ESA-SUBMM	4	12	-	-
4220025-001	13/04/2007	OT-ESA-SUBMM	4	12	-	-
Total number of frames			75	228	270	225

Table 3.7: Table showing the discarded frames.

Filter	Pointing Number	Frame Number	Reason
S11	3030001_014	F004059008_S004	Artificial stripe pattern
L15	3031001_001	F008043439_L004	Cosmic ray
L15	3031001_004	F008048716_L002	Artificial stripe pattern
L15	3031001_004	F008048716_L003	Artificial stripe pattern
L15	3031001_004	F008048716_L004	Artificial stripe pattern
L15	3031001_004	F008048718_L002	Artificial stripe pattern
L15	3031001_004	F008048718_L003	Artificial stripe pattern
L15	3031001_004	F008048718_L004	Artificial stripe pattern

making ELAIS the largest open time survey performed by ISO (Infrared Space Observatory). The main extragalactic aims of ELAIS were to study star formation over cosmic time, galaxies containing AGN, the dust in distant galaxies and ULIRGs galaxies at high z. The chosen areas all have high Galactic latitudes and hence low zodiacal background light. The ELAIS-N1 field was observed at 15, 90 and 175 μm with ISO (Oliver et al., 2000). ELAIS-N1 is one of three areas of the FU-HYU (Follow-Up Hayai-Yasui-Umai) (PI Pearson, proposal ID FUHYU) survey observed with AKARI. The FU-HYU survey imaged GOODS North (RA = 12h36m50s, Dec = +62°12'58" J2000), Lockman (RA = 10h52m43s, Dec = +57°28'48" J2000) and ELAIS-N1 (RA = 16h09m20s, Dec = +54°57'00" J2000) (Pearson et al., 2010). ELAIS-N1 is one of the deepest surveys performed by AKARI. ELAIS-N1 has the best visibility of the three FU-HYU fields, due to AKARI's high elliptical latitude orbit. See Section 2.1 for a description of the orbit of AKARI. Table 3.8 shows the AKARI/IRC pointings of ELAIS-N1. There are 20 successful observations of ELAIS-N1 for the FU-HYU program. It was observed 6 times using the N4 filter, 6 times using the S11 filter, 7 times using the L15 filter and 7 times using the L18W filter. The N4 filter and S11 filter images were obtained during the same pointings. ELAIS-N1 has a large amount of multi-wavelength data. ELAIS-N1 has follow up observations and spectroscopy in the optical and near-infrared in the U, g, r, i, J and K-bands, observed by the Isaac Newton Telescope (INT) and STELRCam (McMahon et al. (2001) and Väisänen et al.

(2002)). The area was also observed in radio, using the Very Large Array (VLA) at 20 cm (Ciliegi et al., 1999). Follow up observations were also performed in the X-ray, by ROSAT at 0.1 to 2.4 keV and by Chandra at 0.5 to 8 keV (Basilakos et al. (2002) and Manners et al. (2003)). ELAIS N1 was observed by the Spitzer Space Telescope at 24 μm by Multiband Imaging Photometer (MIPS) (Chary et al., 2004). More recently ELAIS N1 has also been observed by the Herschel Space Observatory at 110, 160, 250, 350 and 500 μm as part of the Herschel Multi-tiered Extragalactic Survey (HerMES) (Oliver et al., 2012). With such a large range of multi-wavelength data, ELAIS-N1 is an ideal field to be processed by the optimised AKARI pipeline.

3.4.2 Data Reduction of the AKARI ELAIS North 1 Field

Table 3.8 shows the observation log for the ELAIS-N1 pointings. Since most of these pointings are late Phase 2 the frames suffer from higher Earthshine light. Section 2.4.3.9 shows how the most significant components of the Earthshine light were removed. The later Phase 2 images suffered from more detector deterioration. The time dependent flat field image corrected for some of the deterioration. For the pointings used to create the flat field images see Tables 3.9 and 3.10. The deterioration in the MIR-S and MIR-L detectors caused by damaged 'hot' pixels were masked using a new hot pixel mask, shown in Section 2.4.3.5. As discussed in Section 2.4.3.13, there was an increase in MIR-S detector temperature close to the amplifier; this area of the frames required masking. Several of the ELAIS-N1 MIR-S and MIR-L frames had memory effects which required masking. Figure 2.27 shows examples of these artefacts. The standard pipeline coadds a pointing, then masks, which means that the jitter increases the sky area affected by bad pixels. Since the frames are masked before coadding, in the optimised pipeline, the intrinsic jitter of the telescope can be used to increase the total useable area of the frames. Furthermore the optimised pipeline also astrometry corrects individual frames before coadding. Two of the ELAIS N1 pointings, 1320235-002 and 1320235-003, had offsets of up to 135 arcseconds and 318 arcseconds respec-

tively. This extreme case of astrometry error is illustrated in Figure 3.2, which shows an astrometry drift of approximately 125 pixels, corresponding to 318 arcseconds, over the duration of a single pointing. It is thought that this is caused by the star tracker and telescope observing different parts of the sky. These large astrometry offsets for two of the L15 pointings were corrected by the optimised pipeline. The standard pipeline was unable to coadd these two pointings. See Figure 3.3 for a comparison between optimised pipeline coadd and the standard pipeline coadd for pointing 1320235-003. The individual frames were checked for possible image ghosts discussed in Murata et al. (2013), but none were found. Table 3.11 shows the frames, which were not used to create the ELAIS-N1 deep field image. The artificial stripe pattern, listed in Table 3.11, is caused by a cosmic ray hitting the detector and saturating the entire node. This effect lasts for a few minutes, and can be seen in subsequent frames. The single frame with many hot pixels was probably caused by protons or electrons trapped by the Earth's magnetic field hitting the detector. Figure 3.4 show ELAIS-N1 deep field images from the optimised pipeline at 4, 11, 15 and 18 μm. The survey area of ELAIS-N1 is 0.028 square degrees. The source extraction for the ELAIS-N1 field is described in Section 3.6.1 and the galaxy number counts are described in Section 3.7.6.

3.5 AKARI Deep Field South

3.5.1 The AKARI Deep Field South Survey Area and Ancillary Data

The AKARI Deep Field South (hereafter ADF-S) is near to the South Ecliptic Pole and one of the AKARI Mission Programme extragalactic deep fields. This 12 square degree region centred on RA = 04h44m00s, Dec = -53°20'00" J2000 was observed by all 4 bands of the FIS at 65, 90, 140 and 160 μm (PI Matsuura, Matsuura et al. (2011)). The central 1 square degree area of the ADF-S was also observed in Open Time, using the IRC (PI Pearson, proposal ID IRSEP). The ADF-S was chosen as a

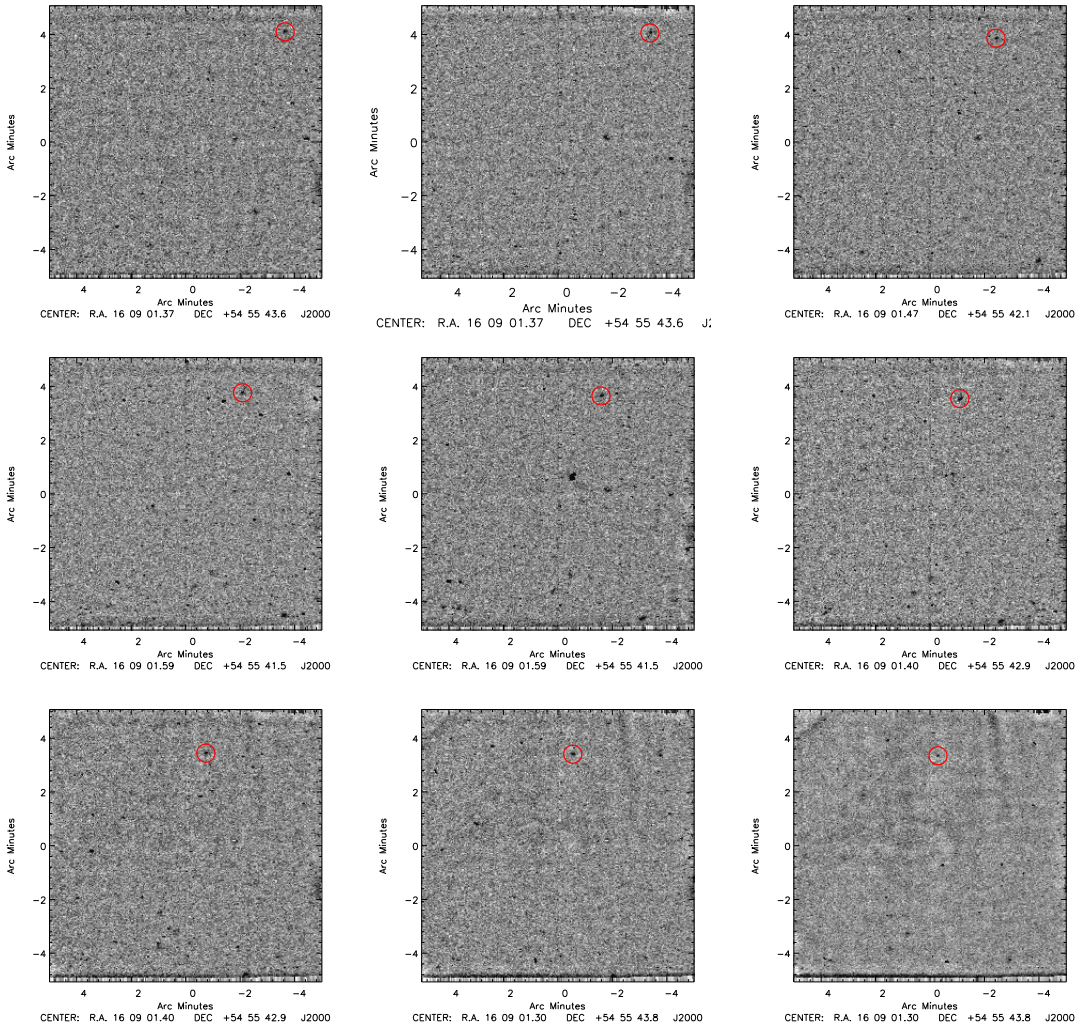

Figure 3.2: L15 frames over a single pointing, note the drift in astrometry, the same galaxy is circled.

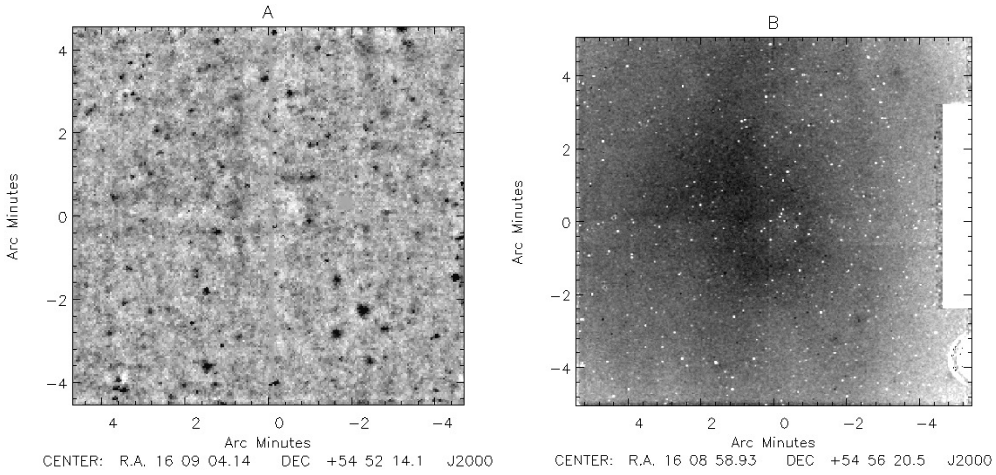

Figure 3.3: (A) shows a single pointing processed by the optimised pipeline, (B) shows the same pointing processed by the standard pipeline.

Table 3.8: Observation log for the ELAIS North 1 pointings.

Pointing Number	Date	Filter	AOT
1320226-001	19/07/2007	N4 & S11	IRC05
1320226-003	19/07/2007	N4 & S11	IRC05
1320226-004	19/07/2007	N4 & S11	IRC05
1320226-005	19/07/2007	N4 & S11	IRC05
1320226-006	20/07/2007	N4 & S11	IRC05
1320226-007	20/07/2007	N4 & S11	IRC05
1320235-001	21/07/2007	L15	IRC05
1320235-002	21/07/2007	L15	IRC05
1320235-003	21/07/2007	L15	IRC05
1320235-005	22/07/2007	L15	IRC05
1320013-001	16/01/2007	L15	IRC05
1320014-001	15/01/2007	L15	IRC05
1320015-001	17/01/2007	L15	IRC05
1320232-001	20/07/2007	L18W	IRC05
1320232-002	20/07/2007	L18W	IRC05
1320232-003	20/07/2007	L18W	IRC05
1320232-004	21/07/2007	L18W	IRC05
1320232-005	22/07/2007	L18W	IRC05
1320232-006	22/07/2007	L18W	IRC05
1320232-007	22/07/2007	L18W	IRC05

Table 3.9: Pointings used to create flat fields for the L15 ELAIS North 1 images 12/01/2007 to 21/01/2007.

Pointing Number	Date	Observation Programme	Number
1300009-001	12/01/2007	MP-CLEVL	12
1300010-001	12/01/2007	MP-CLEVL	12
1300011-001	12/01/2007	MP-CLEVL	12
1300012-001	12/01/2007	MP-CLEVL	12
1300015-001	13/01/2007	MP-CLEVL	12
1400002-001	18/01/2007	MP-ISMGN	12
1400017-001	18/01/2007	MP-ISMGN	12
1400018-001	19/01/2007	MP-ISMGN	12
1400054-001	13/01/2007	MP-ISMGN	12
1500001-001	20/01/2007	MP-SOSOS	12
1500810-001	21/01/2007	MP-SOSOS	09
1500816-001	16/01/2007	MP-SOSOS	12
1700202-001	14/01/2007	MP-AGBGA	12
1700205-001	12/01/2007	MP-AGBGA	12
1700207-001	14/01/2007	MP-AGBGA	12
1700209-001	14/01/2007	MP-AGBGA	12
1700210-001	12/01/2007	MP-AGBGA	12
1700212-001	12/01/2007	MP-AGBGA	12
1800046-001	17/01/2007	MP-VEGAD	12
1800168-001	19/01/2007	MP-VEGAD	12
2110527-001	20/01/2007	LS-LSNEP	09
2110559-001	19/01/2007	LS-LSNEP	09
2110602-001	12/01/2007	LS-LSNEP	09
2110603-001	18/01/2007	LS-LSNEP	09
2110658-001	12/01/2007	LS-LSNEP	09
4090016-001	13/01/2007	OT-ESA-CERN2	09
4090017-001	14/01/2007	OT-ESA-CERN2	09
4150001-001	12/01/2007	OT-ESA-EGALS	09
4150001-002	12/01/2007	OT-ESA-EGALS	09
4150001-003	12/01/2007	OT-ESA-EGALS	09
Total number of frames			327

Table 3.10: Pointings used to create flat fields for ELAIS North 1 images 19/07/2007 to 22/07/2007, and the pointings used to create the later Phase 2 bad pixel mask.

Pointing Number	Date	Programme	N4	S11	L15	L18W
1300327-007	15/07/2007	MP-CLEVL	-	-	-	30
1300327-008	15/07/2007	MP-CLEVL	-	-	-	30
1300327-009	17/07/2007	MP-CLEVL	-	-	-	30
1300327-010	17/07/2007	MP-CLEVL	-	-	-	30
1300327-011	18/07/2007	MP-CLEVL	-	-	-	30
1402001-001	20/07/2007	MP-ISMGN	-	-	12	-
1402699-001	19/07/2007	MP-ISMGN	-	-	12	-
1402701-001	19/07/2007	MP-ISMGN	04	-	-	-
1501107-001	18/07/2007	MP-SOSOS	04	12	12	-
1501108-001	18/07/2007	MP-SOSOS	-	12	09	-
1501225-001	16/07/2007	MP-SOSOS	04	12	09	-
1501226-001	17/07/2007	MP-SOSOS	04	12	09	-
1501227-001	16/07/2007	MP-SOSOS	04	12	09	-
1501228-001	17/07/2007	MP-SOSOS	04	-	12	-
1501229-001	17/07/2007	MP-SOSOS	-	-	12	-
1501230-001	18/07/2007	MP-SOSOS	04	-	12	-
1501231-001	17/07/2007	MP-SOSOS	04	-	12	-
1501232-001	18/07/2007	MP-SOSOS	04	-	12	-
1501814-001	23/07/2007	MP-SOSOS	04	-	12	-
1701139-001	15/07/2007	MP-AGBGA	04	12	09	-
1701140-001	15/07/2007	MP-AGBGA	04	12	12	-
1701143-001	15/07/2007	MP-AGBGA	04	12	09	-
1701144-001	15/07/2007	MP-AGBGA	04	12	09	-
1701150-001	24/07/2007	MP-AGBGA	04	12	12	-
1800526-001	22/07/2007	MP-VEGAD	-	-	12	-
3141006-001	16/07/2007	OT-ISAS-FIREC	04	12	12	-
3141010-001	18/07/2007	OT-ISAS-FIREC	-	12	12	-
3141011-001	15/07/2007	OT-ISAS-FIREC	-	12	09	-
3221005-001	23/07/2007	OT-ISAS-SHARP	-	12	09	-
4231010-001	15/07/2007	OT-ESA-EROMU	04	12	12	-
5121034-001	16/07/2007	DT-DTIRC	02	06	09	09
5122034-001	16/07/2007	DT-DTIRC	02	06	09	09
5124112-001	23/07/2007	DT-DTIRC	02	06	-	-
5124113-001	24/07/2007	DT-DTIRC	02	06	-	-
5124114-001	24/07/2007	DT-DTIRC	02	06	-	-
Total number of frames			78	210	279	168

Table 3.11: ELAIS North 1 discarded frames.

Filter	Pointing Number	Frame Number	Reason
L18W	1320232_003	F009136797_L004	Artificial stripe pattern
L18W	1320232_003	F009136798_L002	Artificial stripe pattern
L18W	1320232_003	F009136798_L003	Artificial stripe pattern
L18W	1320232_003	F009136798_L004	Artificial stripe pattern
L18W	1320232_004	F009145059_L004	Many hot pixels

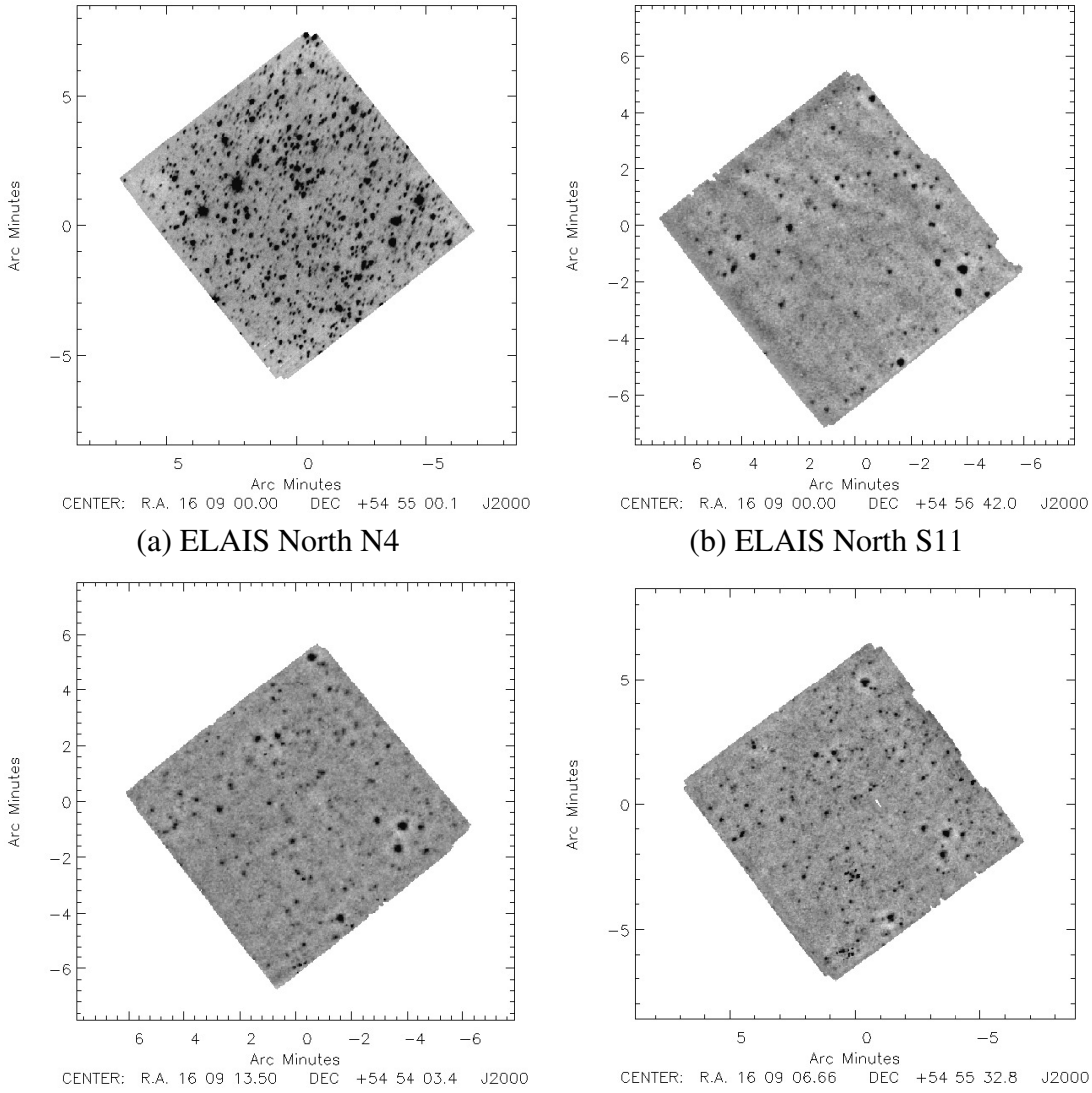

(a) ELAIS North N4

(b) ELAIS North S11

(c) ELAIS North L15

(d) ELAIS North L18

Figure 3.4: The four ELAIS North 1 mosaicked images.

Mission Programme deep field due to it being a low Galactic cirrus region. The ADF-S is an ideal area for AKARI to observe, due to the fact that the satellite is in a polar orbit, so AKARI was able to make many multiple pointings of the region, see Section 2.2.1 for details about the orbit of AKARI. During AKARI Phase 2, there were 23 successful IRC pointings of the ADF-S. Table 3.12 shows the AKARI/IRC pointings of ADF-S. IRC02 was used and hence the pointings are all dithered. The 23 pointings were observed using the N3, N4, S7, S11, L15 and L24 filters. There has been subsequent multi-wavelength follow up of the ADF-S. The region has been observed in the UV by GALEX (White et al., 2012). In the optical, the R-band has been observed by MOSAIC-II and the U, B, V and I-bands has been observed by MOSAIC, both part of the Cerro Tololo Inter-American Observatory (CTIO) (Barrufet et al., in prep). The area has been observed in the submillimetre by Ballon-borne Large Aperture submillimetre Telescope (BLAST) at 250, 350 and 500 μm (Valiante et al., 2010) and by the Atacama Pathfinder EXperiment/Large Apex BOlometer CAmera (APEX/LABOCA) at 870 μm (White et al., 2012). The ADF-S has been observed in the millimetre by the AzTEC on the Atacama submillimetre Telescope Experiment (ASTE) at 1.1 mm Hatsukade et al. (2011), and in the radio at 20 cm by the Australian Telescope Compact Array (ATCA) (White et al. (2012)). There are also spectroscopic data taken with AAT AAOmega and IMACS Magellan (Sedgwick et al. (2011) and White et al. (2012)). The ADF-S was observed by Spitzer/MIPS as part of the Spitzer Wide-Area Infrared Extragalactic Survey (SWIRE) at 24 and 70 μm (Scott et al. (2010a) and Clements et al. (2011)). The Herschel Space Observatory observed the ADF-S at 110, 160, 250, 350 and 500 μm as part of the HerMES survey (Oliver et al., 2012). Although the AKARI/IRC survey of the ADF-S is a shallow field, the ADF-S have a concentration of multi-wavelength data, and thus is of importance to analyse.

3.5.2 Data Reduction of the AKARI Dark Field South

Table 3.12 shows the observation log for the ADF-S pointings. The ADF-S as observed by AKARI/IRC is a shallow field. The main difference with creating a mosaicked shallow field as opposed to a deep field, is that the bad pixels, which were not flagged in the cosmic ray removal, are not removed during the coadding stage. The mosaicked image of the ADF-S is only 3 to 4 frames deep in the N3 and N4 filter images, whereas the N4 ELAIS-N1 mosaicked image is 30 frames deep. Due to this, many of the NIR frames require individual masking to remove an artefact only present in that frame, which is also visible in the coadded image. This also occurrs in several of the MIR-S and MIR-L frames. The NIR frames also require extra masking due to the muxbleed discussed in Section 2.4.3.1. When there are several saturated pixels together caused by overly bright stars, there is a horizontal line in the initial coadd. Because the pointings were dithered, the star and horizontal line changed position on the image. By masking the horizontal line on the individual frames, the total area of the coadded image, which is masked is a lot less than just masking the coadded image. The ghosts and artefacts mentioned in Murata et al. (2013) are visible in one pointing, see Figure 3.5, and have been masked. Table 3.13 shows the pointings used to create the time dependent flat field images, and Table 3.14 shows the list of frames not used. The reason for the artificial stripe pattern and the cause of the many hot pixels are discussed in Section 3.4. The protons or electrons causing the hot pixels in this extragalactic field probably originate from the radiation belt and the South Atlantic Anomaly (SAA). The flux error listed in Table 3.14 is always on a final imaging frame in a pointing and is caused by the shutter closing when the frame was taken. Frames which have been badly damaged by a bright cosmic ray impact have also been removed. The effect of the cosmic ray lasts for a few minutes and can be seen in subsequent frames. Figure 3.6 shows the mosaicked ADF-S images in the six AKARI/IRC filters at 3, 4, 7, 11, 15 and 24 μm. The survey area of the ADF-S is 0.46 square degrees. The source extraction for the ADF-S is described in Section 3.6.1 and the galaxy number counts are described in

Table 3.12: Observation log for ADF-S.

Pointing Number	Date	Filter	AOT
320001-001	03/02/2007	N3 N4 S7 S11 L15 L24	IRC02
320002-001	04/02/2007	N3 N4 S7 S11 L15 L24	IRC02
320003-001	04/02/2007	N3 N4 S7 S11 L15 L24	IRC02
320004-001	05/02/2007	N3 N4 S7 S11 L15 L24	IRC02
320005-001	03/02/2007	N3 N4 S7 S11 L15 L24	IRC02
320006-001	04/02/2007	N3 N4 S7 S11 L15 L24	IRC02
320007-001	05/02/2007	N3 N4 S7 S11 L15 L24	IRC02
320008-001	06/02/2007	N3 N4 S7 S11 L15 L24	IRC02
320009-001	03/02/2007	N3 N4 S7 S11 L15 L24	IRC02
320010-001	05/02/2007	N3 N4 S7 S11 L15 L24	IRC02
320011-001	05/02/2007	N3 N4 S7 S11 L15 L24	IRC02
320012-001	06/02/2007	N3 N4 S7 S11 L15 L24	IRC02
320013-001	09/02/2007	N3 N4 S7 S11 L15 L24	IRC02
320014-001	08/02/2007	N3 N4 S7 S11 L15 L24	IRC02
320015-001	07/02/2007	N3 N4 S7 S11 L15 L24	IRC02
320016-001	07/02/2007	N3 N4 S7 S11 L15 L24	IRC02
320017-001	09/02/2007	N3 N4 S7 S11 L15 L24	IRC02
320018-001	08/02/2007	N3 N4 S7 S11 L15 L24	IRC02
320019-001	07/02/2007	N3 N4 S7 S11 L15 L24	IRC02
320021-001	09/02/2007	N3 N4 S7 S11 L15 L24	IRC02
320042-001	07/02/2007	N3 N4 S7 S11 L15 L24	IRC02
320046-001	08/02/2007	N3 N4 S7 S11 L15 L24	IRC02
320050-001	05/02/2007	N3 N4 S7 S11 L15 L24	IRC02

Section 3.7.6.

3.6 Galaxy Catalogues

3.6.1 Source Extraction and Photometry

3.6.1.1 SExtractor

SExtractor is a source extraction software created by Bertin & Arnouts (1996). SExtractor is able to separate blended objects, perform photometry in the extracted sources and classify the sources. The software has six steps: estimating the sky background, thresholding (locating the sources), deblending, filtering of the detections, photometry and star/galaxy separation.

Table 3.13: Pointings used to create flat fields for ADF-S images 01/02/2007 to 09/02/2007.

Pointing Number	Date	Programme	N3	N4	S7	S11	L15	L24
1100013-001	08/02/2007	MP-AGNUL	01	-	-	-	-	-
1300006-001	09/02/2007	MP-CLEVL	04	04	12	12	12	12
1300008-001	09/02/2007	MP-CLEVL	04	04	12	12	12	12
1300137-001	07/02/2007	MP-CLEVL	-	05	-	30	-	30
1300137-002	07/02/2007	MP-CLEVL	-	05	-	-	-	30
1300137-003	08/02/2007	MP-CLEVL	-	05	-	30	-	30
1300158-001	08/02/2007	MP-CLEVL	-	05	-	-	-	30
1400421-001	08/02/2007	MP-ISMGN	04	04	12	12	-	-
1500705-001	04/02/2007	MP-SOSOS	01	-	-	-	-	-
1700039-001	04/02/2007	MP-AGBGA	-	-	-	-	12	12
1700040-001	03/02/2007	MP-AGBGA	-	-	-	-	12	12
1800014-001	05/02/2007	MP-VEGAD	-	-	-	-	12	12
1800015-001	05/02/2007	MP-VEGAD	-	-	-	-	12	12
1800065-001	07/02/2007	MP-VEGAD	04	04	12	-	-	-
1800172-001	03/02/2007	MP-VEGAD	04	04	12	-	-	-
1800183-001	03/02/2007	MP-VEGAD	-	-	-	-	12	12
2110508-001	04/02/2007	LS-LSNEP	03	02	09	06	09	06
2110529-001	06/02/2007	LS-LSNEP	03	03	09	09	09	09
2110562-001	09/02/2007	LS-LSNEP	03	03	09	09	09	09
2110607-001	08/02/2007	LS-LSNEP	03	02	09	06	09	06
2110664-001	08/02/2007	LS-LSNEP	03	02	09	06	09	09
2110732-001	01/02/2007	LS-LSNEP	03	02	09	06	09	06
2110813-001	02/02/2007	LS-LSNEP	03	02	09	06	09	06
2110905-001	02/02/2007	LS-LSNEP	03	02	09	06	09	06
3230001-001	02/02/2007	OT-ISAS-Z1LBG	04	04	-	-	12	12
3230001-002	08/02/2007	OT-ISAS-Z1LBG	03	04	-	-	09	12
3230001-003	08/02/2007	OT-ISAS-Z1LBG	04	04	-	-	12	12
3230002-001	05/02/2007	OT-ISAS-Z1LBG	04	04	12	12	12	12
3230002-002	05/02/2007	OT-ISAS-Z1LBG	04	04	12	12	12	12
3230002-003	05/02/2007	OT-ISAS-Z1LBG	04	04	12	12	12	12
4040001-004	01/02/2007	OT-ESA-IRLBG	05	-	30	30	-	
4040001-005	01/02/2007	OT-ESA-IRLBG	05	-	-	-	30	-
4230006-001	03/02/2007	OT-ESA-EROMU	03	04	09	-	09	12
5121024-001	05/02/2007	DT-DTIRC	03	02	-	-	09	06
5122024-001	06/02/2007	DT-DTIRC	-	-	-	-	09	06
Total number of frames			85	88	207	180	282	348

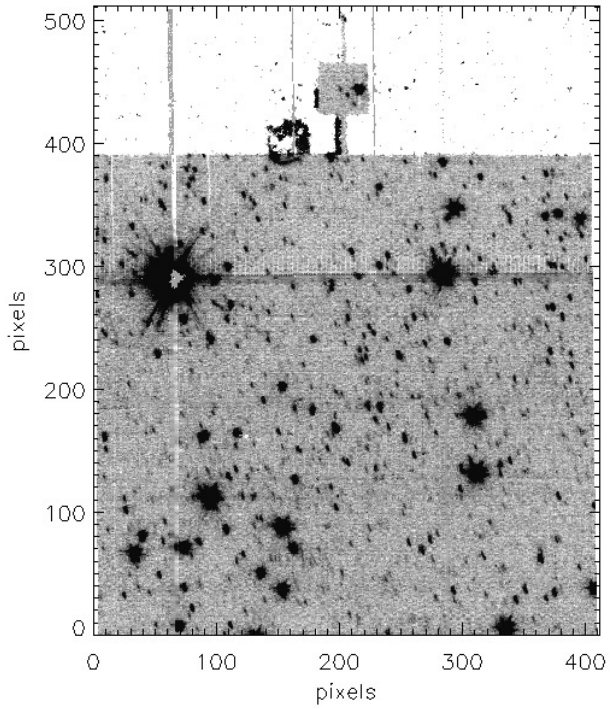

Figure 3.5: Image showing the ghost near the top left of the image.

Table 3.14: ADF-S discarded frames.

Filter	Pointing Number	Frame Number	Reason
N4	3200002_001	F006033902_N002	Many hot pixels
S7	3200004_001	F006038908_S004	Flux error
L15	3200003_001	F006036697_L003	Cosmic ray
L15	3200003_001	F006036697_L004	Cosmic ray
L15	3200004_001	F006038908_L004	Flux error
L24	3200003_001	F006036693_L004	Many hot pixels
L24	3200003_001	F006036699_L002	Cosmic ray
L24	3200003_001	F006036699_L003	Cosmic ray
L24	3200003_001	F006036699_L004	Cosmic ray
L24	3200006_001	F006034162_L002	Artificial stripe pattern
L24	3200006_001	F006034162_L003	Artificial stripe pattern
L24	3200006_001	F006034162_L004	Artificial stripe pattern

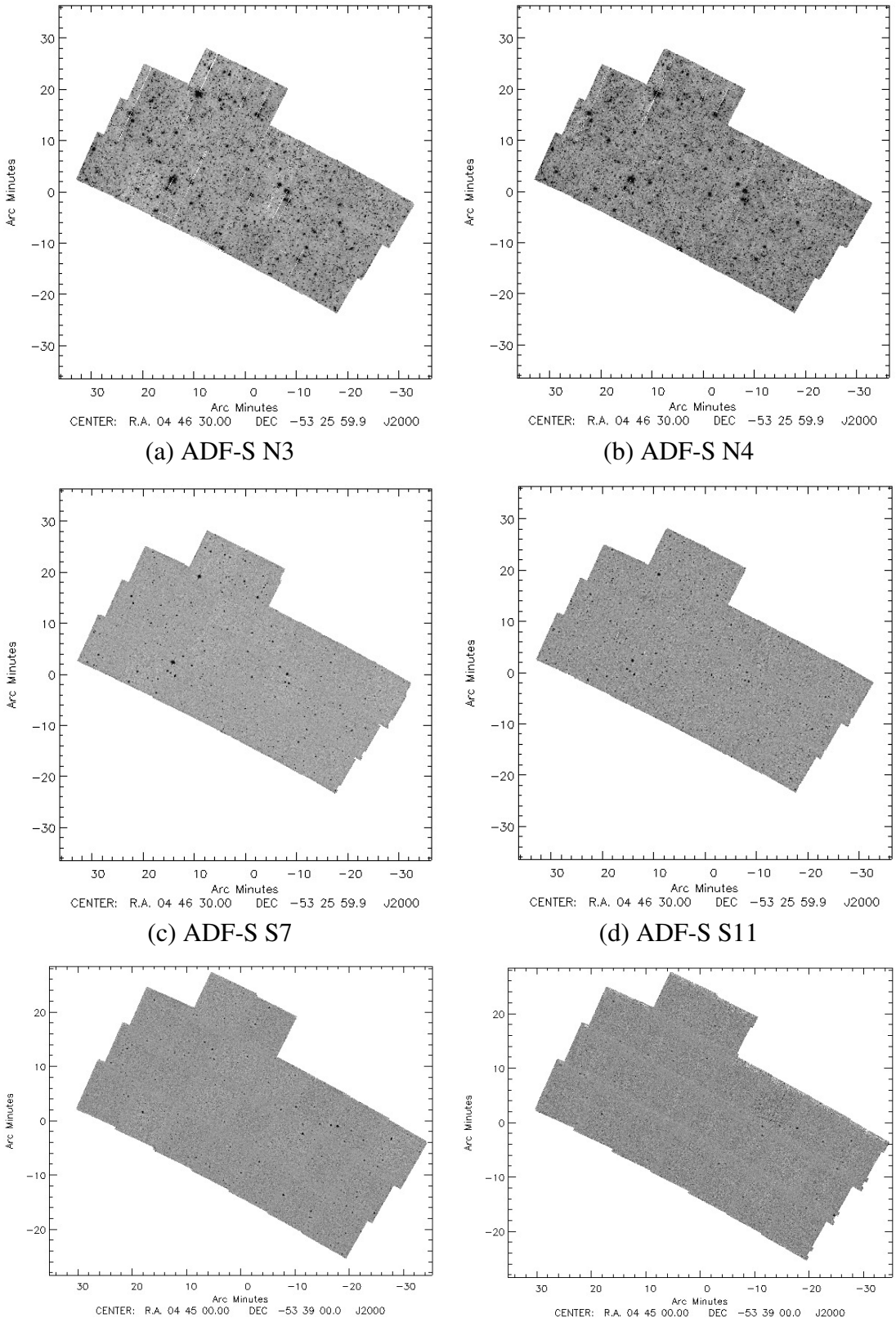

(a) ADF-S N3 (b) ADF-S N4

(c) ADF-S S7 (d) ADF-S S11

(e) ADF-S L15 (f) ADF-S L24

Figure 3.6: The six ADF-S mosaicked images.

The first step SExtractor performs on an image passed through it, is to estimate the sky background. The sky background is a background map of what the image would look like if there were no sources. This step is separating the flux of each individual pixel into background flux and flux from the source. Firstly, sigma clipping is used to test for crowded/uncrowded areas. For uncrowded fields the interim sky background is given by the mean of the clipped histogram, and for crowded fields the interim map is given the mode of the histogram. Then a median filter is applied to the interim map; this removes over dense regions caused by bright stars.

The second step is detecting the sources by using a thresholding method. This flags pixels above a certain threshold as possible sources and extracts a specific number of pixels from around the source. Bertin & Arnouts (1996) have chosen a thresholding method because it works well at finding low surface brightness sources.

Step three performs the deblending of merged objects. This step separates two (or more) sources which have merged together to appear as one source. Bertin & Arnouts (1996) use the theory that each source will have its own flux peak within the area of the total flux. A model of the light distribution is created for each set of pixels extracted in the detection step. The model is created by applying 3D thresholds to each set of pixels, from the peak flux to the lowest flux. An algorithm is then used to test for blended sources. Figure 3.7 shows a 2D representation of how the algorithm works. The algorithm begins at the peak flux and descends down the branch. At a flux trough the algorithm will flag the flux on the other side of the trough as a source, if the integrated pixel intensity of the possible second source is greater than a specific percentage of the total luminosity of the extracted pixels. The algorithm will then continue down to smaller fluxes, creating the 'tree like structure' in Figure 3.7

The fourth step filters the detections, checking the faint sources for false detections. This step subtracts the contribution to the mean surface brightness of the object in question. If, after subtraction, the flux of the object is below the flux threshold, then the object is classed as a false detection, and is not flagged as a source.

The fifth step calculates the photometry of the detected sources. SExtractor has three

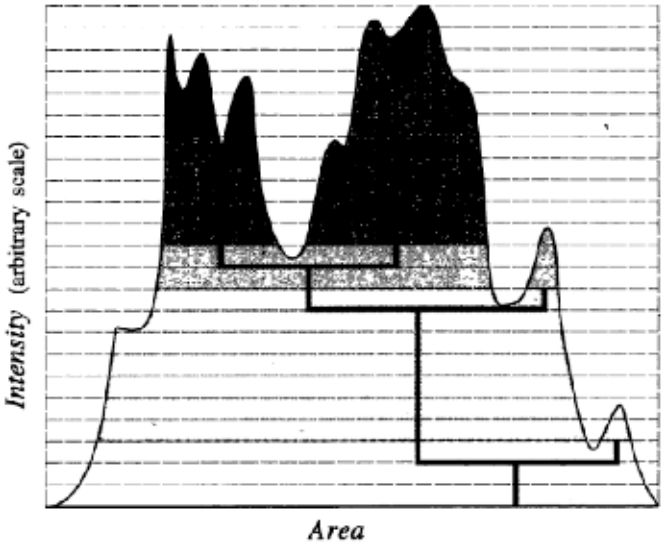

Figure 3.7: A 2D representation of how deblending is performed in SExtractor. The outline is the flux profile. The thick lines, which represent a tree-like structure, show the path the algorithm takes. The shaded areas represent the luminosity above the horizontal branch (Bertin & Arnouts, 1996).

different methods for finding the photometry. The three methods are: corrected isophotal magnitudes, adaptive aperture magnitudes and an estimate of the 'total' magnitude of the source. For the work of this thesis the adaptive aperture magnitude setting was used, see Section 3.6.1.3 for a description of the procedure.

The sixth and final step in SExtractor performs a star-galaxy separation. This step classifies sources as well as separating galaxies and stars. SExtractor uses a neural network to distinguish between galaxies and stars. It had been shown that SExtractor does not correctly class faint stars, but classifies them as galaxies; as SExtractor is unable to distinguish between a point source of a faint star and a point source of a galaxy. The galaxies in ELAIS-N1 and ADF-S are very rarely extended sources, they are nearly all point sources, and hence morphologically look like stars. For this reason, for the work of this thesis, the inbuilt star/galaxy separation in SExtractor was not used, and stellar subtraction was performed independently.

3.6.1.2 How Source Extraction Was Performed

To create the source catalogue for the IRAC Dark Field, ELAIS-N1 and ADF-S mosaicked images, SExtractor was used (Bertin & Arnouts, 1996). Section 3.6.1.1 gives a summary of how SExtractor performs source extraction. The SExtractor settings used for the source extraction are shown in Table 3.15. These settings are based on those used in Murata et al. (2013) for the North Ecliptic Pole (NEP) survey. The main differences from the NEP settings and the ones used in the work of this thesis, are that for the NIR and MIR-L detector images the minimum area = 5 and the threshold = 3, and for the MIR-S detector the minimum area = 5 and the threshold = 3.5. The settings were optimised to have the least number of false source detections (see Section 3.7.3) and the greatest number of true source detections.

In the ADF-S NIR and MIR-S mosaicked images, the brightest stars had diffraction spikes, and SExtractor extracted these spikes as sources. Due to this the brightest stars were masked.

3.6.1.3 Photometry

As stated in Section 3.6.1.1, this thesis uses the adaptive aperture magnitude method (as described below) in SExtractor to calculate the photometry of the detected sources. Bertin & Arnouts (1996) chose to use an adaptive aperture to correct for the fact that normal aperture photometry does not work so well in crowded fields and because using an adaptive aperture allows the source extraction to run more quickly.

The adaptive aperture photometry method was chosen because it works better for calculating the photometry of non-stellar sources than the isophotal method.

Adaptive aperture photometry uses an algorithm to calculate second order moment (with mean standard deviation σ_{iso}) of the profile of the extracted source. $6\sigma_{iso}$ are used to calculate the elliptical aperture, where the ellipticity of the aperture is given by ε, and the position angle is given by θ. $6\sigma_{iso}$ is approximately equal to 2 isophotal radii. The first moment for this aperture is then calculated using Equation 3.13. The

Table 3.15: SExtractor parameters.

Parameter	value
DETECT_TYPE	CCD
DETECT_MINAREA	5
DETECT_THRESH	3
ANALYSIS_THRESH	1.5
FILTER	Y
FILTER_NAME	gauss_2.5_5x5.conv
DEBLEND_NTHRESH	32
DEBLEND_MINCONT	0
CLEAN	N
CLEAN_PARA	1.0
MASK_TYPE	CORRECT
PHOT_APERTURES	8
PHOT_AUTOPARAMS	2.5, 3.5
SATUR_LEVEL	50000.0
MAG_ZEROPOINT	0.0
MAG_GAMMA	4.0
GAIN	1.0
PIXEL_SCALE	0
SEEING_FWHM	1.2
BACK_SIZE	64
BACK_FILTERSIZE	3
BACKPHOTO_TYPE	GLOBAL
BACKPHOTO_THICK	24
WEIGHT_GAIN	Y
WEIGHT_IMAGE	YES
WEIGHT_TYPE	MAP_RMS

Table 3.16: Table showing the flux conversion and aperture corrections for the filters used in the IRAC Dark Field, ELAIS-N1 and ADF-S, for ADU to micro-Janskey.

Filter	Flux Conversion	Aperture Correction
N3	0.4394	0.873
N4 IRC03	0.2584	0.871
N4 IRC05	0.1753	0.871
S7	1.022	0.918
S11	0.7732	0.902
L15	1.691	0.852
L18W	1.146	0.793
L24	0.04892	0.685

parameters $\varepsilon k r_1$ and $k r_1/\varepsilon$ give the semimajor and minor axes of the elliptical area that the flux of the source is contained within. ε is the ellipticity of the aperture and r_1 is the first moment as calculated by Equation 3.13. Bertin & Arnouts (1996) recommend a value of $k = 2$, as this is when systematic and random errors are at a minimum.

$$r_1 = \frac{\sum rI(r)}{\sum I(r)} \tag{3.13}$$

The flux of the extracted sources were in analogue to digital units (ADU). To calculate the galaxy flux from ADU to Janskys, the flux conversion from Tanabé et al. (2008) was used. The Jansky (Jy) is a non-standard SI unit, used to measure flux. $1\,\mathrm{Jy} = 10^{-26}\mathrm{Wm}^{-2}\mathrm{Hz}^{-1}$. An aperture correction is required to correct for galaxy flux not included within the aperture radius. After this, the aperture correction from Arimatsu et al. (2011) was applied. Table 3.16 shows the flux conversion and aperture correction for each of the filters in the IRAC Dark Field, ELAIS-N1 and ADF-S.

3.6.2 Positional Uncertainty

The locations of the galaxies in the IRAC Dark Field, ELAIS-N1 and ADF-S source catalogues have a positional error. The likely reasons for this uncertainty are small inaccuracies in the distortion correction, in the location assigned to the source during source extraction, a small error in astrometry correction, which in turn could be due to

a positional error of the WISE/2MASS catalogue used to align the individual frames. The source position uncertainty was calculated separately for each field and filter discussed in this thesis. In calculating the positional uncertainty it was assumed that all galaxies in the same image have the same uncertainty. For each mosaicked image discussed in this thesis, the AKARI extracted source positions were compared with the location of the WISE galaxy positions. For all AKARI point sources (i.e. non-extended sources) and with no other nearby AKARI sources, the AKARI source location was extracted along with the location of the nearest WISE source. For all the pairs of locations in the image, the WISE position was subtracted from the AKARI position. The combined positional uncertainty of AKARI and WISE right ascension is given by the σ of the *x*-axis, and the total combined positional uncertainty in the declination is given by the σ of the *y*-axis. By subtracting the mean WISE positional uncertainty in quadrature from the total uncertainty, gives the AKARI positional uncertainty.

3.6.3 IRAC Dark Field and ELAIS-N1 Confusion Limit

The confusion limit of a survey is reached when the sources are too closely spaced to be able to be resolved. The confusion limit is often reached in deep surveys. Below the confusion limit, the fluctuations in the image are dominated by galaxies with flux too faint to be detected by the source detection. The confusion limit is reached when there are about $20-40$ beams per source. This is shown analytically below. The source count slope can be given by Equation 3.14, where $N(>S)$ are the number of sources within the interval $S \rightarrow S+dS$, k is a constant and α is the gradient of the number count slope.

$$N(>S) = kS^{-\alpha} \tag{3.14}$$

Differentiating Equation 3.14 with respect to S gives:

$$dN = \alpha k S^{-\alpha} S^{-1} dS \tag{3.15}$$

Using Equation 3.14 gives:

$$dN = \alpha(N(>S)/S)dS \tag{3.16}$$

Thus the number of sources per beam is given by Equation 3.17, where Ω is the beam.

$$\Omega dN = \alpha\Omega(N(>S)/S)dS \tag{3.17}$$

Assuming Poisson statistics, hence the variance equals the mean. Equation 3.17 gives the variance in the number of sources, but the variance in flux of the sources is required. This is given by the variance of the number of sources times S squared. Thus the variance in the flux of the sources is given by $\alpha\Omega S(N(>S)dS$. Using Equation 3.14 gives: $\alpha\Omega SkS^{-\alpha}dS$. Integrating this from $S = 0$ to $S = S_{lim}$, i.e. from the zero flux to the confusion limit, with respect to S gives Equation 3.18.

$$var(S) = \int_0^{lim} \alpha\Omega k S^{1-\alpha} dS \tag{3.18}$$

$$var(S) = \frac{\alpha}{2-\alpha}\Omega k S_{lim}^{2-\alpha} - 0 \tag{3.19}$$

Using Equation 3.14 once again, gives Equation 3.20

$$var(S) = \frac{\alpha}{2-\alpha}\Omega N(>S_{lim})S_{lim}^2 \tag{3.20}$$

Thus the standard deviation (σ) is given by Equation 3.21, where $\Omega N(>S_{lim})$ is the number of sources per beam.

$$\sigma = \Big(\frac{\alpha}{2-\alpha}\Omega N(>S_{lim})\Big)^{\frac{1}{2}} S_{lim} \tag{3.21}$$

Assuming that the fluctuations of the background objects are within 5σ of the confusion limit, hence $S_{lim} = 5\sigma$

$$\sigma = \left(\frac{\alpha}{2-\alpha}\Omega N(> S_{lim})\right)^{\frac{1}{2}} 5\sigma \tag{3.22}$$

Another way of looking at the confusion limit, is that it is the minimum number of beams per source, before the limit is reached. Leading on from 3.22, this is given by Equation 3.25

$$\left(\frac{\alpha}{2-\alpha}\Omega N(> S_{lim})\right)^{-\frac{1}{2}} = 5 \tag{3.23}$$

$$\left(\frac{\alpha}{2-\alpha}\Omega N(> S_{lim})\right)^{-1} = 25 \tag{3.24}$$

$$\left(\Omega N(> S_{lim})\right)^{-1} = \frac{25\alpha}{2-\alpha} \tag{3.25}$$

At the faint end number counts, the gradient of the counts is nearly flat, i.e. as it approaches the value of the CIB, thus in a Euclidian normalised plot $\alpha < 2.5$ (Condon (1974) and Serjeant (2010)).

The confusion limit can take a range of values of about 1 source per 15 to 50 beams (Hogg, 2001). For the work of this thesis a conservative limit has been chosen for the definition of a confusion limited image, and uses that of Berta et al. (2010), of 1 source per 40 beams; and the area of the FWHM has been used as the beam area. Table 3.17 gives the number of beams per source for the IRAC Dark Field and ELAIS-N1. As can be seen in Table 3.17, the IRAC Dark Field has reached the confusion limit in the N4 filter, and is fairly close in the other three filters; while the ELAIS-N1 survey is confusion limited only in the N4 filter. Because the ADF-S is a shallow field, the number of beams per source will not be close to the confusion limit.

Table 3.17: Table showing the number of beams per source in the four IRAC Dark Field and ELAIS-N1 filters.

Filter	IRAC Dark Field	ELAIS-N1
N4	27	40
S11	67	130
L15	75	103
L18W	81	83

3.7 Number Counts

3.7.1 Raw Number Counts

Section 3.2.1 gives the theory behind differential galaxy number counts. The raw differential galaxy number counts for each mosaicked image were calculated using the extracted source catalogue produced by SExtracter (see Section 3.6.1.2). The first step was to use the extracted source catalogue to create a frequency histogram of galaxies according to their flux. The flux bins have a width, in log space, of $d\lg(S) = 0.1$. Figure 3.8 shows the raw frequency histogram for the IRAC Dark Field number counts, Figure 3.9 shows those for the ELAIS-N1 number counts, and Figure 3.10 shows those for the ADF-S number counts. Section 3.2.1 gives the derivation of Euclidean normalised number counts. Using Equation 3.12, the number count for each flux bin was calculated using Equation 3.26, where nc is the number count value, n is the number of galaxies in the flux bin, S is the centre flux of the bin in mJy, ΔS is the difference in flux across the bin (i.e. the maximum of the flux bin minus the minimum of the flux bin in mJy) and A is the area in steradians:

$$nc = \frac{n \times S^{2.5}}{\Delta S \times A} \tag{3.26}$$

Equation 3.26 is divided by the survey area, thus the number counts are per unit area, and can be compared with other surveys. The flux is measured in mJy, as the near and mid-infrared number counts range approximately from $\sim$0.01 mJy to $\sim$10 mJy thus mJy is an appropriate flux unit. The raw number counts calculated for the IRAC

Dark Field are shown as the open circles in Figure 3.15, those for ELAIS-N1 are shown in Figure 3.16 and those for ADF-S are shown in Figure 3.17.

All fields and filters had successful source extraction apart from the ADF-S L24 filter. As can be seen in Figure 3.10.f, SExtractor was only able to extract 10 sources from the ADF-S L24 filter. This is due to the fact that AKARI's near and mid-infrared observations of ADF-S are shallow, only one pointing deep, and the L24 filter is not as sensitive as the other 8 AKARI filters. It was decided that further research of the ADF-S L24 image would not be beneficial, as there already exists a large amount of deep Spitzer/MIPS 24 μm data. Some of the deep MIPS 24 μm number counts include that of the Guaranteed Time Observations (GTO) and Spitzer Wide-area InfraRed Extragalactic Survey (SWIRE) (Papovich et al. (2004) and Shupe et al. (2008)). From this point on the thesis, when the ADF-S data is analysed, only the 5 filters, N3, N4, S7, S11 and L15 are being discussed.

3.7.2 Stellar Subtraction

The sources extracted by SExtractor contain both stars and galaxies. To create galaxy catalogues and galaxy number counts, the sources which are stars need to be removed. There are several different methods to perform stellar subtraction.

Solarz et al. (2012) discuss one method of galaxy and star separation. This method, which has been tested on the AKARI NEP survey, uses multi-colour plots. The galaxies and stars are separated by plotting the fluxes of the detected sources on a multi-colour plot, e.g. $N2 - N3$ against $S7 - S11$. This is possible because the NEP survey has coverage in all of the nine IRC filters. The ELAIS-N1 deep field has observations in only four filters. Solarz et al. (2012) do not have a suitable multi-colour plot for the ELAIS-N1 N4 filter image. The N4 image is the most important image to remove stars, as it is the shortest wavelength image, it will have the greatest number of stellar sources. For this reason the galaxy and star separation method of Solarz et al. (2012) was not used.

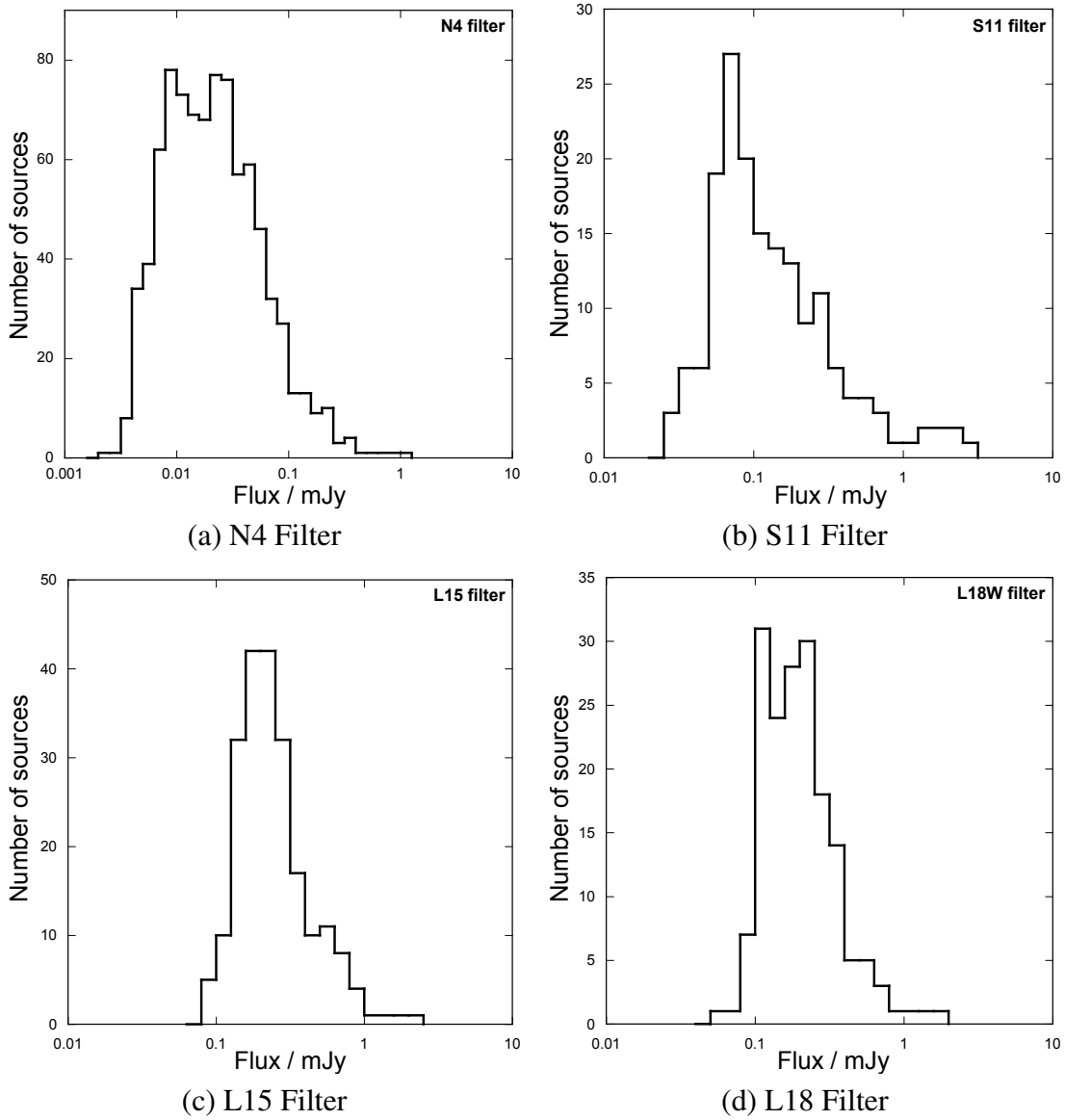

(a) N4 Filter (b) S11 Filter

(c) L15 Filter (d) L18 Filter

Figure 3.8: The IRAC Dark Field raw histograms.

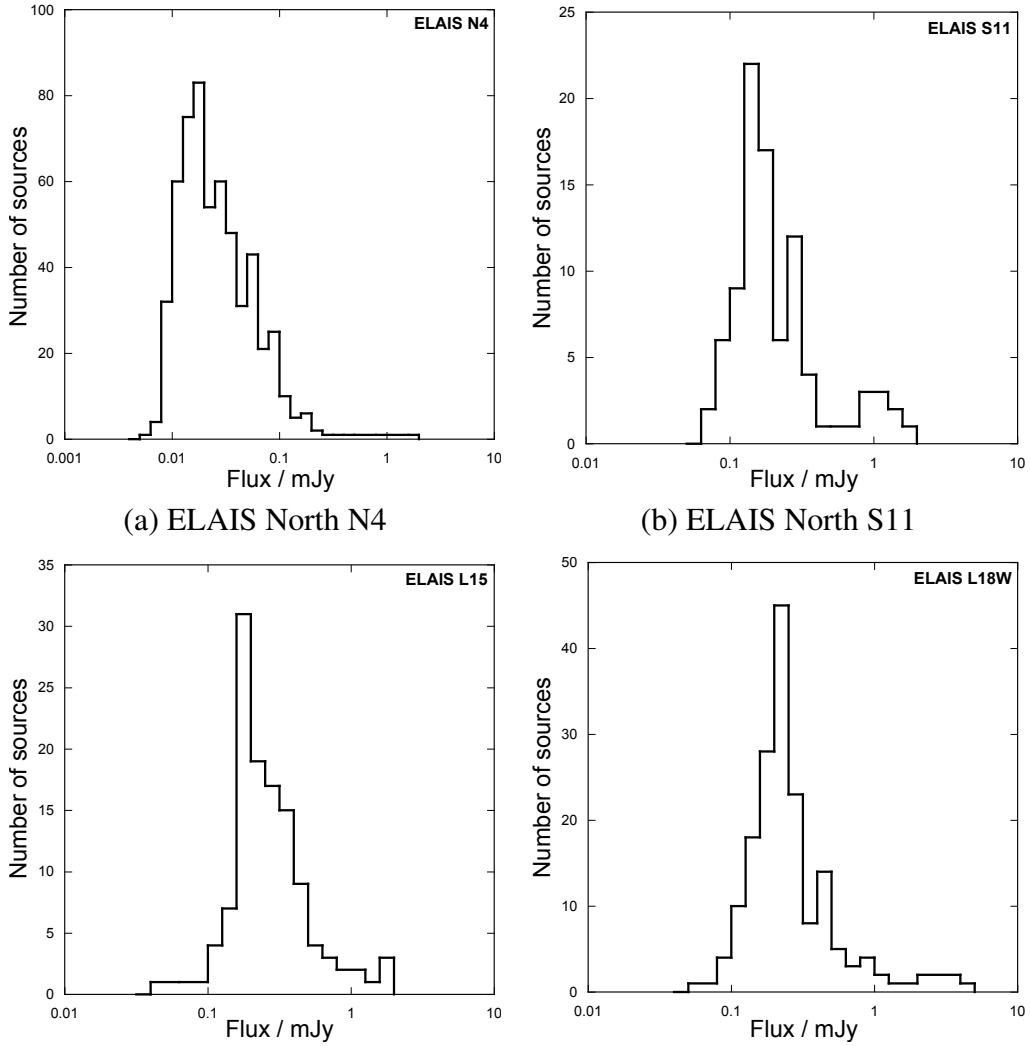

(a) ELAIS North N4

(b) ELAIS North S11

(c) ELAIS North L15

(d) ELAIS North L18W

Figure 3.9: The ELAIS-N1 raw histograms.

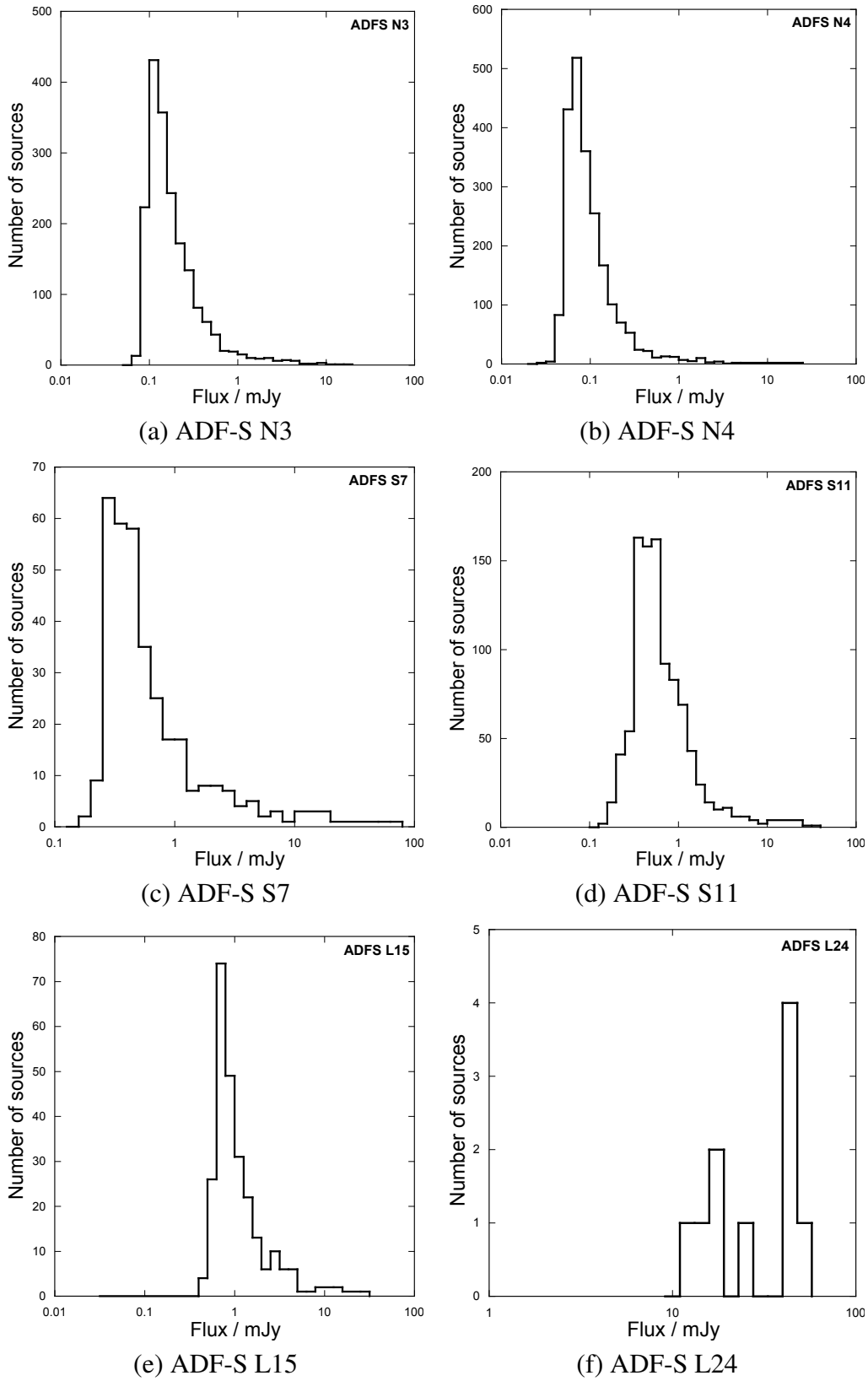

(a) ADF-S N3 (b) ADF-S N4

(c) ADF-S S7 (d) ADF-S S11

(e) ADF-S L15 (f) ADF-S L24

Figure 3.10: The ADF-S raw histograms.

A second method for stellar subtraction is to cross correlate the table of extracted sources created by SExtractor with an existing star catalogue.

The star positions were found in all the IRAC Dark Field and ELAIS-N1 images, and the ADF-S N3, N4, S7 and S11 images, by using the catalogue created by the Automatic Plate Measuring (APM) facility at Cambridge. The APM scans glass plates with images from the Palomar Observatory (for the Northern hemisphere) and from the UK Schmidt Telescope Unit (UKSTU) (for the Southern hemisphere). The facility used a laser to measure the transmission of emulsion in the glass plates. Once the data had been stored digitally, the facility performed galaxy and star separation. The separation was performed by looking at the shape of the object, and using the assumption that stars and galaxies have different intrinsic profiles (Maddox et al., 1990). The ELAIS-N1 images use the star catalogue from the first Palomar Observatory sky survey (Minkowski & Abell, 1963), observed using the 48 inch Samuel Oschin Telescope. The observations were performed between November 1949 and December 1958 using an E (red) plate and an O (blue) plate (Reid & Djorgovski, 1993).

The extracted source catalogue created in SExtractor, which contained both galaxy and star positions, was crossed matched with the APM star positions, with a search radius of 4 arcseconds. A single extracted source within this radius was removed from the galaxy source catalogue in question. On the rare occasion that there were two or more extracted sources within the radius, the extracted source closest to the APM location was removed. Table 3.18 shows the stellar number counts for the IRAC Dark Field, Table 3.19 shows those for ELAIS-N1 and Table 3.20 shows those for ADF-S. Just using the sources not identified as stars, galaxy catalogues were created for the IRAC Dark Field N4, S11, L15 and L18, ELAIS-N1 N4, S11, L15 and L18, and ADF-S N3, N4, S7 and S11.

Stellar subtraction was performed on the ADF-S L15 image using the method described above, but where an R-band star catalogue from MOSAIC and MOSAIC-II observations, from the CTIO 4-m Blanco telescope, Chile (Muller et al., 1998), was used instead of the APM. The R-band catalogue was created using the Mosaic Cam-

era Pipeline and source extraction was performed using SExtractor (Barrufet et al., in prep). This method of stellar subtraction worked well for the L15 mosaicked image. The CTIO data were not used for ADF-S N3, N4, S7 and S11 because the data did not cover all of the NIR and MIR-S mosaicked images. The MIR-L mosaicked image covers a slightly different area, due to the fact that the MIR-L observing area is offset from the NIR and MIR-S observing area by $\sim$20 arcmin. The area with no coverage from the CTIO was within the region covered by NIR and MIR-S, but not by MIR-L. It was attempted to use the CTIO R-band star catalogue for the regions in the ADF-S NIR and MIR-S mosaicked images, which had CTIO data, and then to calculate a stellar fraction for the smaller area with no CTIO data. The raw number counts in each of the regions of the mosaicked image without CTIO data were then scaled by the stellar fraction. Plotting the stellar subtracted number counts showed that there was an excess in the number counts between ~ 0.2 mJy to ~ 0.8 mJy. The CTIO star catalogue was created using SExtractor. As stated in Section 3.6.1.1, SExtractor does not perform a good galaxy and star separation at fainter fluxes. We believe this excess is mainly due to the faint stars not having been correctly identified as stars, and hence not being removed from the galaxy catalogue. As discussed above the APM star catalogue was used for the ADF-S N3, N4, S7 and S11 mosaicked images, as it is believed the catalogue includes more fainter stars than the catalogue created by SExtractor. A comparison between using the R-band star catalogue and the stellar catalogue created by the APM is shown in Figure 3.11. Table 3.20 shows the stellar number counts for the ADF-S mosaicked images.

3.7.3 Reliability

Section 3.2.2 gives a summary of why galaxy number counts may require a reliability correction, and some of the different ways the reliability of the counts can be tested. The Section also states which method was used to test reliability. Reliability tests were performed after stellar subtraction, but before completeness correction. Table 3.21

Table 3.18: IRAC Dark Field stellar fraction tables.

Flux / mJy	N4 %	S11 %	L15 %	L18W %
0.008	0.0	-	-	-
0.010	1.35	-	-	-
0.013	0.0	-	-	-
0.016	2.86	-	-	-
0.020	1.28	-	-	-
0.025	1.30	0.00	-	-
0.032	1.72	0.00	-	-
0.040	3.28	3.33	-	-
0.050	4.17	17.39	-	-
0.063	3.03	12.90	-	0.00
0.079	15.63	9.09	0.0	0.00
0.100	7.14	25.00	0.0	0.00
0.126	27.78	0.0	3.03	0.00
0.158	30.77	18.75	0.0	4.00
0.200	16.67	25.00	6.67	0.00
0.251	50.00	8.33	3.03	3.13
0.316	55.56	14.29	5.56	0.00
0.398	80.00	20.00	0.00	0.00
0.501	66.67	20.00	0.00	16.67
0.631	66.67	25.00	0.00	0.00
0.794	100.00	0.00	0.0	0.00
1.000	50.00	0.00	0.00	0.00
1.259	-	0.00	-	-
1.585	100.00	-	0.00	0.00

Table 3.19: The ELAIS-N1 stellar fraction table.

Flux / mJy	N4 %	S11 %	L15 %	L18W %
0.008	0.0	-	-	-
0.010	0.0	-	-	-
0.013	0.0	-	-	-
0.016	1.32	-	-	-
0.020	0.0	-	-	-
0.025	2.60	-	-	-
0.032	3.45	-	-	-
0.040	3.33	-	0.0	-
0.050	8.00	-	-	0.0
0.063	7.69	00	0.0	-
0.079	6.25	11.37	-	0.0
0.100	14.29	24.36	0.0	0.0
0.126	13.64	4.89	0.0	0.0
0.158	11.11	7.99	0.0	0.0
0.200	46.15	0.0	4.93	0.0
0.251	42.86	6.64	0.0	12.50
0.316	71.43	19.57	0.0	0.0
0.398	75.00	0.0	0.0	0.0
0.501	80.00	0.0	33.33	-
0.631	83.33	31.72	0.0	-
0.794	0.0	0.0	0.0	0.0
1.000	0.0	-	-	0.0
1.259	-	0.0	0.0	0.0
1.585	-	0.0	0.0	-
1.995	0.0	-	0.0	-
3.981	100.00	-	-	0.0

Table 3.20: The ADF-S stellar fraction table.

Flux / mJy	N3 %	N4 %	S7 %	S11 %	L15 %
0.025	-	0.0	-	-	-
0.032	-	0.0	-	-	-
0.040	-	0.0	-	-	-
0.050	-	0.0	-	-	-
0.063	0.0	0.0	-	-	-
0.080	0.0	0.25	-	-	-
0.100	0.0	3.10	-	-	-
0.126	0.0	5.30	-	0.0	-
0.158	0.33	7.81	0.0	0.0	-
0.200	1.30	22.82	29.91	8.44	-
0.251	4.02	18.76	21.19	8.44	0.0
0.316	13.07	38.99	18.31	10.39	0.0
0.398	19.50	41.42	31.22	11.33	0.0
0.501	18.80	71.20	41.74	11.00	3.85
0.631	37.21	68.42	53.63	11.52	12.16
0.794	49.37	84.21	65.28	14.44	18.37
1.000	59.48	84.21	61.74	15.31	12.90
1.259	76.91	90.95	81.35	22.03	18.18
1.585	80.07	90.23	74.51	34.23	53.85
1.995	86.16	63.16	48.42	50.66	50.00
2.512	88.77	92.63	86.44	37.25	50.00
3.162	96.09	89.16	90.79	29.80	50.00
3.981	81.46	-	81.72	75.99	33.33
5.012	75.20	84.21	98.87	70.37	100.00
6.310	100.00	78.95	80.89	46.06	100.00
7.943	95.84	100.00	84.74	50.66	100.00
10.000	83.55	100.00	95.34	54.28	100.00
12.589	100.00	63.16	76.27	100.00	100.00
15.849	96.41	63.16	42.37	100.00	100.00
19.953	83.55	-	95.33	0.0	-
25.119	62.66	100.00	84.74	100.00	100.00
31.623	62.66	-	100.00	100.00	-
39.811	100.00	-	-	-	-
63.096	-	-	100.00	-	-
158.489	-	-	100.00	-	-

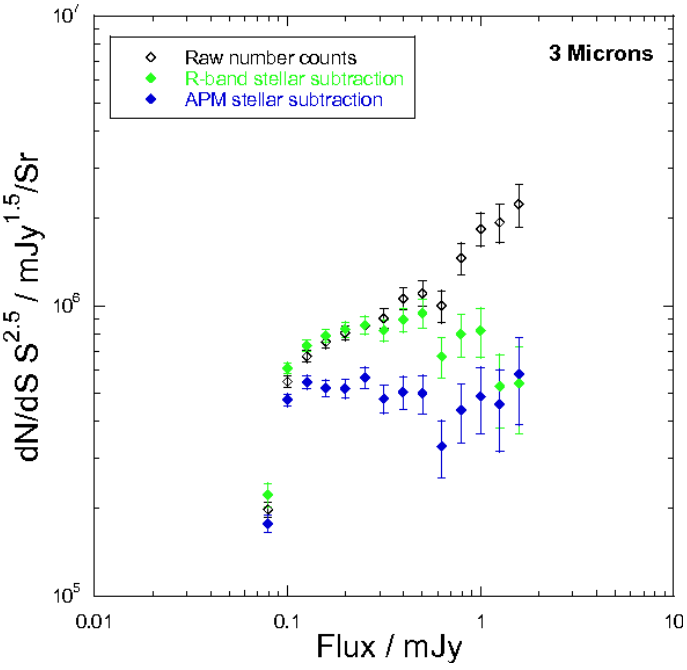

Figure 3.11: Figure showing the raw 3 μm number counts (empty diamonds), completeness corrected number counts using the R-band catalogue for stellar subtraction (green diamonds) and using the stellar catalogue created by the APM (blue diamonds).

gives the percentage of unreliable sources for the IRAC Dark Field, ELAIS-N1 and ADF-S.

For the mosaicked images which had extracted negative sources greater than 1% of the total number of sources, a reliability correction was performed. The images which required a reliability correction were: S11 and L15 IRAC Dark Field, S11, L15 and L18 ELAIS-N1 and S11 ADF-S. The large number of spurious sources in all the of the ELAIS-N1 MIR images may be due to Earthshine light not having been fully removed. Masking areas badly affected by Earthshine light (i.e. at the edges of the image) reduced the number of extracted negative sources. The negative image was run through the same source extraction software as the mosaicked image. Thus it was possible to subtract the frequency distribution of the negative sources from the frequency distribution of the extracted galaxies. This therefore generated a reliability corrected frequency distribution which was used to make reliability corrected galaxy number counts.

Table 3.21: Table showing the percentage of negative sources.

Field	Filter	Negative sources / %
IRAC Dark Field	N4	0.21
IRAC Dark Field	S11	5.05
IRAC Dark Field	L15	2.67
IRAC Dark Field	L18W	0
ELAIS-N1	N4	0
ELAIS-N1	S11	9.48
ELAIS-N1	L15	2.42
ELAIS-N1	L18W	6.15
ADF-S	N3	0.03
ADF-S	N4	0.06
ADF-S	S7	0
ADF-S	S11	3.57
ADF-S	L15	0
ADF-S	L24	0

3.7.4 Completeness

Section 3.2.3 summarises why galaxy number counts need a completeness correction, the different ways completeness can be corrected for and the method chosen for completeness correction.

The test for completeness correction was carried out after reliability had been corrected. Completeness was tested by creating 1000 random locations on the image which was being tested for completeness. 1000 fake sources per flux bin were then injected one at a time into the mosaicked image. After one fake source was injected, the image was run through SExtractor, with the same settings as for the original source extraction. The extracted catalogue was then passed back to the completeness program. The program then performed a cross-matching with a four arcsecond radius on the location of the injected source. The program logged the number of correctly extracted fake sources for each flux bin. The completeness code checked for multiple sources extracted in the source radius. By running the completeness code over the ten images, the code only ever extracted zero or one source in the search radius. Once the completeness code had finished running, the code returned, for each flux bin, the com-

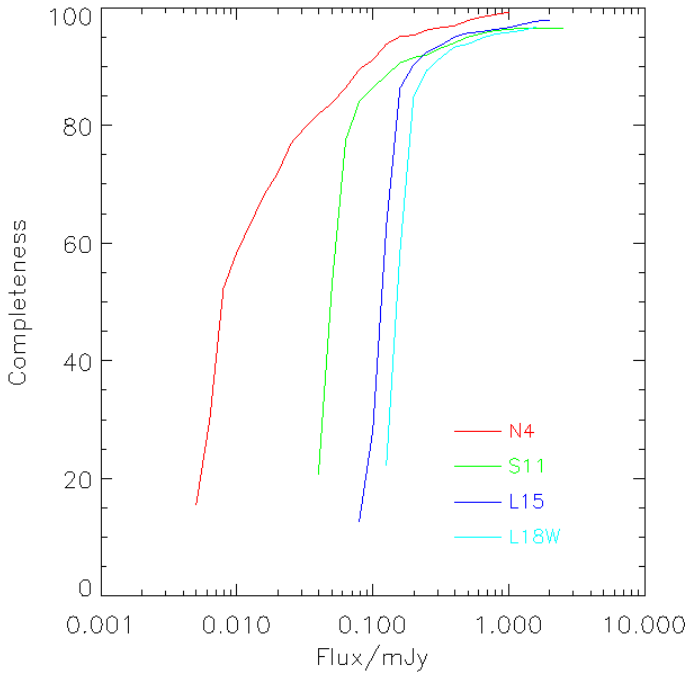

Figure 3.12: The completeness curves for IRAC Dark Field. The red line is N4, the green line is S11, the blue line is L15 and the cyan line is L18W.

pleteness number as a percentage. The bins in the frequency distribution of extracted sources were then scaled up to give the total number of galaxies in the image, using the percentages found in the completeness testing. Figures 3.12, 3.13 and 3.14 show the completeness curves for the IRAC Dark Field, ELAIS-N1 and ADF-S number counts respectively.

3.7.5 Galaxy Number Count Errors

After performing stellar subtraction and correcting for reliability and completeness, there still remains a Poisson uncertainty in the number count measurement. Poisson statistics assume that the mean of the data equals the variance. Thus the standard deviation (sd) equals the square root of the mean. Using the number count value as an unbiased estimator of the mean of the data, the uncertainties in the number counts are simply given by Equation 3.27, where the variables are defined in Section 3.7.1.

$$\text{error} = \frac{\sqrt{n} \times S^{2.5}}{\Delta S \times A} \tag{3.27}$$

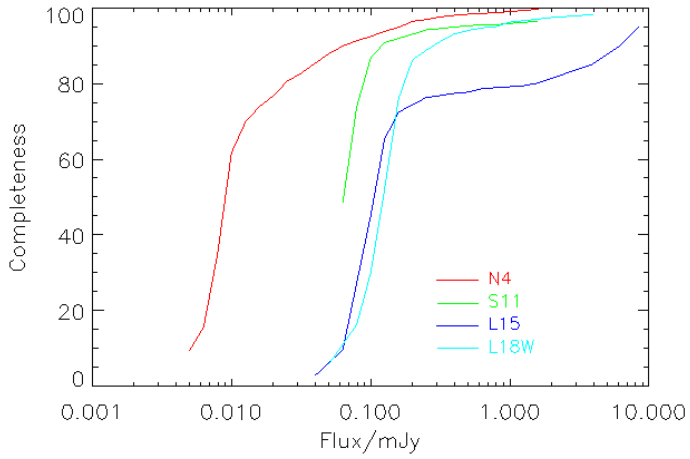

Figure 3.13: The completeness correction curves for ELAIS-N1. The red line is N4, the green line is S11, the blue line is L15 and the cyan line is L18W.

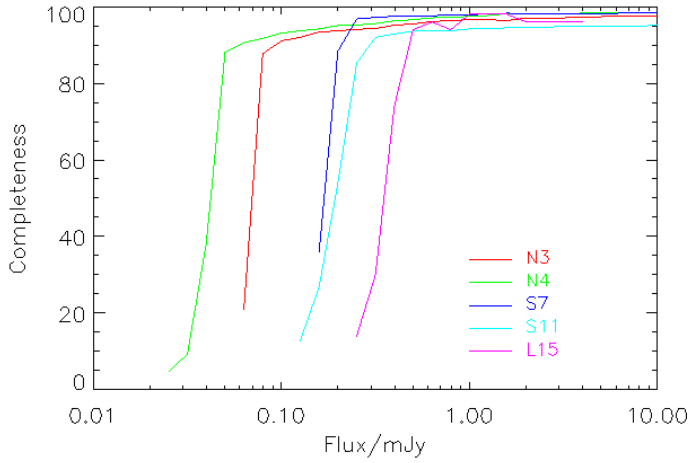

Figure 3.14: The completeness correction curves for ADF-S. The red line is N3, the green line is N4, the blue line is S7, the cyan line is S11 and the magenta line is L15.

The number count work in this chapter also includes a term in the uncertainty due to the completeness correction. The uncertainties due to the number count measurement and due to the completeness correction are combined into an absolute uncertainty by the use of formal propagation of error.

The number count value can be expressed as the function $N_{true} = F(N_{obs}, f_{rel}, f_{com})$, where N_{true} is the number count value, N_{obs} is the number of galaxies in the flux bin in question, f_{rel} is the reliability fraction, and f_{com} is the completeness fraction. Using the propagation of error, the uncertainty in $F(N_{obs}, f_{rel}, f_{com})$ is given by the square root of Equation 3.28, which is the variance of N_{true}:

$$\sigma^2(N_{true}) = \sigma^2(N_{obs})\left(\frac{\partial F}{\partial N_{obs}}\right)^2 + \sigma^2(f_{rel})\left(\frac{\partial F}{\partial f_{rel}}\right)^2 + \sigma^2(f_{com})\left(\frac{\partial F}{\partial f_{com}}\right)^2 \quad (3.28)$$

N_{true} is also defined as Equation 3.29.

$$N_{true} = \frac{N_{obs} \times f_{rel}}{f_{com}} \quad (3.29)$$

Thus Equation 3.28 can be re-written as Equation 3.30

$$\sigma^2(N_{true}) = \sigma^2(N_{obs})\left(\frac{f_{rel}}{f_{com}}\right)^2 + \sigma^2(f_{rel})\left(\frac{N_{obs}}{f_{com}}\right)^2 + \sigma^2(f_{com})\left(\frac{N_{obs} f_{rel}}{f_{com}^2}\right)^2 \quad (3.30)$$

Using the fact that $\sigma(f_{com}) = \Delta f_{com}$ and $\sigma(f_{rel}) = \Delta f_{rel}$, also using Poisson statistics $\sigma(N_{obs}) = \sqrt{N_{obs}}$, Equation 3.30 can be written as:

$$\sigma^2(N_{true}) = N_{obs}\left(\frac{f_{rel}}{f_{com}}\right)^2 + (\Delta f_{rel})^2\left(\frac{N_{obs}}{f_{com}}\right)^2 + \Delta f_{com}^2\left(\frac{N_{obs} f_{rel}}{f_{com}^2}\right)^2 \quad (3.31)$$

Equation 3.31 can be rearranged to give:

$$\sigma^2(N_{true}) = N_{obs}\left(\frac{f_{rel}}{f_{com}}\right)^2 + N_{obs}^2\left(\frac{\Delta f_{rel}}{f_{com}}^2 + \left(\Delta f_{com}\frac{f_{rel}}{f_{com}^2}\right)^2\right) \tag{3.32}$$

Converting Equation 3.32 from the variance of the number counts to the standard deviation of the number counts gives:

$$\sigma(N_{true}) = \sqrt{N_{obs}}\left[\left(\frac{f_{rel}}{f_{com}}\right)^2 + N_{obs}\left(\frac{\Delta f_{rel}}{f_{com}}^2 + \left(\Delta f_{com}\frac{f_{rel}}{f_{com}^2}\right)^2\right)\right]^{\frac{1}{2}} \tag{3.33}$$

For the number counts in this chapter Δf_{com} is given by $\frac{\sqrt{f_{com}(1-f_{com})}}{T}$, where T is the total number of injected sources for the flux bin in question. For the work in this chapter it has been assumed that the uncertainty in reliability (where applied) is negligible and hence is assumed not to contribute to the absolute uncertainty. Tables 3.27 to 3.35 show that the reliability percentage is small, and for some filters non-existent. $\Delta f_{rel} = 0$ and $f_{rel} = 1$, thus Equation 3.33 is then reduced to:

$$\sigma(N_{true}) = \sqrt{N_{obs}}\left[\left(\frac{1}{f_{com}}\right)^2 + N_{obs}\left(\left(\Delta f_{com}\frac{1}{f_{com}^2}\right)^2\right)\right]^{\frac{1}{2}} \tag{3.34}$$

Equation 3.34 gives the absolute uncertainty in the number counts, including the error due to the completeness correction.

Equation 3.34 breaks down for small number statistics, specifically where there is just one galaxy in the flux bin. This is because Equation 3.34 includes the term $\sqrt{N_{obs}}$, i.e. the square root of the number of galaxies. When calculating the uncertainty for just one galaxy in the flux bin, the value is replaced by $1^{+0.95}_{-0.827}$ (Gehrels, 1986).

Equation 3.34 gives the absolute uncertainty in the number counts. To calculate the absolute uncertainty for Euclidean normalised number counts per unit area, each number count uncertainty is required to be multiplied by $S^{2.5}/(\Delta S \times A)$, thus Equation 3.34 becomes:

Table 3.22: Table showing the minimum flux of the sources extracted and the sigma value per pixel, of source extraction for each filter in each field.

Field	Filter	Minimum flux/mJy	σ of detections per pixel
IRAC Dark Field	N4	0.008	3
IRAC Dark Field	S11	0.050	3.5
IRAC Dark Field	L15	0.126	3
IRAC Dark Field	L18W	0.158	3
ELAIS-N1	N4	0.010	3
ELAIS-N1	S11	0.079	3.5
ELAIS-N1	L15	0.158	3
ELAIS-N1	L18W	0.126	3
ADF-S	N3	0.079	3
ADF-S	N4	0.050	3
ADF-S	S7	0.200	3
ADF-S	S11	0.316	3.5
ADF-S	L15	0.631	3

$$\sigma(N_{true}) = \sqrt{N_{obs}}\left[\left(\frac{1}{f_{com}}\right)^2 + N_{obs}\left(\left(\Delta f_{com}\frac{1}{f_{com}^2}\right)^2\right)\right]^{\frac{1}{2}} \times \frac{S^{2.5}}{\Delta S \times A} \tag{3.35}$$

3.7.6 Final Galaxy Number Counts

The final number counts for The IRAC Dark Field are shown in figure 3.15, those for the ELAIS-N1 are shown in Figure 3.16 and the final ADF-S number counts are shown in Figure 3.17. Table 3.22 gives the minimum flux and the sigma value of the extracted sources for each filter in each field. The number counts tables for the IRAC Dark Field can be found in tables 3.23 to 3.26, the number count tables for ELAIS-N1 are given in Tables 3.27 to 3.30, and the ADF-S number counts tables can be found in Tables 3.31 to 3.35.

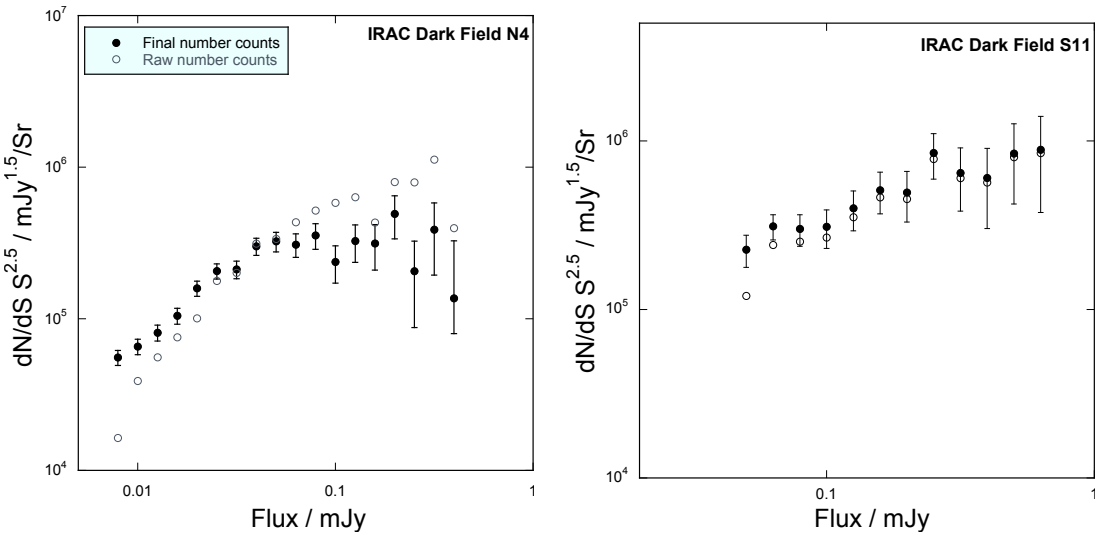

(a) N4 Filter (b) S11 Filter

(c) L15 Filter (d) L18 Filter

Figure 3.15: The figure presents the IRAC Dark Field number counts. The open circles give the raw number counts, and the filled circles give the completeness, reliability and stellar subtracted galaxy number counts.

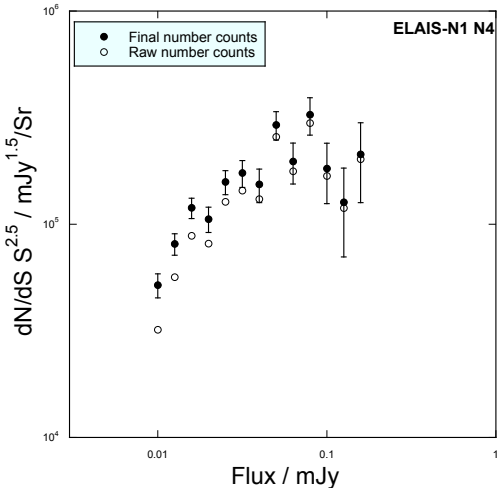

(a) ELAIS North N4 number counts

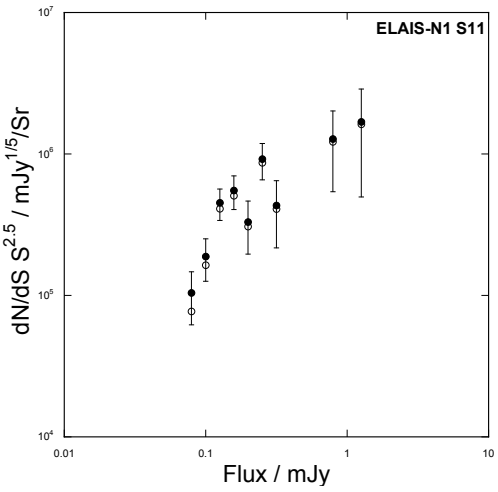

(b) ELAIS North S11 number counts

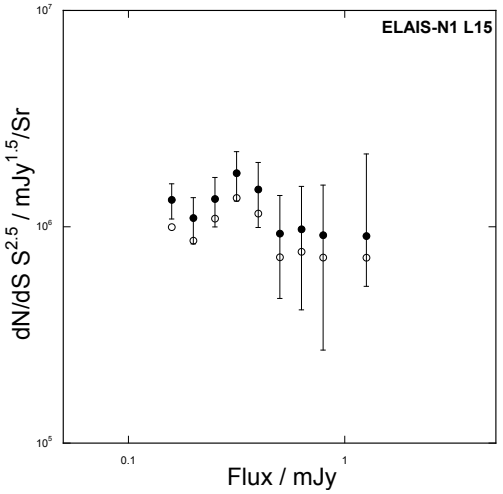

(c) ELAIS North L15 number counts

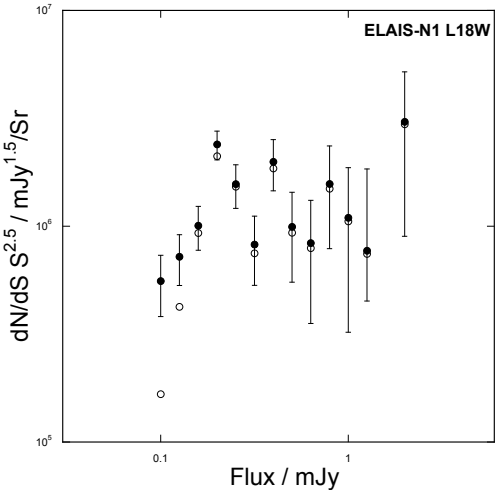

(d) ELAIS North L18 number counts

Figure 3.16: The ELAIS-N1 number counts. The open circles give the raw number counts, and the filled circles give the completeness, reliability and stellar subtracted galaxy number counts.

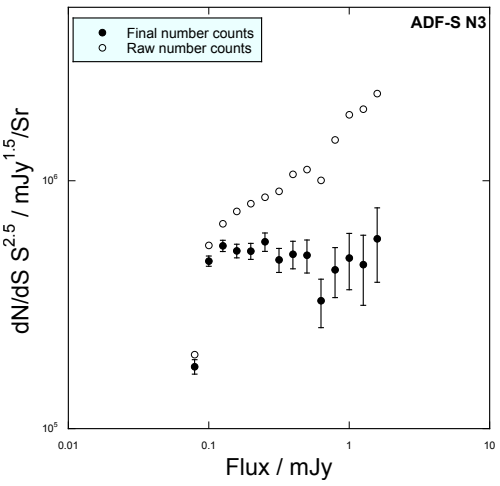

(a) ADF-S N3 number counts

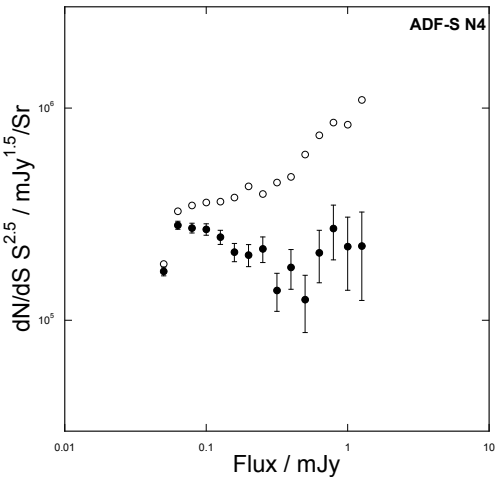

(b) ADF-S N4 number counts

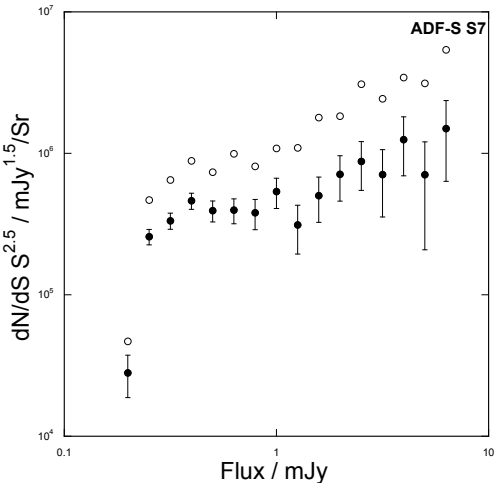

(c) ADF-S S7 number counts

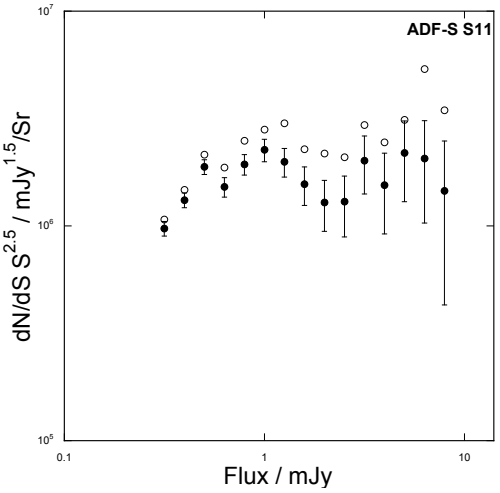

(d) ADF-S S11 number counts

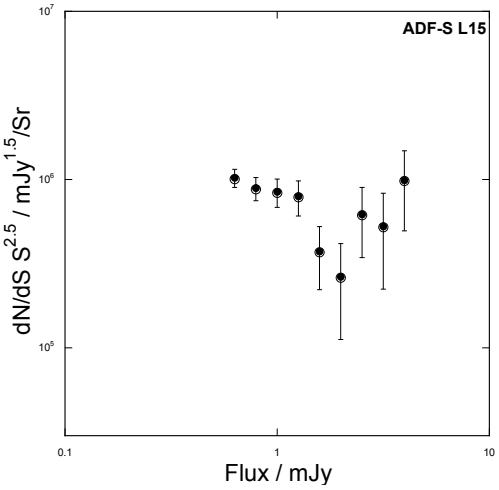

(e) ADF-S L15 number counts

Figure 3.17: The ADF-S number counts. The open circles give the raw number counts, and the filled circles give the completeness, reliability and stellar subtracted galaxy number counts.

Table 3.23: Table presenting the final differential number counts for N4 IRAC Dark Field.

Log Flux / mJy	Flux / mJy	Raw Counts	Final Counts	Uncertainty	Reliability/%	Completeness/%
-2.10	0.008	4.46	4.74	0.05	100.0	52.3
-2.00	0.010	4.58	4.82	0.05	100.0	58.5
-1.90	0.013	4.71	4.91	0.05	100.0	63.3
-1.80	0.016	4.85	5.02	0.05	100.0	68.2
-1.70	0.020	5.06	5.20	0.05	100.0	71.9
-1.60	0.025	5.20	5.32	0.05	100.0	77.0
-1.50	0.032	5.23	5.37	0.06	100.0	79.6
-1.40	0.040	5.39	5.48	0.06	100.0	81.9
-1.30	0.050	5.43	5.51	0.06	100.0	83.8
-1.20	0.063	5.43	5.49	0.08	100.0	86.4
-1.10	0.079	5.50	5.55	0.08	100.0	89.5
-1.00	0.100	5.34	5.38	0.12	100.0	91.1
-0.90	0.126	5.49	5.51	0.12	100.0	93.8
-0.80	0.158	5.48	5.50	0.14	100.0	95.1
-0.70	0.200	5.67	5.69	0.14	100.0	95.3
-0.60	0.251	5.30	5.32	0.25	100.0	96.2
-0.50	0.316	5.57	5.59	0.22	100.0	96.6
-0.40	0.398	5.12	5.13	0.18	100.0	96.9

Table 3.24: Table presenting the final differential number counts for S11 IRAC Dark Field.

Log Flux / mJy	Flux / mJy	Raw Counts	Final Counts	Uncertainty	Reliability/%	Completeness/%
-1.30	0.050	5.08	5.36	0.09	89.46	53.1
-1.20	0.063	5.38	5.49	0.07	77.62	77.5
-1.10	0.079	5.40	5.48	0.09	89.06	84.0
-1.00	0.100	5.43	5.49	0.11	100.0	86.4
-0.90	0.126	5.55	5.60	0.12	100.0	88.5
-0.80	0.158	5.67	5.71	0.12	100.0	90.6
-0.70	0.200	5.66	5.69	0.14	100.0	91.5
-0.60	0.251	5.89	5.93	0.13	100.0	92.0
0.50	0.316	5.78	5.81	0.18	100.0	93.1
-0.40	0.398	5.75	5.78	0.22	100.0	94.0
-0.30	0.501	5.90	5.93	0.22	100.0	95.0
-02.0	0.631	5.9	5.95	0.25	100.0	95.6

Table 3.25: Table presenting the final differential number counts for L15 IRAC Dark Field.

Log Flux / mJy	Flux / mJy	Raw Counts	Final Counts	Uncertainty	Reliability/%	Completeness/%
-0.90	0.126	5.84	6.04	0.08	95.06	63.0
-0.80	0.158	6.11	6.17	0.06	89.51	86.3
-0.70	0.200	6.26	6.30	0.07	93.47	90.3
-0.60	0.251	6.29	6.32	0.08	100.0	92.5
-0.50	0.316	6.16	6.19	0.11	100.0	93.6
-0.40	0.398	6.08	6.11	0.14	100.0	95.0
-0.30	0.501	6.27	6.29	0.13	100.0	95.7
-0.20	0.631	6.29	6.30	0.15	100.0	95.9
-0.10	0.794	6.14	6.15	0.22	100.0	96.3
0.00	1.000	5.68	5.70	0.18	100.0	96.6

Table 3.26: Table presenting the final differential number counts for L18W IRAC Dark Field.

Log Flux / mJy	Flux / mJy	Raw Counts	Final Counts	Uncertainty	Reliability/%	Completeness/%
-0.80	0.158	5.98	6.21	0.08	100.0	58.5
-0.70	0.200	6.16	6.23	0.08	100.0	84.9
-0.60	0.251	6.09	6.14	0.10	100.0	89.4
-0.50	0.316	6.13	6.17	0.12	100.0	91.5
-0.40	0.398	5.83	5.86	0.19	100.0	93.3
-0.30	0.501	5.98	6.01	0.19	100.0	93.8
-0.20	0.631	5.91	5.93	0.25	100.0	94.8

Table 3.27: Table presenting the final differential number counts for N4 ELAIS-N1.

Log Flux / mJy	Flux / mJy	Raw Counts	Final Counts	Uncertainty	Reliability/%	Completeness/%
-2.00	0.010	4.51	4.71	0.06	100.0	61.7
-1.90	0.013	4.75	4.91	0.05	100.0	69.8
-1.80	0.016	4.95	5.08	0.05	100.0	73.9
-1.70	0.020	4.91	5.02	0.06	100.0	76.7
-1.60	0.025	5.11	5.20	0.06	100.0	80.6
-1.50	0.032	5.16	5.24	0.06	100.0	82.7
-1.40	0.040	5.12	5.19	0.08	100.0	85.3
-1.30	0.050	5.41	5.47	0.07	100.0	87.9
-1.20	0.063	5.25	5.30	0.09	100.0	89.9
-1.10	0.079	5.47	5.51	0.09	100.0	91.3
-1.00	0.100	5.23	5.26	0.14	100.0	92.4
-0.80	0.158	5.31	5.33	0.18	100.0	94.8

Table 3.28: Table presenting the final differential number counts for S11 ELAIS-N1.

Log Flux / mJy	Flux / mJy	Raw Counts	Final Counts	Uncertainty	Reliability/%	Completeness/%
-1.10	0.079	4.89	5.02	0.18	100.0	73.9
-1.00	0.100	5.21	5.28	0.14	100.0	86.7
-0.90	0.126	5.61	5.66	0.11	62.2	90.8
-0.80	0.158	5.71	5.74	0.12	78.8	91.9
-0.70	0.200	5.49	5.52	0.18	100.0	93.0
-0.60	0.251	5.94	5.96	0.13	100.0	94.2
-0.50	0.316	5.61	5.64	0.22	100.0	94.5
-0.10	0.794	6.01	6.11	0.25	100.0	95.5
0.10	1.259	6.21	6.23	0.31	100.0	96.2

Table 3.29: Table presenting the final differential number counts for L15 ELAIS-N1.

Log Flux / mJy	Flux / mJy	Raw Counts	Final Counts	Uncertainty	Reliability/%	Completeness/%
-0.80	0.158	6.00	6.12	0.08	96.8	72.4
-0.70	0.200	5.94	6.04	0.10	94.8	74.4
-0.60	0.251	6.04	6.13	0.11	94.1	76.3
-0.50	0.316	6.13	6.25	0.11	100.0	76.8
-0.40	0.398	6.06	6.17	0.14	100.0	77.4
-0.30	0.501	5.86	5.97	0.22	100.0	77.7
-0.20	0.631	5.88	5.99	0.25	100.0	78.6
-0.10	0.794	5.86	5.96	0.31	100.0	78.9
0.10	1.259	5.86	5.96	0.18	100.0	79.4

Table 3.30: Table presenting the final differential number counts for L18W ELAIS-N1.

Log Flux / mJy	Flux / mJy	Raw Counts	Final Counts	Uncertainty	Reliability/%	Completeness/%
-0.90	0.126	5.63	5.86	0.11	89.0	52.1
-0.80	0.158	5.97	6.00	0.10	82.2	76.0
-0.70	0.200	6.32	6.38	0.07	97.8	86.2
-0.60	0.251	6.18	6.20	0.10	91.2	88.8
-0.40	0.398	6.27	6.30	0.12	100.0	93.1
-0.30	0.501	5.97	6.00	0.19	100.0	94.0
-0.20	0.631	5.90	5.92	0.25	100.0	94.7
-0.10	0.794	6.17	6.20	0.22	100.0	95.0
0.00	1.000	6.02	6.04	0.31	100.0	96.2
0.10	1.259	5.87	5.89	0.18	100.0	96.6
0.30	1.996	6.47	6.48	0.31	100.0	97.4

Table 3.31: Table presenting the final differential number counts for N3 ADF-S.

Log Flux / mJy	Flux / mJy	Raw Counts	Final Counts	Uncertainty	Reliability/%	Completeness/%
-1.10	0.079	5.30	5.25	0.03	100.0	87.7
-1.00	0.100	5.74	5.67	0.02	100.0	91.1
-0.90	0.126	5.83	5.73	0.02	100.0	92.0
-0.80	0.158	5.88	5.71	0.03	100.0	93.4
-0.70	0.200	5.91	5.71	0.03	99.9	93.7
-0.60	0.251	5.93	5.75	0.04	100.0	94.1
-0.50	0.316	5.96	5.68	0.05	100.0	94.3
-0.40	0.398	6.03	5.72	0.06	100.0	95.2
-0.30	0.501	6.05	5.70	0.07	100.0	95.5
-0.20	0.631	6.00	5.51	0.10	100.0	96.1
-0.10	0.794	6.16	5.64	0.10	100.0	96.4
0.00	1.000	6.27	5.69	0.11	100.0	96.6
0.10	1.259	6.29	5.66	0.14	100.0	96.6
0.20	1.585	6.35	5.77	0.14	100.0	96.4
0.30	1.995	6.45	5.96	0.14	100.0	97.0
0.40	2.512	6.48	5.89	0.18	100.0	96.9
0.50	3.162	6.72	6.10	0.16	100.0	97.1
0.60	3.981	6.70	6.19	0.18	100.0	97.2
0.70	5.012	6.72	5.86	0.31	100.0	97.4
0.80	6.310	6.84	6.01	0.31	100.0	97.6
0.90	7.943	7.08	6.33	0.25	100.0	97.5

Table 3.32: Table presenting the final differential number counts for N4 ADF-S.

Log Flux / mJy	Flux / mJy	Raw Counts	Final Counts	Uncertainty	Reliability/%	Completeness/%
-1.30	0.050	5.27	5.23	0.02	100.0	88.1
-1.20	0.063	5.51	5.45	0.02	100.0	90.6
-1.10	0.079	5.54	5.43	0.0	100.0	91.7
-1.00	0.100	5.56	5.43	0.03	100.0	93.1
-0.90	0.126	5.56	5.39	0.03	100.0	93.7
-0.80	0.158	5.58	5.32	0.04	100.0	94.2
-0.70	0.200	5.63	5.31	0.05	100.0	95.1
-0.60	0.251	5.60	5.34	0.06	100.0	95.2
-0.50	0.316	5.65	5.14	0.09	100.0	95.6
-0.40	0.398	5.68	5.25	0.09	100.0	96.3
-0.30	0.501	5.78	5.10	0.13	100.0	96.6
-0.20	0.631	5.87	5.32	0.12	100.0	97.1
-0.10	0.794	5.93	5.43	0.13	100.0	97.2
0.00	1.000	5.92	5.35	0.16	100.0	97.5
0.10	1.259	6.04	5.35	0.19	100.0	97.7

Table 3.33: Table presenting the final differential number counts for S7 ADF-S.

Log Flux / mJy	Flux / mJy	Raw Counts	Final Counts	Uncertainty	Reliability/%	Completeness/%
-0.70	0.200	4.67	4.45	0.14	100.0	88.4
-0.60	0.251	5.67	5.41	0.05	100.0	96.8
-0.50	0.316	5.81	5.52	0.06	100.0	97.2
-0.40	0.398	5.945	5.67	0.06	100.0	97.5
-0.30	0.501	5.87	5.60	0.07	100.0	97.5
-0.20	0.631	6.00	5.60	0.09	100.0	97.6
-0.10	0.794	5.91	5.58	0.11	100.0	97.9
0.00	1.000	6.03	5.73	0.11	100.0	97.9
0.10	1.259	6.04	5.49	0.16	100.0	98.1
0.20	1.585	6.25	5.70	0.15	100.0	98.3
0.30	1.995	6.26	5.85	0.15	100.0	98.2
0.40	2.512	6.49	5.94	0.16	100.0	98.2
0.50	3.162	6.39	5.85	0.22	100.0	98.2
0.60	3.981	6.54	6.10	0.19	100.0	98.2
0.70	5.012	6.50	5.85	0.31	100.0	98.2
0.80	6.310	6.73	6.18	0.25	100.0	98.3

Table 3.34: Table presenting the final differential number counts for S11 ADF-S.

Log Flux / mJy	Flux / mJy	Raw Counts	Final Counts	Uncertainty	Reliability/%	Completeness/%
-0.50	0.316	6.03	5.99	0.03	100.0	92.9
-0.40	0.398	6.17	6.12	0.03	100.0	93.6
-0.30	0.501	6.33	6.28	0.03	99.49	93.7
-0.20	0.631	6.27	6.18	0.05	100.0	93.7
-0.10	0.794	6.40	6.29	0.05	100.0	94.2
0.00	1.000	6.45	6.35	0.05	100.0	94.2
0.10	1.259	6.48	6.30	0.07	100.0	94.5
0.20	1.585	6.36	6.19	0.09	100.0	94.7
0.30	1.995	6.34	6.11	0.12	100.0	94.7
0.40	2.512	6.32	6.11	0.14	100.0	94.8
0.50	3.162	6.47	6.30	0.13	100.0	95.0
0.60	3.981	6.39	6.19	0.18	100.0	95.0
0.70	5.012	6.49	6.34	0.18	100.0	95.0
0.80	6.310	6.73	6.31	0.22	100.0	94.9
0.90	7.943	6.54	6.16	0.31	100.0	95.2

Table 3.35: Table presenting the final differential number counts for L15 ADF-S.

Log Flux / mJy	Flux / mJy	Raw Counts	Final Counts	Uncertainty	Reliability/%	Completeness/%
-0.20	0.631	6.00	6.01	0.05	100.0	98.3
-0.10	0.794	5.94	5.95	0.07	100.0	98.4
0.00	1.000	5.92	5.93	0.08	100.0	98.6
0.10	1.259	5.90	5.90	0.10	100.0	98.9
0.20	1.585	5.57	5.57	0.18	100.0	99.0
0.30	1.995	5.42	5.42	0.25	100.0	98.8
0.40	2.512	5.79	5.79	0.19	100.0	99.1

3.8 Non-Evolving Galaxy Model

3.8.1 Explanation of Non-Evolving Galaxy Model

Non-evolving galaxy source count models assume that there is no change in luminosity with redshift. These type of models take into account the expansion of the Universe. If the Universe was steady state, i.e. not expanding, and if there was no galaxy evolution, the Euclidean normalised number counts should lie long a horizontal line. As can be seen in Figure 3.18, (which plots Euclidean normalised number counts) the deeper number counts, 4, 7, 11 and 15 μm, and the no-galaxy evolution models all clearly deviate from a horizontal line. This is observational evidence to rule out an un-expanding and non-evolving universe. The reason why the faint end of the non-evolving galaxy number counts model, and deep observed number counts, curve away from the Euclidean slope, is due to the fact that the Universe had a smaller comoving volume in a redshift interval δz at high redshifts. Moving from $z = 0$ to greater redshifts, $\mathrm{d}V_{\mathrm{comoving}}/\mathrm{d}z$ increases and then decreases. The comoving volume enclosed by redshift z is proportional to z^3 at low redshifts, from Hubble's Law. As redshift tends to infinity (the particle horizon), the comoving volume enclosed by very high redshifts tends to a constant (which is the volume of the observable Universe). Hence for a constant comoving number density of galaxies, at high redshifts, $\mathrm{d}V_{\mathrm{comoving}}/\mathrm{d}z$ decreases, thus the number of galaxies in δz reaches a maximum, and then decreases at high redshifts. In actual fact there is also an evolution in comoving number density of galaxies. In Figures 3.18.d and e, the faint ends of the number counts decline more sharply than the non-evolving model. This is likely to be caused by the fact that the

deepest number counts are probing galaxies pre-peak of star formation, hence they are less luminous than their star forming counterparts. In Figures 3.18.b, d and e there is a 'bump' in the number counts. This is also due to galaxy evolution. This is likely to be caused by galaxies at the peak epoch of star formation rate, and hence their flux output is boosted, compared with their quiescent state, assuming pure luminosity evolution. The Madau diagram (which is shown in Figure 1.2 and discussed in Section 1.4), shows that cosmic star formation peaks at $z \sim 2$.

3.8.2 Comparison of Number Counts with Non-Evolving Galaxy Number Count Model

Figure 3.18 shows the IRAC Dark Field, ELAIS-N1 and ADF-S number counts compared with the non-evolving galaxy model of Pearson et al. (2014) at 3, 4, 7, 11, 15 and 18 μm. Each graph in Figure 3.18 is discussed separately below. The main outcome of comparing the observed number counts with the non-evolving model, is that the model does not fit the observed data well, apart from possibly in the case of the 4 μm number counts, shown in Figure 3.18.b. The fact that the number counts are not in agreement with the model indicates that, unsurprisingly, galaxies evolve and that the Universe is not in a steady state.

The ADF-S 3 μm number counts, plotted with the non-evolution galaxy model, are shown in Figure 3.18.a. The number counts are above the non-evolving galaxy population model. This would indicate that there are a greater number of more luminous galaxies than predicted by the model, and could indicate that the model is getting the old stellar populations wrong. Another option is, that the stellar subtraction in the number counts has been performed incorrectly.

The IRAC Dark Field, ELAIS-N1 and ADF-S 4 μm number counts are plotted in Figure 3.18.b. The figure shows that the observed 4 μm number counts follow the non-evolving galaxy model fairly well at bright fluxes. This may be due to the fact that at these fluxes a majority of the galaxies will be from the local Universe, thus a small time

range is being sampled, and very little evolution of galaxy populations as a function of redshift. At fluxes $\lesssim 0.1$ mJy the number of galaxies rises from that predicted by the model. The number counts rise to a peak at ~ 0.06 mJy, and then decline a little more steeply than predicted by the model. The peak in the 4 μm number counts is caused by galaxy evolution.

Figure 3.18.c shows the ADF-S 7 μm number counts compared with the non-evolving galaxy model. The 7 μm counts, like the 3 μm counts, are above those predicted by the non-evolving galaxy model. Thus more galaxies have been observed at 7 μm than predicted by the model. Unlike the 3 μm counts, the 7 μm counts show a decrease at fainter fluxes, driven partly by dV/dz trends as discussed above. There is a possible 'bump' at ~ 0.4 mJy. This 'bump' is caused by galaxy evolution.

Figure 3.18.d shows the 11 μm IRAC Dark Field, ELAIS-N1 and ADF-S number counts, plotted with the non-evolving galaxy model. The slope of the 11 μm number counts does not match the gradient of the non-evolving galaxy model. Similar to 3 and 7 μm, the observed counts all lie above the model. This would suggest that more galaxies have been observed at 11 μm than predicted by the model. The observed counts tail off sharply at fainter fluxes. Again this is due to galaxy evolution.

Figure 3.18.e shows the 15 μm IRAC Dark Field, ELAIS-N1 and ADF-S number counts. The observed 15 μm counts are not fitted by the non-evolving galaxy model. The observed counts have a 'bump' at ~ 0.3 mJy, which is not seen in the model, once again this 'bump' is due to galaxy evolution.

The IRAC Dark Field and ELAIS-N1 18 μm number counts are shown in Figure 3.18.f. The number count errors are quite large, thus this figure is not as conclusive as the other five figures in Figure 3.18. The number counts are all greater than the non-evolving model. Thus more galaxies have been observed than predicted by the model.

The following section compares the number counts of this thesis with evolving galaxy source count models and published number counts.

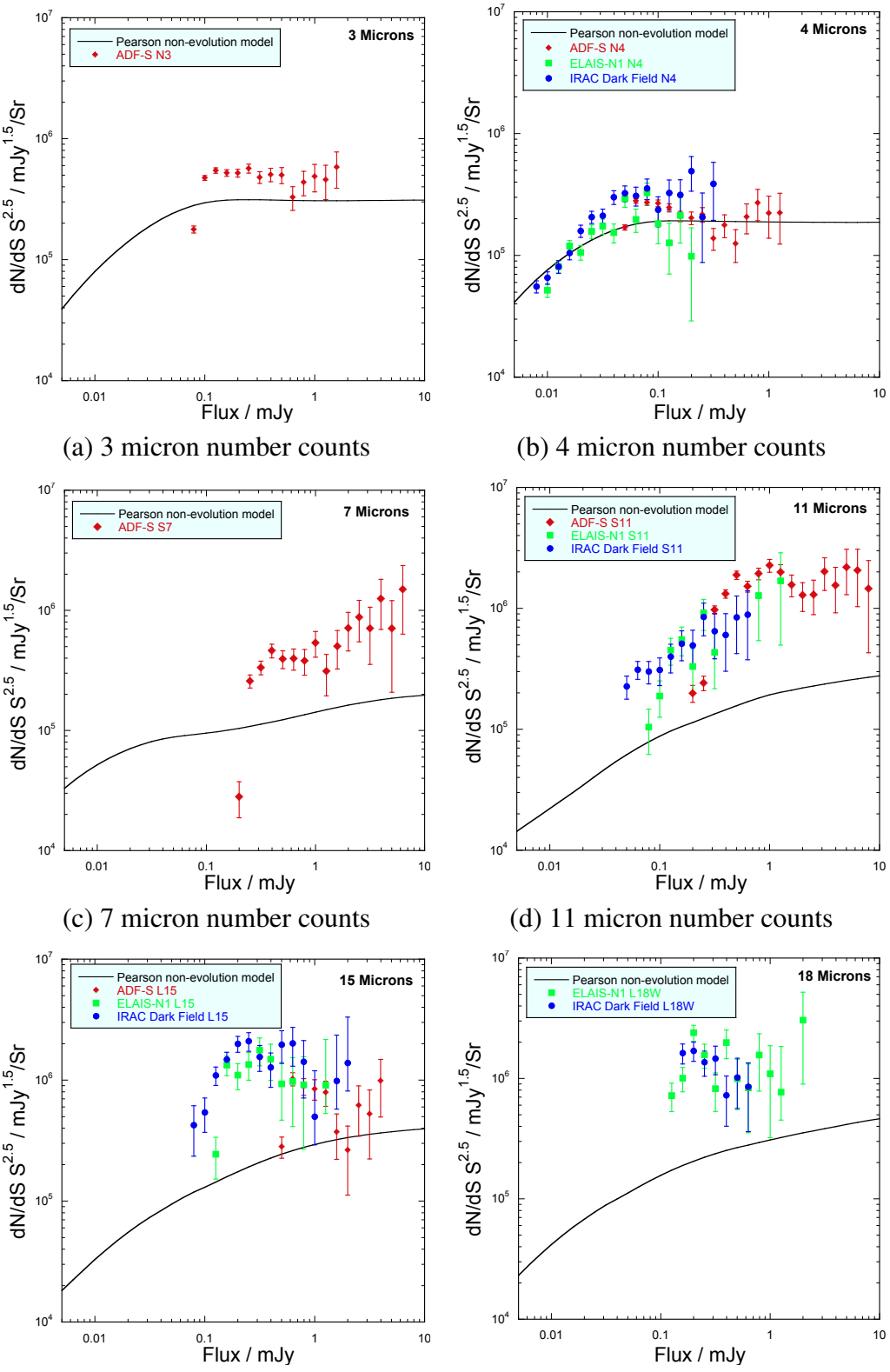

(a) 3 micron number counts

(b) 4 micron number counts

(c) 7 micron number counts

(d) 11 micron number counts

(e) 15 micron number counts

(f) 18 micron number counts

Figure 3.18: IRAC Dark Field, ELAIS-N1 and ADF-S number counts compared with the non-evolution galaxy number counts model from Pearson et al. (2014). The IRAC Dark Field counts are shown as blue circles, ELAIS-N1 counts are the green squares, ADF-S counts are the red diamonds and the black line is the number counts predicted by the non-evolution galaxy model.

3.9 Models and Published Number Counts

3.9.1 Models

There are many galaxy evolution models. Described below are several of the more recent models, which cover the infrared wavelength range. Some are post-Herschel Gruppioni et al. (2011), Béthermin et al. (2012), Cai et al. (2013) and Pozzi et al. (2015), and one is pre-Herschel, Pearson (2005).

The Pearson phenomenological backwards evolution model (Pearson, 2005) has provided a good fit to number counts from the near-infrared to millimetre wavelengths using IRAS, ISO and Spitzer data. A phenomenological model means that, although consistent with fundamental theories, the model is created by starting with observational evidence e.g. a specific galaxy spectrum. A backwards evolution model means that the different galaxy populations begin at a redshift of $z = 0$, and then are modelled backwards. How the different galaxy populations making up the model evolve with redshift can also be investigated. The Pearson model is made up of six different types of galaxies; normal (spiral), elliptical, star forming, luminous infrared galaxies (LIRGs), ultra luminous infrared galaxies (ULIRGs) and AGN. The model of Pearson (2005) was created to reproduce the strong galaxy evolution seen in the infrared surveys, observational evidence for this is discussed in more detail in Section 1.3. The Pearson model evolves the separate galaxy populations in luminosity (F(z)) and density (G(z)), both as a function of redshift. The parameterisation for both the evolution in luminosity and density are described as a double power law up to $z \sim 2$. For $0 < z \lesssim 1$, they are modelled by a steep power law, and then as a shallower power law from $1 \lesssim z \lesssim 2$. At $z \gtrsim 2$ there is negative evolution in both.

These models are based on the far-infrared models of Pearson (2001) and Pearson & Rowan-Robinson (1996), adapted to the mid-infrared by using the ISO 15 μm luminosity function of Pozzi et al. (2004), for the normal, star forming, LIRG and ULIRG; and the luminosity functions of Matute et al. (2002) and Rush et al. (1993) were used to adapt the AGN far-infrared models to the mid-infrared. For the normal galaxies (i.e

quiescent non-star forming galaxies) the spectral energy distribution (SED) of Dale et al. (2001) was used. The elliptical SED of Mobasher & Mazzei (2000) was used for the elliptical model. A synthesis of SED were used to create the star forming, LIRG, ULIRG and AGN templates, and are described below. To model star forming, LIRG and ULIRG the Pearson model used seven SED templates created from the radiative transfer models of Efstathiou et al. (2000). These templates model the evolution of optically thick Giant Molecular Clouds (GMC) heated by massive stars within them. The templates use a Saltpeter initial mass function (IMF) of $0.1 - 125\,\mathrm{M}_{\odot}$, and an e-folding time of 20 Myr. These models have two free parameters, the age of the starburst and the optical depth of the GMC. The SED templates were combined with those of specific objects e.g. the starburst template M82, a cold LIRG and a hot LIRG, which is heated by an AGN. The AGN model also used a combination of the models of Rowan-Robinson (1995) and King & Rowan-Robinson (2003). For any templates which did not originally have an optical component, Pearson (2005) added the component by using the SED template of a HII galaxy from Calzetti & Kinney (1992). The Pearson galaxy evolution model has strong links with AKARI, as it was used to decide the wavelength of the near and mid-infrared filters. This model is compared with the number counts created in the work of this thesis.

Gruppioni et al. (2011) discuss their backward evolution model for the infrared wavelengths. They state that the unique thing about the model is that each galaxy population is modelled separately. The model is comprised of five different galaxy populations: spiral, starburst, low luminosity AGN, type 1 AGN and type 2 AGN. When creating the model, Gruppioni et al. (2011) evolved the local luminosity function for each galaxy population backwards. For the spiral, starburst, low luminosity AGN and type 2 AGN, the population density was also evolved backwards. Gruppioni et al. (2011) compare their number counts predictions with observational data. The model fits the 15, 100, 350, 500 μm number counts well, and fits the 24 and 250 μm counts very well. They also compare the model's predictions for the total infrared luminosity density with observational data and find that the predictions fit well. Using the evolution model,

Gruppioni et al. (2011) have made the first estimate of black hole mass accretion density in the infrared and find this is in agreement with estimates at other wavelengths.

Béthermin et al. (2012) describe a fairly simple empirical galaxy evolution model, based on the assumption that there are two modes of star formation: main sequence and starburst. This model covers the mid-infrared to radio wavelengths. Unlike the other models discussed in this section, this model has been created just using SEDs; luminosity functions have not been included. When creating the model, Béthermin et al. (2012) parameterise the specific star formation rate for the two types of star formations and evolve the two galaxy populations' SEDs backwards as a function of redshift. They also include a term in their model for AGN emission in the mid-infrared. Béthermin et al. (2012) compare the predictions of their model with 24, 70, 100, 160, 250, 350, 500 and 1100 μm and 1.4 GHz observed number counts. They find that the model fits the number counts fairly well; but at 24, 70, 160, 250, 350, 500 and 1100 μm, the model over predicts the number of faint end galaxies. They state that unlike previous models, they have not 'fine tuned' the model parameters to fit the observed data.

The galaxy evolution model of Cai et al. (2013) (also known as the SISSA model) simultaneously attempt to fit the wavelength range from the mid-infrared to millimetre wavelengths, for $0 < z < 2.5$. This is a hybrid model comprised of a physical model and a phenomenological model. The galaxy populations have been divided into high-z, proto-spheriods and AGN, $z \gtrsim 1.5$ and low-z, late type 'cold' galaxies and 'warm' starburst galaxies, $z \lesssim 1.5$. To model the high-z population, Cai et al. (2013) use a bolometric luminosity function for spheroidal galaxies and SEDs for the high-z AGN; and use these in a physical forward evolution model, based on the Granato et al. (2004) model. To model the low-z populations Cai et al. (2013) use a parametric phenomenological backward evolution model. The low-z population is subdivided into 'warm' starburst galaxies, 'cold' late type galaxies, type 1 AGN and type 2 AGN; where the AGN have been 'reactivated'. They find that that late type galaxies only evolve in luminosity, whereas the starbursts are found to evolve in both luminosity and density. A 'warm' and a 'cold' SED are used in the model. The Cai et al. (2013) model assumes

that early type galaxies are more dominate at $z > 1.5$ and late type galaxies are more dominate at $z < 1.5$. Using their galaxy evolution models, Cai et al. (2013) have created luminosity functions, SEDs and number count models, which they compare with observational data. They find that the model's predicted infrared luminosity functions at $z = 0.5$ and $z = 2.2$ fit observational data well, but the fit is not so goof at $z = 1.4$. The model appears to fir observational number counts well from $15 - 1380\,\mu$m. This model is also compared with the number counts created in the work of this thesis.

Pozzi et al. (2015) present a hybrid, backward evolution galaxy model, which fits the near to far-infrared wavelengths. One of the motivations behind the model is to investigate whether 'Herschel observed' high-z star forming galaxies are progenitors to present day elliptical galaxies (proto-spheroids). The model is hybrid because the galaxies are separated into two types: spiral (late type) and spheroids. Pozzi et al. (2015) modelled the spiral galaxies using a parametric phenomenological method, where the local luminosity function of Gruppioni et al. (2011) was evolved backwards with redshift. For modelling the spheroid galaxies Pozzi et al. (2015) evolved a physical chemo-spectrophotometric SED of a proto-spheroid galaxy backwards as a function of redshift. Pozzi et al. (2015) compare the $160\,\mu$m number counts and K-band rest frame luminosity function predicted by their model with observational data. For both comparisons the model fits the observed data well. Pozzi et al. (2015) state that there are several unique things about their model. One of which is that both the far-infrared dust from star formation and emission from old stellar populations in the near-infrared have been evolved backwards separately. Another unique thing about their model is that unlike the previous models, they have not used a dark matter halo merging history model when calculating the density of spheroid galaxies. They have used one which is purely phenomenological. Pozzi et al. (2015) state that they feel that their model is superior to the one of Cai et al. (2013) because they have not separated galaxies on their redshift, but on the evolution of the galaxy population's redshift density function. Pozzi et al. (2015) state that they did not attempt to model disk/bulge composite objects.

3.9.2 Published Number Counts

There already exist published number counts for AKARI/IRC. These have mainly been calculated from the North Ecliptic Pole (NEP) wide and deep surveys (Murata et al. (2014a) and Kim et al. (2012)).

Pearson et al. (2010) presented AKARI 15 μm galaxy number counts from the NEP wide and NEP deep surveys. These number counts are in agreement with the Euclidean slope between $1-10$ mJy. At less than ~ 1 mJy these number counts deviate from the Euclidean slope. This excess peaks at $0.25 < S < 0.3$ mJy, and then declines.

Hopwood et al. (2010) present analysis of AKARI data of the gravitationally lensed cluster Abell 2218 at 15 μm. This work also shows that there is a rise in number counts from the Euclidean slope between $0.1-1$ mJy. Because this work used lensed galaxies, this is the deepest number count measurement at 15 μm.

Pearson et al. (2014) presented the first 18 μm galaxy number counts, from the AKARI NEP wide and NEP deep surveys. This work showed a similar number count excess from the Euclidean slope between $0.1-1$ mJy, with a peak at ~ 0.25 mJy. At fluxes below this there is a sharp decline.

The first analysis of galaxy number counts over all IRC filters was performed by Murata et al. (2014a). This work also used the NEP deep survey. The paper showed that for all IRC wavelengths, galaxy number counts with flux greater than 1.5 mJy are in agreement with the Euclidean slope. The NIR (2, 3 and 4 μm) number counts deviate from the Euclidean slope at fluxes less than ~ 0.2 mJy. It is thought this could be due to source confusion. If so, it is an artefact of their analysis. The 7 μm number counts are in a general agreement with the Euclidean slope. The 11 μm number counts show a decrease from the Euclidean slope at fluxes less than ~ 0.2 mJy. The 11, 15 and 18 μm number counts all show the increase from the Euclidean slope as shown in the previous published results, in fluxes less than 0.4 mJy. The 11 μm number counts only have a small 'bump' peaking at ~ 0.4 mJy. The detection limit of the 24 μm filter was too high to calculate number counts less than 0.4 mJy. Between $0.4-1$ mJy the number

counts appear to deviate from the Euclidean slope.

It is thought that the excess in galaxy number counts in the mid-infrared at fluxes less than ~ 1 mJy is due to luminous dusty galaxies evolving quickly (Pearson et al., 2014). The Spitzer/IRAC covers part of the AKARI wavelength range, with filters centred on 3.6, 4.5, 5.8 and 8 μm.

Fazio et al. (2004) presented galaxy number counts from three different survey areas for all four IRAC filters. The three extragalactic fields are of different sized area. The deep field is close to QSO HS1700+6416, the intermediate depth field is part of the Extended Groth Strip (EGS), and the wide area survey is a region in Boötes. The results from all three areas showed that the 3.6 and 4.5 μm number counts have a similar excess from the Euclidean slope at fainter fluxes, as also seen in the mid-infrared AKARI number counts.

Ashby et al. (2015) presented warm phase Spitzer/IRAC 3.6 and 4.5 μm number counts. The number counts are from the Spitzer-Cosmic Assembly Deep Near-Infrared Extragalactic Legacy Survey (S-CANDLES), which is comprised of data from five extragalactic deep fields: United Kingdom InfraRed Telescope (UKIRT) Infrared Deep Sky Survey (UKIDSS) Ultra Deep Survey, the Extended Chandra Deep Field South/Goods South, Cosmic Evolution Survey (COSMOS), the HST Deep Field North/Goods North and the Extended Groth Strip (EGS). At fluxes greater than ~ 1 mJy, Ashby et al. (2015) showed that the counts at 3.6 and 4.5 μm increase more sharply from the Euclidean slope than the number counts of Fazio et al. (2004). Ashby et al. (2015) stated that their published number counts include Galactic stars. Due to this, Ashby et al. (2015) number counts are not suitable for comparison with the AKARI galaxy number counts for this thesis.

Other Spitzer number counts in the AKARI/IRC wavelength range include those observed by the Spitzer Peak-Up Imaging (PUI), which is part of the Infrared Spectrometer (IRS). These 16 μm number counts are presented by Teplitz et al. (2011). The 16 μm number counts show the same rise in number counts between $0.1 - 1$ mJy as Hopwood et al. (2010).

3.9.3 Comparison of Number Counts with Models and Published Results

The IRAC Dark Field, ELAIS-N1 and the ADF-S number counts have been plotted with the NEP Deep AKARI number counts of Murata et al. (2014a), the AKARI 15 μm number counts of Abell 2218 from Hopwood et al. (2010), the Spitzer/IRAC 3.6, 4.5, 5.8 and 8.0 μm number counts of Fazio et al. (2004), the Spitzer/IRS number counts at 16 μm of Teplitz et al. (2011), and the models of Pearson (2005) and Cai et al. (2013). The 3, 4, 7 and 11 μm ADF-S number counts are inconsistent with those of the ELAIS-N1 and the IRAC Dark Field. They are also inconsistent with the published NEP number counts. This offset is too large to have been caused by an incorrect survey area. The survey area in the ADF-S images was calculated using the same method as for the ELAIS-N1 and IRAC Dark Field, both of which do not show this rise in bright end number counts. This difference is thought to be due to an incorrect stellar subtraction. Section 3.7.2 describes the two different methods used to remove the stars in the ADF-S. Figure 3.11 shows the large difference in the bright end slope by using the two different stellar subtraction methods. As there are not many sources in the bright end flux bins, a change of one or two will make quite a significant difference. As the survey area of the ELAIS-N1 and IRAC Dark Field is $\lesssim 10\%$ the survey area of ADF-S, one would expect the ADF-S to have over 10 times the number of stars as the ELAIS-N1 and IRAC Dark Field.

The ADF-S number counts also suffer from a possible incorrect completeness, because the faintest flux number count has a much smaller value than the number count values. An incorrect completeness could be due to the fact that a Gaussian point spread function (PSF) was used to test for incompleteness. An analytical PSF created using AKARI data may give a better completeness correction.

The 3 μm ADF-S number counts are shown in Figure 3.19, and have been plotted with the published NEP and IRAC 3.6 μm counts and the model of Pearson (2005). The possible error due to incorrect stellar subtraction has been discussed above. The NEP

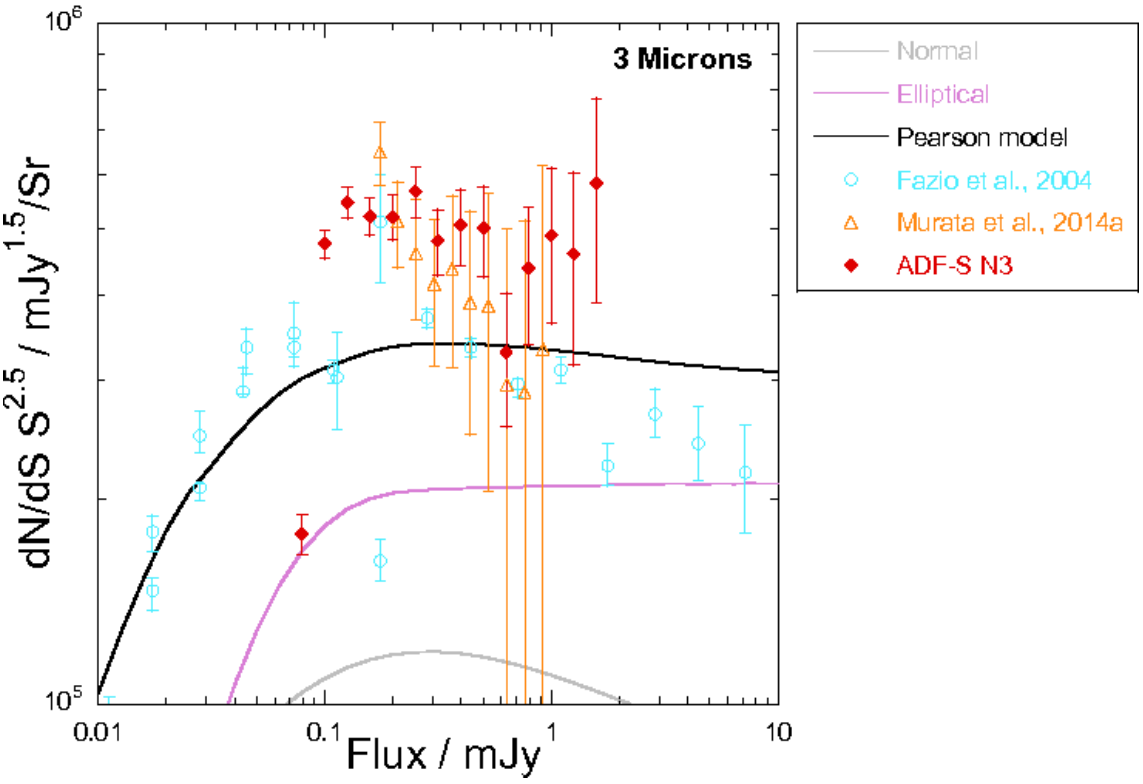

Figure 3.19: The 3 microns number counts. Comparison of the ADF-S number counts with AKARI NEP survey number counts (Murata et al., 2014a), Spitzer/IRAC number counts (Fazio et al., 2004) and Pearson model (Pearson, 2005). The ADF-S number counts are shown as red diamonds, the AKARI NEP number counts are shown as orange open triangles, the Spitzer/IRAC number counts are shown as cyan open circles. The Pearson model is shown as a solid black line, the grey line is the contribution of normal type galaxies and the magenta line is the contribution of elliptical type galaxies.

number counts seem to be showing a rise at fainter fluxes, which is inconsistent with galaxy evolution models. The Pearson model does not seem to fit the counts of the ADF-S, AKARI NEP or the IRAC 3.6 μm number counts.

The 4 μm has been observed by ELAIS-N1, IRAC Dark Field and ADF-S. These counts have been plotted in Figure 3.20 with the AKARI NEP counts, the IRAC 4.5 μm counts and the Pearson model. The 4 μm number counts figure is a good example of what was hoped to be achieved with the AKARI data, by using deep and shallow field data. The ELAIS-N1 and IRAC Dark Field both have a small survey area ($\sim$ 10 arcmins by $\sim$ 10 arcmins), but are both deep fields, thus probing the fainter flux number counts. The ADF-S is a wide, but shallow field, and hence probes the brighter end of the counts. As can be seen in Figure 3.20, the ADF-S does indeed constrain the

brighter fluxes, and the two deep fields, ELAIS-N1 and IRAC Dark Field constrain the fainter number counts. The ELAIS-N1, IRAC Dark Field and the IRAC 4.5 μm number counts are all similar at fainter fluxes. They all have fewer fainter flux counts than predicted by the Pearson model. This seems to imply that one (or several) of the galaxy models making up the Pearson model are over predicted. Most likely the model has over predicted the number of star forming galaxies. Over all fluxes, the IRAC Dark Field, ADF-S and the IRAC 4.5 μm counts are in good agreement. The Pearson model does not fit them very well. Surprisingly all counts seem to show a peak at ~ 0.1 mJy, the galaxy evolution models do not predict a peak in the 4 μm counts.

Figure 3.21 shows the AKARI ADF-S 7 μm number counts plotted with the AKARI NEP counts, the IRAC 8 μm, the Pearson model and SISSA model. The ADF-S counts seem to be in better agreement with the IRAC 8 μm counts than the NEP counts. The SISSA models appear to fit the ADF-S counts better than the Pearson models, but as discussed above, the ADF-S count may not have a correct stellar subtraction. The counts may, in fact, be lower.

The 11 μm number counts are shown in Figure 3.22. ELAIS-N1, IRAC Dark Field and the ADF-S all have observations at 11 μm. These counts are plotted with the AKARI NEP counts, the Pearson model and the SISSA model. The IRAC Dark Field and the NEP counts appear to be in agreement. The Pearson model fits the IRAC Dark Field better at fainter fluxes, whereas the SISSA model appears to fit the brighter counts better. The variation in the ELAIS-N1 counts could be due to a remnant of Earthshine light. The removal of the Earthshine light was discussed in Section 2.4.3.9. Due to the angle of the telescope between the Earth, the ELAIS-N1 images are the most affected by the Earthshine light, and out of the four filters observed in the ELAIS-N1, S11 contained the most amount of Earthshine light. The sudden drop in ELAIS-N1 counts at fainter fluxes could be due to an incorrect completeness correction. As discussed above for the ADF-S, using a non-Gaussian PSF for completeness may improve the completeness correction. The ADF-S counts are greater than the other surveys, this could be due to an incorrect stellar subtraction, as discussed above.

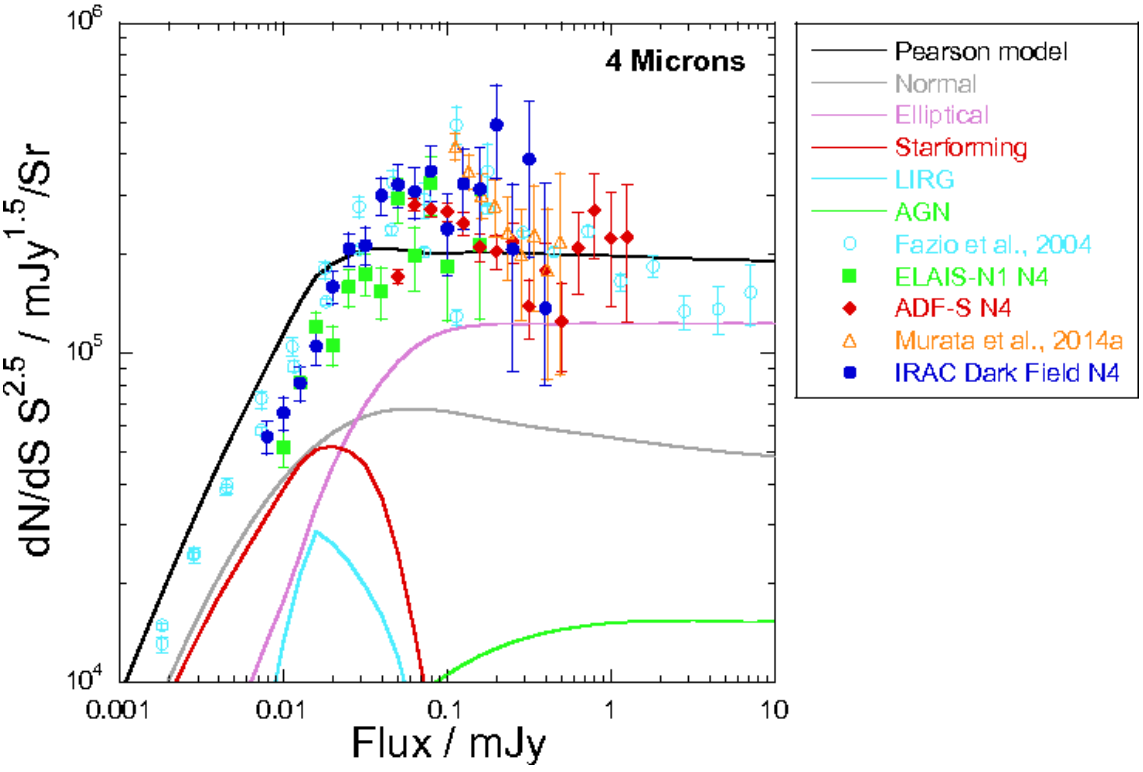

Figure 3.20: The 4 microns number counts. Comparison of the AKARI IRAC Dark Field, ELAIS-N1 and ADF-S number counts with AKARI NEP survey number counts (Murata et al., 2014a), Spitzer/IRAC number counts (Fazio et al., 2004) and Pearson model (Pearson, 2005). The IRAC Dark Field number counts are shown as blue circles, ELAIS-N1 number counts are shown as green squares, the ADF-S number counts are shown as red diamonds, the AKARI NEP number counts are shown as open orange triangles and the Spitzer/IRAC number counts are shown as open cyan circles. The SISSA model is shown as a dashed line. The Pearson model is shown as a solid line, the grey line is the contribution of normal type galaxies, the magenta line is the contribution of elliptical type galaxies, the red line is the contribution of star forming galaxies, the cyan line is the contribution of LIRGs and the green line is the contribution of AGN.

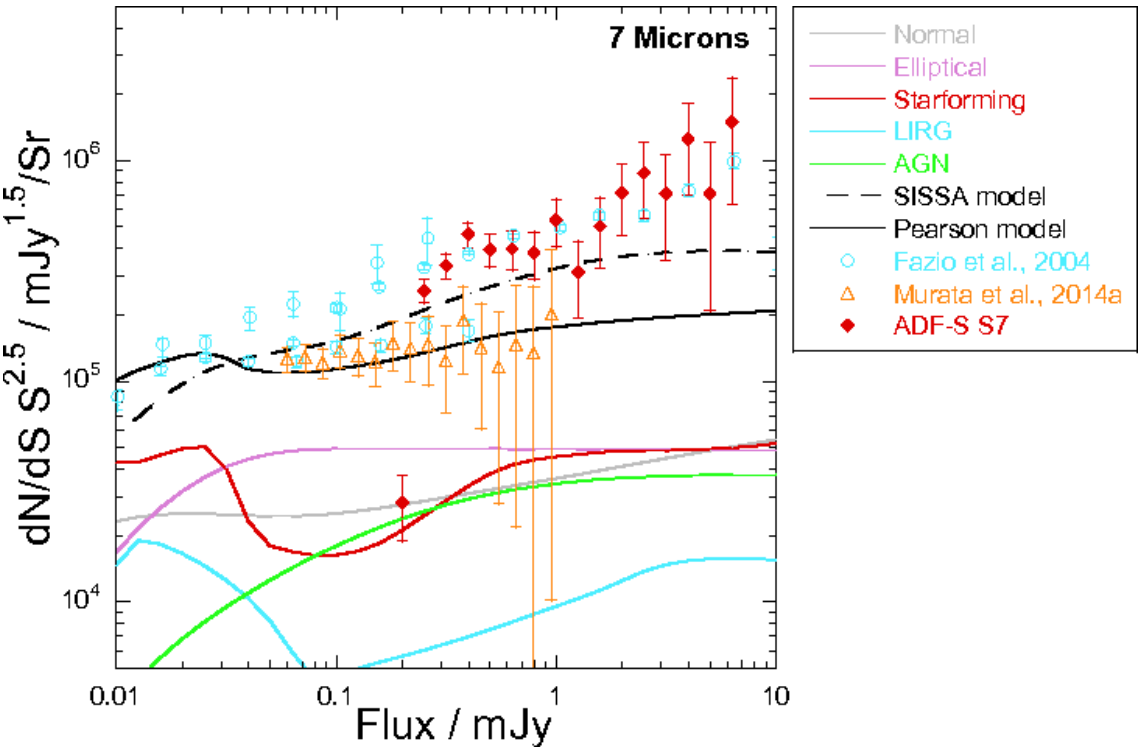

Figure 3.21: The 7 microns number counts. Comparison of the AKARI ADF-S number counts with AKARI NEP survey number counts (Murata et al., 2014a), Spitzer/IRAC number counts (Fazio et al., 2004), Pearson model (Pearson, 2005) and SISSA model (Cai et al., 2013). The ADF-S number counts are shown as red diamonds, the AKARI NEP number counts are shown as open orange triangles and the Spitzer/IRAC number counts are shown as open cyan circles. The SISSA model is shown as a dashed line. The Pearson model is shown as a solid line, the grey line is the contribution of normal type galaxies, the magenta line is the contribution of elliptical type galaxies, the red line is the contribution of star forming galaxies, the cyan line is the contribution of LIRGs, the blue line is the contribution of ULIRGs and the green line is the contribution of AGN.

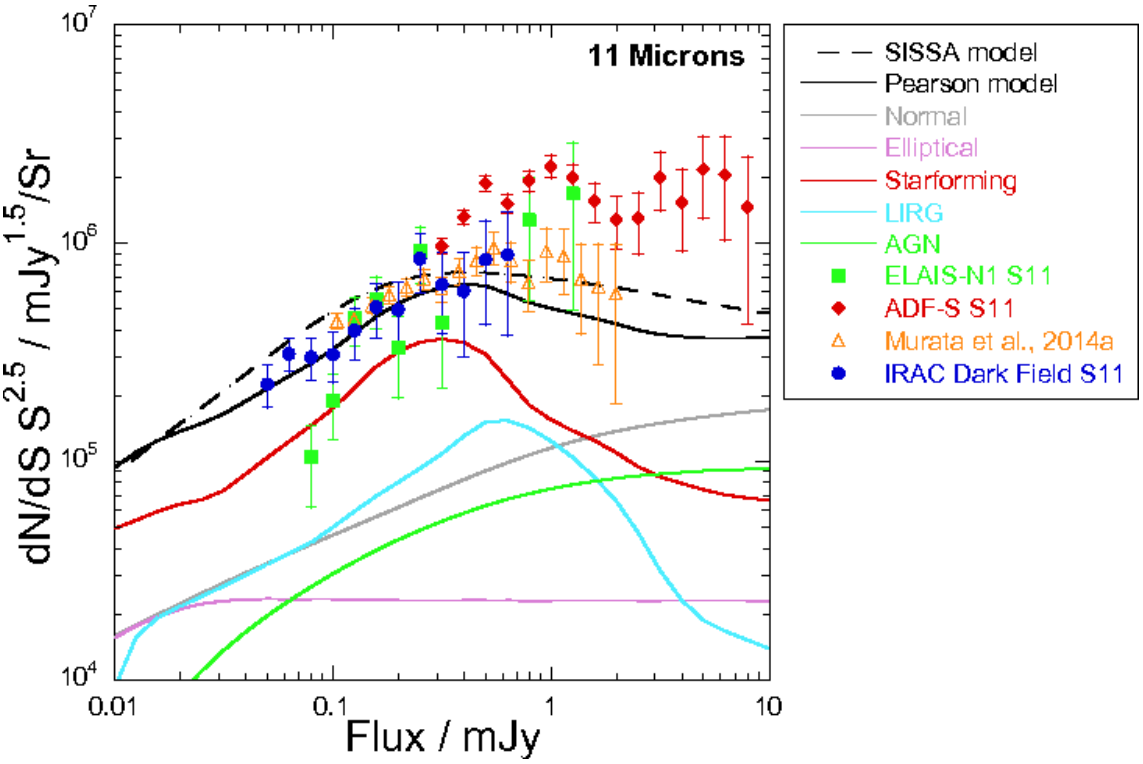

Figure 3.22: The 11 microns number counts. Comparison of the AKARI IRAC Dark Field, ELAIS-N1 and ADF-S number counts with AKARI NEP survey number counts (Murata et al., 2014a), Pearson model (Pearson, 2005) and SISSA model (Cai et al., 2013). The IRAC Dark Field number counts are shown as blue circles, ELAIS-N1 number counts are shown as green squares, the ADF-S number counts are shown as red diamonds and the AKARI NEP number counts are shown as open orange triangles. The SISSA model is shown as a dashed line. The Pearson model is shown as a solid line, the grey line is the contribution of normal type galaxies, the magenta line is the contribution of elliptical type galaxies, the red line is the contribution of star forming galaxies, the cyan line is the contribution of LIRGs and the green line is the contribution of AGN.

AKARI is the only satellite to have an 11 μm channel. The other extensive work on the AKARI S11 number counts is of NEP observations by Murata et al. (2014a), which are shown as orange triangles in Figure 3.22. As can be seen in Figure 3.22, the IRAC Dark Field and the ELAIS-N1 number counts go down to fainter fluxes, hence are deeper than those of Murata et al. (2014a). The ELAIS-N1 number counts tail off at fainter fluxes possibly due to the raw frames containing Earthshine light. As discussed above, the ELAIS-N1 frames were badly effected by Earthshine light, because they were observed late Phase 2. The 11 μm IRAC Dark Field number counts do not show a drop off at fainter fluxes. The IRAC Dark Field pointings were early and mid Phase 2, hence not badly affected by Earthshine light, and thus more reliable. Figure 3.22 shows that the S11 number counts are deeper than those of Murata et al. (2014a). Thus the AKARI IRAC Dark Field 11 μm image created in the work of this thesis, shown in Figure 3.1.b, is likely to be the deepest 11 μm image.

ELAIS-N1, the IRAC Dark Field and the ADF-S were also all observed at 15 μm. These number counts are shown in Figure 3.23. Also plotted are the AKARI NEP counts, the AKARI 15 μm number counts of Hopwood et al. (2010), the Spitzer/IRS 16 μm number counts of Teplitz et al. (2011), the Pearson model and the SISSA model. Like the 4 μm, the 15 μm number count figure, this is another good example of what was hoped to be achieved with the deep and shallow AKARI surveys. There is a probable incorrect completeness correction for the faintest flux bin of ELAIS-N1 and ADF-S. Due to the fact that less Galactic stars are observable at 15 μm, the wavelength will require less stars to be removed from galaxy catalogues. As can be seen in Figure 3.23, the ADF-S counts seem to be in much better agreement with the ELAIS-N1 and the IRAC Dark Field than at the shorter wavelengths. Both the number counts of Hopwood et al. (2010) and Teplitz et al. (2011) go deeper than the AKARI number counts of this thesis. The number counts of Hopwood et al. (2010) appear to match the AKARI IRAC Dark Field number counts better than those of Teplitz et al. (2011). The Pearson model and the SISSA model are fairly similar at this wavelength, thus it is inconclusive which model fits the number counts of this thesis better. The Pearson

model does not fit the Teplitz et al. (2011) numbers, but the model does fit the number counts of Hopwood et al. (2010); although the final bin of the number counts of Hopwood et al. (2010) show an increase in number from that predicted by the Pearson model. According to the Pearson model, the faint end number counts are dominated by star forming galaxies.

The 18 μm number counts are shown in Figure 3.24. The figure shows the ELAIS-N1 and IRAC Dark Field number counts, plotted with them are the AKARI NEP number counts and the Pearson model. The 18 μm data for ELAIS-N1 and the IRAC Dark Field do not look as reliable as that for the other filters, they appear more inconsistent and have larger errors on average. The 18 μm IRAC Dark Field is only 5 pointings deep, see Table 3.1. The 18 μm ELAIS-N1 survey was deeper by two pointings, see Table 3.8, but as the data were observed towards the end of Phase 2, the frames were badly affected by Earthshine light. The number counts show that possibly the Earthshine light has not been completely removed.

If two deep field number counts do not exactly match, this does not mean that one of the counts is necessarily wrong. There is an uncertainty in the number of galaxies in a given volume density, caused by large-scale density fluctuations. This is known as cosmic variance (Somerville et al., 2004). The percentage of cosmic variance is greater for deep, narrow fields. Figure 3.25 shows the cosmic variance predictions of Moster et al. (2011), assuming a stellar mass range of $\log(m/M_{\odot}) \sim 10.25$. Using the results for the GOODS field (10 x 16 arcminutes) for ELAIS-N1 and the IRAC Dark Field, and the EGS (10 x 70 arcminutes) for ADF-S, the figures show that for galaxies at a redshift of $z = 1$, the ELAIS-N1 and the IRAC Dark Field have a cosmic variance of $\sim 14\%$ and the ADF-S has a cosmic variance of $\sim 9\%$. Cosmic variance could account for small differences in the ELAIS-N1 and the IRAC Dark Field number counts.

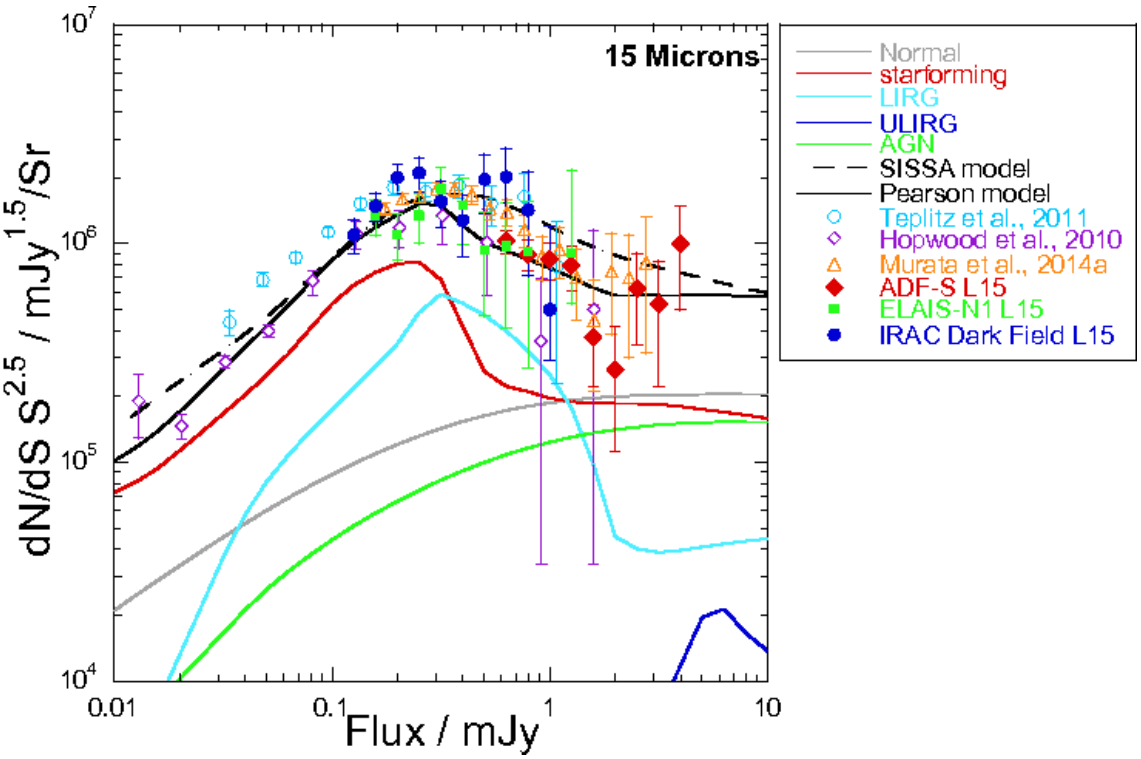

Figure 3.23: The 15 microns number counts. Comparison of the AKARI IRAC Dark Field, ELAIS-N1 and ADF-S number counts with AKARI NEP survey number counts (Murata et al., 2014a), the AKARI Abell 2218 number counts (Hopwood et al., 2010), Spitzer/IRS number counts (Teplitz et al., 2011), Pearson model (Pearson, 2005) and SISSA model (Cai et al., 2013). The IRAC Dark Field number counts are shown as blue circles, ELAIS-N1 number counts are shown as green squares, the ADF-S number counts are shown as red diamonds, the AKARI NEP number counts are shown as open orange triangles, the AKARI Abell 2218 number counts are shown as open purple diamonds and the Spitzer/IRS number counts are shown as open cyan circles. The SISSA model is shown as a dashed line. The Pearson model is shown as a solid line, the grey line is the contribution of normal type galaxies, the red line is the contribution of star forming galaxies, the cyan line is the contribution of LIRGs, the blue line is the contribution of ULIRGs and the green line is the contribution of AGN.

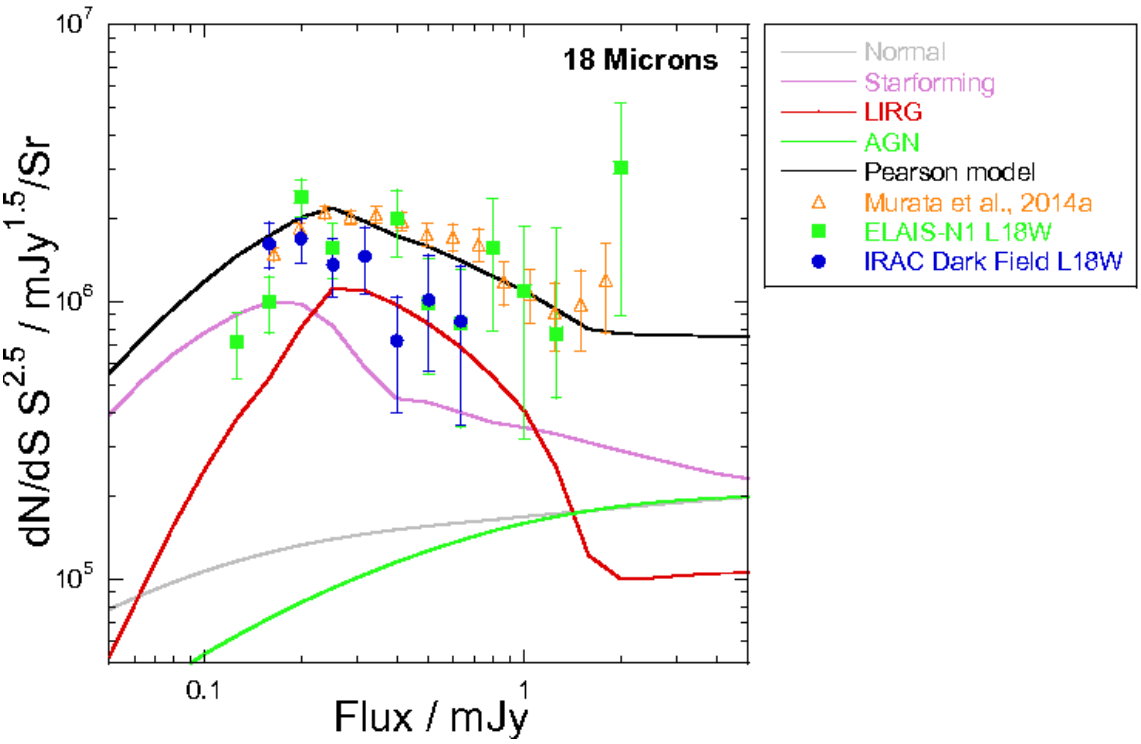

Figure 3.24: The 18 microns number counts. Comparison of the AKARI IRAC Dark Field and ELAIS-N1 number counts with AKARI NEP survey number counts (Murata et al., 2014a) and Pearson model (Pearson, 2005). The IRAC Dark Field number counts are shown as blue circles, ELAIS-N1 number counts are shown as green squares and the AKARI NEP number counts are shown as open orange triangles. The Pearson model is shown as a solid line, the grey line is the contribution of normal type galaxies, the red line is the contribution of star forming galaxies, the cyan line is the contribution of LIRGs and the green line is the contribution of AGN.

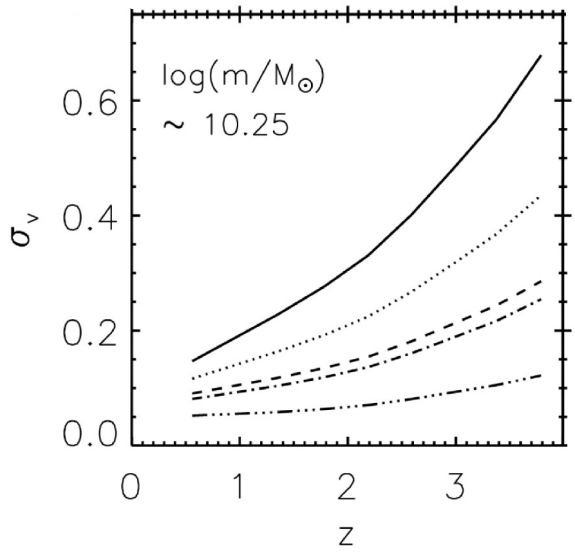

Figure 3.25: The Cosmic Variance fraction from Moster et al. (2011) for the Ultra Deep Field (UDF) (3.3 x 3.3 arcminutes) shown as a black line, Great Observatories Origins Deep Survey (GOODS) (10 x 16 arcminutes) field shown as a dotted line, the Galaxy Evolution from Morphology and SEDs survey (GEMS) (28 x 28 arcminutes) shown as a dashed line, the Extended Groth Strip (EGS) (10 x 70 arcminutes) shown as a dot-dashed line and the Cosmic Evolution Survey (COSMOS) (84 x 84 arcminutes) shown as a dot-dot-dashed line.

3.10 Conclusions of Number Count Work

This chapter introduces the three extragalactic fields: the IRAC Dark Field, ELAIS-N1 and the ADF-S. Data from all AKARI/IRC Phase 2 observations of these fields were processed by the optimised pipeline, discussed in Chapter 2. This chapter then describes how galaxy catalogues were made for these fields and how the number counts work was performed.

The number count results presented in this chapter are in general agreement with the previous published results, apart from the deep lensed 15μm counts. This is a good validation of the performance of the optimised pipeline, discussed in Chapter 2, which was used to create the number counts.

The NEP deep field number counts of Murata et al. (2014a) at 3, 4 and 11 μm all have a faint number count 'up turn' (see Figures 3.19, 3.20 and 3.22). This 'up turn' is not seen in any of the number count work of this thesis, or in the models. This feature is possibly due to over completeness correction at the faintest counts of Murata et al.

(2014a).

As can be seen in Figure 3.21, there is tension in the published number counts. The ADF-S number counts of this thesis and the IRAC 8 μm of Fazio et al. (2004) are in agreement and are best fitted by the Cai model; whereas the NEP deep 7 μm number counts of Murata et al. (2014a) are best fit by the Pearson model. The cause of this tension could be due to cosmic variance in the NEP deep field. The ADF-S is a wide field and the IRAC 8 μm number counts are a combination of three deep fields, hence both would have less cosmic variance.

As can be seen in Figure 3.23 there is a tension between the 15 μm Abell 2218 number counts of Hopwood et al. (2010) and those from Spitzer/IRS 16 μm of Teplitz et al. (2011). The 15 μm IRAC Dark Field number counts of this thesis do not extend to faint enough fluxes to resolve this tension. The following chapter continues the number count work, by investigating below the detection level of the AKARI images and probing the fainter fluxes of the Pearson number count model.

Chapter 4

P(D) Analysis of the AKARI IRAC Dark Field Number Counts

O this learning, what a thing it is!

Taming of the Shrew - William Shakespeare

4.1 Introduction

Probability of Deflection (P(D)) analysis is a method to investigate the faint end number counts and to constrain the galaxy number count model below the minimum flux of detected sources. In deep surveys the source detection can be close to, or at, the confusion limit for the survey, hence the fluxes of very faint galaxies, contributing to the flux of the image, are blended together (see Section 3.6.3 for an explanation of the confusion limit). Section 4.2 gives examples of past galaxy number count work using P(D) analysis. The P(D) analysis work on the AKARI IRAC Dark Field is shown in Section 4.3

4.2 P(D) Analysis

P(D) analysis uses the flux histogram of the pixels in the image; this histogram is dependent on the sources in the image, both resolved and unresolved. This method does not use any source detection algorithms. A model is created to fit the number counts, and various parameters of the model are varied during Monte Carlo simulations to constrain the faint end slope of the number counts. Thus predictions can be made about the galaxies below the detection limit of the survey (Oliver et al. (1997), Patanchon et al. (2009) and Glenn et al. (2010)).

The method of using P(D) to gain information about sources below the confusion limit of a survey was first discussed by Scheuer et al. (1957), and then subsequently in Condon (1974). In these theoretical papers, it is stated how to calculate P(D) analytically for radio sources.

Oliver et al. (1997) performed the first P(D) analysis on the 6.7 and 15 μm Infrared Space Observatory (ISO) Hubble Deep Field number counts. These were the first 6.7 μm number counts, and at the time the observations were the deepest mid-infrared survey. In their P(D) analysis, they fitted a model to the shape of the pixel flux histogram of the image. They varied the parameters of the model to find the best fit to the data. The P(D) analysis suggested that the faint end number count slope is steeper than predicted by the models at the time of Pearson & Rowan-Robinson (1996) and Saunders et al. (1990), hence the results of the P(D) analysis show there are fewer fainter galaxies than predicted by previous models. Oliver et al. (1997) also state that galaxy the non-evolution model of Pearson & Rowan-Robinson (1996) did not fit the 15 μm number counts, hence there must be a strong evolution of galaxies observable in the mid-infrared.

Weiß et al. (2009) used P(D) analysis on Large Apex Bolometer Camera (LABOCA) data at 870 μm of the Chandra Deep Field South. They use four different models, a power law, a broken power law, a Schechter function and the power law in Barger et al. (1999), which has constant counts for the fainter fluxes. Weiß et al. (2009) varied

the parameters of these four different number count models to create simulated pixel flux histograms. They used the χ^2 statistic to measure the probability that the flux histogram for a specific model with a specific set of parameters is the same flux histogram as the data. They found that the single power law model fits the number counts best. Weiß et al. (2009) tested the variation of number counts across the field, which is the first time that this had been performed. They found that there is some clustering in the field. Weiß et al. (2009) also found that there is an under density of submm galaxies in the field, and that the submm cosmic background light is dominated by star forming galaxies.

Scott et al. (2010b) used a similar method to perform P(D) analysis on 1.1 mm data of the GOODS South observed using the AzTEC camera, when it was a guest instrument on the Atacama submillimetre Telescope Experiment. They used a two parameter Schechter model for the number count model and created simulated images using this model. They compared the pixel flux histogram of the simulated images with the pixel flux histogram of the observed image. They used maximum likelihood to find the best fit model. Scott et al. (2010b) also investigated how important the choice of model is. They used a power law to model the number counts, and found that they got different results. They concluded that the model must be a good estimate of the data. Using their results from the P(D) analysis, Scott et al. (2010b) stated that $\sim 26\%$ of sources in the GOODS South observed by AzTEC are in fact blended sources. Blended sources will increase the number of bright sources in the number counts.

Patanchon et al. (2009) performed P(D) analysis on 250, 350 and 500 μm data of the GOODS South field observed by Balloon-borne Large Aperture submillimetre Telescope (BLAST). Instead of creating simulated images from a model of the number counts, they used a probability distribution function (pdf). Their pdf was a non-physical parametric model. The pdf for the flux of the pixels in the image is a convolution of the pdf for each flux interval in the image. When using a pdf, the P(D) is calculated in Fourier Space and a likelihood test is used to examine how similar the flux histogram created by the pdf is to the flux histogram of the data. Patanchon et

al. (2009) stated that using P(D) analysis, they predict a break in the faint end number count slope at ~ 0.015 Jy, where the steep slope changes to a shallower slope.

Glenn et al. (2010) also used a pdf when performing P(D) analysis on Herschel/SPIRE 250, 350 and 500 μm number counts. For this work they used data from three of the five science demonstration phase survey areas, GOODS North, Lockman-North and Lockman-SWIRE. They used the same method as described in Patanchon et al. (2009), but used the χ^2 statistic as a 'goodness of fit' between their model and the pixel flux histogram. Similar to Oliver et al. (1997), Glenn et al. (2010) stated that the faint end number count slope is steeper than predicted by number count models. They also found a break in the number counts, similar to Patanchon et al. (2009).

Glenn et al. (2010) stated that when performing P(D) analysis, the best way to compare a model with the observed data is to directly compare the histogram of the pixel flux of the edited model with the pixel flux histogram of the data. By varying only one parameter of the faint end slope of the model, hence avoiding degeneracies between parameters, this thesis will present work using direct comparison between flux histograms.

4.3 Performing P(D) Analysis

P(D) analysis was performed on both the S11 and L15 IRAC Dark Field number counts. The phenomenological backward evolution galaxy number count model of (Pearson, 2005), discussed in Section 3.9.1, is the number count model used in the P(D) analysis. This model was found to fit the AKARI IRAC Dark Field 11 and 15 μm number counts. Figure 4.1 shows the graph of the L15 number count model and the L15 IRAC Dark Field counts. See Figure 3.22 for the S11 IRAC Dark Field counts and the 11 μm Pearson model.

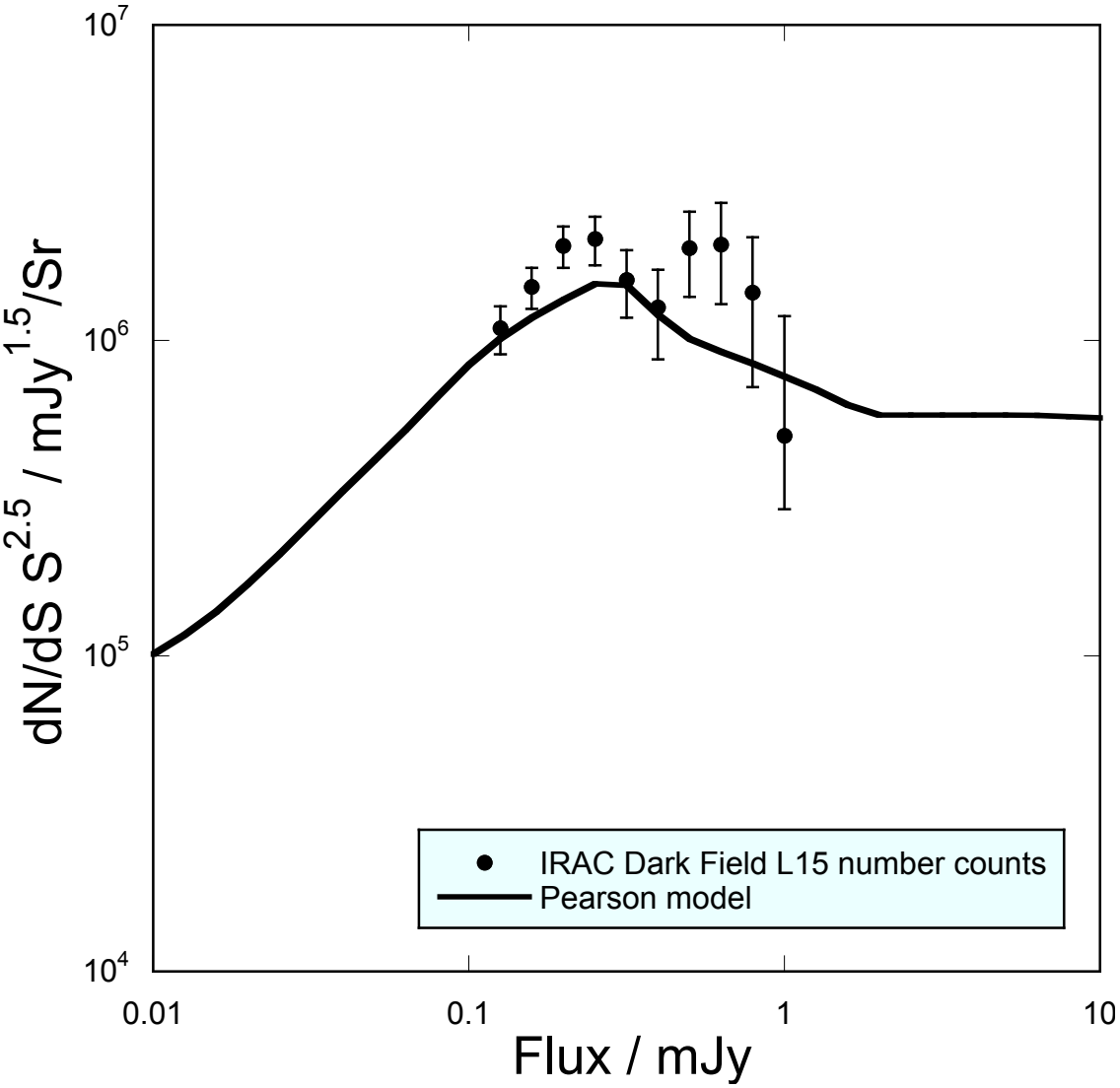

Figure 4.1: A graph showing IRAC Dark Field number counts, shown as circles, and the number count model, shown as the solid line. The L15 filter is given as an example, see Figure 3.22 for a comparison between the Pearson model and S11 IRAC Dark Field number counts.

4.3.1 Method

The first step in the P(D) analysis is to create a flux histogram of the mosaicked image. Figure 4.2 shows an example flux histogram. This specific flux histogram is of the L15 mosaicked image, a similar histogram was created for the S11 mosaicked image. This flux histogram will be compared with the simulated flux histograms in a later step.

The second step is to perturb the faint end slope of the number count model. This corresponds to fluxes fainter than the faintest flux in the number counts. This perturbation is a power law scaling of the faint end slope, given by Equation 4.1, where M' is the scaled differential number count model, M is the original differential model, S_0 is the flux of the differential number count model where the faint end slope joins onto the non-scaled part of the model, S is flux and α is a power. α took the values: $0.8, 1.0, 1.2, 1.4, 1.6, 1.8$.

$$M' = \left(\left[\frac{S}{S_0} \right]^{\alpha} \right) M_0 \tag{4.1}$$

Figure 4.3 shows the increase and decrease to the faint end slope. Again the 15 μm model is shown as an example, the same scaling was used on the 11 μm model. This method has only investigated the simplest alteration to the model, i.e. only a first order scaling has been performed to the faint end of the Pearson model. The model was 'tweaked' by a first order scaling; where $\alpha = 1.0$ is the un-perturbaited model. If the results show that α is greatly different to 1.0, then this would suggest that the model may be incorrect, or that the scaling needs to be of a higher order. An initial test of the P(D) analysis using far fewer simulated images, suggested that $0.8 < \alpha < 2.0$, thus this range of α was chosen for the P(D) analysis work.

The third step is to create a background image into which the the fake sources are injected. The background image was created using the coadded noise image made during the coadding stage, from the empirical noise image associated with each individual frame. This coadded noise image was multiplied by a random Gaussian image to create a noise fluctuation image. The noise fluctuation image was used as the background

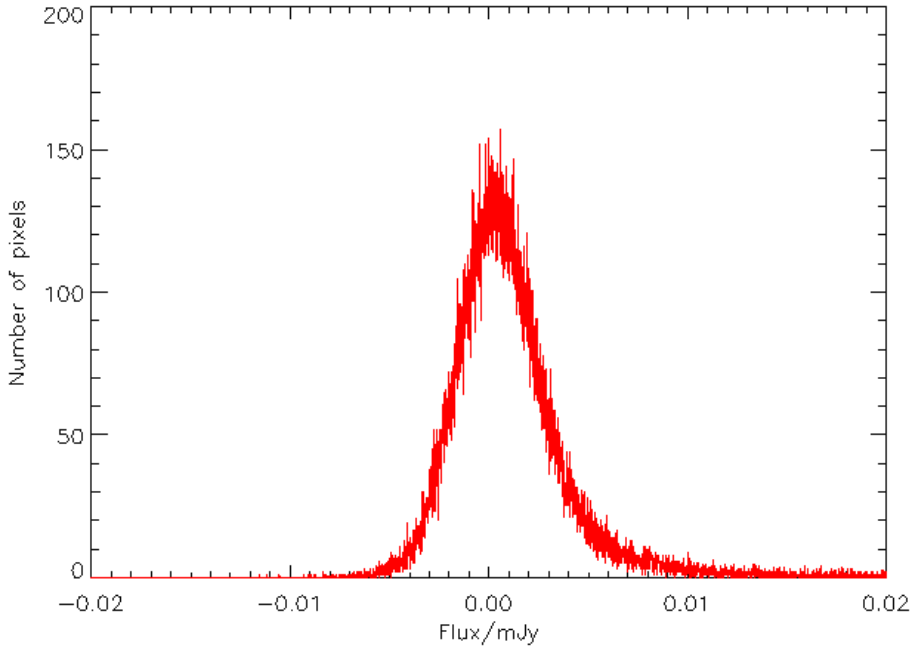

Figure 4.2: A flux histogram for an IRAC Dark Field mosaicked image. The L15 filter is given as an example.

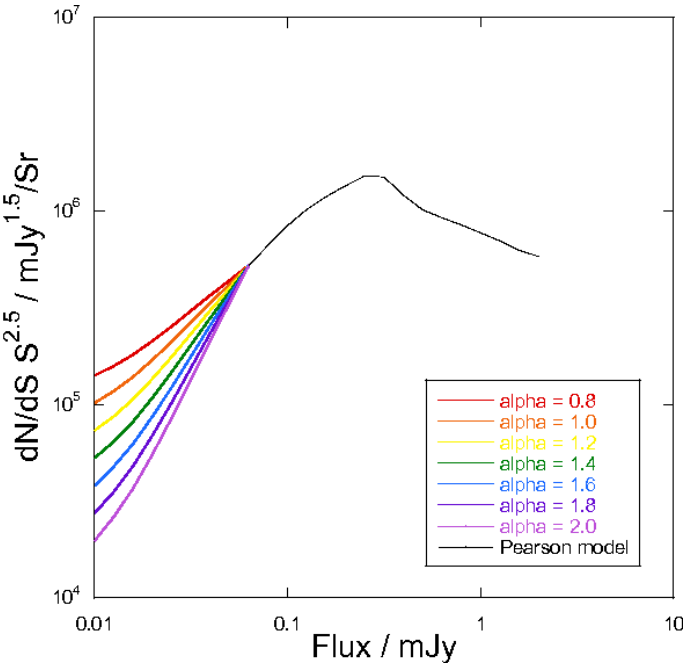

Figure 4.3: A graph showing the perturbations to the faint end number count slope of the model. The black line shows the Pearson model, and the multi-coloured lines show the faint end perturbations calculated using Equation 4.1. The 15 μm Pearson model is given as an example.

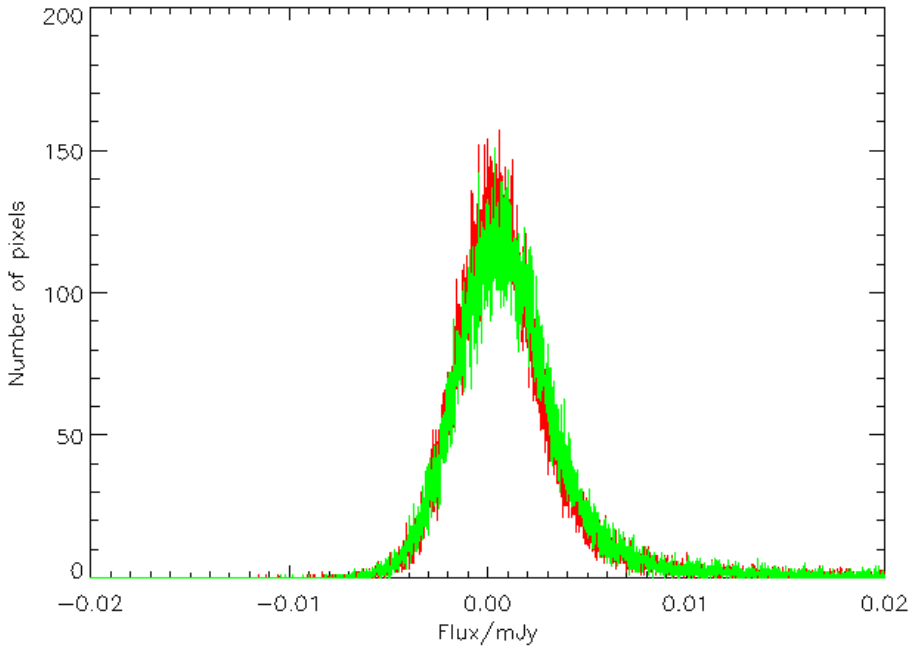

Figure 4.4: A graph showing the flux histogram for an IRAC Dark Field mosaicked image in red, and the flux histogram for a simulated image with fake sources injected into it in green. Again the L15 filter is shown as an example.

image.

The fourth step is to inject fake point sources into the background image. This is done by counting the number of galaxies predicted by the perturbed number count model, for each flux bin, where the flux bin width is the same width as in the original number counts. The number of galaxies predicted by the model in each flux bin are then injected into the background image. The fake point sources were injected into random locations in the image. The fake sources were not given the flux of the centre of each flux bin, which was done for testing for completeness. The flux of each source was a random value between the maximum and minimum of the flux bin.

Step five is to create a flux histogram of the simulated image, with the fake sources injected into it. Figure 4.4 shows the flux histogram of a simulated image compared with the flux histogram of the mosaicked image. Again the L15 filter flux histograms of the mosaicked and simulated images are shown as an example. The same was performed for the S11 filter. For the work of this analysis, steps four and five are repeated 100 times for each perturbation of the number count model.

Initially an analytical fake source, created using a Gaussian point spread function (PSF) was injected into the background image. Using this method, the fake source in the simulated image did not greatly resemble those in the mosaicked image. A fake source with an empirical PSF was used instead. The empirical PSF was created by stacking the positions of point sources in the mosaicked image. The brightest 10% of the point sources were not included in the stack, because they were possibly extended. The brightest sources in the mosaicked S11 and L15 AKARI images appear to be extended sources, and not point sources. As described above, the fake sources injected into the simulated images are all point sources, see Figure 4.5 for an example of part of two simulated images and the real image. This difference may cause the bright end of the simulated pixel flux histogram to be greater than that of the mosaicked image histogram. This is due to the fact that the flux from the extended sources is spread over a greater area, and hence the individual pixels will not be as bright. An improvement to the P(D) analysis method would be to create an extended PSF for the brightest sources, and use this PSF when injecting bright sources into the simulated images.

Comparison of ~ 50 simulations at both L15 and S11 was made with the observed data, for all α values. Both S11 and L15 observations showed residual Earthshine features present as faint large-scale structure. This was removed by convolving both observations and simulations with a large-scale-structure-removing kernel: a narrow positive Gaussian ($\sigma = 1.76$ pixels) plus a broad negative Gaussian ($\sigma = 2.82$ pixels), with a net total of zero. Such kernels effectively remove large scale structure (e.g. Vio et al. (2002)).[1] Both S11 and L15 simulations had more negative pixels than the observations, due to the morphologies of the local galaxies. To avoid excessive $P(D)$ dependence on a few local resolved galaxies, the $P(D)$ constraints were taken from the positive $\sim 0-4\sigma$ pixels only. A mean simulated $P(D)$ was calculated for each α. The χ^2 statistic is misleading because the numbers in each bin are not statistically independent, so a different figure of merit was used: $\Sigma(\log(N_{\rm bin}) - \log(\bar{N}_{\rm simulation}))$, with the confidence of rejecting a model based on the distribution of $\Sigma(\log(N_{\rm simulation}) -$

[1] S.Serjeant performed this step and corrected a bug in the Monte Carlo code.

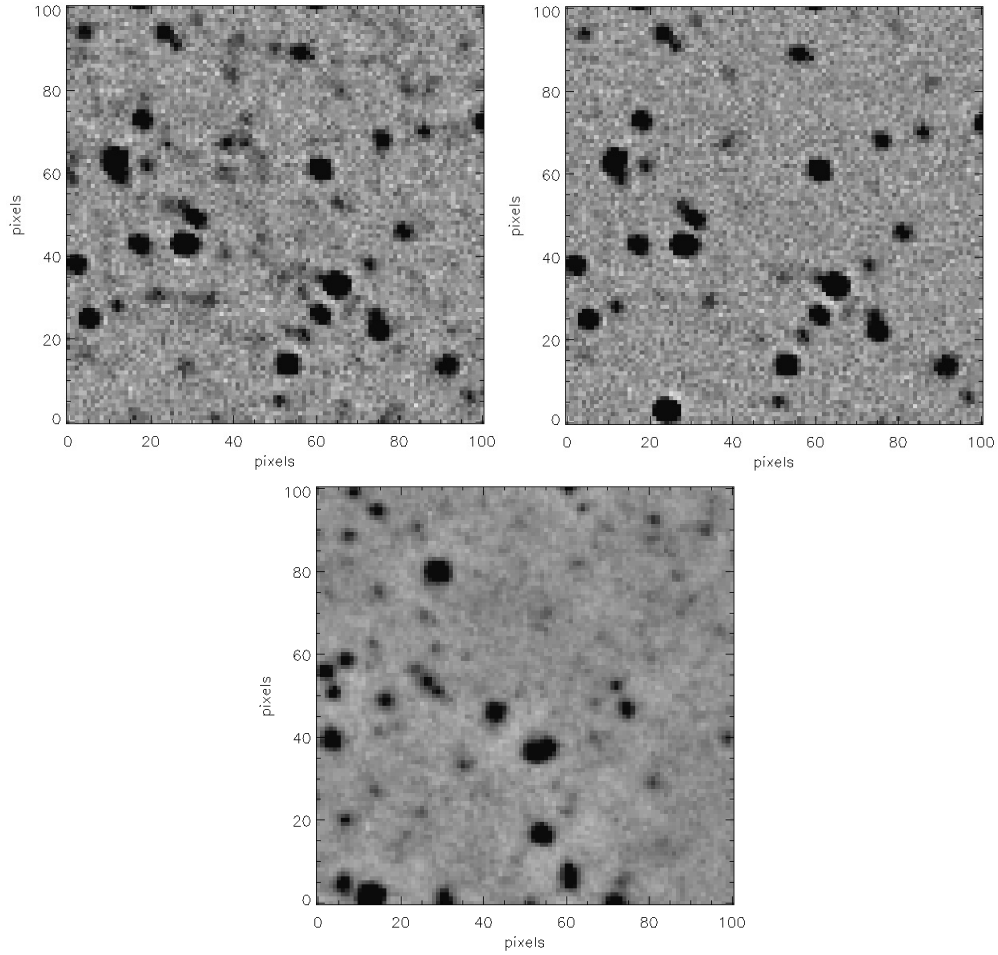

Figure 4.5: The image on the upper left shows part of a simulated image, created using the smallest value for α, the image on the upper right shows part of a simulated image, created using the largest value for α and the image at the bottom shows part of the 11 μm IRAC Dark Field mosaicked image. All images are before being convolved with a large-scale-structure-removing kernel.

$\log(\bar{N}_{\rm simulation})$).

4.3.2 Results from the P(D) Analysis

The results of performing P(D) analysis on the IRAC Dark Field S11 and L15 number counts are shown in Figures 4.6 and 4.7. At 11μm, the model is excluded at 1σ, but not at the 2σ level, thus the model cannot be excluded, see Figure 4.6. At 15μm, all faint end 'tweaks' are excluded at $< 2\sigma$ significance, to our surprise, see Figure 4.7. This is not due to large scale structure: Figure 4.5 shows the two most extreme models and the 15μm observations; the latter has more small scale structure than the models.

From Figure 4.6 and 4.7, the results show that the Pearson model is not ruled out for the 11 μm number counts, but the model is not consistent with the 15 μm number counts. The AKARI 15 μm number counts of Abell 2218 by Hopwood et al. (2010), also plotted in Figure 4.7, are inconsistent with the results of the P(D) analysis. This may be due to cosmic variance in the small high-magnification region probed by the Hopwood et al. (2010) survey. The Spitzer/IRS number counts are within the lower limit of the 15 μm P(D) analysis.

As can be seen in Figure 4.7, the 15 μm P(D) analysis shows that there are more galaxies at fainter fluxes than predicted by the Pearson model. Although this is not ruled out in the 11 μm P(D) analysis, it is not strongly evident. As can be seen in Figure 3.23 the largest component of the Pearson model at 15 μm fainter fluxes is that of star forming galaxies. The 15 μm P(D) analysis suggests that the Pearson model under predicts faint star forming galaxy evolution. In the 11 μm Pearson model, the star forming galaxies component is not quite as large at fainter fluxes, see Figure 3.22. Thus if this component of the model was incorrect, then it would not effect the total model to such a large extent.

The 15 μm P(D) analysis shows that the SISSA model may be in better agreement with the observed data, than the Pearson model. The 15 μm SISSA model is plotted with the 15 μm Pearson model in Figure 3.23. This figure shows that the SISSA model predicts a greater number of fainter galaxies than the Pearson model, which is in agreement with the 15 μm P(D) analysis.

4.4 Conclusions of P(D) Analysis

This chapter presents the method used to perform P(D) analysis on the 11 and 15 μm AKARI IRAC Dark Field images. A discussion on the processing of these images is given in Chapter 3.

The results of the P(D) analysis show that the Pearson model is ruled out at the 1 σ significance level at 11 μm, but not at the 2 σ significance. Thus the Pearson model

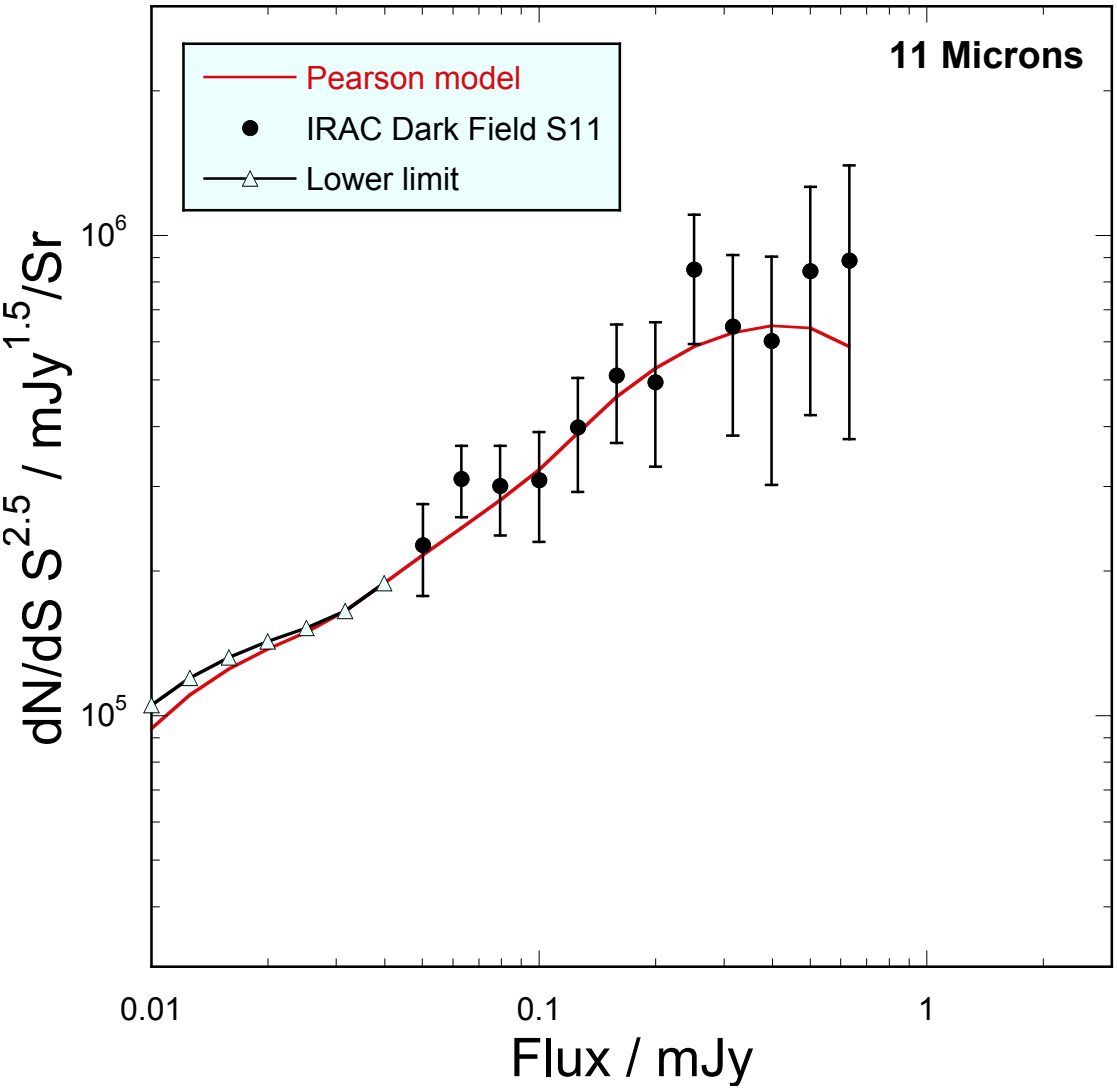

Figure 4.6: Figure showing the results of the 11 μm P(D) fluctuation analysis. The black line with the upward triangles shows the lower limits for the results of the P(D) analysis, the red line is the Pearson model (Pearson, 2005) and the AKARI 11 μm IRAC Dark Field number counts are shown as black circles.

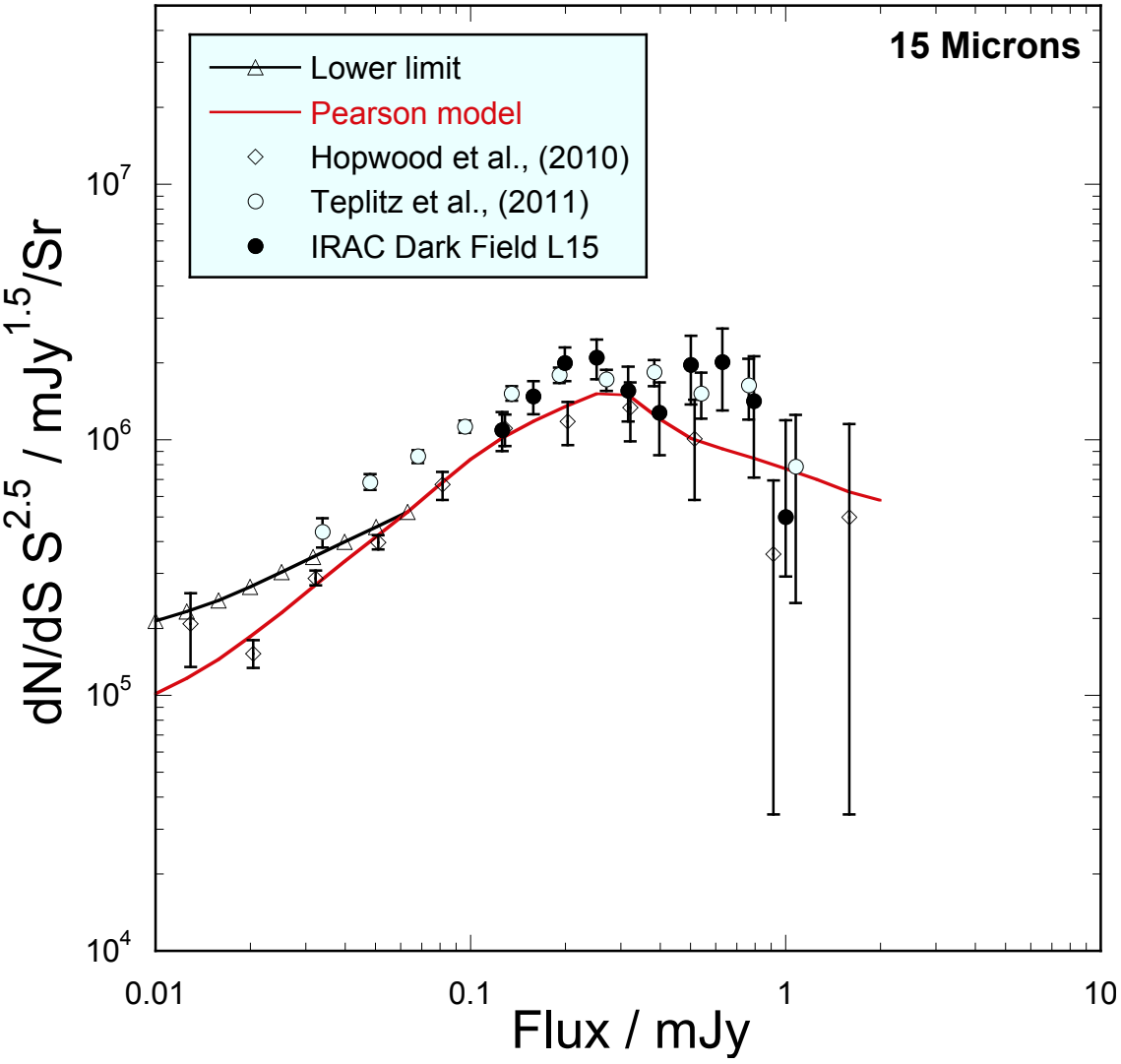

Figure 4.7: Figure showing the results of the 15 μm P(D) fluctuation analysis. The black line with the upward triangles shows the lower limits for the results of the P(D) analysis, the red line is the Pearson model (Pearson, 2005), the AKARI 15 μm IRAC Dark Field number counts are shown as black circles, the AKARI 15 μm Abell 2218 number counts of Hopwood et al. (2010) are shown as open diamonds and the Spitzer/IRS 16 μm number counts of Teplitz et al. (2011) are shown as open circles.

cannot be excluded at 11 μm. The Pearson model is excluded at the 2 σ significance at 15 μm. A possible reason why the Pearson model does not fit the 15 μm P(D) analysis, is that the evolution of star forming galaxies is under predicted. The SISSA model fits the P(D) analysis results better then the Pearson model.

Discussed in Chapter 3, there is tension in the 16 and 15 μm number counts results of Teplitz et al. (2011) and Hopwood et al. (2010), respectively. The number counts of this work do not go deep enough to resolve this tension. The P(D) analysis work of this chapter is in agreement with the number counts of Teplitz et al. (2011)

Chapter 5

Spectral Energy Distributions of Infrared-Selected Galaxies in the ELAIS-N1 and IRAC Dark Field

Spectrum is red

Captain Scarlet - Gerry Anderson

5.1 Introduction

Most galaxies are observed by AKARI as point sources, but their intrinsic properties nevertheless can be modelled. To do this the galaxy is required to have been observed over a large wavelength range. In a rest frame wavelength of a galaxy, the far-infrared emission peaks at $\sim 100\,\mu$m. This is due to dust contained within Giant Molecular Clouds (GMC) absorbing UV photons from OB association stars, and dust within the Interstellar Medium (ISM) absorbing ambient starlight, both of which re-radiate this thermally in the infrared. The spectra of Active Galactic Nuclei (AGN) have a peak at $\sim 10\,\mu$m, due to thermal emission from the torus. Galaxies with low dust obscuration will have observable starlight emission in the optical, and emission from young OB associations in the UV. By modelling spectral energy distributions (SEDs) the intrin-

sic properties of a galaxy can be modelled. This includes star formation rate, spatial distribution of stars and dust, and dust opacity (Noll et al. (2009) and Popescu & Tuffs (2009)). By fitting SED templates or models to the observed multi-wavelength galaxy data, the above properties of the galaxies can be explored. A photometric redshift estimate can also be determined from the 'best fit' SED model (Farrah et al. (2003) and Ilbert et al. (2009)).

Section 5.2 discusses the ancillary multi-wavelength data sets combined with the AKARI data, in ELAIS-N1 and the IRAC Dark Field. A summary of the cross-matching between the ancillary data and the AKARI data is given in Section 5.3. Section 5.4 gives a description of how the SED fitting was performed using LePhare. Section 5.5 presents the colour-colour diagrams using the band-merged catalogues.

5.2 Ancillary Multi-Wavelength Data Sets

5.2.1 ELAIS North 1

The ELAIS-N1 survey area and a brief summary of the multi-wavelength coverage is discussed in Section 3.4.1. There exists a comprehensive band-merged catalogue of ELAIS-N1 sources as part of the Spitzer Data Fusion (Vaccari et al. (2010), Marchetti et al. (2016) and Vaccari (2016)). This band-merged catalogue of the ELAIS-N1 deep field is one of eight multi-wavelength catalogues which make up the Spitzer Data Fusion. The eight catalogues are six of the Spitzer Wide-area InfraRed Extragalactic (SWIRE) survey fields (ELAIS-S1, XMM-LSS, CDF-S, Lockman hole, ELAIS-N1 and ELAIS-N2) (Lonsdale et al., 2003), the Boötes Field and the Extragalactic First Look Survey (XFLS) field. Table 5.1 gives the 27-bands in the Spitzer Data Fusion ELAIS-N1 merged catalogue. The Spitzer Data Fusion ELAIS-N1 catalogue contains two bands from the UV space telescope, Galaxy Evolution Explorer (GALEX). Data are from the FUV (1538.62 Å) and the NUV (2315.66 Å) (Martin et al., 2005). The data are from the all sky survey, which GALEX observed between June 2003 and April

2008. The data in the Spitzer Data Fusion catalogue were from the GR 6 + 7 data release (Bianchi et al., 2014).

The Spitzer Data Fusion ELAIS-N1 catalogue contains two sets of optical data both with u, g, r, i and z-band data. The deepest data set of these two is data taken with the Wide Field Camera on the Isaac Newton Telescope (INT) at the Observatoris del Roque de Los Machachos, La Palma. The observations, data reduction and band merging are discussed in González-Solares et al. (2011). The data were processed using the Cambridge Astronomical Survey Unit (CASU) (Irwin & Lewis, 2001). The source extraction was also performed using CASU. González-Solares et al. (2011) created a 5-band merged catalogue, using a 1.2 arcsec search radius; where multiple matches occurred, they used the nearest neighbour. The other optical data in the Spitzer Data Fusion ELAIS-N1 are from the Sloan Digital Sky Survey (SDSS) (Stoughton et al., 2002). The SDSS uses a dedicated 2.5 m telescope at Apache Point Observatory (APO), New Mexico. The data are initially processed at the APO, and then transferred to Fermilab, where further data reduction are performed. The Spitzer Data Fusion catalogues contain SDSS data release 12.

The Spitzer Data Fusion ELAIS-N1 also contains two sets of near-infrared data in the J, H and K-bands. One set of near-infrared data are from the UKIRT Infrared Deep Sky Survey (UKIDSS), observed by the Wide Field Camera on the UK Infrared Telescope (UKIRT) at the Mauna Kea Observatory, Hawaii (Lawrence et al., 2007). The data for the Spitzer Data Fusion catalogue are from the WFCAM Science Archive (WSA) DR10 data release. The other near-infrared data are from 2MASS (Skrutskie et al., 2006).

The Spitzer Data Fusion catalogues were created to cross match Spitzer Data with follow up observations and ancillary data. The Spitzer Data Fusion ELAIS-N1 contains deep Spitzer/IRAC 3.6 and 4.5 μm data. This data are from the Spitzer Extragalactic Representative Volume Survey (SERVS), taken during Spitzer's post cryogenic phase (Mauduit et al., 2012). The observations for the SERVS ELAIS-N1 took place from 28 July 2009 to 05 August 2009 and have a total observing time of 153.4 hours. The

data were initially processed by the Spitzer Science Centre (SSC), and then processed by a pipeline written for processing SWIRE data. Source extraction were performed on the SERVS data using SExtactor (Mauduit et al., 2012).

The Spitzer/IRAC 3.6, 4.5, 5.8 and 8.0 μm data and Spitzer/MIPS 24, 70 and 160 μm data included in the Data Fusion ELAIS-N1 catalogue are from the SWIRE survey. The IRAC ELAIS-N1 data were observed from 14 January 2004 to 20 January 2004, and the ELAIS-N1 MIPS data were observed 21 January 2004 to 29 January 2004. Both the IRAC and the MIPS data were initially processed by the standard data reduction at SSC and then through a data reduction pipeline created for the SWIRE data. Source extraction were performed on the IRAC data and the MIPS 24 μm data using SExtractor. For the MIPS 70 μm data source extraction were performed using Mosaicker and Point Source Extractor (MOPEX), also at the SSC (Surace et al., 2005). The source extraction for MIPS 160 μm was performed using APEX (Vaccari, 2016).

The Spitzer Data Fusion ELAIS-N1 contains some spectroscopic redshifts and many photometric redshifts. The spectroscopic redshifts are from NASA/IPAC Extragalactic Database (NED). The photometric redshifts are from SDSS data release 12 and from SWIRE fields photometric data release (Rowan-Robinson et al. (2013) and Rowan-Robinson et al. (2008a)). The SWIRE fields photometry used the SWIRE sources with their optical and near-infrared counterparts. SED templates used for the photo-z are a version of empirical templates created by Yoshii & Takahara (1988) and Calzetti & Kinney (1992). These modified templates are of optical, AGN and starburst galaxies (Rowan-Robinson et al., 2008b).

For the work in this thesis, it was advised (Vaccari, priv. comm.) that the order to select a redshift for a matched source, was the NED spectroscopy, then the SDSS photometry and finally the photometry of Rowan-Robinson et al. (2013) and Rowan-Robinson et al. (2008a).

ELAIS-N1 was observed as part of the Herschel Multi-tieried Extragalactic Survey (HerMES) (Oliver et al., 2012). The HerMES observations were carried out between 12 September 2009 and 25 October 2009. ELAIS-N1 was observed in parallel mode,

i.e. the field was observed by both Spectral and Photometric Imaging Receiver (SPIRE) and Photodetector Array Camera and Spectrograph (PACS), with a total observing time of $\sim$ 50 hours. The SPIRE data, including source catalogues for ELAIS-N1 are publicly available at the Herschel database at Marseille (HeDaM). These catalogues used Spitzer/MIPS 24 μm positions as a prior to detect the Herschel sources, using the methodology of Roseboom et al. (2010) and Roseboom et al. (2012). There are currently no publicly available PACS source catalogues. The PACS individually coadded pointings are available from the Herschel archive.

Vaccari (2016) gives details about how the Spitzer Data Fusion band-merged catalogues were created. The first data to be merged were the IRAC 3.6 and 4.5 μm SWIRE single-band catalogues. The two catalogues were cross-matched using a search radius of 1 arcsec. Cross-matched source positions were calculated as an average of the 3.6 and 4.5 μm positions. This two-band catalogue was then cross-matched with the SWIRE 5.8 and 8.0 μm catalogues, using a 1.5 arcsec search radius. Then the MIPS 24 μm catalogue was cross-matched, using a search radius of 3 arcsec. The 70 and 160 μm single-band catalogues were then cross-matched with the merged 24 μm catalogue. A 6 arcsec search radius was used to cross-match MIPS 70 μm, and the MIPS 160 μm catalogue was cross-matched with a 6 arcsec search radius.

The IRAC 3.6 and 4.5 μm SERVS two single-band catalogues were cross matched with a 1 arcsec search radius. The 2-band catalogue was then cross-matched with the 7-band Spitzer SWIRE catalogue, using a 1 arcsec search radius. Then finally all the other ancillary data, GALEX, SDSS, INT, 2MASS and UKIDSS were cross-matched using a 1 arcsec search radius to create the 27-band merged Spitzer Data Fusion ELIAS-N1 catalogue.

5.2.2 IRAC Dark Field

The AKARI IRAC Dark Field galaxy catalogues have been cross-matched with the multi-wavelength catalogue created by Krick et al. (2009). The IRAC Dark Field sur-

Table 5.1: Spitzer Data Fusion multi-wavelength catalogue.

Wavelength	Telescope	Reference
153.862nm	GALEX/FUV	Martin et al. (2005)
231.566	GALEX/NUV	Martin et al. (2005)
354.3nm (u-band)	SDSS	Stoughton et al. (2002)
364.0nm (u-band)	INT	González-Solares et al. (2011)
477.0nm (g-band)	SDSS	Stoughton et al. (2002)
484.6nm (g-band)	INT	González-Solares et al. (2011)
623.1nm (r-band)	SDSS	Stoughton et al. (2002)
624.0nm (r-band)	INT	González-Solares et al. (2011)
762.5nm (i-band)	SDSS	Stoughton et al. (2002)
774.3nm (i-band)	INT	González-Solares et al. (2011)
876.3nm (z-band)	INT	González-Solares et al. (2011)
913.4nm (z-band)	SDSS	Stoughton et al. (2002)
1.17μm (J-band)	UKIRT	Lawrence et al. (2007)
1.24μm (J-band)	2MASS	Skrutskie et al. (2006)
1.49μm (H-band)	UKIRT	Lawrence et al. (2007)
1.66μm (H-band)	2MASS	Skrutskie et al. (2006)
2.03μm (K-band)	UKIRT	Lawrence et al. (2007)
2.16μm (K-band)	2MASS	Skrutskie et al. (2006)
3.6μm (SERVS)	Spitzer/IRAC	Mauduit et al. (2012)
3.6μm (SWIRE)	Spitzer/IRAC	Lonsdale et al. (2003)
4.5μm (SERVS)	Spitzer/IRAC	Mauduit et al. (2012)
4.5μm (SWIRE)	Spitzer/IRAC	Lonsdale et al. (2003)
5.8μm (SWIRE)	Spitzer/IRAC	Lonsdale et al. (2003)
8.0μm (SWIRE)	Spitzer/IRAC	Lonsdale et al. (2003)
24μm	Spitzer/MIPS	Surace et al. (2005)
70μm	Spitzer/MIPS	Surace et al. (2005)
160μm	Spitzer/MIPS	Surace et al. (2005)

Table 5.2: Herschel/SPIRE multi-wavelength catalogue.

Wavelength	Telescope	Reference
24μm	Spitzer/MIPS	Surace et al. (2005)
250μm	Herschel Space Telescope	Oliver et al. (2012)
350μm	Herschel Space Telescope	Oliver et al. (2012)
500μm	Herschel Space Telescope	Oliver et al. (2012)

vey area is discussed in Section 3.3.1. Section 3.3.1 also gives a brief summary of the multi-wavelength data in the IRAC Dark Field. The work of Krick et al. (2009) describes how the Spitzer data were processed and cross-matched with publicly available data sets of the survey area. The multi-wavelength data set is shown in Table 5.3.

The Multi-wavelength data had optical data from Palomar/Hale LFC, HST/ACS and MMT/Megacam. The optical wavelengths observed by the Large Format Camera (LFC) are in the u (350 nm), g (470 nm), r (630 nm) and i (770 nm) bands. The LFC is on the Hale telescope at Palomer (Simcoe et al., 2000). The observation dates were 22 July 2004 to 24 July 2004 and 08 August 2004 to 10 August 2004. The total exposure time for the four bands was 6.0 (u-band), 6.2 (g-band), 4.1 (r-band) and 4.7 (i-band) hours per pixel. The data reduction were performed using IRAF procedures. The source extraction was performed using SExtractor. Longer wavelength optical data were observed by the Wide Field Camera, part of the Advanced Camera for Surveys (ACS) on board the Hubble Space Telescope (HST), at 814 nm (Lucas et al , 2016). This data were observed between 28 November 2006 and 07 December 2006, with a total observing time of 1.4 hours per pixel. The data were reduced using the standard ACS pipeline CALARS, and SExtractor was used for source extraction. The z-band (911 nm) was observed by the Megacam camera on the Multiple Mirror Telescope (MMT) at Whipple Observatory (McLeod et al., 2015). The observations were performed 01 June 2007 to 04 June 2007, with a total observation time of 3.6 hours per pixel. The data were reduced on the standard pipeline at the Smithsonian Astrophysical Observatory (SAO) telescope data centre. Source extraction was also performed using SExtractor.

The near-infrared data in the multi-wavelength catalogue were observed by the Wide-field Infrared Camera (WIRC) on the Hale Telescope at Palomar (Wilson et al., 2003) in the J (1.25 μm), H (1.63 μm) and K (2.15 μm) bands. The data were observed 05 May 2006, 15 May 2008 to 18 May 2008, and 27 June 2008 to 28 June 2008. The total observing time was 0.8 (J-band), 0.7 (H-band) and 1.6 (K-band) hours per pixel. The data were reduced using a custom pipeline written in IDL and source extraction was

performed in SExtractor.

Krick et al. (2009) discuss other near-infrared data of the IRAC Dark Field. The J-band has been observed by the Florida Infrared Imaging Multi-Object Spectrograph (FLAMINGOS) imaging camera on the Kitt Peak National Observatory (KPNO) 4 m telescope. The J and H-bands have also been observed by Smithsonian Widefield Infrared Camera (SWIRC) on the MMT (Brown et al., 2008), observed on the 29 to 30 August 2006. This data had not been included in the multi-wavelength catalogue. The FLAMINGOS J-band had less observing time than that of the WIRC J-band, of only 0.5 hours per pixel. For the J and H-band observations with SWIRC, Krick et al. (2009) report that for four of the eight observing nights the observation was performed through thin cirrus and hence the conditions were not photometric. Furthermore on the other four nights, only the J-band was observed.

As stated in Section 3.3.1, the IRAC Dark Field was used for instrumental background calibration for Spitzer/IRAC. As the area was observed every two to three weeks over a five year period, this multi-wavelength catalogue created by Krick et al. (2009), contains very deep IRAC data at 3.6, 4.5, 5.8 and 8.0 μm. The catalogue contains part of the five year survey, with observations from December 2003 to January 2005. The total observing time per filter for the IRAC data are 40 hours, with a median observation time of $\sim 8-10$ hours per pixel. Basic reduction of the data were performed by the basic calibration data pipeline at the SSC and then further reduction was performed using the pipeline written for processing SWIRE data. The source extraction was initially performed using SExtactor. The source catalogue created by SExtractor was then cross-matched with the HST/ACS data. For the sources which were successfully cross-matched, the ACS galaxy shape was used for the aperture. The objects which did not have cross-matches used the standard SExtractor photometry. The Spitzer/MIPS data for the field are not as deep as the IRAC data. The MIPS 24 μm observation had an exposure time of 1 hour per pixel. The data were processed using the BCD pipeline. Source extraction was performed using the IRAF procedure DAOFIND. The MIPS 70 μm data had an exposure time of 1.6 hours per pixel. The data were processed

using the Germanian Preprocessing Tools (GPT) pipeline. The source extraction was performed using MOPEX from the SSC.

The multi-wavelength catalogue from Krick et al. (2009) contained AKARI/IRC sources. These AKARI sources are detected from the same observations as described in Section **??**, but have been processed by the standard AKARI pipeline.

To create the multi-wavelength catalogue, Krick et al. (2009) cross-matched one band at a time. The algorithm used to cross-match the ACS sources with the IRAC sources is discussed above. All the shorter wavelength catalogues were then cross-matched with the ACS/IRAC cross-matched catalogue. Krick et al. (2009) used a search radius for the matches of roughly equal to the band's PSF. Where the band had a very different PSF size, i.e. the MIPS catalogues, a larger PSF was matched with another larger PSF. Thus the MIPS 24 μm catalogue was cross-matched with the IRAC sources, and then the MIPS 70 μm catalogue was cross-matched with the MIPS 24 μm matches.

Krick et al. (2009) mainly use photometric redshifts for the sources in the multi-wavelength catalogue. They state that it would be impractical to obtain spectroscopic redshifts for all 80,000+ sources, as this would require a large amount of telescope time. To calculate the photometric redshifts, they use the Polletta templates, empirical templates created from the SWIRE data (Polletta et al., 2007). They use HYPERZ, a minimum χ^2 fitting program, to perform SED fitting to the u, g, r, i, F814W, z, J, H, K, 3.6 μm, 4.5 μm, 5.8 μm and 8.0 μm data. The photometric redshift of a source is included in the catalogue, if the χ^2 is less than 50.

There exists a small amount of ancillary spectroscopic data for the IRAC Dark Field. Krick et al. (2009) use the spectroscopic redshifts for about 200 sources observed by Carnegie Observatories Spectroscopic Multi-slit and Imaging Camera (COSMIC) on the Hale telescope at Palomar. The spectroscopic data are in the optical ($3500 - 9000$ Å) and was observed over four nights in June 2007. The data reduction were performed in the IRAF procedure BOGUS2006. There also exists prism ($1.7 - 5.5\,\mu$m) and grism ($5.5 - 8.3$ and $17.7 - 25.0\,\mu$m) spectroscopy observed by AKARI/IRC (PI Egami). The data were observed 06 October 2006, 15 October 2006, 02 November

Table 5.3: Krick et al. (2009) multi-wavelength data catalogue.

Wavelength	Telescope	Reference
358.0nm (u-band)	Hale Telescope	Simcoe et al. (2000)
475.4nm (g-band)	Hale Telescope	Simcoe et al. (2000)
620.4nm (r-band)	Hale Telescope	Simcoe et al. (2000)
630.0nm	HST	Lucas et al (2016)
966.5nm (z-band)	MMT	McLeod et al. (2015)
1.2μm (J-band)	Hale Telescope	Wilson et al. (2003)
1.6μm (H-band)	Hale Telescope	Wilson et al. (2003)
2.2μm (K-band)	Hale Telescope	Wilson et al. (2003)
3.6μm	Spitzer/IRAC	Krick et al. (2009)
4.5μm	Spitzer/IRAC	Krick et al. (2009)
5.8μm	Spitzer/IRAC	Krick et al. (2009)
8.0μm	Spitzer/IRAC	Krick et al. (2009)
11μm	AKARI/IRC	Murakami et al. (2007)
15μm	AKARI/IRC	Murakami et al. (2007)
18μm	AKARI/IRC	Murakami et al. (2007)
24μm	Spitzer/MIPS	Krick et al. (2009)
70μm	Spitzer/MIPS	Krick et al. (2009)

2006, 23 April 2007 to 30 April 2007 and 08 May 2007 to 11 May 2007. This data are part of the same survey as the imaging AKARI/IRC IRAC Dark Field data discussed in this chapter. Krick et al. (2009) do not use the AKARI spectroscopic data for their multi-wavelength catalogue.

Separate to the Krick et al. (2009) multi-wavelength catalogue, there exists Herschel/SPIRE data of the IRAC Dark Field at 250, 350 and 500 μm (Pearson et al., in prep). The creation of this cross-matched galaxy catalogue is discussed in more detail on Section 6.3.1. This data were observed after the compilation of the Krick et al. (2009) catalogue, and hence is not in the catalogue of Krick et al. (2009).

5.3 Creating the ELAIS North 1 and IRAC Dark Field Band-Merged Catalogues

5.3.1 Cross-Matching of the AKARI Galaxy Catalogues

The software TOPCAT (Taylor, 2005) was used to cross-match the AKARI catalogues with the existing band-merged catalogues. The first step in the cross-matching was to merge the four single-band AKARI galaxy catalogues, the N4, S11, L15 and L18W. A 4 arcsec search radius was used to cross-match both the ELAIS-N1 and IRAC Dark Field AKARI catalogues. It is commonplace to use a search radius equal to the full width half maximum (FWHM). In the AKARI filters used in ELAIS-N1 and IRAC Dark Field, the FWHM goes from 2.0 arcsec (N4) to 5.4 arcsec (L18W). A 4 arcsec search radius was also used for testing for the completeness when performing the number count work. A 4 arcsec search radius for the injected fake source always found only the one (or no) source. The cross-matching was performed simultaneously across all four bands. Within the search radius the nearest neighbour was selected. All of the S11, L15 and L18W sources were included in the band-merged catalogue. Only N4 sources which had a match in at least one of the other bands, were included in the catalogue. This is because this work is focusing on the mid-infrared bands, which have not been covered at any great depth by Spitzer, e.g., S11, L15 and L18W.

The galaxy position in the cross-matched AKARI catalogues was taken as the position of the shortest wavelength cross-match, i.e. N4, then S11, then L15 and then L18W. The shortest wavelength was chosen because it had the smallest FWHM. This galaxy position was used when cross-matching with the ancillary catalogues. Because the AKARI cross-matched catalogue contains 4 μm data, the IRAC 4.5 μm detection has not been included in the final matched catalogue.

5.3.2 Cross-Matching of the ELAIS North 1 Galaxy Catalogues

The AKARI ELAIS-N1 4-band merged catalogue was cross-matched with two separate band-merged catalogues, the Spitzer Data Fusion ELAIS-N1 27-band merged catalogue, covering the wavelength range UV to MIPS 160 μm (Vaccari, 2016) and the Herschel/SPIRE 4-band merged catalogue (Oliver et al., 2012). Section 5.2.1 gives further details about the wavelengths used and how the two ancillary catalogues were created. Table 5.1 shows the multi-wavelength data in the Spitzer Data Fusion ELAIS-N1 catalogue and Table 5.2 shows the multi-wavelength data in the Herschel/SPIRE catalogue.

The AKARI galaxy positions were cross-matched with the SERVS galaxy positions in the Spitzer Data Fusion catalogue. The SERVS catalogue contains the Spitzer/IRAC galaxies from the post cryogenic phase, hence just 3.6 and 4.5 μm data. The Spitzer Data Fusion ELAIS-N1 catalogue contains two sets of optical bands, u, g, r, i and z (SDSS and INT) and two sets of sources in the near-infrared J, H and K-bands (2MASS and UKIDSS). Marchetti (priv. comm.) recommends using the INT for the optical bands, and UKIDSS for the near-infrared bands. The data from the INT are about a magnitude deeper than the data from SDSS (Surace et al., 2005). When performing the cross-matching, the wavelength closest to the SERVS wavelength was chosen, e.g. the N4 galaxy position was used. For sources with no N4 galaxy position, the S11 position was used, if no S11 detection then the L15 position was used, and for no L15 detection the L18W position was used. The cross-matching was performed using a 3 arcsec search radius. For the flux of the source in the IRAC band and MIPS 24 μm Vaccari (2016) recommends using aper2. This corresponds to an aperture radius of 1.9 arcsec for all of the IRAC detections, and a radius of 5.25 arcsec for the MIPS 24 μm sources. Figure 5.1 plots the AKARI N4 flux against the IRAC 4.5 μm flux for all the cross-matched sources. Only sources which have both an AKARI and SERVS detection are added to the band-merged catalogue.

As stated in Section 5.2.1, the Herschel/SPIRE ELAIS-N1 catalogue sources were de-

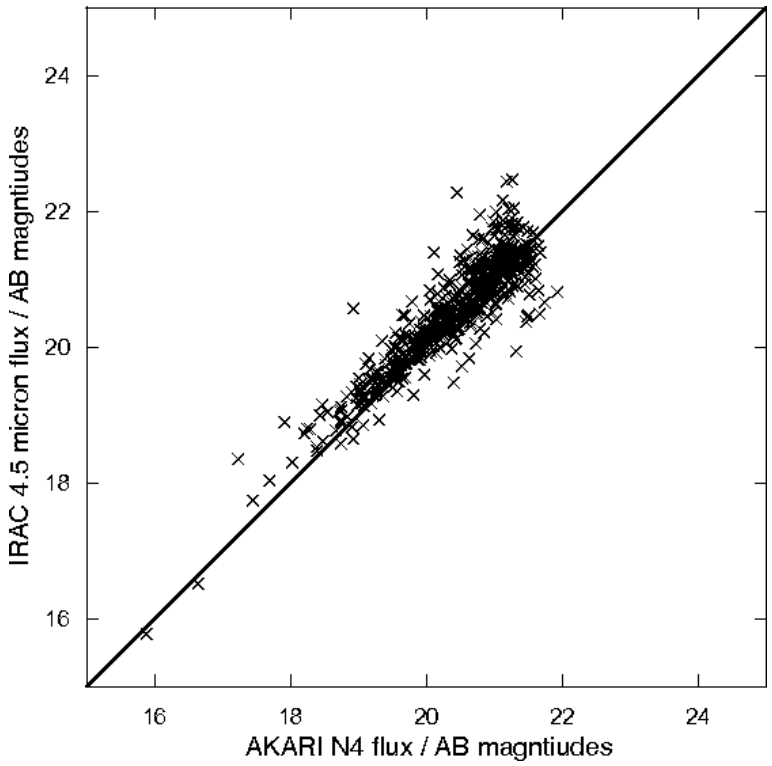

Figure 5.1: Figure plotting the flux of the AKARI N4 sources against the flux of the IRAC 4.5 μm sources for ELAIS-N1 sources, cross-matched with a 3 arcsecond search radius.

tected using MIPS 24 μm positions. This catalogue was chosen over the standard Herschel/SPIRE band-merged catalogue; the SPIRE images have a larger resolution than the AKARI images, hence several AKARI sources could correlate with the one SPIRE source. By using the MIPS 24 μm position, the AKARI source should be matched to the correct SPIRE source.

There are 6% more MIPS 24 μm sources in the band-merged Spitzer Data Fusion catalogue, than in the band-merged Herschel/SPIRE catalogue, thus in the final ELAIS-N1 band-merged catalogue the Spitzer Data Fusion ELAIS-N1 MIPS 24 μm sources are used. No cross-matches were detected between the AKARI galaxy positions and the INT H-band catalogue. Cross-matching the AKARI 4-band catalogue with the SDSS H-band catalogue did not produce any cross-matches either. As recommended by the creators of the Spitzer Data Fusion catalogue, the INT J and K-bands were used. The final ELAIS-N1 23-band matched catalogue contains 191 sources. Table 5.4 gives the 23 wavelengths used in the final matched catalogue.

Table 5.4: ELAIS-N1 band-merged catalogue.

Wavelength	Telescope	Reference
153.862nm	GALEX/FUV	Martin et al. (2005)
231.566	GALEX/NUV	Martin et al. (2005)
364.0nm (u-band)	INT	González-Solares et al. (2011)
484.6nm (g-band)	INT	González-Solares et al. (2011)
624.0nm (r-band)	INT	González-Solares et al. (2011)
774.3nm (i-band)	INT	González-Solares et al. (2011)
876.3nm (z-band)	INT	González-Solares et al. (2011)
1.17μm (J-band)	UKIRT	Lawrence et al. (2007)
1.49μm (H-band)	UKIRT	Lawrence et al. (2007)
2.03μm (K-band)	UKIRT	Lawrence et al. (2007)
3.6μm (SERVS)	Spitzer/IRAC	Mauduit et al. (2012)
4μm	AKARI/IRC	Davidge et al. (in prep)
5.8μm (SWIRE)	Spitzer/IRAC	Lonsdale et al. (2003)
8.0μm (SWIRE)	Spitzer/IRAC	Lonsdale et al. (2003)
11μm	AKARI/IRC	Davidge et al. (in prep)
15μm	AKARI/IRC	Davidge et al. (in prep)
18μm	AKARI/IRC	Davidge et al. (in prep)
24μm	Spitzer/IRAC	Surace et al. (2005)
70μm	Spitzer/IRAC	Surace et al. (2005)
160μm	Spitzer/IRAC	Surace et al. (2005)
250μm	Herschel Space Telescope	Oliver et al. (2012)
350μm	Herschel Space Telescope	Oliver et al. (2012)
500μm	Herschel Space Telescope	Oliver et al. (2012)

5.3.3 Cross-Matching of the IRAC Dark Field Galaxy Catalogues

Similar to the AKARI ELAIS-N1 4-band catalogue, the AKARI IRAC Dark Field 4-band catalogue was also cross-matched with two separate band-merged catalogues. The first band-merged catalogue the AKARI catalogue was cross-matched with, was the 14-band IRAC Dark Field catalogue of Krick et al. (2009), from the u-band to MIPS 70 μm. The second band-merged catalogue the AKARI catalogue was cross-matched with, was the Herschel/SPIRE 3-band catalogue. Section 5.2.2 gives details about the bands in the two merged catalogues and how the catalogues were created.

The AKARI catalogue was cross-matched with the Spitzer/IRAC positions using a 2 arcsec search radius. Originally a 3 arcsec search radius was used. As the IRAC data are very much deeper than the AKARI data, this size of search radius led to many mis-matches. Figure 5.2 plots the N4 flux against the IRAC 4.5 μm flux, for the 2 and 3 arcsec search radius. The 2 arcsec search radius has a much better correlation than using the 3 arcsec search radius.

The same as for the ELAIS-N1 cross-matching, the nearest neighbour within the search radius was selected, and the N4 source position was first cross-matched; if no detection, then the S11 source position was used, and so on, using L15 and finally L18W. Only sources which had both an AKARI detection and a detection in the IRAC Dark Field band-merged catalogue of Krick et al. (2009) were added to the merged catalogue.

The AKARI catalogue was cross-matched with the Herschel/SPIRE catalogue of Pearson et al. (in prep), discussed in Section 6.3.1. The final IRAC Dark Field 21-band catalogue has 243 sources. Table 5.5 gives the 21 wavelengths used in the catalogue.

As mentioned in Section 5.2.2, the multi-wavelength catalogue of Krick et al. (2009) contained AKARI S11, L15 and L18W sources. Compared with the AKARI catalogue of this thesis, the ancillary catalogue only contained 77%, 62% and 72% of the S11, L15 and L18W sources respectively.

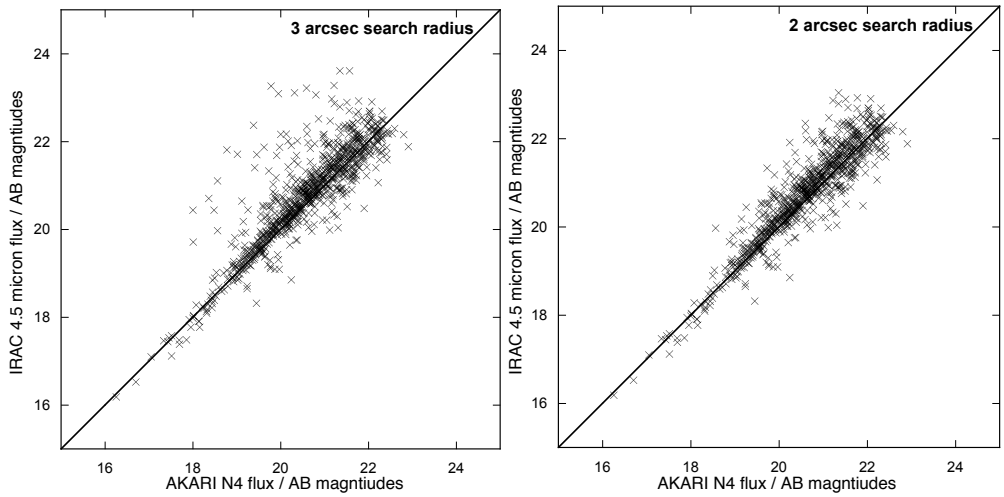

Figure 5.2: Figure plotting the flux of the AKARI N4 sources against the flux of the IRAC 4.5 μm sources for the IRAC Dark Field sources. The figure on the left shows cross-matching with a 3 arcsec search radius, and the figure on the right shows cross-matching with a 2 arcsec search radius.

Table 5.5: IRAC Dark Field band-merged catalogue.

Wavelength	Telescope	Reference
358.0nm (u-band)	Hale Telescope	Simcoe et al. (2000)
475.4nm (g-band)	Hale Telescope	Simcoe et al. (2000)
620.4nm (r-band)	Hale Telescope	Simcoe et al. (2000)
630.0nm	HST	Lucas et al (2016)
966.5nm (z-band)	MMT	McLeod et al. (2015)
1.2μm (J-band)	Hale Telescope	Wilson et al. (2003)
1.6μm (H-band)	Hale Telescope	Wilson et al. (2003)
2.2μm (K-band)	Hale Telescope	Wilson et al. (2003)
3.6μm	Spitzer/IRAC	Krick et al. (2009)
4μm	AKARI/IRC	Davidge et al. (in prep)
5.8μm	Spitzer/IRAC	Krick et al. (2009)
8.0μm	Spitzer/IRAC	Krick et al. (2009)
11μm	AKARI/IRC	Davidge et al. (in prep)
15μm	AKARI/IRC	Davidge et al. (in prep)
18μm	AKARI/IRC	Davidge et al. (in prep)
24μm	Spitzer/MIPS	Krick et al. (2009)
70μm	Spitzer/MIPS	Krick et al. (2009)
250μm	Herschel Space Telescope	Pearson et al. (in prep)
350μm	Herschel Space Telescope	Pearson et al. (in prep)
500μm	Herschel Space Telescope	Pearson et al. (in prep)

5.4 Spectral Energy Distribution Fitting

5.4.1 LePhare

LePhare, created by Arnouts and Ilbert [1] (Arnouts et al. (1999) and Ilbert et al. (2006)), is an SED fitting software using minimum χ^2 fitting. LePhare is also able to calculate photometric redshifts (photo-z) and is able to derive stellar magnitudes. The software runs in Fortran. To fit the photo-z, LePhare uses just the UV/optical/near-infrared fluxes. As well as supplying the multi-wavelength catalogue, the user is also required to supply the SED templates, the dust extinction curves and the filter response curves. LePhare fits the UV/optical/near-infrared separately to the mid/far-infrared. Once the fitting has been performed, LePhare will output the best fit for the UV/optical/near-infrared and for the mid/far-infrared, with associated best fit photo-z. LePhare is also able to output physical parameters about the sources, e.g. the age of the star, the star formation rate.

Discussed below are the templates used to fit the SEDs of the ELAIS-N1 and IRAC Dark Field multi-wavelength catalogues. For the work in this thesis, the photometric and spectroscopic redshifts supplied with the ancillary data were used. Only if a source did not have existing photometric/spectroscopic data, was LePhare used to fit the photo-z. When fitting the ELAIS-N1 and IRAC Dark Field SEDs the dust extinction curves of Bolzonella et al. (2000) and Massarotti et al. (2001) were used. The filter response curves used, were from Vaccari (2016).

5.4.2 Spectral Energy Distribution Templates

It is common practice in fitting SEDs to use separate templates for fitting the UV/optical/near-infrared and mid/far-infrared. This is because distinct regions in a galaxy may be contributing to the different parts of the galaxy spectra. The UV and optical emission of a galaxy will be due to starlight, whereas the far-infrared part of the spectra will

[1] https://people.lam.fr/arnouts.stephane/

be dominated by thermal dust emission from molecular clouds. For the SED fitting in this thesis, the COSMOS templates of Ilbert et al. (2009) have been used for the UV/optical/near-infrared, and for the mid/far-infrared the semi-empirical templates of Berta et al. (2013) have been used,

Ilbert et al. (2009) created SED templates to analyse the photo-z of sources in the 2-deg^2 Cosmological Evolution Survey (COSMOS) field. The templates were created using the SWIRE templates of Polletta et al. (2007) and the starburst templates of Bruzual & Charlot (2003). The templates of Bruzual & Charlot (2003) were chosen because they contain starburst SEDs. The SEDs of Bruzual & Charlot (2003) stop at a rest frame wavelength of 3 μm. Ilbert et al. (2009) use a Polletta et al. (2007) Sdm (a spiral/irregular galaxy) template to extend the Bruzual & Charlot (2003) templates to longer wavelengths than 3 μm. Ilbert et al. (2009) adapt the SED templates to include a contribution from the [OII], Hβ, Hα and Lyα emission lines. Table 5.6 lists the types of galaxies in the Ilbert et al. (2009) SED template library, and Figure 5.3 shows the templates. Ilbert et al. (2009) test their adapted templates on a multi-wavelength catalogue, from the UV to mid-infrared, of the COSMOS field. The UV data are from GALEX, the near-infrared data are from Subaru, Canada France Hawaii Telescope (CFHT), UKIRT, NOAO, and mid-infrared data from Spitzer/MIPS. Ilbert et al. (2009) use LePhare to fit the SEDs. They compare the photo-z with spectroscopic data from the Very Large Telescope (VLT) Visible Multi-Object Spectroscopy (VIMOS) and the Keck Deep Extragalactic Imaging Multi-Object Spectrograph (DEIMOS). Ilbert et al. (2009) state that their photo-z measurements are more accurate than previous COSMOS photo-z analysis by a factor of three. They believe this is due to the fact their multi-wavelength coverage of the COSMOS field has a better filter coverage.

The SED templates of Ilbert et al. (2009) were chosen to fit the UV/Optical/near-infrared data points of the work in this thesis, because the templates have been created for, and tested on, UV to mid-infrared data, a very similar wavelength range to that being fitted in this thesis. Ilbert et al. (2009) state that their SED templates provide a good join between the UV and mid-infrared.

Table 5.6: Table showing the different galaxy types in the Ilbert et al. (2009) SED templates. Where galaxies of the same type are different linear interpolations.

Number	Galaxy type	Galaxy morphology	Colour in Figure 5.3
1	E1	Elliptical	Blue
2	E2	Elliptical	Blue
3	E3	Elliptical	Blue
4	E4	Elliptical	Blue
5	E5	Elliptical	Blue
6	E6	Elliptical	Blue
7	E7	Elliptical	Blue
8	S0	Lenticular	Dark red
9	Sa	Spiral	Mangta
10	Sb	Spiral	Mangta
11	Sb	Spiral	Mangta
12	Sb	Spiral	Mangta
13	Sc	Spiral	Mangta
14	Sc	Spiral	Mangta
15	Sc	Spiral	Mangta
16	Sd	Spiral	Mangta
17	Sd	Spiral	Mangta
18	Sd	Spiral	Mangta
19	Sdm	Spiral/irregular	Pink
20	SB0	Barred spiral	Yellow
21	SB1	Barred spiral	Yellow
22	SB2	Barred spiral	Yellow
23	SB3	Barred spiral	Yellow
24	SB4	Barred spiral	Yellow
25	SB5	Barred spiral	Yellow
26	SB6	Barred spiral	Yellow
27	SB7	Barred spiral	Yellow
28	SB8	Barred spiral	Yellow
29	SB9	Barred spiral	Yellow
30	SB10	Barred spiral	Yellow
31	SB11	Barred spiral	Yellow

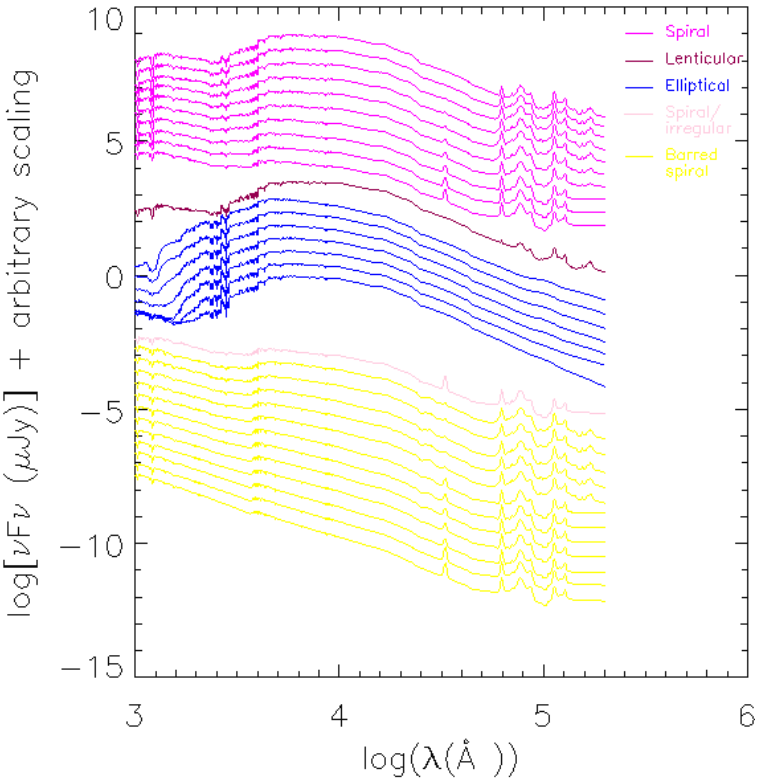

Figure 5.3: Figure showing the SED templates of Ilbert et al. (2009). The blue templates are from Bruzual & Charlot (2003). The green templates are SEDs for spiral galaxies and the red templates are SEDs for elliptical galaxies, both from Polletta et al. (2007).

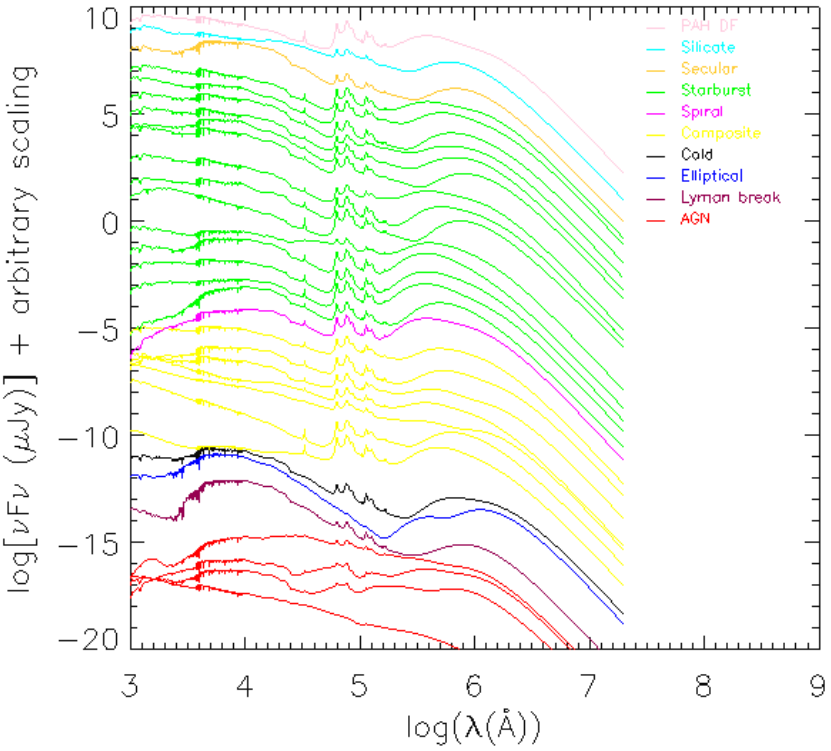

Figure 5.4: Figure showing the SED templates of Berta et al. (2013).

The semi-empirical SED templates of Berta et al. (2013) are made up of three components; stellar emission, thermal dust emission and thermal emission from AGN torus. To create the SED templates, Berta et al. (2013) used sources from GOODS-N, GOOD-S and COSMOS. These fields are some of the deepest and widest surveys observed by the Herschel Space Telescope. They used multi-wavelength data from the UV, optical, near, mid and far-infrared. The sources were separated into different galaxy populations by using an N-dimensional colour space. A median SED template was then created for each of the separate galaxy populations using MAGPHYS (da Cunha et al., 2008). Table 5.7 gives a list of the different types of SED in the library, and Figure 5.4 shows the templates.

The SED templates of Berta et al. (2013) were chosen to fit the mid and far-infrared data in this work because, unlike the templates of Polletta et al. (2007), these templates were created using Herschel Space Telescope data, which the multi-wavelength data in this thesis contains. Berta et al. (2013) state that their SED templates cover a larger wavelength range than Polletta et al. (2007).

Table 5.7: Table showing the different galaxy types in the Berta et al. (2013) SED templates.

Number	Galaxy type	Colour in Figure 5.4
1	Blue star forming galaxy	Green
2	Broad far-infrared star forming galaxy	Green
3	Cold galaxy	Black
4	Elliptical	Blue
5	Lyman break	Dark red
6	Mid-infrared power-law star forming galaxy	Green
7	Mid-infrared excess star forming galaxy	Green
8	Modified star forming galaxy	Green
9	Dust obscured star forming galaxy	Green
10	PAH DF galaxy	Pink
11	Red star forming galaxy 1	Green
12	Red star forming galaxy 2	Green
13	Star forming type 1 AGN 1	Yellow
14	Star forming type 1 AGN 2	Yellow
15	Star forming type 1 AGN 3	Yellow
16	Star forming type 1 AGN 4	Yellow
17	Star forming type 2 AGN 1	Yellow
18	Star forming type 2 AGN 2	Yellow
19	Star forming type 2 AGN 3	Yellow
20	Star forming galaxy 1	Green
21	Star forming galaxy 2	Green
22	Secular galaxy	Mustard
23	Silicate break galaxy	Cyan
24	Spiral galaxy	Magenta
25	AGN Torus	Red
26	Type 1 AGN 1	Red
27	Type 2 AGN 1	Red
28	Type 2 AGN 2	Red
29	Warm star forming galaxy	Green
30	Weak PAH star forming galaxy 1	Green
31	Weak PAH star forming galaxy 2	Green
32	Young star forming galaxy	Green

5.4.3 IRAC Dark Field and ELAIS-N1 SEDs

SED fitting was performed on the cross-matched IRAC Dark Field and ELAIS-N1 multi-wavelength data sets using the fitting software, LePhare. LePhare is described in more detail in Section 5.4.1. The work of this chapter is the first time that AKARI ELAIS-N1 sources have been cross-matched with any other data. Section 5.3 gives details of how the multi-wavelength catalogues were created. Using the criteria, where the source was required to have at least one mid-infrared AKARI detection, the final cross-matched catalogues had 243 and 191 sources in the IRAC Dark Field and ELAIS-N1 respectively. Once all sources were run through LePhare, those which were successfully fitted had a visual inspection for any obvious fitting issues. Also sources with a χ^2 greater than 100 in the mid and far-infrared fit, were rejected. Table 5.8 gives the final numbers of sources in each cross-match for each category in the IRAC Dark Field and ELAIS-N1 deep fields. Figure 5.5 shows example SEDs of a star forming galaxy, AGN and star forming/AGN composite from the IRAC Dark Field and ELAIS-N1 fitting. The complete sample of successfully fitted SEDs for the IRAC Dark Field and ELAIS-N1 can be found in Appendix A. For the SED templates chosen for the work of this thesis, the optical and near-infrared fit gives the galaxy morphology (see Table 5.6), and is denoted as the black lines in Figure 5.5. The optical and near-infrared also gives the source's photometric redshift, when not supplied by the ancillary data. The mid and far-infrared SED fit gives the galaxy type (e.g. AGN, star forming etc.) (see Table 5.7), and is denoted as the red lines in Figure 5.5. Thus having a far-infrared/submillimetre detection greatly improves the fitting and hence the galaxy classification. The only far-infrared/submillimetre detections in the two cross-matched catalogues are those from Herschel/SPIRE. Table 5.9 gives the number of Herschel detections in the two fields, for both the cross-matched catalogues and the SED fitted sources. For ELAIS-N1 SED fitted sources 70 % have at least one Herschel detection, whereas in the IRAC Dark Field only 17 % of the sources have a Herschel detection. This is due to the fact that the IRAC Dark Field Herschel/SPIRE catalogue is the first

Table 5.8: Table showing the number of sources in each cross-match for each category.

Galaxy type	IRAC Dark Field	ELAIS-N1
AGN	30	24
Composite	16	9
Elliptical	7	2
Spiral	5	7
Star forming	42	31
Other	18	17
Total	118	90

Table 5.9: Table showing the percentage of AKARI sources cross matched with SPIRE sources.

Field	All cross matches at least one source	All cross matches three SPIRE detections	SED fitted sources at least one source	SED fitted sources three SPIRE detections
ELAIS-N1	51%	38%	70%	34%
IRAC Dark Field	18%	13%	17%	12%

analysis of the data. Further work will be done in deblending sources and using Spitzer source positions as priors for source detection.

5.5 Colour-Colour Diagrams

5.5.1 Mid-Infrared Galaxy Emission

By studying the mid-infrared region in the spectra of a galaxy, the emission can be a useful diagnostic tool to differentiate between different galaxy types. Different types of galaxy have distinctive spectra in the mid-infrared.

The mid-infrared of elliptical galaxies contains the Rayleigh-Jeans tail of the black body emission from evolved stellar populations. Elliptical galaxies which contain some dust and gas have a Polycyclic Aromatic Hydrocarbons (PAH) emission band at 6.2 μm (Boselli et al., 1998).

Spiral galaxies contain larger amounts of dust and gas than ellipticals, and subsequently some star formation. The mid-infrared spectra of spirals with low or intermediate star formation contain several PAH emission bands at 3.3, 6.2, 7.7, 8.6, 11.3

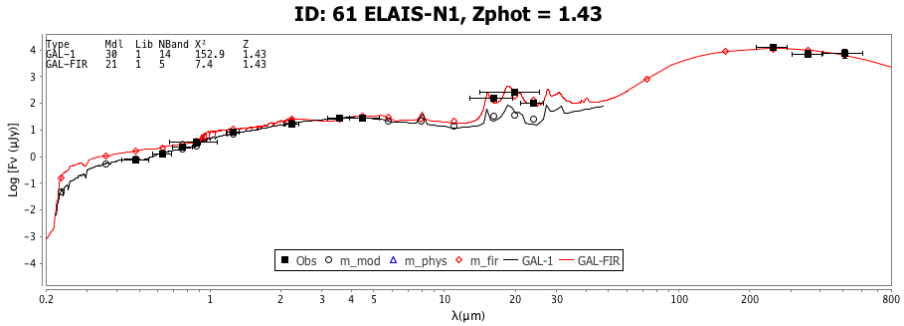

(a) Star forming galaxy

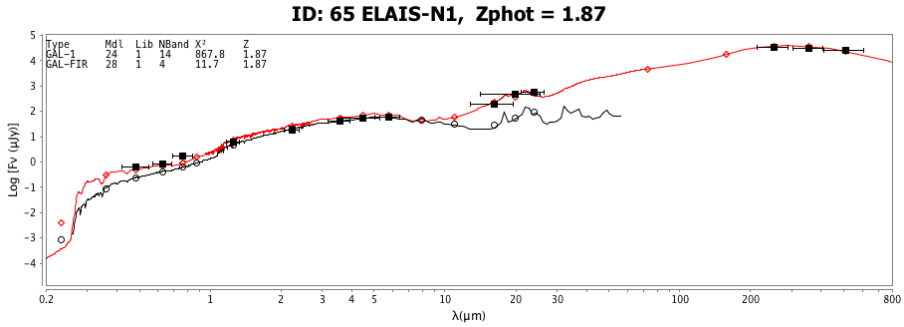

(b) Star forming/AGN composite

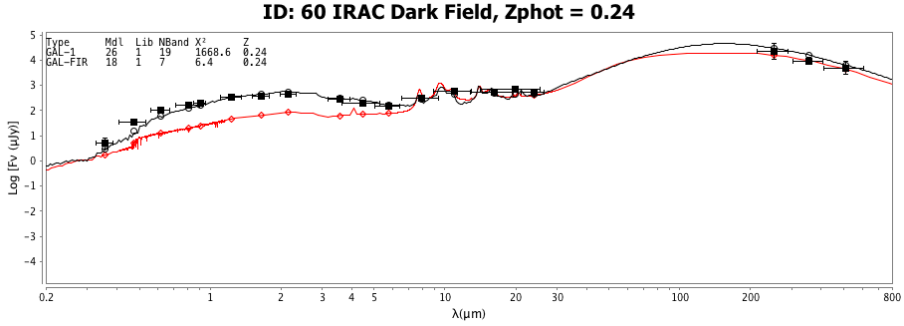

(c) AGN

Figure 5.5: Figure (a) shows a star forming SED, (b) shows a star forming/AGN composite and (c) shows an AGN. Figures (a) and (b) are ELAIS-N1 sources and Figure (c) is an IRAC Dark Field source. ID is the identification number of the source in the cross-matched catalogue.

and 12.7 μm. These emission bands are caused by UV radiation from young stars heating the PAH in photo-dissociated regions (PDR) (Murata et al., 2014b).

The mid-infrared spectra of starburst galaxies are similar to the spectra of 'normal' spiral galaxies discussed above. Due to the thermal emission of very small dust grains, starburst galaxies have a steeply rising continuum at $12-16\,\mu$m. This originates from HII regions where there is intense star formation. The UV radiation from young stars in these regions will cause strong ionising lines in the spectra, [ArII], [ArIII], [SIV], [NeII] and [NeIII]. Starburst mid-infrared spectra also contain silicate absorption features at 9.7 and 18 μm (Takagi & Pearson (2005) and Levenson et al. (2007)).

The spectra of galaxies containing an active galactic nucleus (AGN) have a bright continuum at $3-10\,\mu$m due to the thermal emission from hot dust in the torus around the AGN (Murayama et al., 2000). The spectra may also have a peak between $3-6\,\mu$m due to emission from silicate and graphite dust evaporation close to the AGN. Galaxies containing an AGN can also have weak PAH features in their spectra (Laurent et al., 2000).

X-ray surveys have been found to be successful at detecting non-dust obscured/non-Compton-thick AGN; because the AGN emission in the X-ray is more luminous than in a star forming galaxy, thus it was thought that X-ray surveys should be a good tool to separate AGN from star forming galaxies. About half the AGN are thought to be dust obscured/Compton thick AGN, and hence are not luminous in the X-ray. Thus X-ray surveys are not successful at separating all AGN from star forming galaxies (Donley et al., 2012). Unobscured AGN are detectable in optical galaxy surveys due to the 'big blue bump' peaking in the optical, and visible in the UV and X-ray wavelengths. This emission is caused by gas accreting around the central massive black hole. But for the case where the AGN is obscured, hence the galaxy is AGN dominated, the SED of the source will not have a 'big blue bump' at optical, UV and X-ray wavelengths. Thus dusty AGN and dusty star forming galaxies are hard to detect in UV and optical galaxy surveys, due to dust obscuration (Brand et al., 2006). This section will investigate AGN dominated sources.

By just using the mid-infrared wavelength range it should be possible to separate AGN from star forming galaxies (Haas et al., 2004). As described above both, AGN and star forming galaxies are luminous in the infrared. The majority of cases where an AGN will not be observable in the mid-infrared is the rare occasion that the AGN is edge on to the observer, or is completely hidden in a highly optically-thick dust cloud (Lacy et al., 2004).

Much work has been performed on using the mid-infrared wavelength range to separate star forming galaxies from AGN. Laurent et al. (2000) created an empirical method using nearby star forming galaxies and AGN to differentiate between the two, using observations by the Infrared Camera (ISOCAM) onboard the Infrared Space Observatory (ISO). Laurent et al. (2000) created three SED templates, one of an AGN, one comprised of emission from HII regions and one with emission from PDR. Each of the observed sources were classified by the percentage contribution of each of the templates. This method required spectroscopic data in the mid-infrared, and so is not useful for the work of this thesis.

The following four papers use the location of a source on a colour-colour diagram to separate AGN from other types of galaxies. The papers use the fact that the different galaxy types will occupy different locations on a colour-colour diagram.

Lacy et al. (2004) used the Spitzer First Look Survey (FLS) data and plot the position of the SDSS selected quasars on two colour-colour plots in Spitzer/IRAC and Spitzer/MIPS wavelengths. On the first colour-colour diagram, with the IRAC (5.8 μm/3.6 μm versus 8.0 μm/4.5 μm) filters they identified a region populated by obscured AGN. The obscured AGN region in the second colour-colour plot, using IRAC and MIPS (5.8 μm/3.6 μm versus 24 μm/5.8 μm) filters was not as defined, as the AGN were more dispersed. Lacy et al. (2004) also recommended spectroscopic follow-up work on the selected obscured AGN, to confirm they are AGN.

Stern et al. (2005) used a method similar to Lacy et al. (2004) to create an empirical way of using galaxy positions on a colour-colour diagram to identify both type I and II AGN candidates. Stern et al. (2005) used Spitzer data from the IRAC Shallow Sur-

vey in the Boötes field. They spectroscopically identified AGN, using the AGN and Galaxy Evolution Survey (AGES). Stern et al. (2005) plot their sources on an IRAC filter colour-colour plot, 5.8 μm/8.0 μm verses 3.6 μm/4.5 μm. Similar to Lacy et al. (2004), they found that the AGN occupy a specific region on their diagram.

Krick et al. (2009) plotted the sources from the IRAC Dark Field multi-wavelength catalogue (discussed in Section 5.2.2) on an IRAC/MIPS colour-colour plot. They compared the positions of AGN, which in the catalogue had been classified using SED template fitting. Krick et al. (2009) compared the positions of their AGN on the colour-colour diagrams with the obscured AGN regions predicted by Lacy et al. (2004) (5.8 μm/3.6 μm versus 8.0 μm/4.5 μm) and Stern et al. (2005) (5.8 μm/8.0 μm versus 3.6 μm/4.5 μm). Figure 5.8.b, shows the Lacy et al. (2004) AGN selection criteria. Krick et al. (2009) stated that there is a small amount of contamination of other galaxy types in the Lacy et al. (2004) region, and that there is a larger contamination of non-AGN sources in the region predicted by Stern et al. (2005). Krick et al. (2009) stated that the galaxy contamination is probably due to the fact that the IRAC Dark Field survey is much deeper than the Spitzer FLS and the IRAC Shallow Survey.

Donley et al. (2012) used IRAC data from the COSMOS field, and created an empirical method for detecting obscured AGN. Instead of using spectroscopic or photometric redshifts, they selected AGN on the power law of their gradient of the continuum. They plotted these sources on the same colour-colour diagrams as Lacy et al. (2004) and Stern et al. (2005), showing their AGN selection regions and those of Lacy et al. (2004) and Stern et al. (2005). The AGN section regions of Donley et al. (2012) are smaller than those of Lacy et al. (2004) and Stern et al. (2005), and contain less contamination from other types of galaxies, thus the regions of Donley et al. (2012) are better suited for deep IRAC surveys.

Brand et al. (2006) used a different method from Lacy et al. (2004), Stern et al. (2005) and Donley et al. (2012) for separating AGN dominated galaxies from star forming galaxies. They used Spitzer observations of the Boötes field, and calculated the MIPS 24 μm/IRAC 8 μm flux ratio for the sources. They found this to have a bimodal distri-

bution. Brand et al. (2006) believed the sources for one peak to be AGN and the other peak to be star forming galaxies. Due to silicate absorption features and PAH emission bands, they stated this method is not suitable for detecting AGN with a redshift of $z < 0.6$. They also stated this classification method will not work if the AGN are enveloped in a cooler dust cloud.

Most of the work using mid-infrared colour-colour diagrams to differentiate between AGN and star forming galaxies has been performed using the IRAC and MIPS filters. There is some published work on using the AKARI/IRC mid-infrared filters. Hanami et al. (2012) used sources from the AKARI/IRC observations of the NEP and spectroscopic data from Subaru to separate AGN dominated galaxies and star forming galaxies, by using the PAH emission bands. Hanami et al. (2012) used two methods to detect star forming galaxies. For one method the sources are plotted on a colour-colour diagram, and sources are separated into AGN and star forming. The other method looks for PAH features in the mid-infrared spectra. These sources with PAH features are identified as star forming galaxies, and those with little or no PAH emission features are classed as AGN. For those galaxies which have been selected as star forming, Hanami et al. (2012) calculated the star formation rate by using the PAH features. There has been some work performed on studying the PAH features using AKARI NEP data. Murata et al. (2014b) discovered that some of the star forming galaxies in the NEP are deficient in PAH emission. This is possibly caused by UV photons from young stars destroying the PAHs, or that the UV photons are absorbed by HII regions and do not excite the PAHs. With this in mind, the method of Hanami et al. (2012) may fail to detect some star forming galaxies. Solely using PAH detection to separate AGN from star forming galaxies may not work, as AGN can have PAH emission (Laurent et al., 2000).

5.5.2 AKARI Colour-Colour Diagrams

In this section the colour-colour diagrams in the mid-infrared, specifically AKARI N4, S11, L15 and L18W and MIPS 24 μm are investigated. To understand how different galaxy types populate and move around a colour-colour diagram, it is informative to plot the tracks of specific SED templates, in redshift intervals, on the diagram. On the colour-colour diagrams the tracks for four different types of galaxies, all luminous in the mid-infrared, are plotted. A summary of the different types of galaxies luminous in the mid-infrared and their main spectral features is given in Section 5.5.1. The four different types of galaxies are: starburst, spiral, silicate break and AGN dominated. Also plotted is an elliptical galaxy track. Normal elliptical galaxies are non-star forming galaxies, and thus should not be very luminous in the mid-infrared. These five SED templates are from Berta et al. (2013), and shown in Figure 5.6.

Figure 5.7 shows the colour-colour diagrams for the AKARI/IRC filters used in ELAIS-N1 and the IRAC Dark Field multi-wavelength catalogues, Spitzer/MIPS 24 μm and the tracks of the five SED templates. The colour ratio of the x-axes in Figure 5.7 all show the ratio of warm dust emission (for star forming galaxies) against old stellar population emission, and also the ratio of AGN torus emission against old stellar population emission. The emission from the warm dust features, PAHs, are wavelength dependent, and discussed below. The AGN torus emission peaks at rest frame $\sim 10\,\mu$m; thus will travel through the S11, L15, L18W and MIPS 24 μm filters. The y-axes in Figure 5.7 shows the ratio of warm dust emission at different wavelengths (for star forming galaxies), and also for AGN galaxies the flux ratio of the torus emission at the two different wavelengths.

Due to the fact that the AKARI mid-infrared filters were designed to study the PAH features, which are prominent in star forming and AGN composite objects, star forming and spiral galaxies, and to a lesser extent in AGN; the tracks of these types of galaxies cover much of the AKARI colour-colour space. Thus many different galaxy types lie in the same region of the AKARI colour-colour plots. This is a feature seen in all AKARI

colour-colour plots, and an indication that the AKARI colour-colour space is not ideally suited for galaxy separation. In the mid-infrared colour-colour diagrams at $z \lesssim 2$, the starburst and spiral galaxy tracks occupy a similar location on the plot. Both tracks are dominated by PAH features, as the features travel through the different filters. It is the PAHs which are mainly causing the changes in track angle. When studying the tracks of a low star forming galaxy (e.g. a spiral galaxy) on a colour-colour diagram, the PAH features are less than those for a galaxy with high star formation (e.g. a starburst galaxy). Although this would not be evident in the ratio between PAH flux and the total galaxy flux, this is due to spiral galaxies being less luminous than starburst galaxies. Due to this the change in track angle in the spiral galaxy tracks is in general less than for the starburst tracks. On all the colour-colour diagrams the AGN tracks cover a smaller area of the plot than the starburst and spiral galaxy tracks. This is due to the fact that PAH emission tends to be suppressed in AGN dominated galaxies, due to the intense radiation from the AGN, thus the AGN tracks do not have as prominent PAH features travelling through the filters, and causing the tracks to move around the diagram to the same extent as for the starburst and spiral galaxy tracks. In all of the mid-infrared/MIPS 24 μm colour-colour diagrams the high-z star forming and spiral galaxies could be mistaken for AGN in these colour-colour diagrams.

The fifth galaxy track, for an elliptical galaxy, occupies a different region of the colour-colour diagram in all four plots in Figure 5.7, than the other four tracks. This is because elliptical galaxies are non-star forming and hence devoid of PAH emission and because they contain a large old stellar population. The sharp decrease in the y-axis colour for low z ($z \lesssim 0.4$) is due to emission from the Wien tail of the thermal dust emission. This emission drops to a local minima at rest frame $\sim 16\,\mu$m, where the SED emission increases steeply at wavelengths shorter than this, due to emission from old stellar populations. This increase in flux at shorter wavelengths is what causes the x-axis colour to increase at $z \gtrsim 0.4$ in all four plots.

Section 5.5.1 gives several published methods for separating AGN dominated galaxies. Figure 5.8 plots the AGN region of the colour-colour plot presented in Lacy

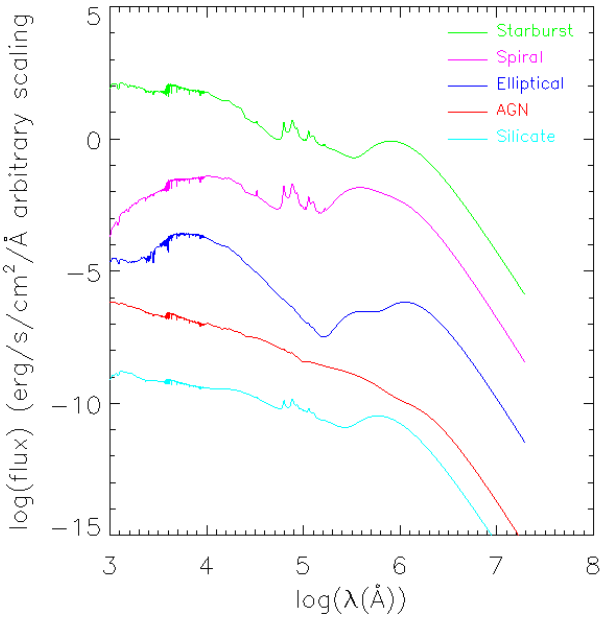

Figure 5.6: Figure showing the five SED templates of Berta et al. (2013) used in the colour-colour track work. The starburst template is shown in green, the spiral galaxy template is shown in magenta, the elliptical galaxy template is shown in blue, the AGN (type 1) template is shown in red and the silicate break galaxy template is shown in cyan.

et al. (2004) for the AKARI selected galaxies, Figure 5.8.a, and from Krick et al. (2009), Figure 5.8.b. Figure 5.8.a shows the colour-colour plot, which uses the IRAC 5.8 μm/IRAC 3.6 μm versus IRAC 8.0 μm/AKARI 4 μm, instead of using the IRAC 4.5 μm colour, which is shown in Figure 5.8.b. In Figure 5.8.a the AKARI mid-infrared selected sources from both the ELAIS-N1 and IRAC Dark Field are plotted. The galaxy classification was performed by the LePhare fitting. There does not appear to be a greater number of AGN contained within the AGN region selected by Lacy et al. (2004). This would indicate that either the selection area is not optimal (which is discussed in subsequent work, see Donley et al. (2012)), or the LePhare fitting has incorrectly classified composite objects as AGN. The AKARI selected sources have a fairly comprehensive coverage in the mid-infrared, but not in the far-infrared. Due to the fact that LePhare uses the mid and far-infrared detections to classify galaxy type, further far-infrared detections are required to confirm galaxy type. In Figure 5.8.b galaxy type have been fitted using the SED templates of Polletta et al. (2007), com-

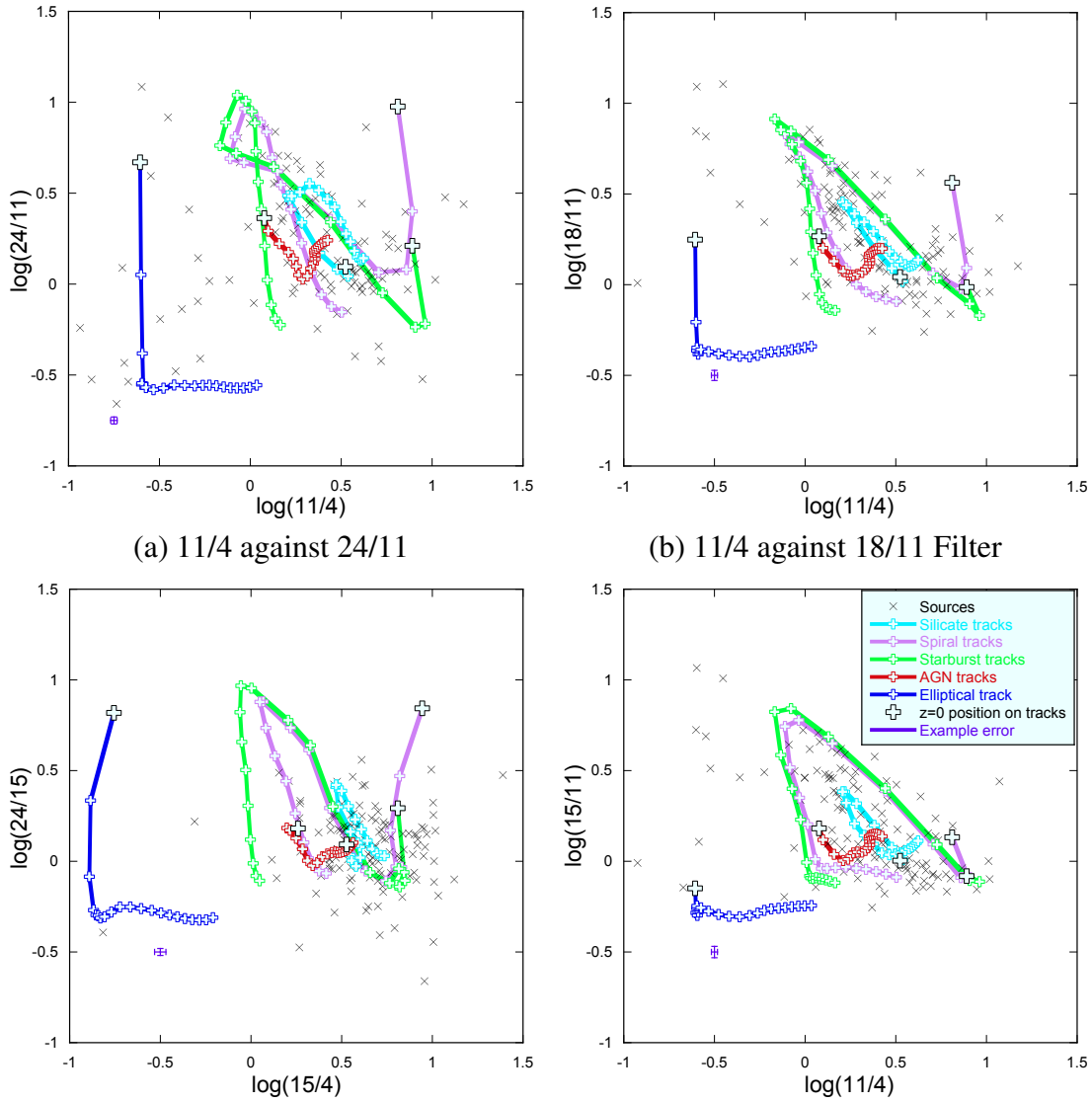

(a) 11/4 against 24/11

(b) 11/4 against 18/11 Filter

(c) 15/4 against 24/15

(d) 11/4 against 15/11 Filter

Figure 5.7: Colour-colour diagrams of the AKARI N4, S11, L15 and L18W filters and MIPS 24 μm filter. The black crosses are the ELAIS-N1 and IRAC Dark Field galaxy colours. The SED tracks go from $z = 0$ to $z = 4$, in steps of $z = 0.2$. $z = 0$ is marked by a larger cross. The elliptical tracks (blue) are discussed at the end of Section 5.5.2. These tracks occupy a different region of the diagrams than the other four galaxy tracks, due to the fact that elliptical galaxies contain very little dust. The silicate break galaxy tracks (cyan) are discussed in Section 5.5.4. The change in direction at $1.1 \lesssim z \lesssim 1.6$ in (a), (b) and (c) is caused by the silicate absorption feature. The starburst tracks (green) and spiral tracks (magenta) are discussed in Section 5.5.5. The changes in direction of these tracks are mainly caused by PAH features. The most pronounced PAH feature at these colour-colour ratios is the 7.7 μm emission band. The AGN tracks are shown in red. An example error for the galaxy flux is shown in purple.

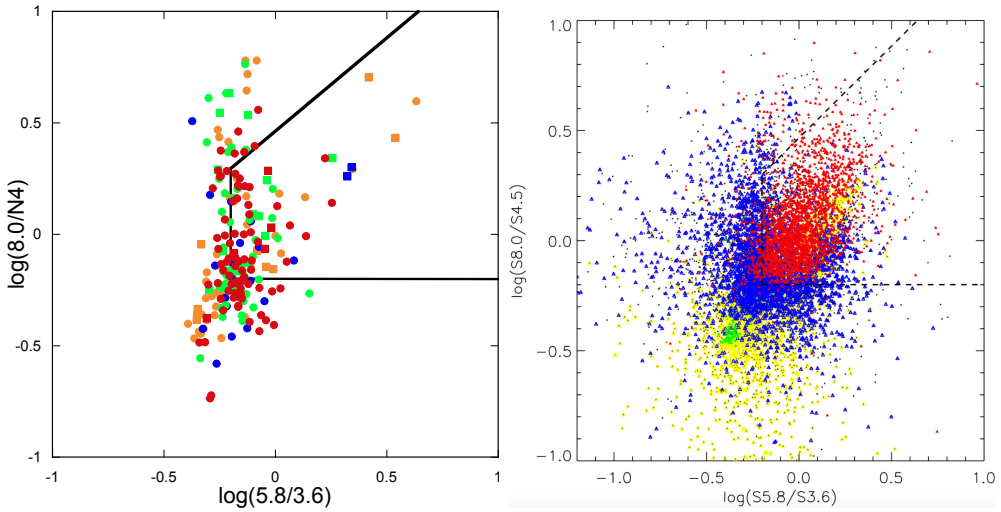

Figure 5.8: The Lacy et al. (2004) AGN selection criteria. The image on the left shows the IRAC 5.8/IRAC 3.6 against IRAC 8.0/N4 colour-colour plot. The red, green, blue and orange points are AGN, starburst, composite and normal galaxies respectively. The circles are from the IRAC Dark Field and the squares are from ELAIS-N1. The image on the right shows the IRAC 5.8/IRAC 3.6 against IRAC 8.0/IRAC 4.5 colour-colour plot from Krick et al. (2009), where the green, yellow, blue, and red are stars, elliptical galaxies, spiral galaxies and AGN, respectively. In both figures, the black/dashed line shows the area possible AGN selection from Lacy et al. (2004).

posite objects have been omitted. Krick et al. (2009) state that there are a high number of AGN within the AGN region, there is also a significant contamination from other galaxy types.

5.5.3 Calculation of Flux Uncertainty of Sources in Colour-Colour Plots

A representative error in the flux of the sources plotted on the colour-colour plots showing sources and galaxy tracks can be seen in purple in Figures 5.7, 5.9 and 5.10. Equation 5.1 shows the uncertainty on a number in log space, where $y = \log x$, δ_y is the total uncertainty in log space and δ_x is the uncertainty of x.

$$\delta_y = \frac{1}{\ln 10} \frac{\delta_x}{x} \tag{5.1}$$

In the case of the colour-colour plots, x is made up of the ratio of two fluxes, thus y is given by Equation 5.2, where F_A is the flux at wavelength A, and F_B is the flux at

wavelength B.

$$y = \log(F_A/F_B) \tag{5.2}$$

Thus the uncertainties need to be combined in quadrature. This is the same method as was used for calculating the uncertainty in the number counts, see Section 3.7.5. Combining the errors in quadrature is shown in Equation 5.3, where δ_A is the uncertainty of the flux of F_A and δ_B is the uncertainty of the flux of F_B.

$$\delta_x = x\sqrt{\left(\frac{\delta_A}{F_A}\right)^2 + \left(\frac{\delta_B}{F_B}\right)^2} \tag{5.3}$$

Combining Equations 5.1 and 5.3 gives Equation 5.4.

$$\delta_y = \frac{1}{\ln 10}\sqrt{\left(\frac{\delta_A}{F_A}\right)^2 + \left(\frac{\delta_B}{F_B}\right)^2} \tag{5.4}$$

Equation 5.4 gives the uncertainty of the source in the x or y-axis. As a representative uncertainty is being sown, δ_A and δ_B are found by taking the mean average flux error for the wavelength A and B respectively, and F_A and F_B are found by taking the mean average of the flux for wavelengths A and B respectively.

As can be seen in Figures 5.7 , 5.9 and 5.10, none of the uncertainties are very large. For all of the colour-colour plots in Figure 5.7, Figure 5.9.a and 5.9.b, and Figure 5.10.d, the uncertainties are about the size of the marker for the source, and are negligible, The errors are the largest in Figure 5.9.c and 5.9.d. The main result of these plots (see Section 5.5.6) is the detection of some high redshift spiral galaxies, which are likely to be luminous galaxies. The distance to a different track (i.e. not the spiral track) for these sources is greater than the uncertainty in flux. In Figure 5.10, which shows an AGN selection region, the starburst and AGN track are further apart than the largest error in the plot. In Figure 5.10.c, a galaxy between the two tracks, could lie on either track. There is a clear distinction between AGN and starburst in the other three plots (see Figure 5.10.a 5.10.b and 5.10.d). Of course sources which are close to overlapping, or very nearly overlapping tracks, could be represented by either track.

But on the whole the uncertainty of flux of a source is small enough, that a source on or very close to a track, is likely to be represented by that track.

5.5.4 Studying the Colour-Colour Diagrams for the Silicate Absorption Feature

The changes in the silicate break track, shown as the cyan lines in Figure 5.7, can mainly be explained by studying the 9.7 μm silicate absorption feature as it travels through the AKARI and MIPS 24 μm filters. Silicate galaxies are discussed in more detail in Section 6.3.3. Figure 5.7.a shows S11/N4 against MIPS 24/S11. At low z the 11/4 ratio decreases as the silicate absorption feature passes through the S11 filter. At $z \sim 1.4$ the 24/11 ratio begins to decrease as the silicate feature enters the MIPS 24 μm filter. Similar to Figure 5.7.a, Figure 5.7.b, which shows S11/N4 against L18/S11, shows the same decrease in 11/4 ratio as the silicate feature passes through the S11 filter. At $z \sim 1.1$ there is a sharp reversal in direction in the y-axis due to the silicate feature moving through the L18W filter. Figure 5.7.c shows 15/4 against 24/15, for low redshift the 15/4 ratio decreases as the silicate feature passes through the L15 filter. Then due to the silicate feature passing through the MIPS 24 μm filter, the 24/15 ratio starts to decrease at $z \sim 1.6$. The S11/N4 against L15/S11 colour-colour plot is shown in Figure 5.7.d. Once again for low redshifts the 11/4 ratio decreases. At $z \sim 1.1$ the 15/11 ratio has a sharp turnaround and begins to decrease. This is too high a redshift to be due to the silicate absorption feature. This could possibly be due to the 6.2 μm PAH feature entering the S11 filter. A study of how the PAH features affect the star forming galaxy tracks is discussed below.

5.5.5 Studying the Colour-Colour Diagrams for PAH Features

By looking at the SED tracks on the individual colour-colour diagrams, the PAH features peak at a rest frame wavelength of 3.3, 6.2, 7.7, 8.6, 11.3 and 12.7 μm can clearly be seen in the starburst and spiral galaxy tracks. One of the motivations for the choice

of wavelength and width of the AKARI filters, was to track the PAH features; but these PAH features complicate the AKARI filter colour-colour plots. The tracks of star forming galaxies with strong PAH features move around much of the area of these colour-colour plots, meaning star forming galaxies overlap in colour-colour space with other types of galaxies.

Figure 5.7.a shows S11/N4 against MIPS 24/S11. The changes in direction of the starburst track can be explained by the PAH features. At $z \sim 0.4$ the S11/N4 flux ratio decreases, while the MIPS 24/S11 flux ratio increases. This is due to the 7.7 μm PAH feature leaving the S11 filter at increasing redshift. The sharp decrease in the MIPS 24/S11 flux ration, but only a small change in the S11/N4 flux ratio, is again due to the 7.7 μm PAH emission band, as the feature leaves the MIPS 24 filter.

Figure 5.7.b shows S11/N4 against L18W/S11. This is a fairly similar plot to Figure 5.7.a. This is unsurprising, as the L18W is a wide filter and covers the 24 μm range. The plot shows the same 7.7 μm PAH feature increasing the S11 flux at $z \sim 0.2$, and the suppression of the L18W flux at $z \sim 1.4$ due to the same PAH feature. The main difference in Figures 5.7.a and 5.7.b is that the 7.7 μm PAH feature suppression of the MIPS 24/L18W flux ratio happens at a lower redshift in Figure 5.7.b, due to the fact that L18W is at a shorter wavelength than MIPS 24 μm.

Figure 5.7.c shows L15/N4 against MIP 24/L15. This diagram is similar to Figures 5.7.a and 5.7.b. This figure shows the same increase in L15 flux at $z \sim 0.5$ due to the 7.7 μm PAH feature and the MIPS 24 flux decrease, also due to the 7.7 μm PAH feature.

Figure 5.7.d shows S11/N4 against L15/S11. The sharp decrease in the flux ratio L15/S11 and only a small increase in the S11/N4 flux ratio at the $z \sim 1.4$ is due to the 6.2 μm PAH feature leaving the L15 filter; the slight increase in the S11/N4 flux at higher z is due to the 3.3 μm PAH feature entering the S11 filter.

5.5.6 AKARI, Herschel/SPIRE and Spitzer/MIPS colours

Plotted in Figure 5.9 are four AKARI, SPIRE and MIPS colour-colour diagrams. Over plotted are the ELAIS-N1 and IRAC Dark Field sources, and the starburst, spiral galaxy, silicate break galaxy and AGN tracks created from the Berta et al. (2013) SED templates, discussed in Section 5.5.2. The *x*-axis in Figure 5.9.a shows the ratio of warm dust emission (PAH), or the AGN torus emission against old stellar population. The *y*-axis shows the cooler dust emission against the warmer dust emission. In Figures 5.9.b, 5.9.c and 5.9.d, the *x*-axes are similar to that in Figure 5.7, which shows the ratio of either the warm dust emission at two wavelengths, or the torus emission from two wavelengths. The *y*-axes give the ratio of the cooler dust emission against the old stellar population emission and can be used to calculate the specific star formation rate. Both of the colour-colour diagrams in Figure 5.9 show that not many of the AKARI selected sources are detected as AGN at 250 μm. The AKARI selected galaxies appear to be mainly star forming galaxies, with some high redshift spiral galaxies. These high redshift spiral galaxies are probably luminous galaxies. This is in agreement with the findings of Elbaz et al. (2011) and Sargent et al. (2014), which state that some high redshift ULIRGs lie on the star forming 'main sequence', whereas low redshift ULIRGs lie off it. This means that high redshift ULIRGs are similar to low redshift 'normal' spiral galaxies, rather than low redshift ULIRGs.

5.5.7 Galaxy Separation using AKARI Colours

It was investigated whether AGN dominated galaxies could be separated from starburst galaxies by just using the AKARI colours. Figures 5.10.a and 5.10.b show colour-colour diagrams of the AKARI filters. The starburst track (green) and the AGN track (red) are plotted, and go from $0 < z < 2$. For this range of redshifts the AGN track clearly occupies a different region from the starburst track. For the galaxies in these two plots $\sim 75\%$ have $z < 2$, so this is not an unreasonable redshift cut off. By including the MIPS 24 μm colour, the redshift range can be increased. Figures 5.10.c and

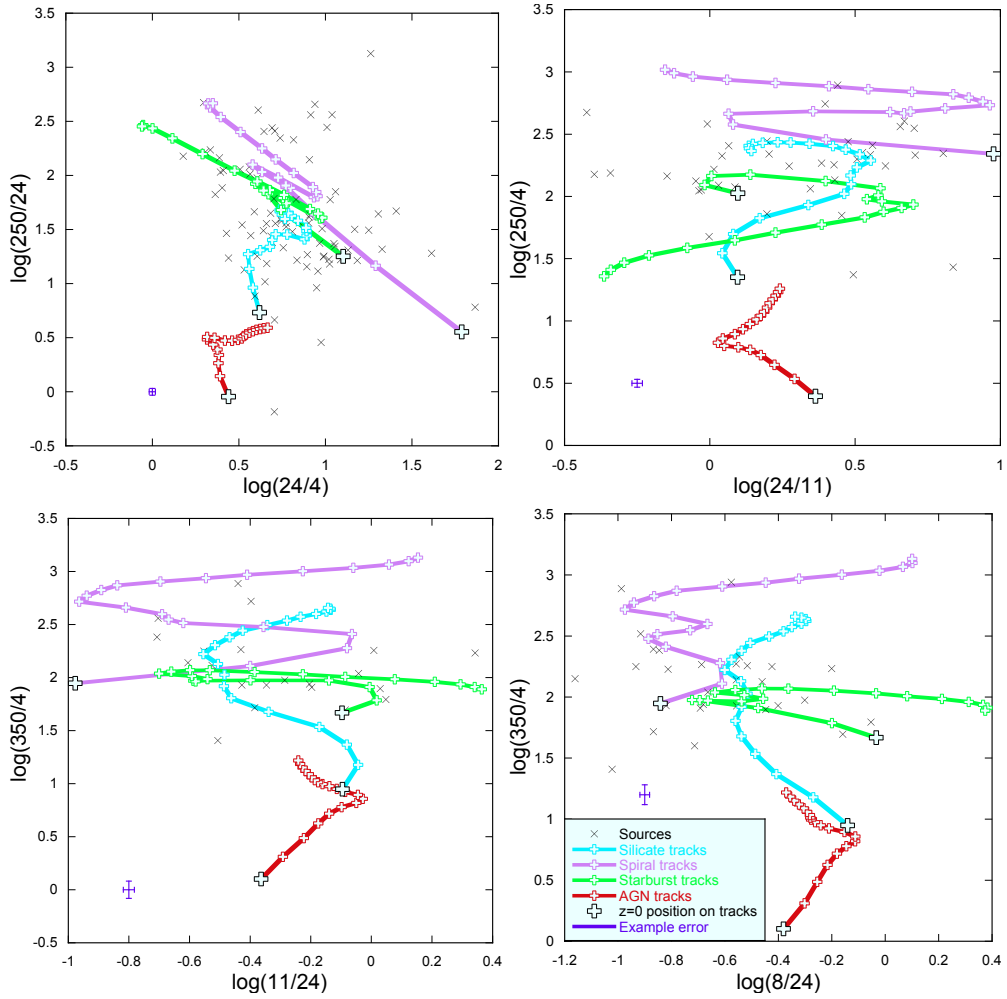

Figure 5.9: Colour-colour diagrams of the AKARI N4 and S11 filters, MIPS 24 μm filter and Herschel/SPIRE 250 μm filter. The black crosses are the ELAIS-N1 and IRAC Dark Field galaxy colours. The SED tracks go from $z = 0$ to $z = 4$, in steps of $z = 0.2$. $z = 0$ is marked by a larger cross. The star forming track is shown as green, the spiral galaxy track is shown as magenta, the silicate break galaxy track is shown as cyan and AGN track is shown as red. An example error for the galaxy flux is shown in purple.

5.10.d show two of the MIPS 24 μm and AKARI filters colour-colour diagrams. In these two diagrams the starburst and AGN tracks go from $0 < z < 2.8$. Again the AGN track occupies a different region from the starburst track. As can be seen in Figure 5.10, the galaxies do not just populate the starburst and the AGN tracks, but are also found in regions between, indicating that many of the sources are composite objects. This indicates that to reliably confirm galaxy type, SED fitting is required.

5.6 Conclusions of AKARI Galaxies Multi-Wavelength Data

By combining the AKARI deep field catalogues created in the work of Chapter 3 with multi-wavelength ancillary data, further information about the sources can be extracted e.g. the galaxy type and redshift. A simple method to separate different galaxy types, is to find a region of a galaxy type on a specific colour-colour diagram. Figure 5.10 shows an AGN dominated galaxy type selection criteria using AKARI colours. Figure 5.10.a, shows 11 μm/4 μm against 18 μm/11 μm and Figure 5.10.b, shows the 11 μm/4 μm against 15 μm/11 μm; this demonstrates that there is a region for $z < 2$ galaxies, where AGN can be separated from starbursts. By also using the MIPS 24 μm colour, Figures 5.10.c and 5.10.d, show that the AGN and starburst separation region has increased to galaxies at $z < 2.8$. Galaxies which contain strong PAH features in the mid-infrared rest-frame (i.e. star forming galaxies), cover a large region of the colour-colour diagrams of AKARI colours, thus making it difficult to separate galaxy types. This leads to the conclusion that to confirm galaxy type, SED fitting is required. The results from AKARI/MIPS/SPIRE colour-colour plots show that there is a population of high redshifted 'normal' spiral galaxies, which are likely to be ULIRGs. This is in agreement with Elbaz et al. (2011) and Sargent et al. (2014), who state that some high redshift ULIRGs lie on the 'normal' star forming galaxy 'main sequence', whereas low redshift ULIRGs lie off the 'main sequence'.

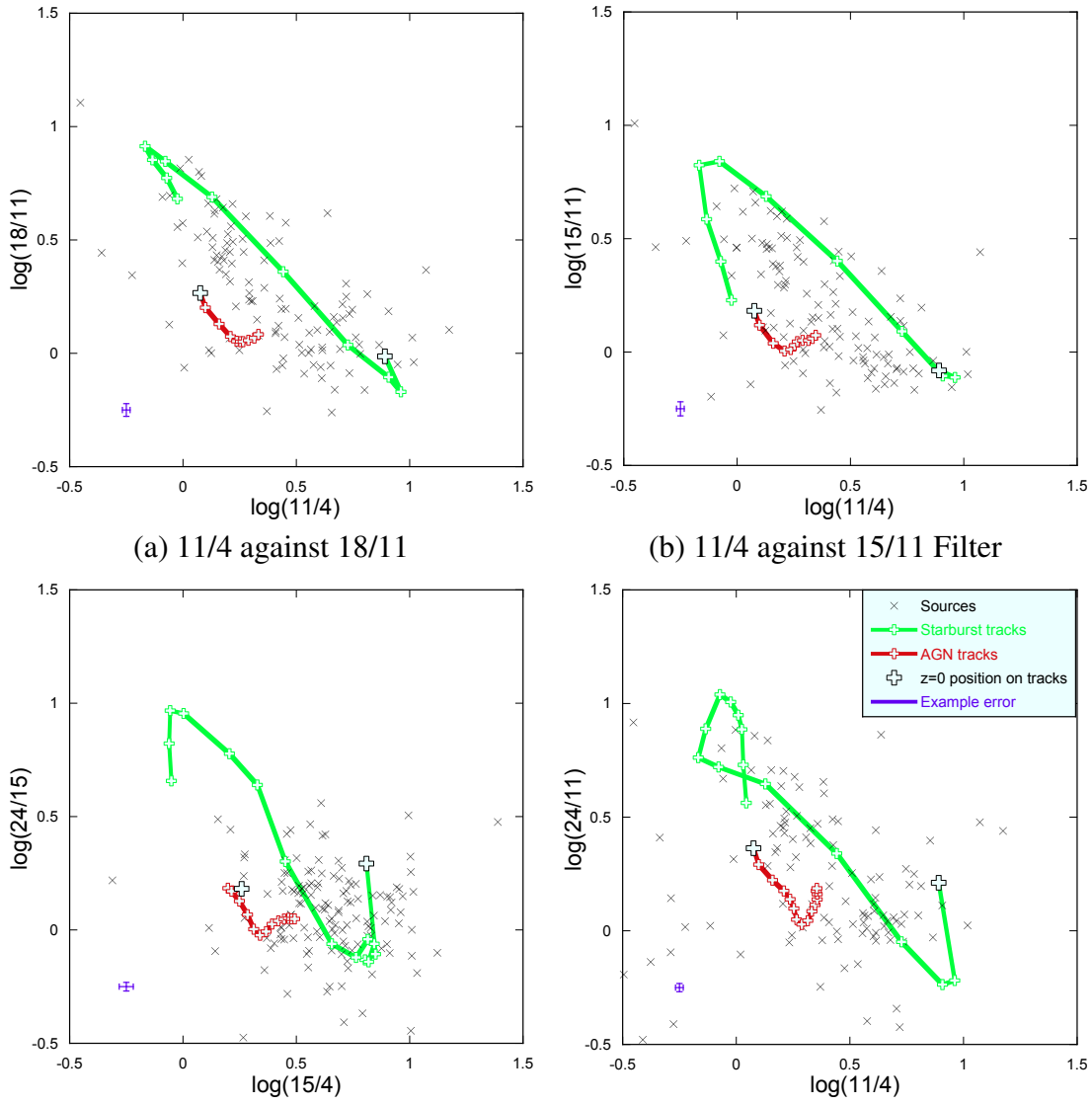

(a) 11/4 against 18/11

(b) 11/4 against 15/11 Filter

(c) 15/4 against 24/15

(d) 11/4 against 24/11 Filter

Figure 5.10: Colour-colour diagrams of the AKARI N4, S11, L15 and L18W filters and MIPS 24 μm filter. The black crosses are the ELAIS-N1 and IRAC Dark Field galaxy colours, the starburst track is in green and the AGN track is in red. The tracks in figures a and b have been cut at $z = 2$ and the tracks in figures c and d have been cut at $z = 2.8$. $z = 0$ is marked by a larger cross. An example error for the galaxy flux is shown in purple.

Chapter 6

Constraints on the Cosmic Infrared Background

A long time ago in a galaxy far, far away

Star Wars - George Lucas

6.1 Introduction

By using the AKARI mid-infrared galaxy positions, an average flux for sources below the detection threshold in longer wavelength images can be found. These unresolved sources contribute to the cosmic infrared background (CIB). The CIB is an isotropic and homogenous all sky background, made up of individual sources.

Section 6.2 discusses the sources contributing to the CIB and past detections. Section 6.3 describes the stacking analysis of the AKARI mid-infrared galaxy positions on the Herschel 250 μm IRAC Dark Field image and the amount of the 250 μm CIB resolved by these sources.

6.2 The Cosmic Infrared Background

CIB is part of the extragalactic background light (EBL), an extragalactic background over the whole of the electromagnetic spectrum. Similar to the rest of the EBL, the CIB is isotropic and homogenous. Unlike the cosmic microwave background (CMB), the CIB is made up of individual sources. The CIB contains the emission of redshifted optical starlight and highly redshifted UV starlight. At longer wavelengths the CIB contains redshifted thermal emission from tori around AGN and redshifted thermal emission from dust, re-radiating starlight (Hauser & Dwek, 2001).

The CIB probes an era between the surface of last scattering and the deepest galaxy surveys. This includes the end of the cosmic dark ages, the Epoch of Reionization and the first starlight in the Universe. Population III stars, the first stars in the Universe, were very massive, due to being devoid of metals, hence they should be very luminous in the UV. The current theory is that population III stars lie at a redshift of $10 \lesssim z \lesssim 30$, hence the UV photons will have been redshifted to $\sim 1-5\,\mu$m. Because these first stars were very luminous, this emission should be detectable in the CIB (Schaerer, 2002). Current telescopes are unable to observe population III stars directly, and it is thought that the next generation of telescopes will not be able to directly detect them, thus studying the CIB is a way to indirectly detect the first stars in the Universe (Cooray et al., 2004). The CIB contains emission from pre-galactic objects and star clusters which formed the first galaxies, light from objects before reionization and the objects which caused reionization (Kashlinsky (2005) and Matsuura et al. (2011)). Studying the power spectrum of the CIB shows the clustering of the sources contributing to the CIB. This on its own is a way to study the distribution of CIB sources and their dark matter halos. By cross correlating the CIB power spectrum with the gravitational lensing of the CMB, a measurement of the correlation between dark matter and the sources contributing to the CIB, can be found, thus showing the relationship between dark and luminous matter over the redshift range $1 < z < 3$ (Viero et al. (2013) and Planck Collaboration et al. (2014)).

The CIB was first postulated by Partridge & Peebles (1967). They discussed galaxy evolution models and how the models would create different sky backgrounds. This led them to theorise that there should be an integrated sky background created by the emission from the first galaxies. They stated that the redshifted emission should peak at about $\sim 5-12\,\mu$m. Partridge & Peebles (1967) did not discuss observing the CIB in the mid and far-infrared, because it was not until the 1970s when galaxy evolution models included thermal emission from dust (Hauser & Dwek, 2001).

The CIB is very difficult to measure using ground based facilities because of the Earth's atmosphere. Section 1.2 discusses the major problems with attempting to observe in the infrared from ground based observatories. Thus it was not until the use of space telescopes that the CIB could be measured. It is also difficult to detect an absolute value for the CIB using a satellite, due to foreground contamination. The main foregrounds which contaminate the CIB signal are; the zodiacal background originating from the solar system, Galactic cirrus in the interstellar medium (ISM), infrared Galactic starlight and faint nearby galaxies which fall below the detection limit of the survey. At wavelengths $\geqslant 400\,\mu$m the CMB contaminates the CIB (Hauser & Dwek (2001), Kashlinsky (2005) and Rowan-Robinson & May (2013)). A summary of the main detections of the CIB are shown in Figure 6.1.

Much work has been done on using galaxies at a shorter wavelength to resolve the CIB at a longer wavelength. Elbaz et al. (2002) used Spectral Energy Distribution (SED) fitting to predict the contribution to the $140\,\mu$m CIB by $15\,\mu$m ISOCAM selected galaxies. They stated that the SEDs predict that the sources would resolve $\sim 64\%$ of the CIB at $140\,\mu$m. For an absolute measurement of the $140\,\mu$m CIB, they used the COBE/DIRBE result from Hauser et al. (1998). Using the SED fits, Elbaz et al. (2002) stated that $\sim 25\%$ of the ISOCAM sources are AGN, whereas the remainder are luminous infrared galaxies (LIRG) where $L_{IR} \geqslant 10^{11} L_{\odot}$. Using Hubble Spectroscopic data, they stated that the ISOCAM sources lie in the redshift range $0.4 < z < 1.3$. If the SED fitting of the ISOCAM selected sources is correct, then over half of the CIB flux at $140\,\mu$m comes from sources at $z < 1.3$.

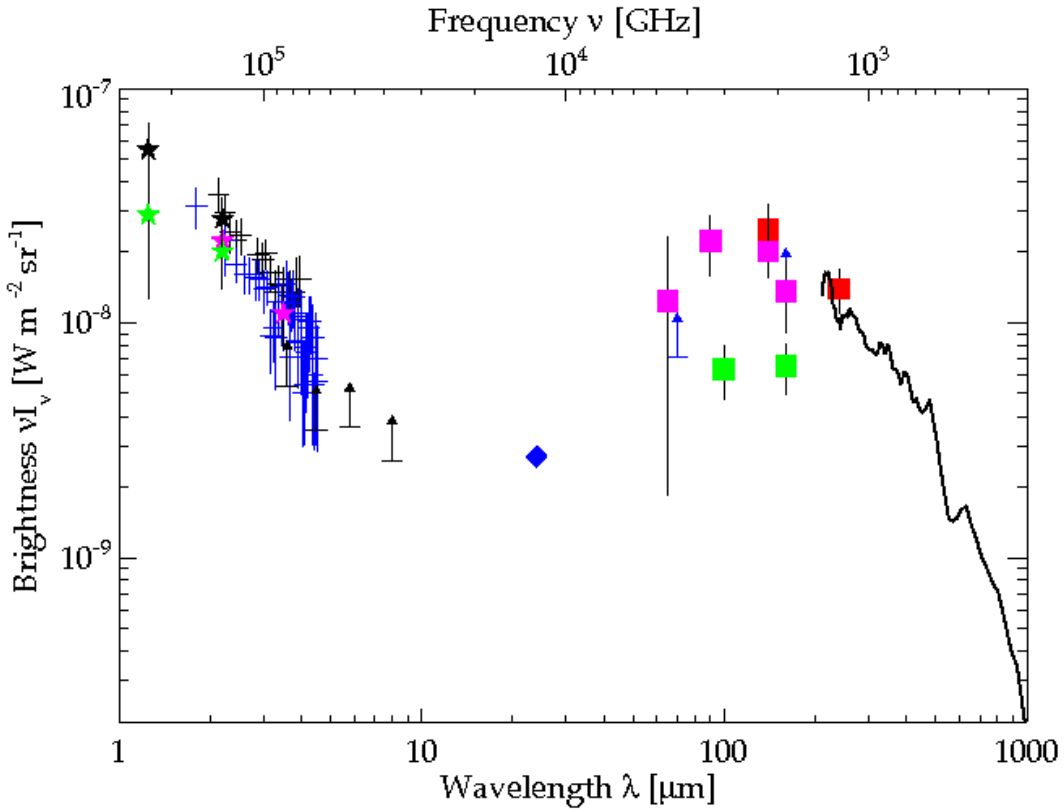

Figure 6.1: Figure showing some of the main detections of the Cosmic Infrared Background. Hauser et al. (1998) COBE/DIRBE shown as red squares, Wright & Reese (2000) COBE/DIRBE shown as green stars, Gorjian et al. (2000) COBE/DIRBE shown as magenta stars, Lagache et al. (2000) ISO/ISOPHOT shows as a black line, Cambrésy et al. (2001) COBE/DIRBE shown as black stars, Matsumoto et al. (2005) IRTS/Near Infrared Instrument shown as black crosses, Fazio et al. (2004) Spitzer/IRAC black arrows showing the lower limit, Dole et al. (2006) shown as a blue diamond and blue errors for lower limits, Berta et al. (2010) Herschel/PACS shown as green squares, Matsuura et al. (2011) AKARI/FIS shown as magenta squares and Tsumura et al. (2013) AKARI/IRC shown as blue crosses.

Dole et al. (2006) performed the first stacking analysis to constrain the contribution of mid-infrared galaxies to the far-infrared CIB. They used Spitzer/MIPS 24 μm source positions and MIPS 70 and 160 μm images of the CDFS, HDFN and the Lockman Hole. To calculate how much the 24 μm selected galaxies contribute to the far-infrared CIB, they stacked the 24 μm galaxy positions on the 70 and 160 μm images. For the values of the CIB at 70 and 160 μm, they used the values predicted by the Lagache et al. (2004) model. Dole et al. (2006) stated that the 24 μm galaxies resolve $\sim 92\%$ of the CIB at 70 μm and $\sim 69\%$ at 160 μm. Most of the 24 μm selected galaxies lie at a redshift $z > 1.5$. This is in disagreement with the findings of Elbaz et al. (2002), who state over half of the 15 μm selected galaxies contributing to the 140 μm CIB have a redshift of $z < 1.3$. The difference could be because Elbaz et al. (2002) used the SEDs of galaxies to predict the flux at 140 μm, whereas Dole et al. (2006) used 70 and 160 μm images. If the template fitting was incorrect, maybe Elbaz et al. (2002) have over predicted the amount of the CIB resolved by the 15 μm galaxies. Both Elbaz et al. (2002) and Dole et al. (2006) stated that the galaxies are predominately LIRGs.

Berta et al. (2011) also performed stacking analysis of MIPS 24 μm sources on 70, 100 and 160 μm Herschel/PACS images. They used data from the PACS Evolutionary Probe (PEP), which had observed GOODS North and South, the Lockman Hole and COSMOS. Berta et al. (2011) stated that they found that for longer wavelengths of the CIB, the sources contributing to it, lie at higher redshifts, compared with the shorter wavelength CIB. They stated that the MIPS 24 μm sources resolve $\sim 89\%$ of the 160 μm CIB, and that $\sim 50\%$ of these sources lie at $z > 1$. This is in agreement with the results of Dole et al. (2006).

6.3 Stacking Analysis

6.3.1 Herschel Image

The IRAC Dark Field is a calibration field for Herschel/SPIRE and hence is one of the deepest extragalactic fields observed by Herschel. The region was observed between March 2010 and July 2012. The total exposure time of each map is 2.5 hours. The data reduction were performed in the Herschel Common Science System HIPE, version 14. The source extraction and photometry was carried out using SUSSEXtractor (Savage & Oliver, 2007). Photometry on the 350 and 500 μm images was performed at the positions of the 250 μm sources.

6.3.2 Method

To prepare the Herschel 250 μm IRAC Dark Field for stacking analysis, first an average of the sky background was calculated and subtracted from the image, thus the mode of the image became 0. Next the flux from the Herschel sources were removed from the image, so just an image of the background would remain for the stacking. The Herschel sources were removed by 'cleaning' the image. An array of the same dimensions as the background subtracted Herschel image was created, this would become the residual map. In the Herschel image the location and flux of the pixel with the greatest flux was found. A Gaussian Point Spread Function (PSF) was created with a flux of 10% of the brightest pixel. This PSF was then subtracted from the Herschel image, with the centre of the PSF corresponding to the location of the brightest pixel. Then the PSF was added to the residual map, in the same locations. This was repeated until all of the Herschel sources had been removed. The residual map contained all the sources, and the remaining Herschel image contained just the background flux, including flux from galaxies below the detection level. Figure 6.2 shows the AKARI L15 positions plotted on the Herschel 250 μm image. The number of cross-matches between the AKARI L15 sources and the SPIRE 250 μm sources is 43, and the number of cross-matches

between AKARI S11 and the SPIRE 250 μm sources is 31. As can be seen in Figure 6.2, the AKARI IRAC Dark Field survey area is about 1/4 the size of the Herschel survey area. The locations of the AKARI S11/L15 sources on the Herschel image were then stacked. This was done by creating a 'postage stamp' 21 by 21 pixels across, with the AKARI galaxy position in the centre. These 'postage stamps' were then averaged together to create a mean average AKARI S11 and L15 galaxy at 250 μm. These two mean postage stamps are shown in Figure 6.3.

The intensity of the CIB is given by Equation 6.1; where A is the area, S_i is the flux of the i^{th} galaxy making up the CIB and N is the number of galaxies in area A contributing to the CIB.

$$I = \frac{\sum_{i=1}^{n} S_i}{A} \tag{6.1}$$

The 'postage stamp' created in the stacking analysis gives the mean average galaxy flux, which is calculated by Equation 6.2, where N is the completeness corrected number of galaxies in the survey, calculated in Section 3.7.4.

$$\bar{S} = \frac{1}{N} \sum_{i=1}^{n} S_i \tag{6.2}$$

Equation 6.3 gives the density of the galaxies in the survey area.

$$\rho = \frac{N}{A} \tag{6.3}$$

The flux of the AKARI selected galaxies per unit area is given by Equation 6.4.

$$\bar{S}\rho = \Big(\frac{1}{N} \sum_{i=1}^{n} S_i\Big) \frac{N}{A} \tag{6.4}$$

$$\bar{S}\rho = \frac{\sum_{i=1}^{n} S_i}{A} \tag{6.5}$$

Hence Equation 6.4 gives the intensity.

$$\bar{S}\rho = I \tag{6.6}$$

The 'postage stamps' were separated into flux bins, the same flux bins as were used to create the number counts of Chapters 3 and 4. For each set of 'postage stamps', a mean average 'postage stamp' was created for the flux bin of the AKARI positions. Then Equation 6.4 was applied to each mean 'postage stamp'. The total CIB flux was calculated by summing all the results of Equation 6.4. This was performed separately for the AKARI S11 and L15 galaxy positions. 165 and 216 source positions were stacked from the AKARI S11 and L15 galaxy catalogues respectively. The value of the CIB resolved by the AKARI S11 and L15 source positions was then compared with the value of the CIB as given in the model of Fixsen et al. (1998). The uncertainties in the percentage measured has been calculated from the upper and lower limits of the Fixsen et al. (1998) model. The AKARI sources at 11 and 15 μm resolved $10.4^{+2.8}_{-1.7}$% and $11.4^{+3.0}_{-1.8}$% respectively, of the 250 μm CIB. This is a fairly small fraction; the possible reasons why, are given below.

6.3.3 Resolving the Cosmic Far-Infrared Background with AKARI Source Positions

One reason that the S11 and L15 AKARI galaxy positions do not resolve more of the 250 μm CIB could be because the sources have not been detected in the S11/L15 filters, due to being silicate break galaxies.

Silicate break galaxies are galaxies with a strong silicate absorption feature centred at rest frame wavelength 9.7 μm. Ultra Luminous Infrared Galaxies (ULIRGs) are known to have this silicate absorption feature. It is believed this feature is suppressed by AGN, and thus will only be prominent in star forming galaxies. Silicate break galaxies can be identified by just using mid-infrared filters. Studying this type of galaxy is important, because it should aid in breaking the degeneracy in different galaxy evolution models

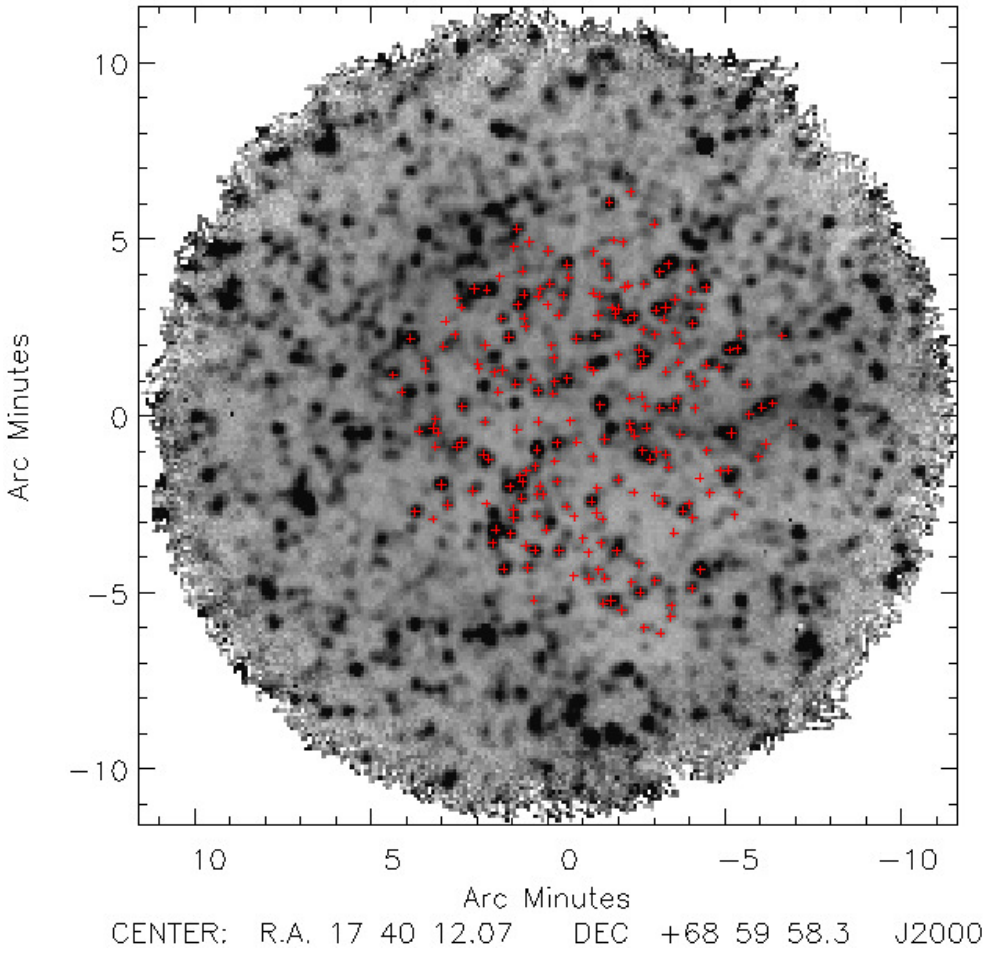

Figure 6.2: The Herschel/SPIRE 250μm image with AKARI L15 sources over plotted as red crosses.

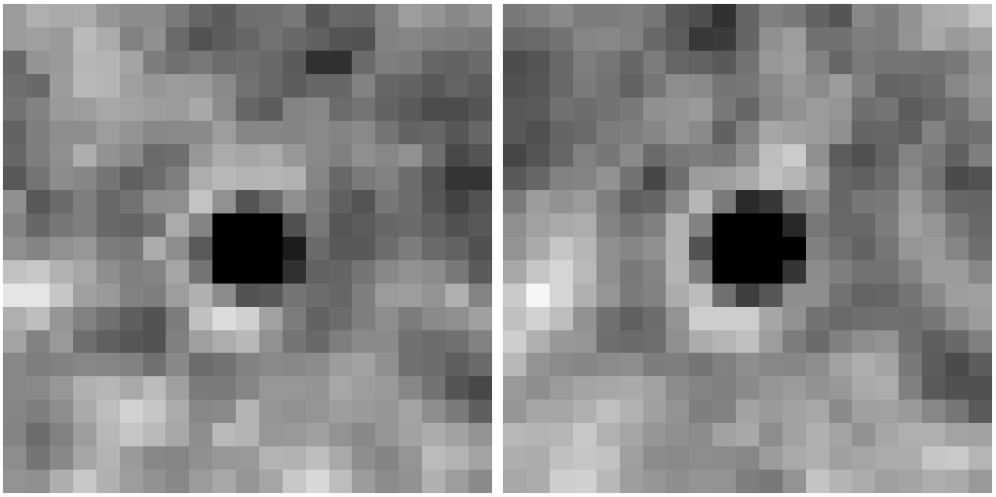

Figure 6.3: The image on the left shows the 'postage stamp' of the mean stacked galaxies for the AKARI S11 positions, and the image on the right shows the 'postage stamp' of the mean stacked galaxies for the AKARI L15 positions.

and can be used to place limits on star formation rates between $1 < z < 2$ (Takagi & Pearson, 2005).

Silicate break galaxies were investigated in both the IRAC Dark Field and ELAIS-N1. The centre of the silicate absorption feature is shifted to 11 and 15 μm at $z = 0.13$ and $z = 0.55$ respectively. The silicate break candidates were first selected as either S11 or L15 dropouts. The S11 dropouts were selected as having a detection in N4 and L15 but not in S11. MIPS 24 μm was used instead of the L18W filter, because the L18W image is shallower than the L15 image (for the IRAC Dark Field the L18W image is only 5 pointings deep, while the L15 image is 10 pointings deep), thus the L15 possible silicate break absorption candidates required detections in N4, S11 and MIPS 24 μm, but not in L15. From these candidates a subsection was selected matching the criteria of lying at the correct redshift. For the IRAC Dark Field, photometric redshifts from the Krick et al. (2009) catalogue were used, and for the ELAIS-N1 the photometric and small amount of spectroscopic redshifts were used from the Spitzer Data Fusion Catalogue (Vaccari, 2016). Finally the locations of these subsets of sources were inspected visually on the S11/L15 image. About half of the locations were at an edge of the image, and hence were not detected. One S11 null detection contained a mismatched source. The remainder are very probably silicate break galaxies. Of the AKARI IRAC Dark Field galaxies cross-matched with the catalogue of Krick et al. (2009) $\sim 0.8\%$ of S11 sources are likely to be silicate break and $\sim 2\%$ for the L15 galaxies. This is very similar to the percentage of silicate break galaxies probably found in AKARI ELAIS-N1, which were cross matched with the Spitzer Data Fusion Catalogue; where the silicate break galaxies were $\sim 1\%$ of the S11 galaxies and $\sim 3\%$ of the L15 galaxies. Since the mean redshift of the AKARI S11 and L15 galaxies is $z = 1.0$ and $z = 1.2$, respectively and, as stated above, the silicate absorption feature will be observed in the S11 and L15 filter at $z \sim 0.13$ and $z \sim 0.55$; the work presented in this thesis should have detected most of the silicate break galaxies.

As the percentage of silicate break galaxies in both the S11 and L15 filter are very small, it is very unlikely that silicate break galaxies are causing the small percentage

detection of the CIB at 250 μm using the AKARI S11 and L15 galaxy positions.

A test was performed as to whether $\sim 10\%$ is a reasonable fraction of the 250 μm CIB for AKARI 11 and 15 μm sources to resolve, using code from Pearson et al. (in prep). Firstly the models of Pearson (2005) were used to predict the numbers of different types of galaxies observed by the 11/15 μm galaxies. Then SED templates were used to predict the expected amount of flux at 250 μm, given the amount of flux observed at 11/15 μm. Figure 6.4 shows the results of this analysis, the AKARI 11 and 15 μm source contribution to the SPIRE 250 μm sources. As can be seen in the figure, the percentage of AKARI sources detected at 250 μm declines steadily. The results from stacking analysis of AKARI sources at 250 μm agree well with the predictions from the simulations that suggest the fractional contribution to the CFIB is around 15% at 11 μm and $< 10\%$ at 15 μm. This means that the sources contributing to the 250 μm CIB mostly lie at a redshift greater than that observed by AKARI. 68% and 54% of the AKARI S11 and L15 galaxies have a redshift of $z < 1$, and 88% and 88% of the AKARI S11 and L15 galaxies have a redshift of $z < 2$. This indicates that many of the sources contributing to the 250 μm CIB lie at a redshift of $z > 2$. This is in general agreement with the results of Dole et al. (2006) and Berta et al. (2011), which are discussed above. Both state that much of the sources contributing to the 160 μm CIB lie at redshifts of $z > 1$. Berta et al. (2011) state that the longer the wavelength of the CIB, the higher redshift the sources contributing to it, lie at; thus the sources contributing to the 250 μm CIB should, on average lie at a higher redshift, than the sources contributing to the 160 μm CIB.

The fraction of the mid-infrared CIB resolved by the AKARI surveys was also investigated. Using the same stacking method as that performed on the Herschel image, the fraction of the CIB resolved in the mid-infrared was calculated by stacking at the AKARI galaxy positions on the 11 and 15 μm AKARI images. The 11 and 15 μm galaxies detected by AKARI were found to resolve $\sim 12\,\%$ and $\sim 20\,\%$ of the 11 and 15 μm CIB flux respectively. As there is currently no absolute measurement of the CIB in the mid-infrared, a predicted value of the CIB has been used, calculated from

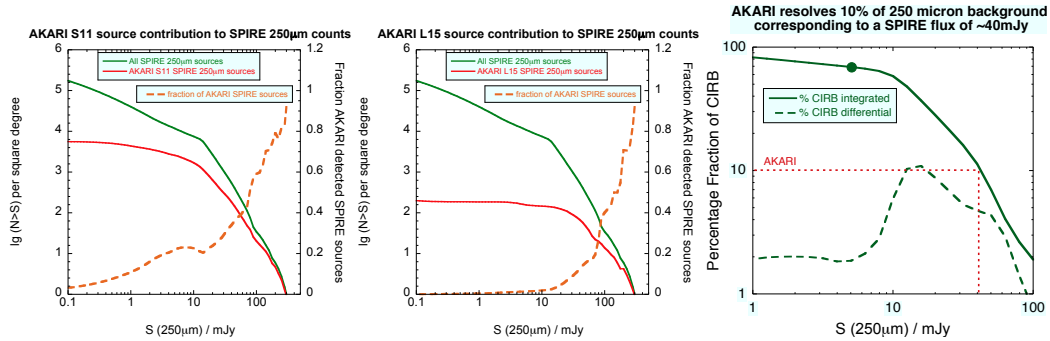

Figure 6.4: The image on the left shows the AKARI S11 source contribution to the SPIRE 250 μm sources. The centre image shows the AKARI L15 source contribution to the SPIRE 250 μm sources. The image on the right shows the 250 μm CIB as observed by Herschel/SPIRE. The SPIRE flux limit is about 40mJy, thus the AKARI sources positions on the SPIRE image would be expected to resolve about 10% of the 250 μm CIB. Both from the work of Pearson et al. (in prep).

the Pearson model.

6.4 Conclusions on the Constraints on the 250 μm Cosmic Infrared Background

This chapter has investigated the AKARI mid-infrared sources, which contribute to the 250 μm CIB. This was performed by stacking the positions of the AKARI sources on the Herschel/SPIRE 250 μm image of the IRAC Dark Field. The results show that the 11 and 15 μm AKARI galaxies resolve $10.4^{+2.8}_{-1.7}$% and $11.4^{+3.0}_{-1.8}$% of the 250 μm CIB, respectively. This is in general agreement with the predictions of the number of AKARI mid-infrared sources detectable at 250 μm, using the model of Pearson (2005). This small fraction indicates that most of the sources contributing to the 250 μm CIB lie at redshifts greater than those detected by AKARI 11 and 15 μm. $\sim$ 88% of the 11 and 15 μm AKARI IRAC Dark Field galaxies lie at $z < 2$, this would suggest that the sources contributing to the 250 μm CIB lie at redshifts $z > 2$.

Chapter 7

Conclusions and Further Work

Here at the end of all things

The Return of the King - J.R.R. Tolkien

7.1 Summary

This thesis presents a new pipeline written to process AKARI/IRC raw frames and the first analysis of AKARI observations of two extragalactic deep fields, ELAIS-N1 and the IRAC Dark Field. The source catalogues extracted from these two deep fields have been used to test different galaxy evolution models. The sources have been combined with existing ancillary data to perform SED fitting and to explore the AKARI/IRC and MIPS 24 μm colour-colour space. The galaxy catalogues have also been used to resolve part of the 250 μm CIB using 11 and 15 μm AKARI source positions.

The new pipeline is described in detail in Chapter 2. This pipeline was optimised for processing AKARI extragalactic deep field images, namely for point source extraction and to create high signal to noise mosaicked images. Compared with the existing standard pipeline the new pipeline provides an improvement for correcting for image distortion, individual frame astrometry correction and a better removal of instrumental artefacts. Although raw frames from only five of the nine AKARI filters have been required to be processed for this work, the new pipeline is able to process raw frames

from all nine of the AKARI/IRC filters observed until the exhaustion of coolant.

Chapter 3 presents the first analysis of the IRAC Dark Field and ELAIS-N1, some of AKARI's deepest observations, and the first number count work of the ADF-S. Chapter 3 gives a description of the data reduction, point source extraction, stellar subtraction and the number count work, including reliability and completeness corrections. The chapter continues by showing that the non-evolution galaxy model of Pearson et al. (2014) does not fit the number counts. The number counts of the IRAC Dark Field, ELAIS-N1 and ADF-S are then compared with published results of AKARI (Murata et al. (2014a) and Hopwood et al. (2010)), Spitzer/IRAC (Fazio et al., 2004) and Spitzer/IRS (Teplitz et al., 2011), and the models of Pearson (2005) and Cai et al. (2013). The number counts show a possible incorrect stellar removal for the shorter ADF-S IRC filters, a possible incorrect completeness correction for ELAIS-N1 and ADF-S faintest fluxes and a possible incorrect Earthshine light removal in the longest wavelength ELAIS-N1 IRC filters. The 4 and 15 μm number counts show how the wide field ADF-S constrains the brighter end of the number counts, while the two deep fields, ELAIS-N1 and the IRAC Dark Field constrain the fainter end. The Pearson model appears to fit the number counts better than the Cai model. The 11 μm number counts show that the AKARI IRAC Dark Field is the deepest image of the sky at 11 μm.

Due to the depth of the IRAC Dark Field, in Chapter 4 P(D) analysis was performed for the 11 and 15 μm images. The result of the 11 *mu*m P(D) analysis is consistent with the Pearson Model, whereas the result of the 15 *mu*m P(D) analysis is inconsistent with the Pearson model.

In Chapter 5 the multi-wavelength band-merged catalogues of ELAIS-N1 and the IRAC Dark Field were created using the four-band galaxy catalogues created in the work of this thesis and ancillary data. The AKARI and MIPS 24 μm colour-colour space was explored, specifically with a view of separating star forming galaxies and AGN. The results show by just using the AKARI filters, there exists an AGN region for $z < 2$, and by including the MIPS 24 μm filter the redshift range increases for $z < 2.8$.

The results show that for a full AGN classification, SED fitting is required.

The final science chapter, Chapter 6, shows the stacking analysis of 11 and 15 μm galaxy positions on a Herschel/SPIRE 250 μm image, to constrain the contribution of the AKARI mid-infrared galaxies to the far-infrared CIB. The Herschel image used is of the IRAC Dark Field, a SPIRE calibration field. The work of this chapter presents the first science performed using the SPIRE IRAC Dark Field. The 11 and 15 μm AKARI galaxies resolved $\sim 10\%$ and $\sim 11\%$ respectively of the CIB at 250 μm. These results are in general agreement with the predictions of the number of SPIRE sources detected by AKARI galaxies, using the model of Pearson (2005). This indicates that most of the sources contributing to the 250 μm CIB, lie at greater redshifts than those detected by AKARI.

7.2 Further Work

The first two science chapters, Chapters 3 and 4, present the number count work of the AKARI deep field and the P(D) analysis. The P(D) analysis work shows that injecting an empirical PSF instead of a Gaussian PSF creates a better simulation of the AKARI images. For any further number count work using AKARI data, an empirical PSF for completeness corrections would probably lead to a more representative completeness in the faint number counts.

In Chapter 5, the SED fitting would be greatly improved if the multi-wavelength catalogues contained more far-infrared detections, ideally from Spitzer/MIPS or from Herschel/PACS. Both the ELAIS-N1 and IRAC Dark Field multi-wavelength catalogues contain MIPS 24 μm data. Only 4% of the ELAIS-N1 sources have a MIPS 70 μm detection, while the IRAC Dark Field does not contain any cross-matches. Neither ELAIS-N1 nor the IRAC Dark Field have any MIPS 160 μm cross-matches. 51% of the ELAIS-N1 sources have a SPIRE 250 μm cross-match, but the IRAC Dark Field catalogue only 18% of the sources have a SPIRE 250 μm detection. Further work on extracting SPIRE IRAC Dark Field sources is discussed below. There are un-

mosaicked PACS data in ELAIS-N1, but no observations could be found in the IRAC Dark Field. Reducing the PACS data and cross-matching the extracted source catalogue with the ELAIS-N1 band-merged catalogue should help with the SED fitting. There also exists some fairly shallow spectroscopic AKARI/IRC data in the IRAC Dark Field, which are currently un-processed. Processing these data and including the spectroscopic redshifts in the IRAC Dark Field band-merged catalogue should help with the SED fitting of those galaxies, as they will then have spectroscopic redshifts.

Chapter 6 presents the first science work performed with the Herschel/SPIRE 250 μm IRAC Dark Field. There also exists SPIRE 350 and 500 μm images. The multi-wavelength data of the IRAC Dark Field are yet to be fully investigated. The field is one of the deepest surveys performed by AKARI/IRC and was observed by both Spitzer/IRAC and Herschel/SPIRE as a calibration field; thus the IRAC Dark Field contains deep data for Spitzer/IRAC, AKARI/IRC and Herschel/SPIRE. It has been discussed that the AKARI 15 μm source positions could act as priors for detecting SPIRE sources. Unfortunately the AKARI survey area only covers $\sim 25\%$ of the total SPIRE survey area (see Figure 6.2). The Spitzer/IRAC survey covers a much larger area, and is also deeper than the AKARI data, and thus it would be better to use the IRAC sources as a prior for detecting SPIRE sources. By using the positions of the IRAC sources, SPIRE sources below the detection limit can be extracted. As can be seen in Figure 6.2, because SPIRE observes at a longer wavelength than AKARI/IRC or IRAC, SPIRE images have a worse spatial resolution, thus several AKARI or IRAC sources can be contained within one SPIRE source. The IRAC sources could also be used to resolve the SPIRE sources. The next science which could be performed on the SPIRE images, is number count work. To fully utilise the deep pointing, the same P(D) analysis used in Chapter 4 could be performed on the SPIRE images. Detecting more SPIRE sources will also help with the IRAC Dark Field SED fitting.

Although only three extragalactic fields have been processed by the new AKARI pipeline presented in this thesis, the pipeline is designed to process any AKARI/IRC deep field observed before the end of the cool phase of the mission. There are still many AKARI

extragalactic deep fields which have not been processed. One such field is the Hubble Ultra Deep Field (HUDF). The HUDF contains much ancillary data, including Spitzer, Herschel and recently deep Atacama Large Millimetre Array (ALMA) (Dunlop et al., 2016). By processing and analysing the AKARI HUDF data, the mid-infrared band gap between Spitzer/IRAC and Spitzer/MIPS will then be filled by the AKARI detections.

7.3 Future Infrared Space Missions

Currently there are only two astronomical satellites observing in the infrared, both of which are now only capable of observing in the near-infrared. Since the exhaustion of liquid coolant on board the Spitzer Space Telescope, the mission has entered the warm phase and only the two shortest wavelength channels on the instrument IRAC (3.6 and 4.5 μm) are still operational. Section 5.3.2 describes how the AKARI ELAIS-N1 galaxy catalogue was cross-matched with Spitzer/IRAC SERVS catalogue, data observed during this warm phase. The second satellite which is capable of observing at the shortest near-infrared wavelengths is the Hubble Space Telescope (HST). The instruments on board the HST, which observe in the infrared wavelength range, are the Advanced Camera for Surveys (ACS) images at $0.35-1.1\,\mu$m and the Wide Field Camera 3 (WFC3) images at $0.8-1.7\,\mu$m. Ancillary data of the IRAC Dark Field observed by ACS have been cross-matched with the AKARI galaxy catalogue in Section 5.3.3.

About 19% of the sources in the ELAIS-N1 band-merged catalogue and about 17% of the sources in the IRAC Dark Field have > 5 detections in the optical and near-infrared. Out of those, most of them just have detections in the IRAC 3.6 and 4.5 μm and AKARI 4 μm, i.e. in the near-infrared. The SED fitting software, LePhare, uses the optical and near-infrared detections to fit the photometric redshifts of the sources. Further imaging of the ELAIS-N1 with both the ACS and WFC3, and the IRAC Dark Field with WFC3, should provide more points for the photometric redshift fitting.

There is currently no satellite observing in the mid and far-infrared. Discussed below are two planned future missions and one, at the time of writing, potential mission.

7.3.1 James Webb Space Telescope

The James Webb Space Telescope (JWST), capable of observing in the near and mid-infrared, has a planned launch date of 2018 (Gardner et al., 2006). JWST is a collaboration between NASA, ESA and the Canadian Space Agency (CSA), and will have four main instruments on board, the Near Infrared Camera (NIRCam), the Near Infrared Imager and Slitless Spectrograph (NIRISS), the Near Infrared Spectrograph (NIRSpec) and the Mid Infrared Instrument (MIRI). NIRCam will have two channels, capable of imaging between $0.6-5.0\,\mu$m. NIRISS will contain a wide field grism ($1.0-2.5\,\mu$m), and single-object grism ($1.0-2.5\,\mu$m). Also part of the NIRISS, but which can also be operated separately, is the Fine Guidance Sensor (FGS), observing at $1.25\,\mu$m. NIRSpec will have a multi-object spectrograph, the first of its kind in a satellite, performing medium resolution spectroscopy ($1-5\,\mu$m) and low resolution spectroscopy ($0.6-5.0\,\mu$m). The mid-infrared instrument, MIRI (Rieke et al., 2015) will image in nine bands ($5.6-25.5\,\mu$m), perform low resolution spectroscopy ($5-12\,\mu$m), medium resolution spectroscopy ($5-12\,\mu$m) and corona graphic imaging at ($10.5-23\,\mu$m).

MIRI will be covering much of the AKARI/IRC wavelength range. Number count work performed using MIRI observations should go to fainter fluxes than the ones presented in this thesis. Nevertheless, it will be interesting to compare the number counts from the two satellites, especially as AKARI has been the only satellite to observe some of those wavelengths. As well as observing galaxies to a lower flux than AKARI, MIRI will also go to higher z. As MIRI data will be deeper than AKARI data, MIRI sources should fill in the missing data in the band-merged catalogues in Chapter 5, specifically where the flux of a galaxy was below the detection limit for the AKARI filter. The longer wavelength MIRI sources will be useful to act as priors for detecting

the Herschel/SPIRE sources.

During its ten year mission, JWST aims to probe the end of the Cosmic Dark Ages, to study large scale structure and galaxy evolution, to study star and planet formation and to observe Solar System objects. JWST will study the evolution of dark matter and content of galaxies (e.g. stars, metals etc.) from the end of the Cosmic Dark Ages to the present day. JWST plans to study high redshift ULIRGs to understand if it is galaxy mergers which are triggering high star formation rates. Using MIRI, JWST will study the 3.3 μm PAH feature out to a redshift of $z \sim 6$, and the 7.7 μm PAH feature out to $z \sim 2.5$. JWST hopes to probe the end of the Cosmic Dark Ages and observe the objects which caused the Epoch of Reionization, by using NIRCam and then performing follow up observations to find the redshifts of the sources using MIRI. Hence JWST plans to observe the first galaxies, and discover at what range of redshifts the Epoch of Reionization occurred. It is thought that JWST will not be able to directly detect population III stars (the first stars in the Universe), but it should be able to detect supernovae from population III stars, and detect individual star clusters containing the first stars (Gardner et al., 2006).

7.3.2 Euclid

The second planned infrared satellite is the ESA Cosmic Vision Mission, Euclid (Laureijs et al., 2011). Euclid has a planned launch date of 2020 (Scaramella et al., 2015) and an expected lifetime of six years. Euclid will have two main instruments on board, VIS (a visual imager) and NISP (a near-infrared spectrograph and photometer). VIS will be capable of visual imaging between $500 - 900$ nm. NISP will be comprised of a near-infrared imaging photometer, observing in the Y, J and H-bands; and a near-infrared spectrograph ($1.1 - 2.0\,\mu$m).

Euclid covers a wavelength range just shorter than that of AKARI. Depending on which extragalactic deep fields Euclid observes, sources which are cross-matched with the multi-wavelength catalogues of Chapter 5 should aid in constraining the redshift

of the sources, as both the ELAIS-N1 and IRAC Dark Field catalogues are, in some sources, lacking optical and near-infrared data.

The main aim of the mission is to understand dark energy and dark matter by mapping the geometry of the Universe. This will mainly be performed by studying weak gravitational lensing (the image distortion due to gravity as it travels through the intervening Universe), and Baryonic Acoustic Oscillation (studying the imprint of the primordial acoustic oscillations on the galaxy power spectrum). The Euclid mission will also produce much legacy science, as it will be observing a wide field, two deep fields and will perform follow-up observations. Euclid should image ~ 1.5 billion galaxies and obtain spectra for ~ 50 million galaxies, up to at least $z = 2$. As Euclid will observe many galaxies in the redshift range $1 < z < 3$, which is the peak of star formation and AGN activity, galaxies observed by Euclid should aid in understanding galaxy evolution. At a higher redshift Euclid should be able to detect galaxies using the Lyman break method. For a redshift $z > 7$, Euclid should detect $\sim$100 galaxies (Laureijs et al., 2011).

7.3.3 SPICA

The possible follow on from the AKARI telescope is the Space Infrared telescope for Cosmology and Astrophysics (SPICA) (Goicoechea & Nakagawa, 2011). The current status of the mission at the time of writing is that SPICA is planned to be submitted to the ESA's fifth medium class mission call, and will be a joint JAXA and ESA mission. If selected, SPICA will have a planned launch date of 2029 and a proposed lifetime of five years. SPICA will have two main instruments on board; the mid-infrared instrument (SMI) and the far-infrared instrument (SAFARI). The SMI is a Japanese led instrument, performing imaging and spectroscopy between $20 - 37\,\mu$m. SAFARI is a European led far-infrared grism spectrometer covering the wavelength range $34 - 230\,\mu$m (Bonato et al. (2015) and Sibthorpe et al. (2016)).

The SMI instrument will observe at a wavelength range just longer than AKARI/IRC.

Thus SMI will be able to trace features in the mid-infrared to a higher redshift than AKARI. These features include PAH emission and the silicate break absorption feature. As the SMI will cover a wavelength range not covered by any other satellite, the sources detected will be useful for constraining more of the mid-infrared wavelength range of the SEDs of galaxies and test galaxy evolution models at wavelengths which have currently not been tested.

SPICA plans to study planet formation, perform direct imaging of giant planets, study galaxy formation and the evolution of galaxies and their contents. The filters of the SMI have been designed to study PAH emission bands and silicate absorption features. As well as studying the features, the PAH bands will be used to determine the redshift of the sources. Both the SMI and SAFARI will cover the JWST and ALMA wavelength gap (Goicoechea & Nakagawa (2011) and Bonato et al. (2015)).

7.4 Conclusions

This thesis has presented work carried out using AKARI galaxy catalogues. These were extracted from mosaicked images, processed by a new optimised pipeline. The optimised pipeline was created during the course of the investigation to process AKARI extragalactic deep field images. Thirteen galaxy catalogues have been created at; 4, 11, 15 and 18 μm in the ELAIS-N1 and IRAC Dark Field and at 3, 4, 7, 11 and 15 μm in the ADF-S.

Galaxy number counts have been created from all thirteen galaxy catalogues. These number counts are in general agreement with published results, e.g. the Spitzer/IRAC 8 μm number counts of Fazio et al. (2004) and the AKARI 15 μm number counts of Hopwood et al. (2010). The specific cases of disagreement could be due to an incorrect stellar subtraction in a particular galaxy catalogue, or an incomplete removal of all instrument artefacts, which plague the later AKARI Phase 2 observations. It should be noted that published results of number counts of the same wavelengths do not always agree, see the 15 μm number counts of Hopwood et al. (2010) and Murata et al.

(2014a). The general agreement with previous number count work validates the optimised pipeline. The galaxy number count work was also compared with the galaxy evolution models of Pearson (2005) and Cai et al. (2013). Performing P(D) analysis on the two deepest fields, the 15 μm IRAC Dark Field ruled out the Pearson model at 15 μm, whereas the results from the 11 μm IRAC Dark Field was not inconsistent with the Pearson model at 11 μm. It is believed that the Pearson model under predicted the evolution of star forming galaxies.

Work has been performed cross-matching the galaxy catalogues with ancillary data of Krick et al. (2009), Oliver et al. (2012), Vaccari (2016) and Pearson et al. (in prep). There is a good correlation in flux between the AKARI 4 μm and Spitzer/IRAC 4.5 μm sources. This validates the positional offset correction of the optimised pipeline, an issue with previous AKARI pipelines.

By creating colour-colour diagrams using the AKARI and Spitzer/MIPS 24 μm filters, an AGN and star forming galaxy separation criteria has been found for galaxies with $z < 2.8$. The positions of the AKARI selected galaxies on these colour-colour plots indicate that many of the sources in the AKARI catalogues are AGN and star forming composite objects. On the AKARI/MIPS/SPIRE colour-colour plots, a population of AKARI mid-infrared selected submm sources are high redshifted 'normal' spiral galaxies. These are likely to be high redshifted ULIRGs, which resemble low redshifted 'normal' spiral galaxies and not local Universe ULIRGs. This is in agreement with the findings of Elbaz et al. (2011) and Sargent et al. (2014), who state that high redshift ULIRGs lie on the star forming galaxy 'main sequence', where as local ULIRGs lie off the 'main sequence'.

The final work which was performed for this thesis, using the AKARI galaxy catalogues is the stacking analysis of the AKARI IRAC Dark Field 11 and 15 μm galaxy positions on the Herschel/SPIRE 250 μm image. This is the first analysis of the SPIRE image, and was carried out to measure the percentage of the 250 μm CIB resolved by the AKARI mid-infrared galaxies. The 11 and 15 μm galaxy catalogues resolved $10.4^{+2.8}_{-1.7}$% and $11.4^{+3.0}_{-1.8}$% of the 250 μm CIB, respectively. This fairly low fraction

indicates that the sources contributing to the 250 μm CIB lie at greater redshift than the galaxies detected by AKARI, since $\sim 68\%$ and $\sim 54\%$ of the 11 and 15 μm galaxies lie at redshifts $z < 1$, and $\sim 88\%$ of galaxies in the 11 and 15 μm catalogues lie at redshifts $z < 2$. The suggested higher redshift range of the 250 μm CIB sources is in agreement with the work of Dole et al. (2006) and Berta et al. (2011). Previous telescopes e.g. ISO, Spitzer, AKARI and Herschel, have provided much information about galaxies at infrared wavelengths. On the horizon the future telescopes of JWST and Euclid will continue this work of understanding how galaxies form and evolve.

Bibliography

Arimatsu, K., Onaka, T., Sakon, I., et al. 2011, PASP, 123, 981

Arnouts, S., Cristiani, S., Moscardini, L., et al. 1999, MNRAS, 310, 540

Ashby, M. L. N., Willner, S. P., Fazio, G. G., et al. 2015, APJS, 218, 33

ASTRO-F User Support Team., 2005, Version 3.2

ASTRO-F User Support Team., 2009, Version 1.2

Aussel, H., Gerin, M., Boulanger, F., et al. 1998, AAP, 334, L73

Barger, A. J., Cowie, L. L., & Sanders, D. B. 1999, APJL, 518, L5

Barrufet, L., et al. in prep

Basilakos, S., Georgantopoulos, I., Pérez-Fournon, I., et al. 2002, MNRAS, 331, 417

Berta, S., Magnelli, B., Lutz, D., et al. 2010, AAP, 518, L30

Berta, S., Magnelli, B., Nordon, R., et al. 2011, AAP, 532, A49

Berta, S., Lutz, D., Santini, P., et al. 2013, AAP, 551, A100

Bertin, E., & Arnouts, S. 1996, AAPS, 117, 393 v

Béthermin, M., Daddi, E., Magdis, G., et al. 2012, APJL, 757, L23

Bianchi, L., Conti, A., & Shiao, B 2014, VizieR Online Data Catalog, 2335,

Boggess, N. W., Mather, J. C., Weiss, R., et al. 1992, APJ, 397, 420

Bolzonella, M., Miralles, J.-M., & Pelló, R. 2000, AAP, 363, 476

Bonato, M., Negrello, M., Cai, Z.-Y., et al. 2015, MNRAS, 452, 356

Boselli, A., Lequeux, J., Sauvage, M., et al. 1998, AAP, 335, 53

Brand, K., Dey, A., Weedman, D., et al. 2006, APJ, 644, 143

Brown, W. R., McLeod, B. A., Geary, J. C., & Bowsher, E. C. 2008, PROCSPIE, 7014, 70142P

Bruzual, G., & Charlot, S. 2003, MNRAS, 344, 1000

Cai, Z.-Y., Lapi, A., Xia, J.-Q., et al. 2013, APJ, 768, 21

Calzetti, D., & Kinney, A. L. 1992, APJL, 399, L39

Cambrésy, L., Reach, W. T., Beichman, C. A., & Jarrett, T. H. 2001, APJ, 555, 563

Cesarsky, C. J., Abergel, A., Agnese, P., et al. 1996, AAP, 315, L32

Chary, R., Casertano, S., Dickinson, M. E., et al. 2004, APJS, 154, 80

Ciliegi, P., McMahon, R. G., Miley, G., et al. 1999, MNRAS, 302, 222

Clegg, P. E., Ade, P. A. R., Armand, C., et al. 1996, AAP, 315, L38

Clements, D. L., Bendo, G., Pearson, C., et al. 2011, MNRAS, 411, 373

Condon, J. J. 1974, APJ, 188, 279

Cooray, A., Bock, J. J., Keatin, B., Lange, A. E., & Matsumoto, T. 2004, APJ, 606, 611

Cowie, L. L., Songaila, A., Hu, E. M., & Cohen, J. G. 1996, AJ, 112, 839

da Cunha, E., Charlot, S., & Elbaz, D. 2008, MNRAS, 388, 1595

Dale, D. A., Helou, G., Contursi, A., Silbermann, N. A., & Kolhatkar, S. 2001, APJ, 549, 215

Davidge, H., et al. in prep

Dole, H., Lagache, G., Puget, J.-L., et al. 2006, AAP, 451, 417

Donley, J. L., Koekemoer, A. M., Brusa, M., et al. 2012, APJ, 748, 142

Dunlop, J. S., McLure, R. J., Biggs, A. D., et al. 2016, arXiv:1606.00227

Dwek, E., & Arendt, R. G. 1998, APJL, 508, L9

Eales, S., Dunne, L., Clements, D., et al. 2010, PASP, 122, 499

Eales, S. A., Raymond, G., Roseboom, I. G., et al. 2010, AAP, 518, L23

Efstathiou, A., Rowan-Robinson, M., & Siebenmorgen, R. 2000, MNRAS, 313, 734

Eggen, O. J., Lynden-Bell, D., & Sandage, A. R. 1962, APJ, 136, 748

Egusa, F., Usui, F., Murata, K., et al. 2015, arXiv:1512.05046

Elbaz, D., Cesarsky, C. J., Fadda, D., et al. 1999, AAP, 351, L37

Elbaz, D., Cesarsky, C. J., Chanial, P., et al. 2002, AAP, 384, 848

Elbaz, D., Hwang, H. S., Magnelli, B., et al. 2010, AAP, 518, L29

Elbaz, D., Dickinson, M., Hwang, H. S., et al. 2011, AAP, 533, A119

Ellis, R. 1987, Observational Cosmology, 124, 367

Farrah, D., Afonso, J., Efstathiou, A., et al. 2003, MNRAS, 343, 585

Farrah, D., Geach, J., Fox, M., et al. 2004, MNRAS, 349, 518

Fazio, G. G., Ashby, M. L. N., Barmby, P., et al. 2004, APJS, 154, 39

Fixsen, D. J., Dwek, E., Mather, J. C., Bennett, C. L., & Shafer, R. A. 1998, APJ, 508, 123

Franx, M., Labbé, I., Rudnick, G., et al. 2003, APJL, 587, L79

Fruchter, A., & Hook, R. N. 1997, PROCSPIE, 3164, 120

Gardner, J. P., Mather, J. C., Clampin, M., et al. 2006, SSR, 123, 485

Gehrels, N. 1986, APJ, 303, 336

Genzel, R., & Cesarsky, C. J. 2000, ARAA, 38, 761

Genzel, R., Tacconi, L. J., Gracia-Carpio, J., et al. 2010, MNRAS, 407, 2091

Glenn, J., Conley, A., Béthermin, M., et al. 2010, MNRAS, 409, 109

Goicoechea, J. R., & Nakagawa, T. 2011, EAS Publications Series, 52, 253

González-Nuevo, J., Lapi, A., Fleuren, S., et al. 2012, APJ, 749, 65

González-Solares, E. A., Irwin, M., McMahon, R. G., et al. 2011, MNRAS, 416, 927

Gorjian, V., Wright, E. L., & Chary, R. R. 2000, APJ, 536, 550

Goto, T., Takagi, T., Matsuhara, H., et al. 2010, AAP, 514, A6

de Graauw, T., Haser, L. N., Beintema, D. A., et al. 1996, AAP, 315, L49

Granato, G. L., De Zotti, G., Silva, L., Bressan, A., & Danese, L. 2004, APJ, 600, 580

Gruppioni, C., Pozzi, F., Zamorani, G., & Vignali, C. 2011, MNRAS, 416, 70

Gruppioni, C., Pozzi, F., Rodighiero, G., et al. 2013, MNRAS, 432, 23

Haas, M., Siebenmorgen, R., Leipski, C., et al. 2004, AAP, 419, L49

Hanami, H., Ishigaki, T., Fujishiro, N., et al. 2012, PASJ, 64,

Hatsukade, B., Kohno, K., Aretxaga, I., et al. 2011, MNRAS, 411, 102

Hauser, M. G., Arendt, R. G., Kelsall, T., et al. 1998, APJ, 508, 25

Hauser, M. G., & Dwek, E. 2001, ARAA, 39, 249

Herschel, F. W. 1800a, Phil. Trans. R. Sco. Lond., 255-283

Herschel, F. W. 1800b, Phil. Trans. R. Sco. Lond., 284-292

Hogg, D. W. 2001, AJ, 121, 1207

Hopwood, R., Serjeant, S., Negrello, M., et al. 2010, APJL, 716, L45

Hughes, D. H., Serjeant, S., Dunlop, J., et al. 1998, NAT, 394, 241

Ilbert, O., Arnouts, S., McCracken, H. J., et al. 2006, AAP, 457, 841

Ilbert, O., Capak, P., Salvato, M., et al. 2009, APJ, 690, 1236

Irwin, M., & Lewis, J. 2001, NAR, 45, 105

Ishihara, D., Onaka, T., Kataza, H., et al. 2010, AAP, 514, A1

Kashlinsky, A. 2005, PHYSREP, 409, 361

Kawada, M., Baba, H., Barthel, P. D., et al. 2007, PASJ, 59, 389

Kennicutt, R. C., Jr. 1998, APJ, 498, 541

Kessler, M. F., Steinz, J. A., Anderegg, M. E., et al. 1996, AAP, 315, L27

Kim, S. J., Lee, H. M., Matsuhara, H., et al. 2012, AAP, 548, A29

King, A. J., & Rowan-Robinson, M. 2003, MNRAS, 339, 260

Krick, J. E., Surace, J. A., Thompson, D., et al. 2009, APJS, 185, 85

Lacy, M., Storrie-Lombardi, L. J., Sajina, A., et al. 2004, APJS, 154, 166

Lagache, G., Puget, J.-L., Abergel, A., et al. 2000, ISO Survey of a Dusty Universe, 548, 81

Lagache, G., Dole, H., Puget, J.-L., et al. 2004, APJS, 154, 112

Laureijs, R., Amiaux, J., Arduini, S., et al. 2011, arXiv:1110.3193

Laurent, O., Mirabel, I. F., Charmandaris, V., et al. 2000, AAP, 359, 887

Lawrence, A., Walker, D., Rowan-Robinson, M., Leech, K. J., & Penston, M. V. 1986, MNRAS, 219, 687

Lawrence, A., Warren, S. J., Almaini, O., et al. 2007, MNRAS, 379, 1599

Le Floc'h, E., Papovich, C., Dole, H., et al. 2005, APJ, 632, 169

Lemke, D., Klaas, U., Abolins, J., et al. 1996, AAP, 315, L64

Levenson, N. A., Sirocky, M. M., Hao, L., et al. 2007, APJL, 654, L45

Lonsdale, C. J., Smith, H. E., Rowan-Robinson, M., et al. 2003, PASP, 115, 897

Lorente, R., Onaka, T., Ita, Y., et al. 2007, AKARI IRC Data User Manual, ver.1.3

Lucas, R. A., et al 2016, ACS Data Handbook, Version 8.0 (Baltimore: STScI)

Lutz, D., Poglitsch, A., Altieri, B., et al. 2011, AAP, 532, A90

Madau, P., Ferguson, H. C., Dickinson, M. E., et al. 1996, MNRAS, 283, 1388

Madau, P., Pozzetti, L., & Dickinson, M. 1998, APJ, 498, 106

Madau, P., & Dickinson, M. 2014, ARAA, 52, 415

Maddox, S. J., Efstathiou, G., Sutherland, W. J., & Loveday, J. 1990, MNRAS, 243, 692

Manners, J. C., Johnson, O., Almaini, O., et al. 2003, MNRAS, 343, 293

Marchetti, L., Vaccari, M., Franceschini, A., et al. 2016, MNRAS, 456, 1999

Markwardt, C. B. 2009, Astronomical Data Analysis Software and Systems XVIII, 411, 251

Martin, D. C., Fanson, J., Schiminovich, D., et al. 2005, APJL, 619, L1

Massarotti, M., Iovino, A., Buzzoni, A., & Valls-Gabaud, D. 2001, AAP, 380, 425

Mather, J. C., Cheng, E. S., Eplee, R. E., Jr., et al. 1990, APJL, 354, L37

Matsuhara, H., Wada, T., Matsuura, S., et al. 2006, PASJ, 58, 673

Matsumoto, T., Matsuura, S., Murakami, H., et al. 2005, APJ, 626, 31

Matsuura, S., Shirahata, M., Kawada, M., et al. 2011, APJ, 737, 2

Matute, I., La Franca, F., Pozzi, F., et al. 2002, MNRAS, 332, L11

Mauduit, J.-C., Lacy, M., Farrah, D., et al. 2012, PASP, 124, 1135

McLeod, B., Geary, J., Conroy, M., et al. 2015, PASP, 127, 366

McMahon, R. G., Walton, N. A., Irwin, M. J., et al. 2001, NAR, 45, 97

Minkowski, R. L., & Abell, G. O. 1963, Basic Astronomical Data: Stars and Stellar Systems, 481

Mobasher, B., & Mazzei, P. 2000, AAP, 363, 517

Mortara, L. and Fowler, A., 1981 Proc. SPIE, 290, 28

Moster, B. P., Somerville, R. S., Newman, J. A., & Rix, H.-W. 2011, APJ, 731, 113

Muller, G. P., Reed, R., Armandroff, T., Boroson, T. A., & Jacoby, G. H. 1998, PROC-SPIE, 3355, 577

Murakami, H., Freund, M. M., Ganga, K., et al. 1996, PASJ, 48, L41

Murakami, H., Baba, H., Barthel, P., et al. 2007, PASJ, 59, 369

Murata, K., Matsuhara, H., Wada, T., et al. 2013, AAP, 559, A132

Murata, K., Pearson, C. P., Goto, T., et al. 2014a, MNRAS, 444, 2346

Murata, K., Matsuhara, H., Inami, H., et al. 2014b, AAP, 566, A136

Murayama, T., Mouri, H., & Taniguchi, Y. 2000, APJ, 528, 179

Negrello, M., Hopwood, R., De Zotti, G., et al. 2010, Science, 330, 800

Neugebauer, G., Habing, H. J., van Duinen, R., et al. 1984, APJL, 278, L1

Noeske, K. G., Weiner, B. J., Faber, S. M., et al. 2007, APJL, 660, L43

Noll, S., Burgarella, D., Giovannoli, E., et al. 2009, AAP, 507, 1793

Nugent, C. R., Mainzer, A., Bauer, J., et al. 2016, AJ, 152, 63

Oke, J. B., Cohen, J. G., Carr, M., et al. 1995, PASP, 107, 375

Oliver, S. J., Goldschmidt, P., Franceschini, A., et al. 1997, MNRAS, 289, 471

Oliver, S., Rowan-Robinson, M., Alexander, D. M., et al. 2000, MNRAS, 316, 749

Oliver, S. J., Wang, L., Smith, A. J., et al. 2010, AAP, 518, L21

Oliver, S. J., Bock, J., Altieri, B., et al. 2012, MNRAS, 424, 1614

Onaka, T., Matsuhara, H., Wada, T., et al. 2007, PASJ, 59, 401

Page, M. J., Symeonidis, M., Vieira, J. D., et al. 2012, NAT, 485, 213

Papovich, C., Dole, H., Egami, E., et al. 2004, APJS, 154, 70

Partridge, R. B., & Peebles, P. J. E. 1967, APJ, 148, 377

Patanchon, G., Ade, P. A. R., Bock, J. J., et al. 2009, APJ, 707, 1750

Pearson, C., & Rowan-Robinson, M. 1996, MNRAS, 283, 174

Pearson, C. P. 2001, MNRAS, 325, 1511

Pearson, C. 2005, MNRAS, 358, 1417

Pearson, C. P., Serjeant, S., Negrello, M., et al. 2010, AAP, 514, A9

Pearson, C. P., Serjeant, S., Oyabu, S., et al. 2014, MNRAS, 444, 846

Pearson, C., et al. in prep

Pilbratt, G. L., Riedinger, J. R., Passvogel, T., et al. 2010, AAP, 518, L1

Planck Collaboration, Ade, P. A. R., Aghanim, N., et al. 2011, AAP, 536, A18

Planck Collaboration, Ade, P. A. R., Aghanim, N., et al. 2014, AAP, 571, A1

Planck Collaboration, Ade, P. A. R., Aghanim, N., et al. 2014, AAP, 571, A18

Planck Collaboration, Aghanim, N., Altieri, B., et al. 2015, AAP, 582, A30

Polletta, M., Tajer, M., Maraschi, L., et al. 2007, APJ, 663, 81

Pope, A., Bussmann, R. S., Dey, A., et al. 2008, APJ, 689, 127-133

Popescu, C. C., & Tuffs, R. J. 2009, EAS Publications Series, 34, 247

Pozzi, F., Gruppioni, C., Oliver, S., et al. 2004, APJ, 609, 122

Pozzi, F., Calura, F., Gruppioni, C., et al. 2015, APJ, 803, 35

Puget, J.-L., Abergel, A., Bernard, J.-P., et al. 1996, AAP, 308, L5

Reid, N., & Djorgovski, S. 1993, Sky Surveys. Protostars to Protogalaxies, 43, 125

Riechers, D. A., Bradford, C. M., Clements, D. L., et al. 2013, NAT, 496, 329

Rieke, G. H., Wright, G. S., Böker, T., et al. 2015, PASP, 127, 584

Rodighiero, G., Daddi, E., Baronchelli, I., et al. 2011, APJL, 739, L40

Roseboom, I. G., Oliver, S. J., Kunz, M., et al. 2010,MNRAS, 409, 48

Roseboom, I. G., Ivison, R. J., Greve, T. R., et al. 2012, MNRAS, 419, 2758

Rowan-Robinson, M. 1967, NAT, 216, 1289

Rowan-Robinson, M., Broadhurst, T., Oliver, S. J., et al. 1991, NAT, 351, 719

Rowan-Robinson, M. 1995, MNRAS, 272, 737

Rowan-Robinson, M., Mann, R. G., Oliver, S. J., et al. 1997, MNRAS, 289, 490

Rowan-Robinson, M., Babbedge, T., Oliver, S., et al. 2008a, VizieR Online Data Catalog, 2290,

Rowan-Robinson, M., Babbedge, T., Oliver, S., et al. 2008b, MNRAS, 386, 697

Rowan-Robinson, M., Gonzalez-Solares, E., Vaccari, M., & Marchetti, L. 2013, VizieR Online Data Catalog, 2326,

Rowan-Robinson, M., & May, B. 2013, MNRAS, 429, 2894

Rush, B., Malkan, M. A., & Spinoglio, L. 1993, APJS, 89, 1

Sargent, M. T., Daddi, E., Béthermin, M., et al. 2014, APJ, 793, 19

Saunders, W., Rowan-Robinson, M., Lawrence, A., et al. 1990, MNRAS, 242, 318

Savage, R. S., & Oliver, S. 2007, Astrophysical Journal, 661, 1339

Scaramella, R., Mellier, Y., Amiaux, J., et al. 2015, arXiv:1501.04908

Schaerer, D. 2002, AAP, 382, 28

Scheuer, P. A. G. 1957, in Proceedings of the Cambridge Philisophical Society, 764Ð773

Scott, K. S., Stabenau, H. F., Braglia, F. G., et al. 2010, APJS, 191, 212

Scott, K. S., Yun, M. S., Wilson, G. W., et al. 2010, MNRAS, 405, 2260

Sedgwick, C., Serjeant, S., Pearson, C., et al. 2011, MNRAS, 416, 1862

Serjeant, S., Dunlop, J. S., Mann, R. G., et al. 2003, MNRAS 344, 887

Serjeant, S., Carrami∼nana, A., Gonzáles-Solares, E., et al. 2004, MNRAS, 355, 813

Serjeant, S. 2010, Observational Cosmology, New York, Cambridge University Press

Shupe, D. L., Rowan-Robinson, M., Lonsdale, C. J., et al. 2008, AJ, 135, 1050

Sibthorpe, B., Helmich, F., Roelfsema, P., Kaneda, H., & Shibai, H. 2016, EAS Publications Series, 75, 411

Simcoe, R. A., Metzger, M. R., Small, T. A., & Araya, G. 2000, Bulletin of the American Astronomical Society, 32, 52.09

Skrutskie, M. F., Cutri, R. M., Stiening, R., et al. 2006, AJ, 131, 1163

Smoot, G. F., Bennett, C. L., Kogut, A., et al. 1991, APJL, 371, L1

Soifer, B. T., Neugebauer, G., & Houck, J. R. 1987, ARAA, 25, 187

Solarz, A., Pollo, A., Takeuchi, T. T., et al. 2012, AAP, 541, A50

Somerville, R. S., Lee, K., Ferguson, H. C., et al. 2004, APJL, 600, L171

Stern, D., Eisenhardt, P., Gorjian, V., et al. 2005, APJ, 631, 163

Stoughton, C., Lupton, R. H., Bernardi, M., et al. 2002, AJ, 123, 485

Surace, J. A., Shupe, D. L., Fang, F., et al. 2005, Bulletin of the American Astronomical Society, 37, 63.01

Takagi, T., Hanami, H., & Arimoto, N. 2004, MNRAS, 355, 424

Takagi, T., & Pearson, C. P. 2005, MNRAS, 357, 165

Takagi, T., Ohyama, Y., Goto, T., et al. 2010, AAP, 514, A5

Tanabé, T., Sakon, I., Cohen, M., et al. 2008, PASJ, 60, 375

Tauber, J. A., Mandolesi, N., Puget, J.-L., et al. 2010, AAP, 520, A1

Taylor, M. B. 2005, Astronomical Data Analysis Software and Systems XIV, 347, 29

Teplitz, H. I., Chary, R., Elbaz, D., et al. 2011, AJ, 141, 1

Tombesi, F., Meléndez, M., Veilleux, S., et al. 2015, NAT, 519, 436

Tsumura, K., Matsumoto, T., Matsuura, S., Sakon, I., & Wada, T. 2013, PASJ, 65,

Usui, F., Kuroda, D., Müller, T. G., et al. 2011, PASJ, 63, 1117

Vaccari, M., Marchetti, L., Franceschini, A., et al. 2010, AAP, 518, L20

Vaccari, M. 2016, arXiv:1604.02353

Väisänen, P., Morel, T., Rowan-Robinson, M., et al. 2002, MNRAS, 337, 1043

Valiante, E., Ade, P. A. R., Bock, J. J., et al. 2010, APJS, 191, 222

Viero, M. P., Wang, L., Zemcov, M., et al. 2013, APJ, 772, 77

Vio, R., Tenorio, L., & Wamsteker, W. 2002, AAP, 391, 789

Wada, T., Matsuhara, H., Oyabu, S., et al. 2008, PASJ, 60, 517

Weiß, A., Kovács, A., Coppin, K., et al. 2009, APJ, 707, 1201

Werner, M. W., Roellig, T. L., Low, F. J., et al. 2004, APJS, 154, 1

White, G. J., Hatsukade, B., Pearson, C., et al. 2012, MNRAS, 427, 1830

White, S. D. M., & Rees, M. J. 1978, MNRAS, 183, 341

Wiegert, P. A., Innanen, K. A., & Mikkola, S. 1997, Nature, 387, 685

Wilson, J. C., Eikenberry, S. S., Henderson, C. P., et al. 2003, PROCSPIE, 4841, 451

Wright, E. L., & Reese, E. D. 2000, APJ, 545, 43

Wright, E. L., Eisenhardt, P. R. M., Mainzer, A. K., et al. 2010, AJ, 140, 1868

Yoshii, Y., & Takahara, F. 1988, APJ, 326, 1

Appendix A

IRAC Dark Field and ELAIS N1 SEDs

Below are the IRAC Dark Field and ELAIS-N1 SEDs fitted in the work of Chapter 5.

The ID refers to the original galaxy ID from the cross-matching.

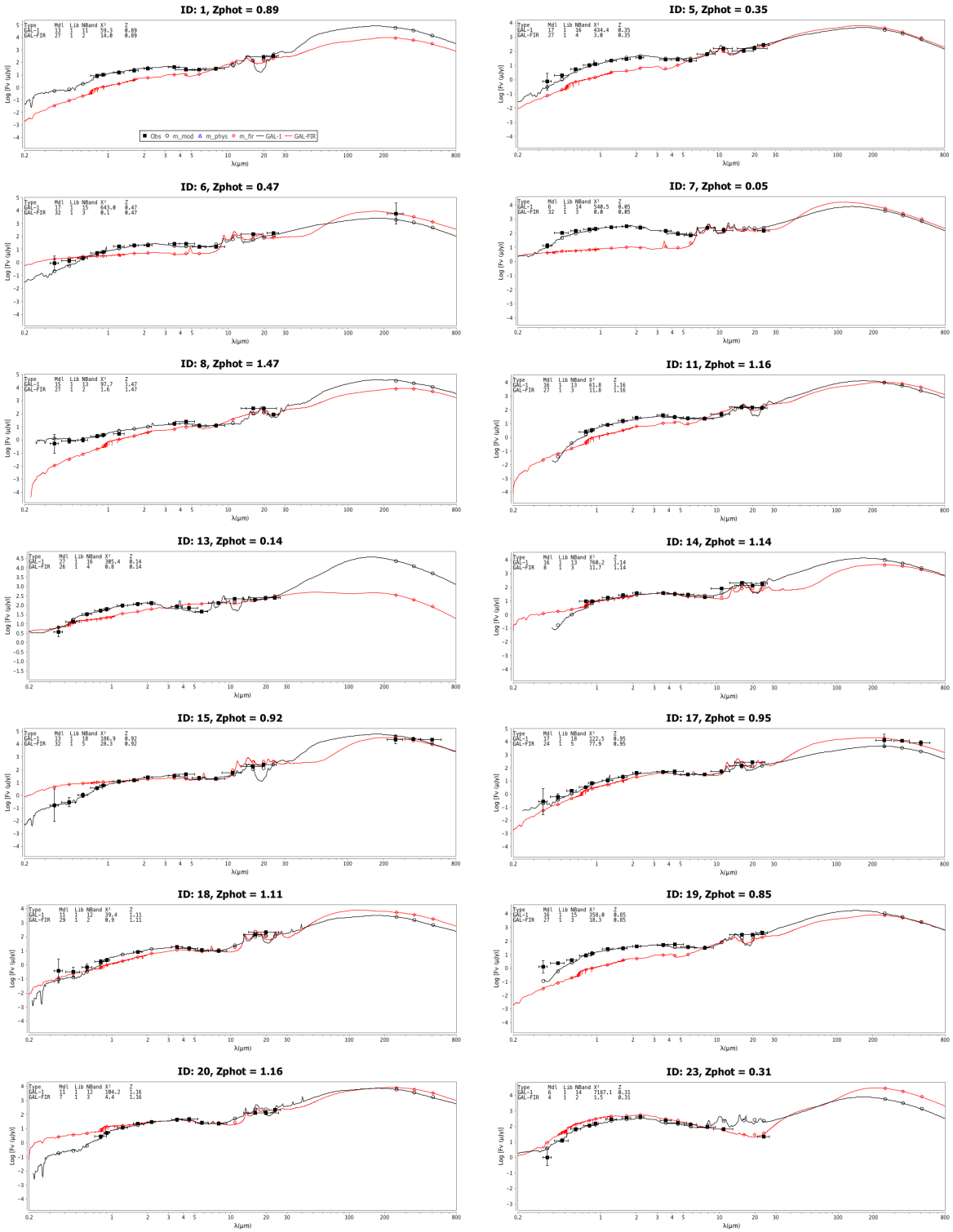

Figure A.1: IRAC Dark Field SEDs 1 - 14

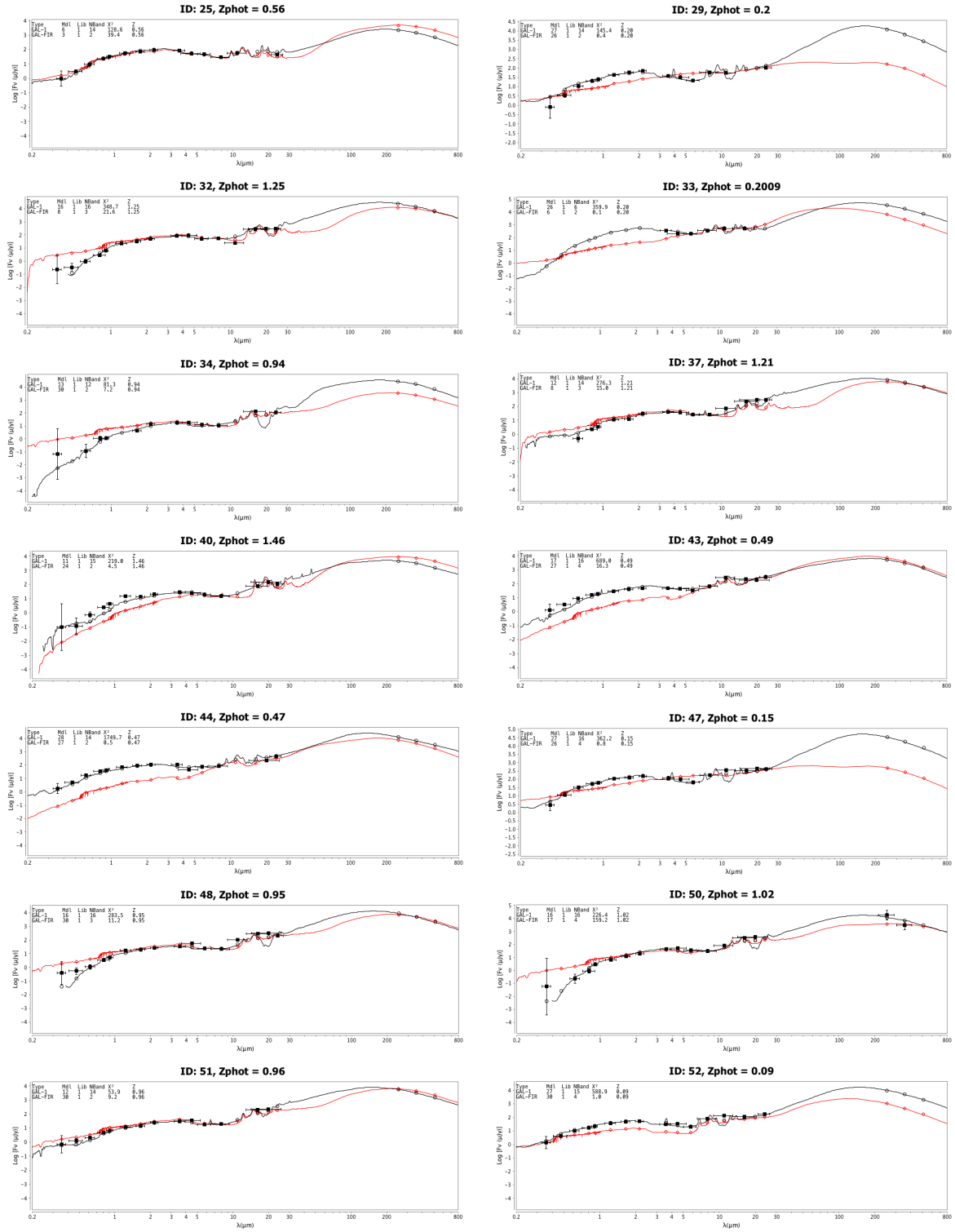

Figure A.2: IRAC Dark Field SEDs 15 - 28

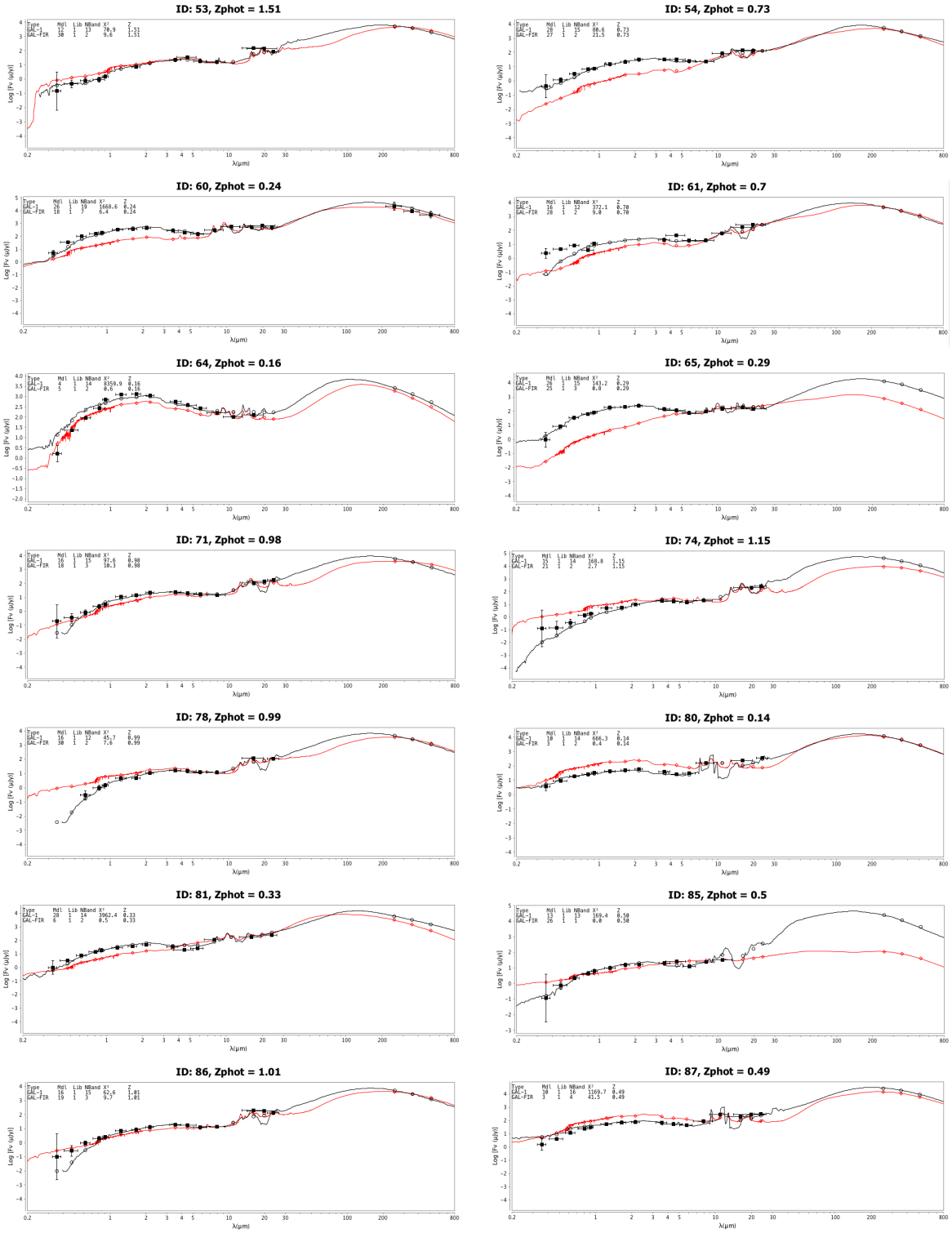

Figure A.3: IRAC Dark Field SEDs 29 - 42

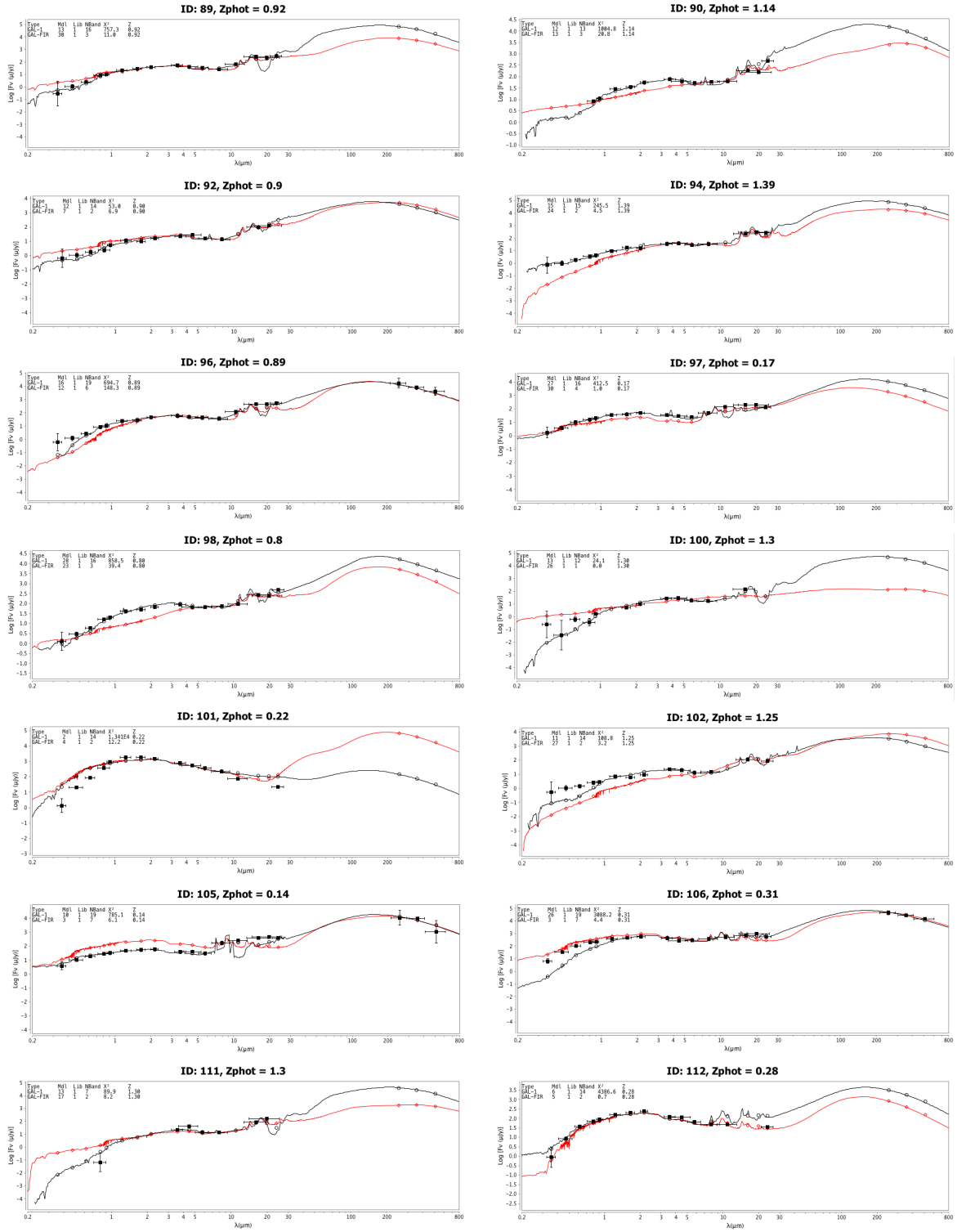

Figure A.4: IRAC Dark Field SEDs 43 - 56

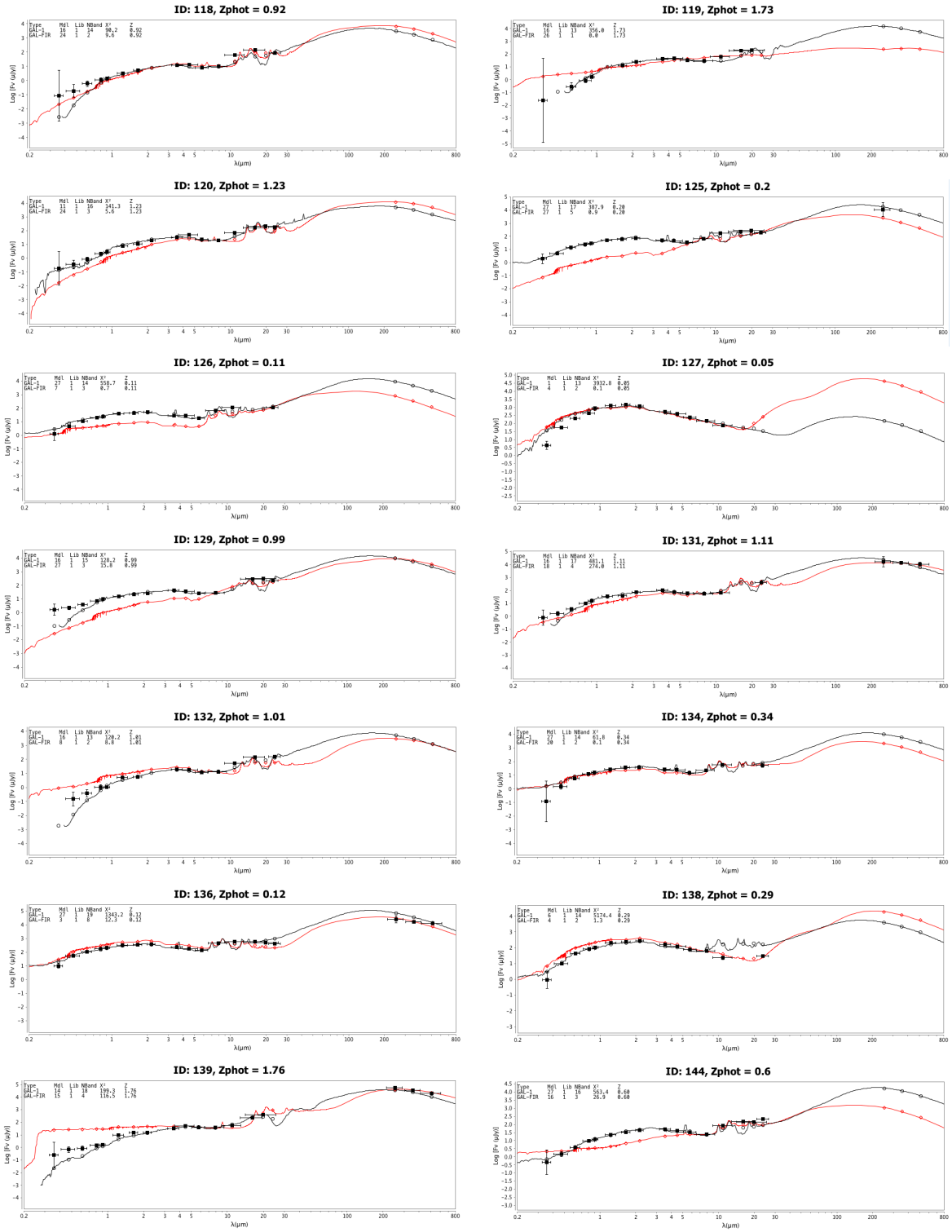

Figure A.5: IRAC Dark Field SEDs 57 - 70

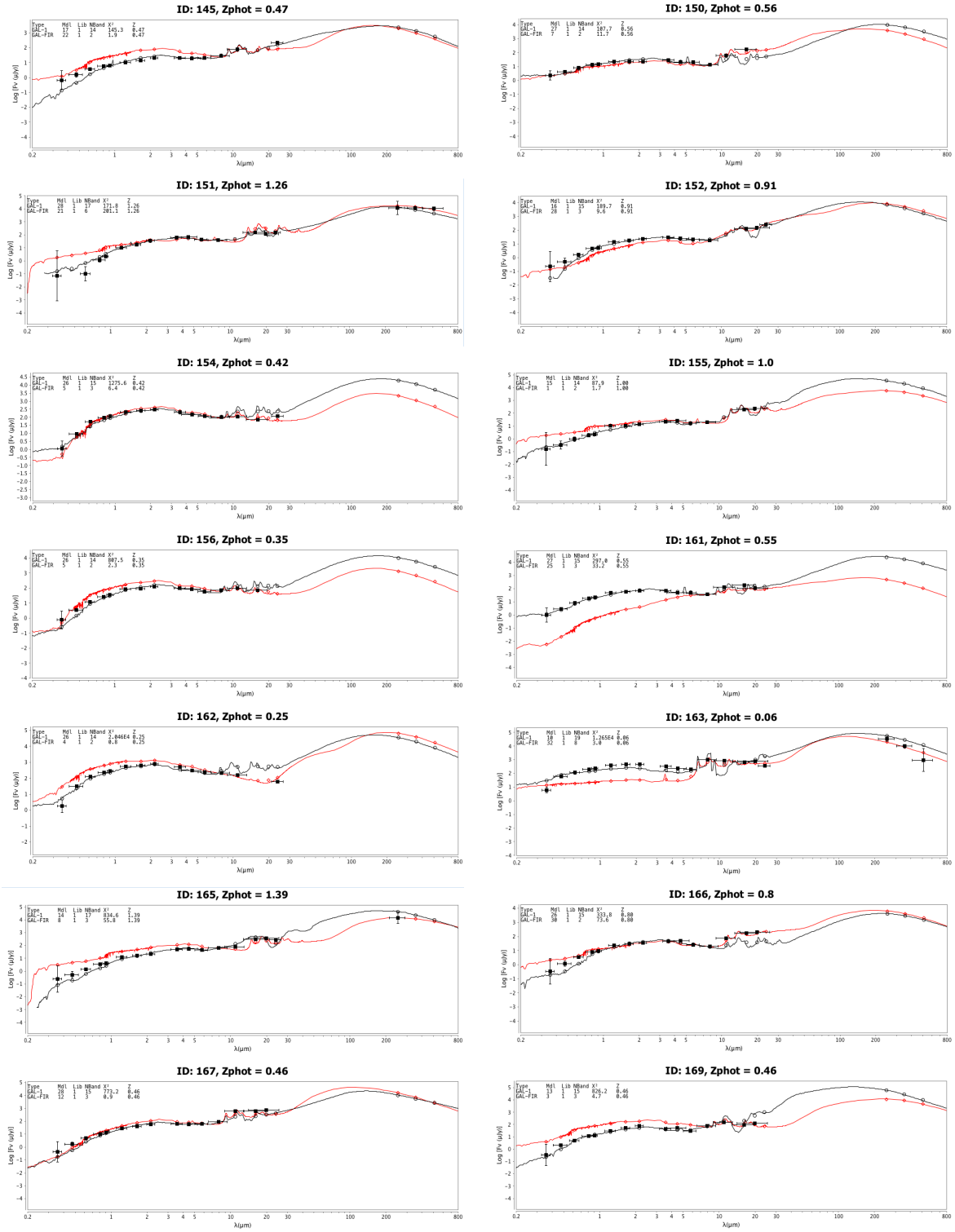

Figure A.6: IRAC Dark Field SEDs 71 - 84

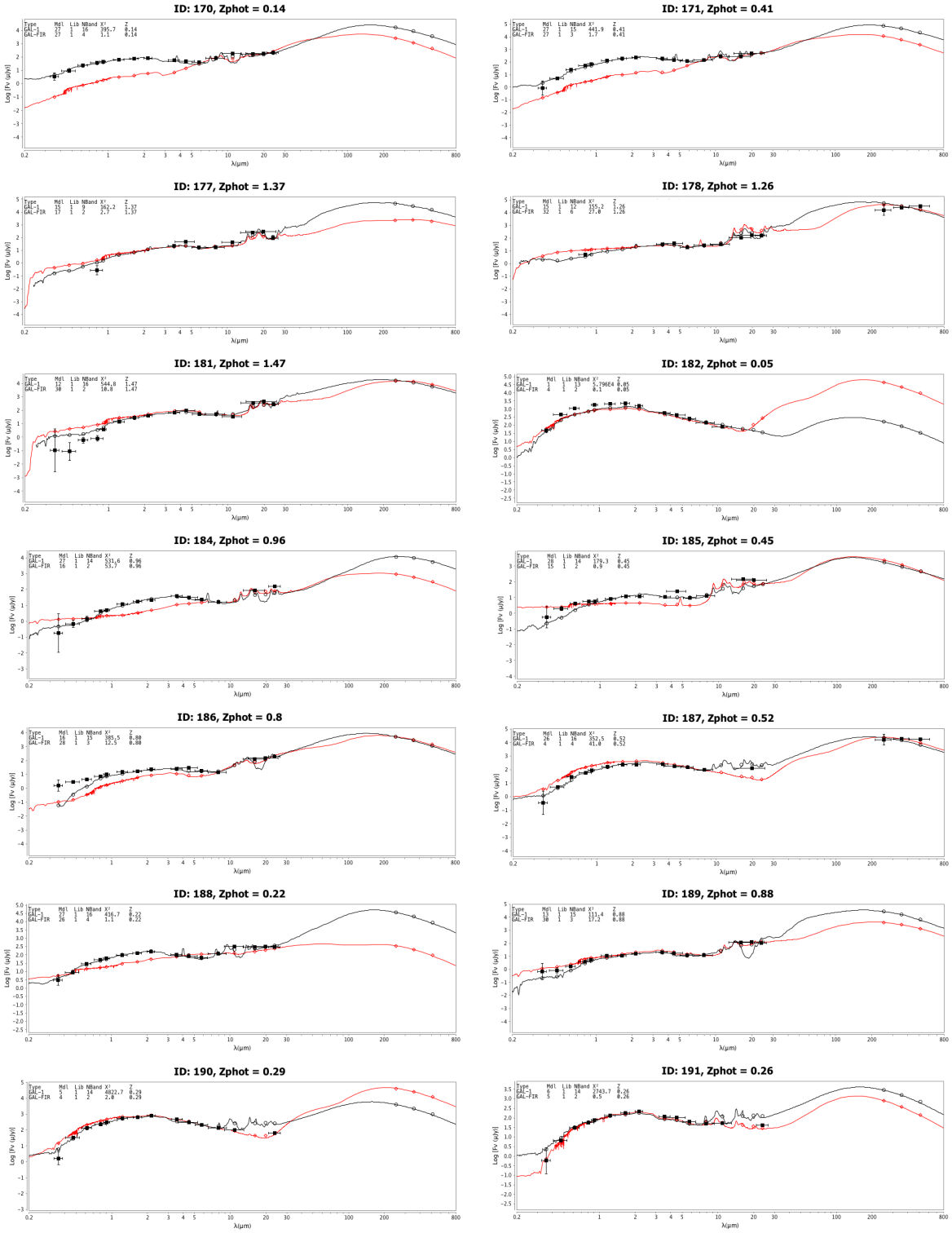

Figure A.7: IRAC Dark Field SEDs 85 - 98

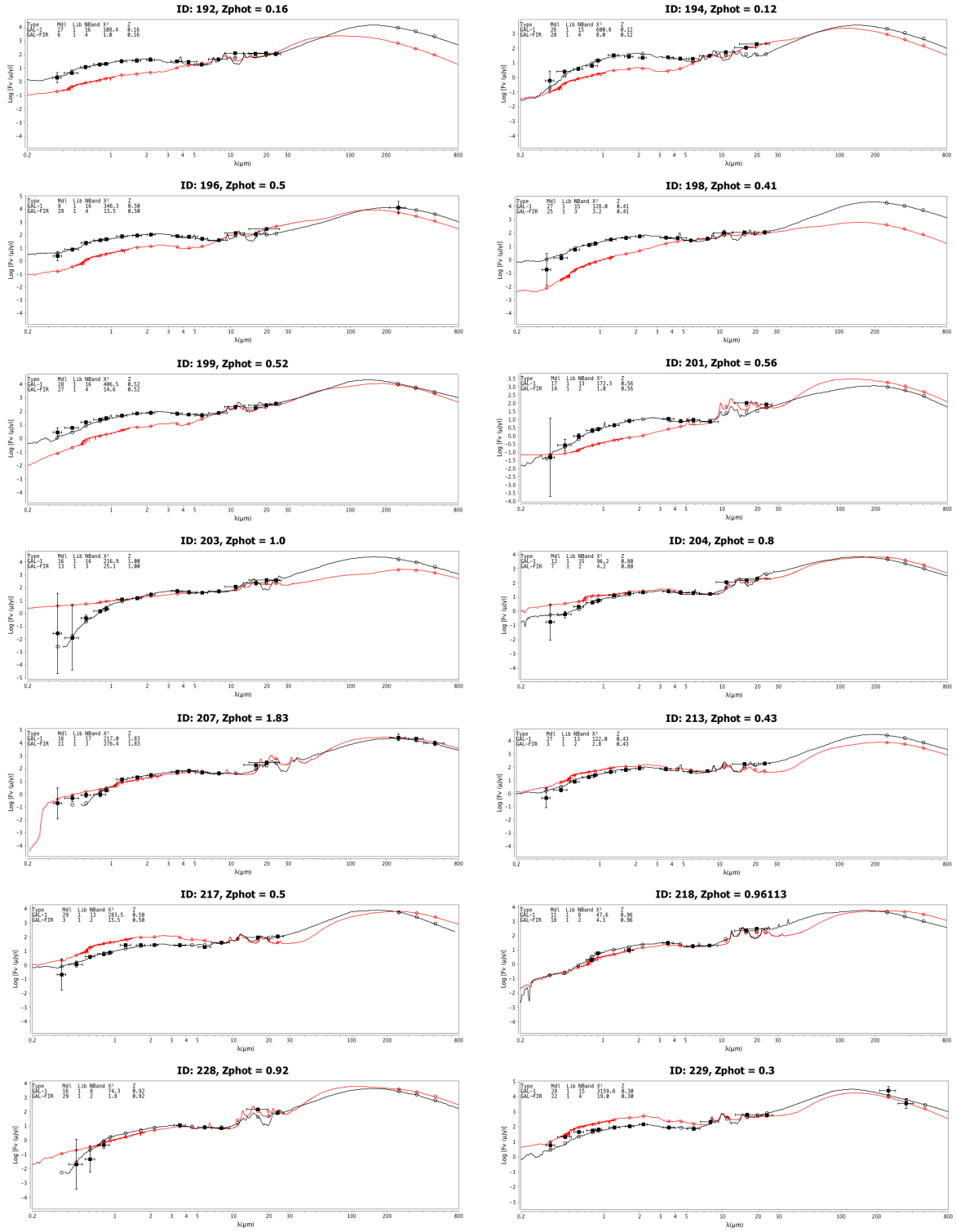

Figure A.8: IRAC Dark Field SEDs 99 - 112

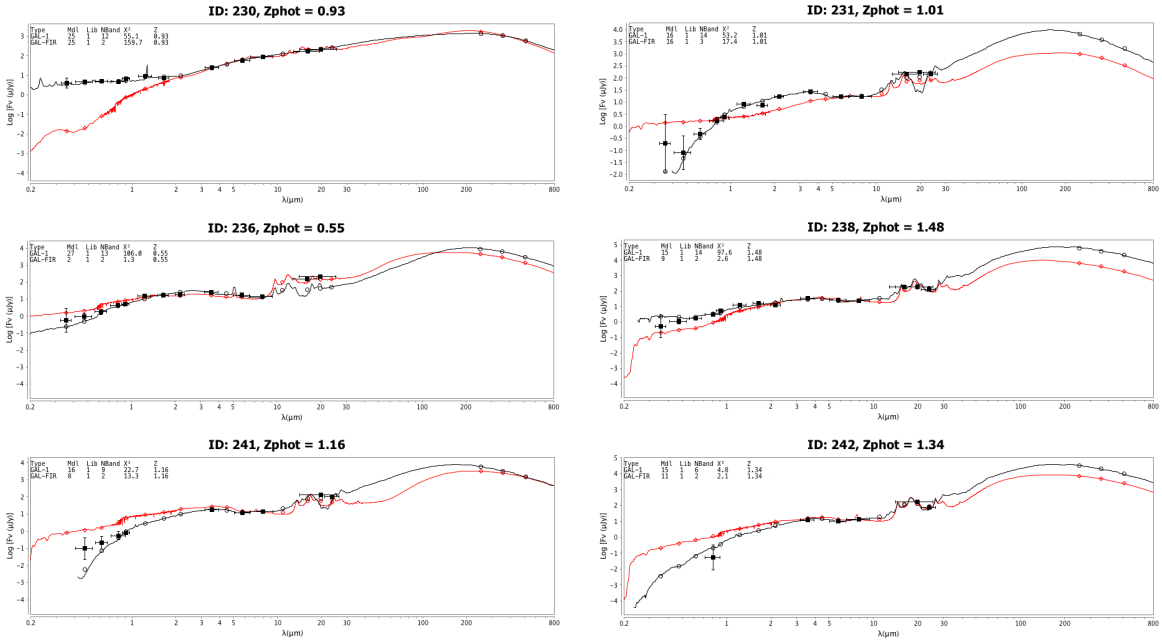

Figure A.9: IRAC Dark Field SEDs 113 - 118

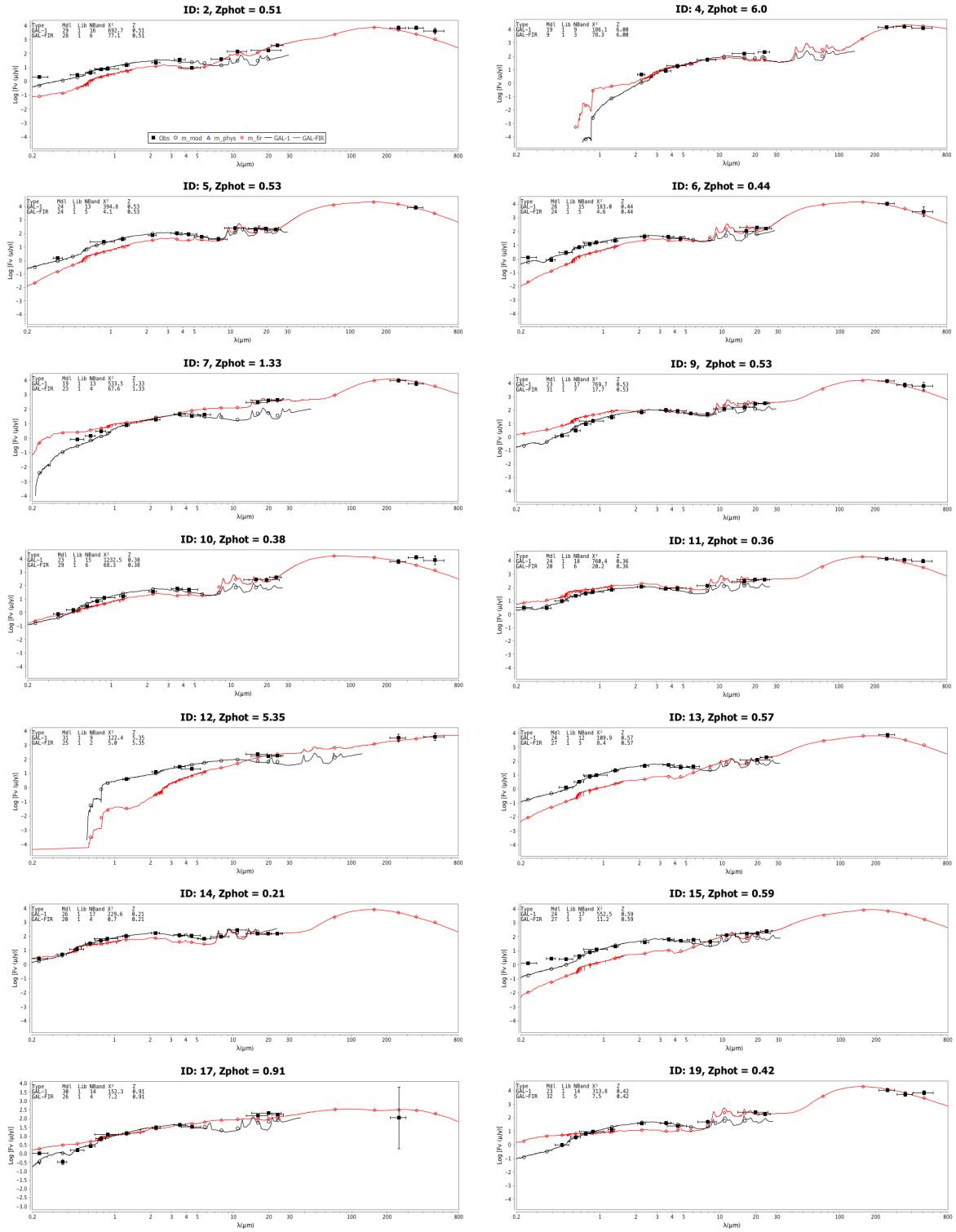

Figure A.10: ELAIS-N1 SEDs 1 - 14

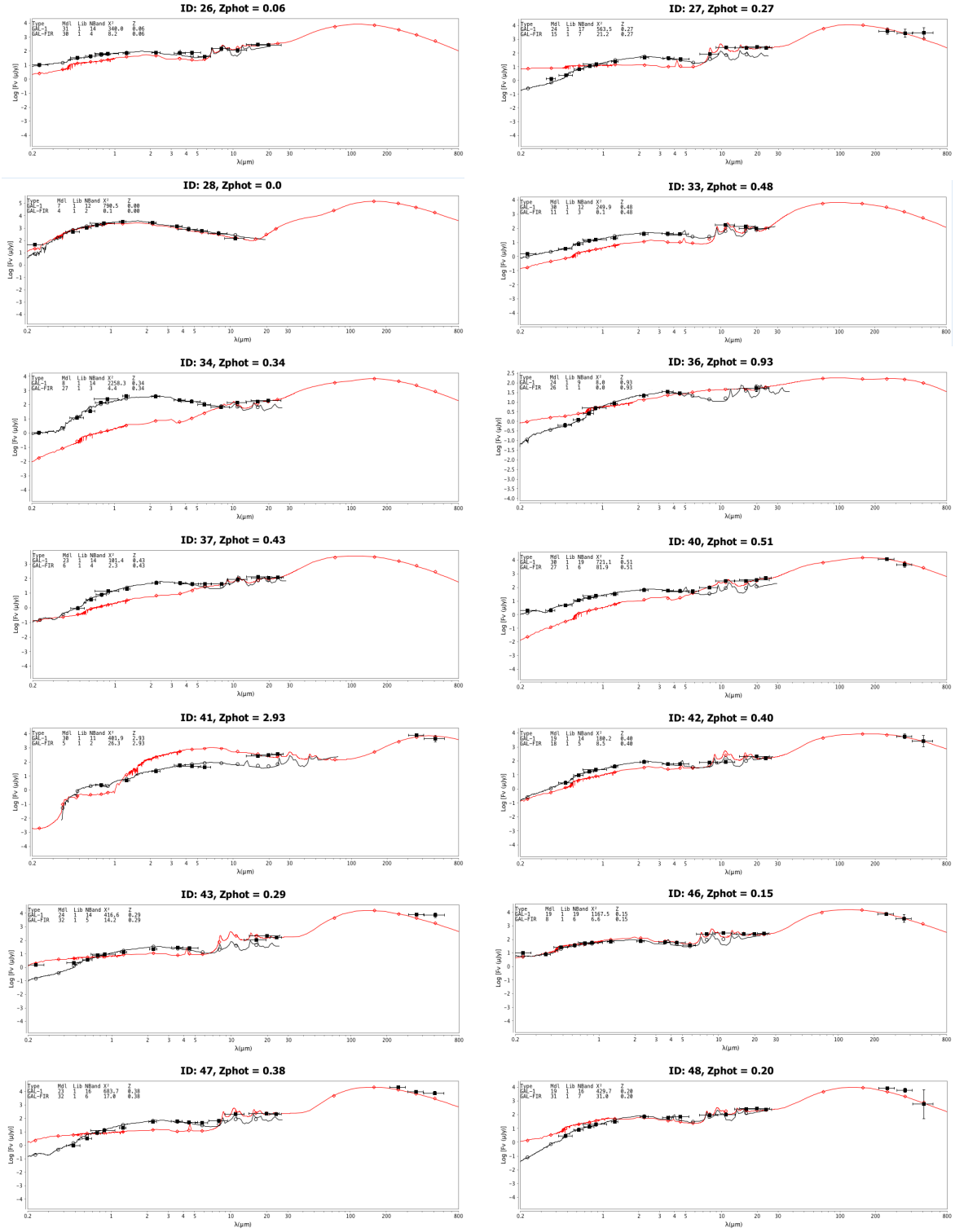

Figure A.11: ELAIS-N1 SEDs 15 - 28

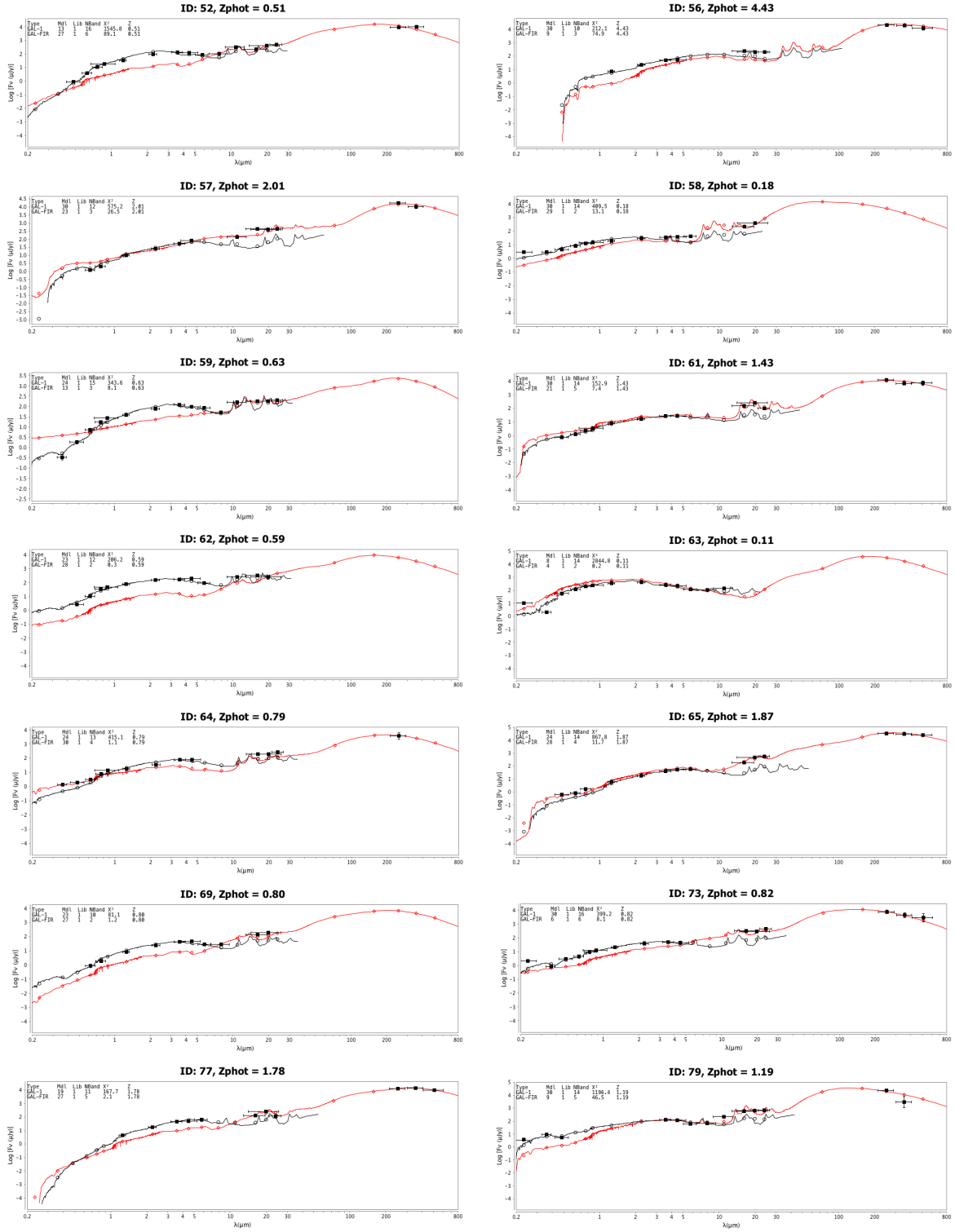

Figure A.12: ELAIS-N1 SEDs 20 - 42

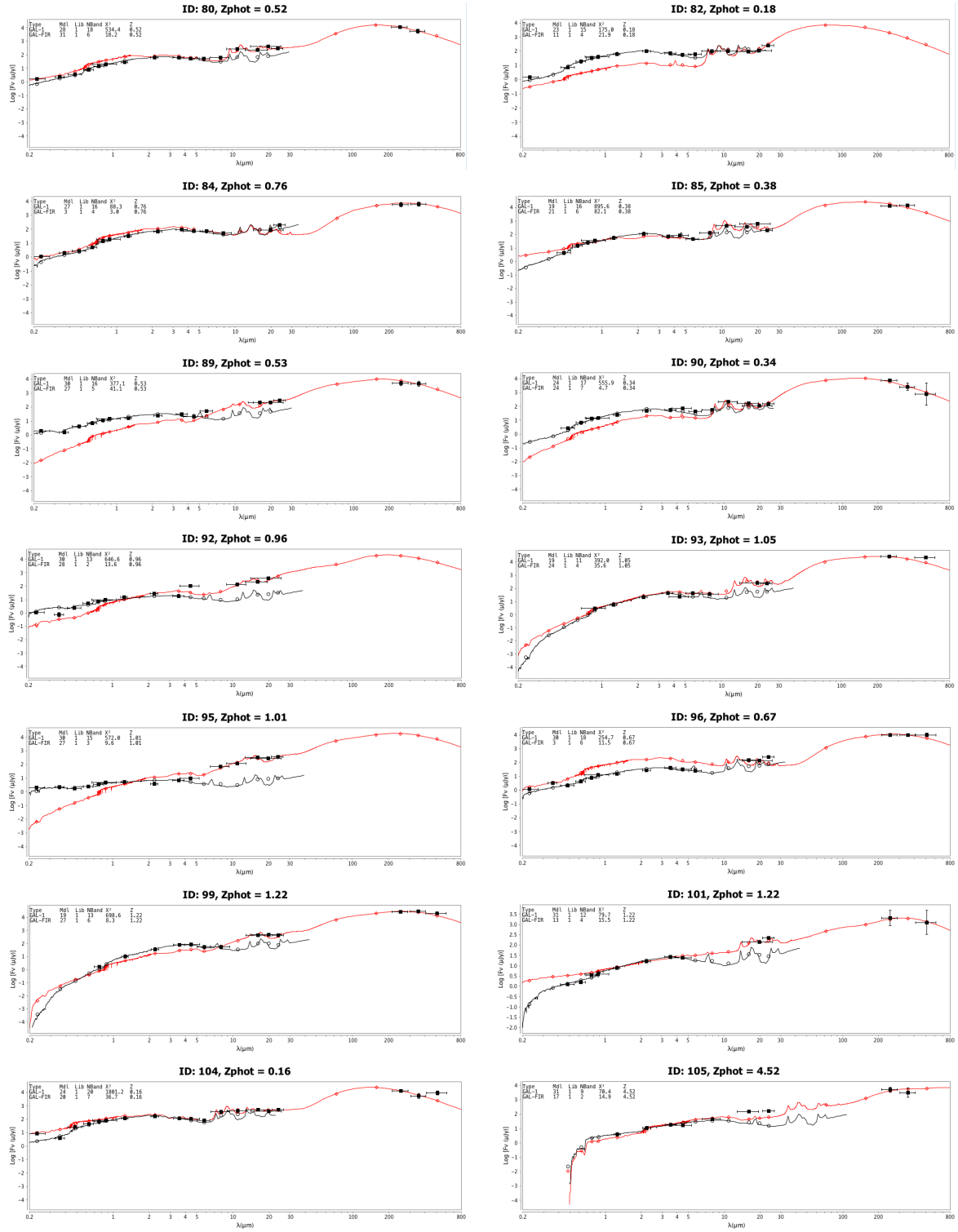

Figure A.13: ELAIS-N1 SEDs 43 - 56

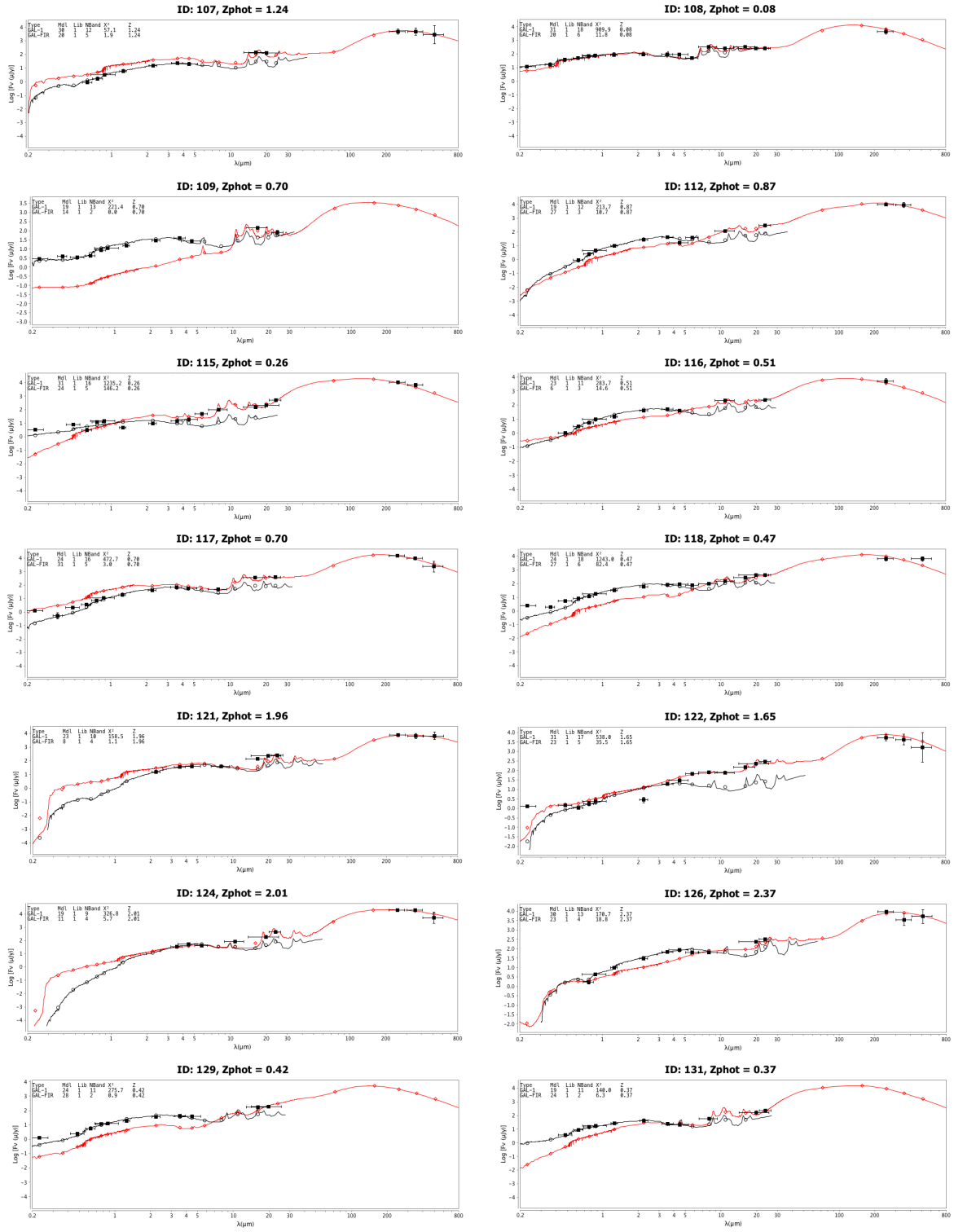

Figure A.14: ELAIS-N1 SEDs 57 - 70

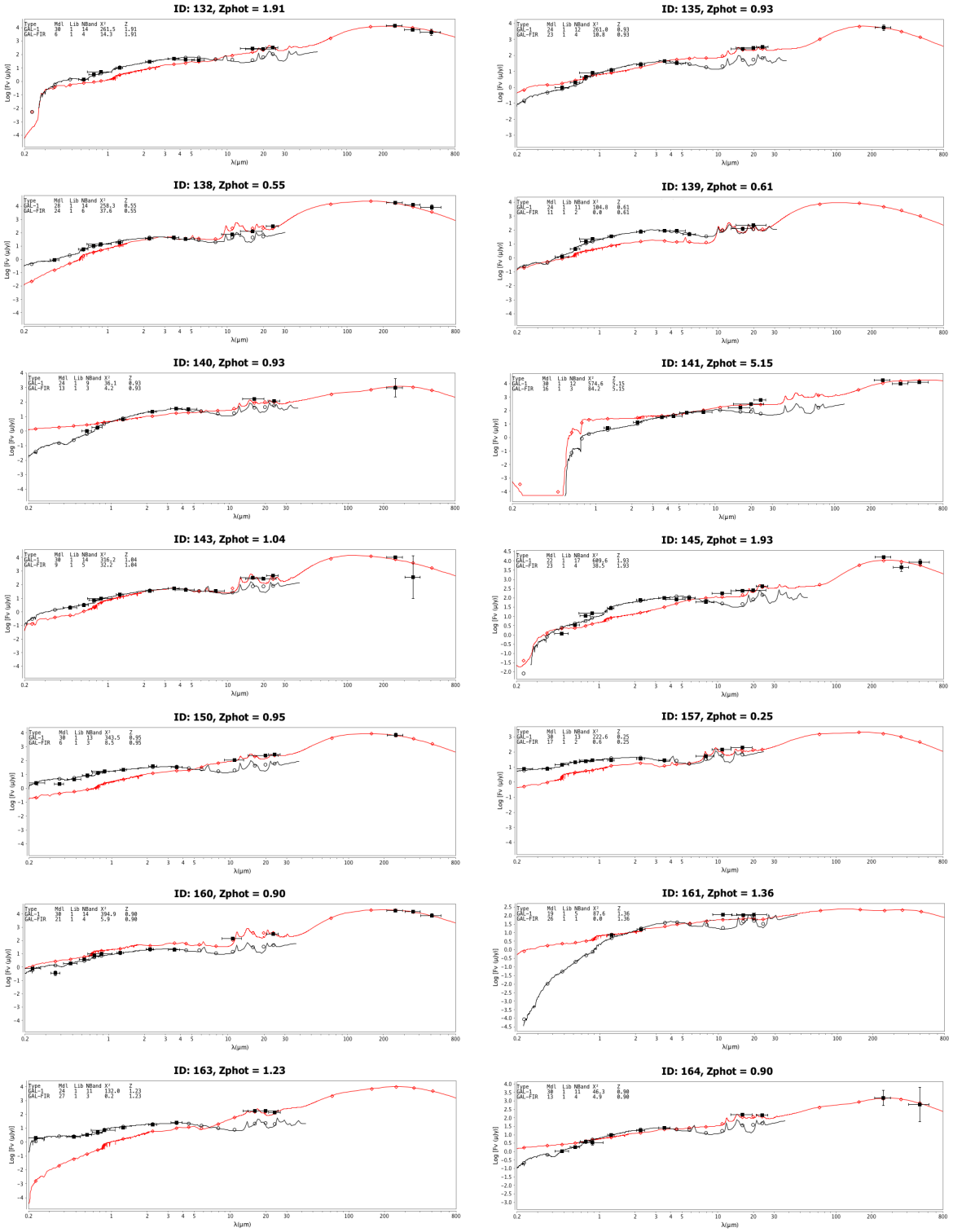

Figure A.15: ELAIS-N1 SEDs 71 - 84

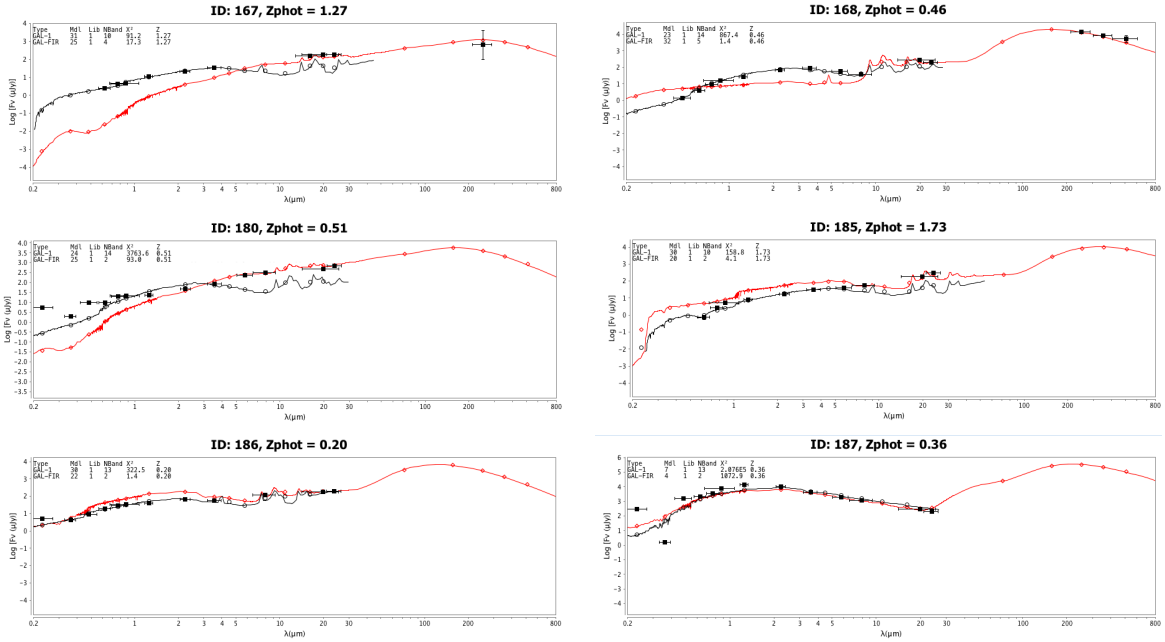

Figure A.16: ELAIS-N1 SEDs 85 - 90